Characterisation of focused ion beam nanostructures by transmission electron microscopy

Susan B. Turnbull M.Sci

Presented as a thesis for the degree of Ph.D. at the
Department of Physics and Astronomy, University of Glasgow
September 2008

Abstract

Ion irradiation is an effective tool for the modification and control of the properties of magnetic thin films. Basic magnetic properties such as coercivity and local anisotropy direction can be altered in NiFe (Permalloy) films, whilst for Co/Pd multilayers, ion irradiation results in a transition from perpendicular to in-plane magnetisation. This ability to tailor magnetic properties in a controlled manner can be used as a tool for nanoscale patterning.

Results are presented from investigations into the effect of Ga^+ ion dose on the magnetic and structural properties of permalloy thin film systems. Systems consisting of a permalloy layer of either 10nm or 20nm, and one or more non-magnetic layers of Al or Au were deposited by thermal evaporation and irradiated in a focused ion beam (FIB) with a 30kV Ga^+ source. The presence of the non-magnetic layers allows irradiation induced mixing with the magnetic layer, effectively creating alloyed regions with different properties to the rest of the film. At low ion doses, no significant effect on either the magnetic or structural properties were observed. Bright field TEM images of the irradiated regions revealed that increasing the dose to 1×10^{15} ions cm^{-2} and above caused an increase in mean grain size from $\sim$5nm to $\sim$30nm. The Fresnel mode of Lorentz microscopy revealed that a reduction in the mean moment was also observed at these doses but no clear changes in coercivity or magnetisation reversal behaviour were observed until the systems were rendered non-magnetic. This occured at 1×10^{16} and 3×10^{16} ions cm^{-2} for systems with 10nm NiFe and 20nm NiFe respectively. Milling of the samples was evident at these high doses, meaning that it was not possible to magnetically pattern these systems without occasioning a change of 2nm and 6nm respectively in the thickness of the samples.

Based on the above, structures were created to control the location of magnetic domain walls (DW). Lines were written by FIB in simple elements with dimensions $<1\mu$m, the aim being to create a higher density of DW than could be realised in equivalent homogeneous elements. Structures containing high DW densities are attractive for measuring domain wall magnetoresistive effects and have potential application in DW-based storage or logic devices. One geometry of interest is an element with 'zigzag' edges. Results are be presented in chapter 4 showing how these can support either quasi-uniform magnetisation or multi-domain structures separated by DW with spacing <100nm.

In chapter 5 irradiation of magnetic structures was again carried out, but this time

on magnetic wires to create defect or pinning sites. Domain wall traps fabricated by ion irradiation were characterised, and irradiation line defects introduced along the wire. The lines were patterned at 90° and 45° to the length of the wire, and successfully pinned the domain walls at predefined locations. A 90° wall irradiated at a dose of 1×10^{15} ions cm^{-2} was not able to provide a strong enough pinning site for a domain wall. However, when the angle of the line was changed to ±45° it was possible to reproducibly pin domain walls at these sites. A relationship between the orientation of the irradiated line and the chirality of the domain wall that pinned at the site was observed.

The effects of irradiation on Co/Pd multilayers with perpendicular magnetic anisotropy was investigated in chapter 6. Irradiation causes magnetic systems with perpendicular magnetisation to undergo a transition from out-of-plane magnetisation to in-plane. A grid pattern was devised so that magnetic states with both in-plane and out-of-plane magnetisation could be observed. A combination of differential phase contrast microscopy and simulations of integrated magnetic induction were used to determine the orientation of magnetisation within the lines.

Acknowledgements

Firstly I would like to thank my supervisors Dr. Stephen McVitie and Professor John Chapman for giving me the opportunity to to work on this project. Their guidance and patience over the years has been greatly appreciated.

I must also say a very big thankyou to Dr. Damien McGrouther for his all his help with the ion irradiation work and all things FIB related. (I'm so glad you came back from Australia!) To Dr. Nils Wiese and Dr. Donald MacLaren, I am grateful for many a useful discussion about my work, but also for many a social discussion over a drink or two out in the west end. For his continued efforts to keep all equipment in the group up and running I am very grateful to Dr. Sam McFadzean, and for help on the FIB and T20 I would like to thank Billy Smith and Colin How.

I would also like to thank my office mates past and present, Aurelie, Catriona and Rafael for being great company and for putting up with me for as long as you all did. Thankyou to all SSP group members, who have been welcoming from the very start. I have thoroughly enjoyed all our group days out and other social events. A quick thankyou to Paolo for his company on our trip to San Francisco, I had such a great time and I'll never look at another pair of white jeans the same again!

I would like to say thankyou to all staff and management at Work Directions in Edinburgh, who have been unbelievably supportive and understanding over the past few months.

I would also like to thank my Mum and Dad for supporting me throughout my education, and for going out of their way to always be there for me when I needed them (even when it meant cutting short weekends away or driving back and forwards across the country to pick up all the things I had forgotten!) Also, thanks to my sister Gillie for all her encouraging messages and thoughtful gifts which helped to keep me going.

Finally, a special mention for Alan who went through it all with me, right from day one!

Declaration

This thesis is a record of the work carried out by myself in the Solid State Physics Group of the Department of Physics and Astronomy at the University of Glasgow during the period 2004 - 2008. The work described herein is my own with the exception of the deposition of the 'trilayer' samples described in chapter 3, which was performed by Dr. Mark Hickey at the University of Leeds in the UK, and the Co/Pd multilayer films which were deposited by and Dr. Justin Shaw at the National Institute of Standards and Technology (NIST), USA.

Some of the work in this thesis has been presented at the following conferences -

1. **'Control of domain structure in magnetic thin films by FIB'**
   2007 Materials Research Society Spring Meeting, San Francisco, CA, USA
   This talk was awarded a Gold Award by the symposium organisers.

2. **'Applications of DualBeam FIB in nanomagnetics'**
   NanoFIB Network Meeting 2007, Manchester, UK
   Invited presentation

3. **'Creation of high density domain structures in permalloy by FIB'**
   2007 Electron Microscopy and Analysis Group Meeting, Glasgow, UK
   This talk was awarded one of three prizes for best student talk.

This thesis has not previously been submitted for a higher degree.

Contents

Abstract i

Acknowledgements iii

Declaration iv

Contents v

1 Properties of ferromagnetic thin films 1

1.1 Introduction 1

1.2 Ferromagnetism in thin films 2

1.3 Magnetic energy terms 3

1.3.1 Exchange energy 3

1.3.2 Anisotropy energy 4

1.3.2.1 Magnetocrystalline anisotropy 4

1.3.2.2 Shape anisotropy 5

1.3.3 Zeeman energy 6

1.3.4 Magnetostatic energy 7

1.3.5 Magnetostriction 8

1.3.6 Domain wall energy 9

1.3.7 Total energy 10
1.4 Magnetisation reversal 11
1.4.1 Hysteresis loop 11
1.4.2 Reversal mechanisms 12
1.5 Effects of ion irradiation on magnetic thin films 13
1.6 Controlling domain walls in magnetic structures 15
1.7 Summary 17

2 Instrumentation and experimental techniques 23

2.1 Introduction 23
2.2 Thin film deposition 24
2.2.1 Thermal evaporation 24
2.2.2 DC sputtering 25
2.3 Transmission electron microscopy (TEM) 27
2.3.1 The TEM 28
2.3.1.1 Electron sources 28
2.3.1.2 The electron column 29
2.3.2 Structural characterisation 31
2.3.2.1 Diffraction 31
2.3.2.2 Bright field & dark field imaging 32
2.4 Magnetic imaging 33
2.4.1 Lorentz microscopy 33
2.4.1.1 Fresnel mode 34
2.4.1.2 Differential phase contrast 36
2.4.1.3 Magnetising experiments 37

2.5 Focused ion beam (FIB) . . . 39
2.5.1 The FIB instrument . . . 39
2.5.2 DualBeam FIB . . . 41
2.5.3 FIB irradiation . . . 43
2.5.3.1 Patterning method . . . 45
2.6 Simulations . . . 46
2.6.1 Stopping range of ions in matter (SRIM) . . . 47
2.6.2 Tridyn . . . 48
2.6.3 Micromagnetic simulations . . . 49
2.6.4 Fresnel image calculation . . . 51

3 Effect of Ga^+ ion irradiation on permalloy multilayers 57

3.1 Introduction . . . 57
3.1.1 Magnetic thin film systems . . . 58
3.1.2 Simulations . . . 59
3.2 Properties of the multilayer systems in the as-deposited state . . . 62
3.2.1 Structural properties of the as-deposited state . . . 62
3.2.2 Magnetic properties of the as-deposited state . . . 64
3.2.2.1 Easy axis behaviour . . . 65
3.2.2.2 Hard axis behaviour . . . 68
3.3 Irradiation method . . . 71
3.4 Irradiation induced alteration on the properties of the multilayer systems . . . 72
3.4.1 Effect of ion irradiation on the physical microstructure . . . 72
3.4.1.1 Grain analysis . . . 72

3.4.1.2 Irradiation induced milling 75

3.4.2 Effect of ion irradiation on magnetic properties 76

3.4.2.1 Reversal of regions irradiated at 1×10^{13} - 1×10^{14} ions cm^{-2} 77

3.4.2.2 Reversal of regions irradiated at 3×10^{14} - 3×10^{15} ions cm^{-2} 80

3.4.2.3 Reversal for doses $> 1\times10^{16}$ ions cm^{-2} 81

3.4.2.4 Effect of irradiation on the magnetic properties of trilayer system 84

3.4.2.5 Summary of effects on magnetic behaviour 89

3.5 Discussion 90

4 Patterning ferromagnetism by FIB for the creation of high density domain structures 95

4.1 Introduction 95

4.1.1 Control of magnetisation direction in magnetic structures . 96

4.2 The 'zigzag' element concept 98

4.3 Micromagnetic simulations of domain states in the 'zigzag' element 99

4.3.1 Introduction of de-coupling lines 100

4.4 Ion beam fabricated zigzag elements 102

4.4.1 Physical characterisation of structures 103

4.4.2 Magnetic characterisation 106

4.5 Discussion 111

5 Domain wall trap structures with irradiated pinning sites 118

5.1 Introduction 118

5.1.1 Domain walls in wires 119

5.2 Creation of domain wall trap structures by focused ion beam . . . 121

5.2.1 Domain wall traps with irradiation induced pinning sites . 124

5.2.1.1 Vertical irradiated pinning sites 124

5.2.1.2 Variation of the orientation of irradiated pinning sites 127

5.3 Magnetic nano-wires with ellipse injection pads 129

5.3.1 Experimental structures 132

5.4 Discussion 136

6 Ion irradiation of perpendicularly magnetised Co/Pd multilayers 141

6.1 Introduction 141

6.2 Co/Pd multilayer system 142

6.3 Geometry of magnetisation in irradiated lines 144

6.4 Simulations of magnetic configurations in irradiated Co/Pd films . 146

6.4.1 Zero moment in irradiated lines 146

6.4.2 Irradiated lines with perpendicular magnetisation 148

6.4.3 Irradiated lines with in-plane magnetisation 151

6.5 Experimental results 152

6.6 DPC results 156

6.7 Conclusions 159

7 Conclusions & future work 164

7.1 Conclusions 164

7.2 Future work 167

Chapter 1

Properties of ferromagnetic thin films

1.1 Introduction

Ion irradiation has been used as a tool for the modification of materials since the 1950's [1]. More recently it has been applied to magnetic thin film systems with a view to gaining control over their magnetic and structural properties [2]. This ability to tailor magnetic properties has been used to create patterned magnetic thin films by irradiation through a mask or directly by a focused ion beam [3, 4]. Non-topographical patterning or purely magnetic patterning, was first demonstrated in 1998 [2] and has been shown to have much potential in the field of magnetoelectronics, particularly in circumstances where planarity of the medium surface is important. Topographic patterning by the sputtering of material is also an important technique due to applications in magnetic data storage and magnetic sensors.

Both patterning techniques described above have been used during the course of this research to create magnetic structures in which magnetic domain structure and magnetic domain walls may be investigated. As well as defining the magnetic structures that are investigated, ion irradiation is used to modify regions of the structures so as to further influence the magnetic behaviour. By this method, a single element can be influenced to form a multi-domain state with domain walls at predefined locations. Irradiation was also used to create artificial pinning sites in magnetic wires, so that the nucleation, propagation and location of the domain

walls within the wire can be studied.

As an introduction to this research, this chapter deals with the basic concept of ferromagnetism, the various energy terms which govern magnetic behaviour in ferromagnetic thin film systems, and magnetisation reversal processes. Ion irradiation and developments in magnetic patterning are discussed further in sections 1.5 and 1.6.

1.2 Ferromagnetism in thin films

Ferromagnetic materials are those which have non-zero magnetic moment in the absence of an applied magnetic field. They may initially have zero moment, but after exposure to a magnetic field, they commonly retain a net magnetic moment along the direction in which the field was applied [5]. This remanent magnetisation, M_R, is due to the preference for parallel alignment of the individual magnetic moments of the atoms. The magnetic moment originates from the interaction of the spin and orbital motion of the electrons, and the total magnetic moment of a material is equal to the vector sum of all the moments within it. In 1907, Weiss [6] described the interaction between neighbouring moments by an internal molecular field, H_m, which is proportional to the magnetisation, M, in the material. Heisenberg [7] then demonstrated that the alignment of the magnetic moments could be explained by taking a quantum mechanical approach where the internal field is due to the interaction of unpaired electrons on adjacent atoms. This exchange interaction is discussed further in section 1.3.1.

The maximum net moment that a ferromagnetic material may attain is known as the saturation magnetisation $\mathbf{M}_S$, and occurs when all the moments in the system are aligned parallel in a sufficiently large magnetic field. It is generally much higher than the remanent magnetisation. The difference between saturation and remanent magnetisation can be explained by the formation of local regions where the magnetisation is uniform but differently orientated. Known as magnetic domains, these form when the material relaxes to its remanent state, and are a result of the high magnetostatic energy cost (section 1.3.4) of the saturated state. Magnetic domains and reversal processes are discussed in section 1.4.

1.3 Magnetic energy terms

There are many magnetic energy terms to be considered when describing a magnetic thin film system and its behaviour [8] and which govern the way the film responds to an externally applied magnetic field. These terms include the interaction between adjacent atomic moments (the exchange energy), the preference of moments to lie along certain crystallographic orientations (anisotropy energy), the energy of the individual atomic moments due to the presence of a magnetic field (the Zeeman energy), and the energy associated with sources of internal or external magnetic field (magnetostatic energy).

1.3.1 Exchange energy

As a result of the quantum mechanical exchange interaction between unpaired electrons on adjacent atoms, there exists an exchange energy contribution to the total energy of a magnetic system. It is responsible for the tendency of the spin moments in a magnetic material to align parallel or anti-parallel to each other. From the Heisenberg treatment of electron spins [7] we can state that the exchange energy is given by

$$e_{ex} = -2J_{12}\mathbf{s}_1 \cdot \mathbf{s}_2 \tag{1.1}$$

where J_{12} is the exchange integral between the two electrons and $\mathbf{s}_1, \mathbf{s}_2$ their spin vectors. The total exchange energy is found by summing over all contributing electrons, although in most situations only the contribution from nearest neighbours need be considered. This is given by

$$E_{ex} = -2JS^2 \sum_{ij} cos\phi_{ij} \tag{1.2}$$

where J is the exchange integral, S is the magnitude of the spin vector, and ϕ_{ij} the angle between i and j. When J is positive, the energy is minimised by having the moments aligned parallel, i.e. when ϕ_{ij}=0. If J is negative then the energy of the system is minimised by having the moments aligned anti-parallel as occurs in anti-ferromagnetic materials [8].

The exchange interaction is a strong interaction, but can be overcome by raising the temperature of the material above a critical value known as the Curie tem-

perature, T_c. Above this temperature the material is said to be paramagnetic, where parallel alignment of the spins can be obtained under the influence of an applied field, but they will relax to a randomly orientated state upon its removal [5].

1.3.2 Anisotropy energy

Another energy term to be considered is the anisotropy energy, of which there are two main classes. The first is magnetocrystalline anisotropy which is associated with the direction of orientation of magnetic moments with respect to the crystal lattice. The second type, known as shape anisotropy is due to magnetostatic effects, and is particularly important when dealing with nanoscale thin film elements such as those in this thesis.

1.3.2.1 Magnetocrystalline anisotropy

Magnetocrystalline anisotropy arises due to the spin-orbit coupling between the magnetic moments and the crystal lattice which make it energetically favourable for the magnetisation to lie along certain crystallographic directions. These preferred directions are referred to as easy axes. To rotate the magnetisation away from an easy direction there is an associated energy cost. Hard axes are those directions which require the most energy to align the magnetisation along.

Anisotropy is dependent on the crystallographic symmetry of the material. The most common symmetries encountered in single crystal ferromagnetic materials are cubic and hexagonal. In the case of a cubic crystal such as Fe, the energy is given by the series expansion,

$$E_k = \int [K_1(m_a^2 m_b^2 + m_b^2 m_c^2 + m_c^2 m_a^2) + K_2(m_a^2 m_b^2 m_c^2)] dV \tag{1.3}$$

where m_a, m_b, m_c are the direction cosines of the magnetisation along a, b, c, the respective crystallographic directions, with K_1 and K_2 anisotropy constants [8]. The first term involving the K_1 constant is usually the dominant term in influencing the easy axis direction of the sample.

For a hexagonal or uniaxial crystal, the anisotropy energy can also be described

by a series expansion,

$$E_k = \int K_1(1 - m_c^2) + K_2(1 - m_c^2)^2 dV. \tag{1.4}$$

In this case, only one direction cosine is necessary to describe the anisotropy due to the lower symmetry. Again K_1 is the dominant term in determining the direction of the anisotropy. The easy axis will prefer to lie parallel to the anisotropy axis if K_1 is large and positive, and perpendicular to the anisotropy axis if K_1 is large and negative. A special case occurs if -2 $<K_1/K_2$ <0, where the easy axis will lie along a cone at an angle of θ to the anisotropy axis .

These descriptions are valid for single crystal materials. However ferromagnetic materials of technological interest such as those investigated in this thesis have a polycrystalline structure. The individual crystallites in a polycrystalline material have random orientations resulting in no overall preferred direction, unless one is induced by deposition of the film in the presence of magnetic field, or by annealing. The variations in crystallite orientation cause fluctuations in the magnetisation, known as magnetisation ripple [9, 10].

1.3.2.2 Shape anisotropy

When a magnetic thin film is patterned into small magnetic elements shape anisotropy becomes important. This is due to magnetostatic effects, discussed in section 1.3.4, which are strongly dependent on the sample geometry [11]. In a uniformly magnetised element, magnetostatic charges build up at the surfaces generating both internal and external magnetic fields. The internal field is also known as the demagnetising field, H_d as it is opposite in direction to the magnetisation. The shape anisotropy energy increases as the demagnetising field increases. If we consider a very oblate ellipsoid, uniformly magnetised along the short axis (as shown in figure 1.1(a)), the magnetic poles are close together resulting in a large H_d. Magnetising the same element along the long axis, as in figure 1.1(b), leads to smaller values of H_d and consequently lower E_k than when it is magnetised along the short axis [12]. The contribution to anisotropy energy from the shape of a system is given by

$$E_k = -\int_V K_{eff} sin^2\theta dV \tag{1.5}$$

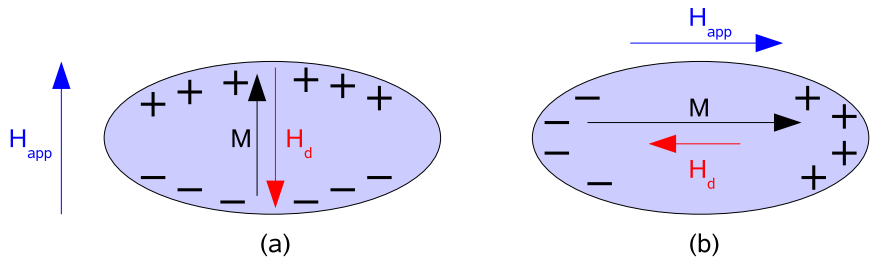

Figure 1.1: Schematic of shape anisotropy in elliptical element. Arrows denote relative sizes of magnetisation and demagnetising fields.

where

$$K_{eff} = \frac{1}{2}(N_b - N_a)M^2 \tag{1.6}$$

and M is the magnetisation, θ is the angle between the long axis and the magnetisation direction, N_a and N_b are the de-magnetising factors along the long and short axes respectively, which are dependent on the sample geometry. For the long wire structures which are investigated later in this thesis, the two long axes, a and b, are very much greater than the sample thickness, c (a>b>>c). In this case the demagnetising factors are given by [13]

$$N_a = \frac{\pi}{4}\frac{c}{a}[1 - \frac{1}{4}\frac{a-b}{a} - \frac{3}{16}(\frac{a-b}{a})^2] \tag{1.7}$$

$$N_b = \frac{\pi}{4}\frac{c}{a}[1 + \frac{5}{4}\frac{a-b}{a} - \frac{21}{16}(\frac{a-b}{a})^2]. \tag{1.8}$$

A review of the effects of shape anisotropy is given in reference [11].

1.3.3 Zeeman energy

The influence a magnetic field has on the individual moments is represented by the Zeeman term. In the presence of an externally applied magnetic field, the moments within the material will attempt to align parallel to the field direction. The Zeeman energy takes into account the orientation of the magnetisation with respect to the applied field and is given by

$$E_Z = -\mu_0 \int_V \mathbf{M} \cdot \mathbf{H} dV \tag{1.9}$$

where μ_0 is the permeability of free space, $\mathbf{M}$ is the magnetisation, $\mathbf{H}$ is the applied field, and V the volume of the sample.

1.3.4 Magnetostatic energy

Magnetostatic energy originates from the interaction between the dipoles in a magnetic specimen and the local magnetic field. Both internal (de-magnetising) fields and external (stray) fields are generated by the poles. The de-magnetising field is so-called as it opposes the direction of magnetisation within the sample. The sum of the internal and external fields is given by

$$H_m = \frac{1}{4\pi}\left(\int_V \frac{-\nabla \cdot \mathbf{M}}{R^2} dV + \int_S \frac{\mathbf{M} \cdot \mathbf{n}}{R^2} dS\right) \tag{1.10}$$

where R is the position at which point the field from the charge is evaluated, and $\mathbf{n}$ is the outward pointing unit vector, normal to the surface [8]. From the first integral which is performed over the volume of the specimen, the term $-\nabla \cdot \mathbf{M}$ is equal to the volume magnetic charge density. In the second integral, performed over the specimen surface, the term $\mathbf{M} \cdot \mathbf{n}$ is the surface magnetic charge density. The energy associated with magnetostatic effects arises from the interaction between the field and the magnetisation of the sample, and can be expressed as

$$E_m = \frac{-\mu_0}{2} \int_V \mathbf{M} \cdot \mathbf{H}_m dV \tag{1.11}$$

The magnetostatic energy of a system can be reduced by reducing the amount of stray field generated at the surface of the material. This can be achieved by the formation of magnetic domains within the solid, as shown in figure 1.2.

In figure 1.2(a) the stray field generated by a single domain state is shown. The multidomain states shown in figure 1.2(b) and (c) may be favoured when strong anisotropy exists directed along the long axis of the element [5]. The flux closure state shown in figure 1.2(d) is the preferred state when there is little or no anisotropy or influence from external fields. However, the multidomain state causes an increase in the exchange energy of the system due to the variation in spin orientation within the domain walls, and thus the magnetostatic and exchange energies are in direct competition.

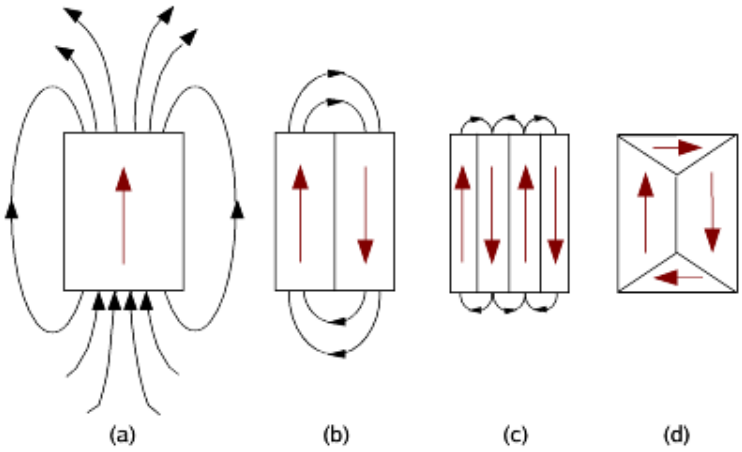

Figure 1.2: Illustration of the stray field generated in (a) single domain state, (b) and (c) multidomain states and (d) a flux-closure state.

1.3.5 Magnetostriction

When a ferromagnetic material experiences a change in magnetisation, it can be subject to a change in its dimensions. This effect is known as magnetostriction and can occur due to the ordering of magnetic moments into domains when cooling below the Curie temperature, or be induced by an applied magnetic field [14].

The origin of the magnetostrictive effect relates to the atomic structure of the material. When the material is placed in a magnetic field, the moments attempt to align with the field, distorting the shape of the electron orbitals and effectively changing their position in the unit cell. This can create a stress within the material, which to an extent can be relieved by a subsequent change in the overall dimensions of the material. The magnetostrictive effect can act in both a positive and negative sense, effecting either an expansion or reduction in the material along the direction of the applied magnetic field. The magnetostriction, λ, can be described as the fractional change in length, l,

$$\lambda = \frac{\delta l}{l} \tag{1.12}$$

where the saturation value λ_s occurs when the magnetisation in the direction of the magnetic field has a value of M_s for the material. The associated energy term arises from the interaction of the strain in the lattice and the magnetisation and

is given by

$$E_\lambda = \int (\frac{3}{2}\lambda_s \sigma sin^2\alpha) dV \tag{1.13}$$

where σ is the stress in the system and α is the angle between the direction of saturation magnetisation and σ. From this it can be determined that for magnetising a sample in a particular direction there is a magnetostrictive energy cost. For the films used in this research magnetostriction effects were minimal.

1.3.6 Domain wall energy

It was stated in section 1.3.4 that magnetic domains are formed in order to reduce the amount of stray field generated in a magnetic system. The transition region between adjacent domains is known as a magnetic domain wall. Within the wall the magnetisation rotates coherently between the directions of mean magnetisation in the domains.

One type of domain wall is a Néel wall where the rotation of the magnetisation direction takes place within the plane of the film [15]. In this case the wall generates magnetostatic charges within the plane of the film, meaning that the stray field also lies within the plane of the film, reducing the associated magnetostatic energy. As the film thickness is increased the formation of a different type of wall

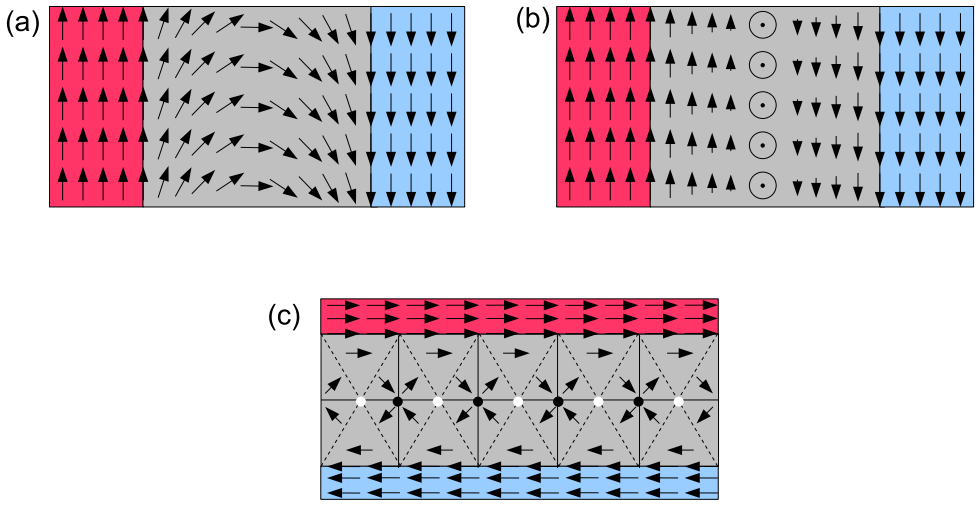

Figure 1.3: Schematic illustrations of (a) Néel wall, (b) Bloch wall, & (c) Cross-tie wall.

known as a Bloch wall is favoured. Here, the magnetisation rotates perpendicular to the plane of the film. Bloch walls occur in thicker films or bulk material due to the cost of the surface magnetostatic energy.

At an intermediate thickness the formation of cross-tie walls are observed [15, 16], which have characteristics of Néel and Bloch type walls. A schematic of each type of wall can be seen in figure 1.3. Other wall structures such as transverse and vortex domain walls can be formed when the dimensions of the material are laterally constrained as in the magnetic nano-elements and nano-wires that are investigated in this thesis. These domain wall structures are discussed in more detail in chapter 5.

Domains are formed in order to reduce the magnetostatic energy of the system, but they can be costly in terms of the exchange and anisotropy energies. In bulk material, the width of the wall δ and its energy E_w are a result of the direct competition between anisotropy energy and exchange energy. The anisotropy energy acts to reduce the wall thickness, as it is minimised by the moments aligning along the anisotropy axis, whereas the exchange energy acts to increase the wall width, as it is a minimum when neighbouring moments are parallel. The width of a Bloch wall in an extended film is given by

$$\delta = \pi\sqrt{\frac{A}{K_u}} \tag{1.14}$$

where A is the exchange stiffness and K_u is the uniaxial anisotropy constant.

To support a Néel wall, a magnetic film will have thickness,

$$t \leq \sqrt{\frac{A}{K_u}}. \tag{1.15}$$

The domain wall width scales with $\sqrt{\frac{A}{K_d}}$, where K_d is the stray field exchange constant and is given by

$$K_d = \frac{\mu_0 M_s^2}{2}. \tag{1.16}$$

As $K_d \gg K_u$, Néel walls are narrower than Bloch walls.

1.3.7 Total energy

The total magnetic energy of a ferromagnet can be expressed as a sum of all the energy components discussed in the previous sections,

$$E_{tot} = E_{ex} + E_k + E_z + E_m + E_\lambda. \tag{1.17}$$

At any time the magnetic system will try to minimise E_{tot}, and as such the magnetic configuration of the sample may be a global minimum or a meta-stable local energy minimum.

1.4 Magnetisation reversal

The magnetisation of a ferromagnetic thin film is dependent upon its magnetic history as well as the applied field. This behaviour is known as hysteresis [5].

1.4.1 Hysteresis loop

A hysteresis loop for a magnetic thin film consists of a plot of magnetisation as a function of applied field (M-H loop), and can yield many valuable pieces of information about the system from which it was aquired. A schematic hysteresis loop is shown in figure 1.4.

Initially we consider a ferromagnetic sample that has been deposited in the absence of an applied field. In this state the material is likely to consist of magnetic domains arranged such that the net magnetisation is close to zero, point (a) on figure 1.4. On application of a magnetic field, a net magnetisation is introduced and will increase in the direction of the field until saturation magnetisation is reached (b). When the applied field is reduced to zero, the magnetisation relaxes to what is known as remanence or the remanent magnetisation, M_r (c). It is necessary to apply a magnetic field in the opposite direction to return the net magnetisation to zero (d). The field at which this occurs is the coercive field, H_c. On further increasing this negative field, the material will saturate in the opposite direction (e). By removing the field, the material will again reach remanence (f) before being demagnetised by the application of another positive field (g). The hysteresis loop is reproducible with the exception of the initial increase from zero magnetisation at zero field, points (a) to (b), which is not repeated unless the ferromagnetic material is demagnetised. A typical loop for a thin ferromagnetic film is symmetric and centred around the origin.

The remanent magnetisation and coercivity are vital parameters in determining the suitability of a magnetic material for a particular application. Materials with a low value of coercivity are often called ‘soft’ magnetic materials, whilst those

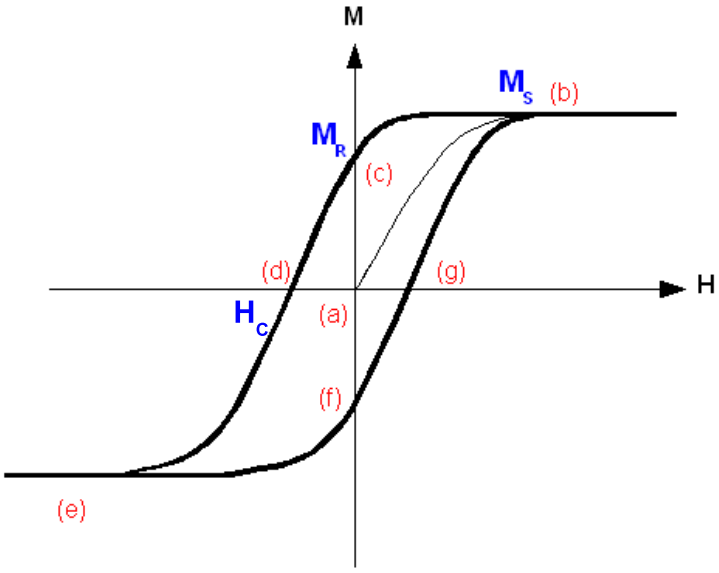

Figure 1.4: Schematic of a typical hysteresis loop for a ferromagnetic material.

with high coercive fields are known as 'hard' magnetic materials [17]. So-called 'soft' magnetic materials can have a large change in their magnetic state for only a small change in applied field, and are ideal candidates for use in magnetic sensors. Hard magnetic materials are much less reactive to their surroundings and so can be used as permanent magnets or to store information on hard disks.

1.4.2 Reversal mechanisms

There are two main mechanisms by which the magnetisation of a ferromagnetic material may change direction to align with an applied magnetic field. The first of these is coherent rotation in which the magnetisation vector rotates from the original direction towards the applied field. The Stoner-Wohlfarth model [18] was developed to describe rotation in a single domain system possessing uniaxial anisotropy, i.e. where there is only one easy direction such as in single domain particles, or small elements with dimensions comparable to the width of a domain wall. This model can be used in a modified form to describe magnetic behaviour in systems where the single domain constraint does not hold. In some larger systems it is energetically favourable for reversal to proceed by domain processes, including the nucleation of domains and domain walls, and subsequent domain wall motion.

The easy and hard axis reversals of a magnetic material involve both these pro-

cesses [19]. During an easy axis reversal there is the nucleation of reversed domains which then grow at the expense of unfavourably aligned ones. As the applied field, H_{app}, is parallel to the mean magnetisation direction, no torque is exerted on the magnetisation and no rotation occurs. Reversal is therefore effected by domain walls moving through the material. The application of a field in the hard direction, will rotate the magnetisation towards the hard axis, reaching it at the value of anisotropy field, H_k, for the sample. On decreasing the field however, both easy directions are equally favourable. Thus, the film splits into a series of anti-parallel domains magnetised along the easy axis.

1.5 Effects of ion irradiation on magnetic thin films

In recent years the effect of ion irradiation on magnetic thin films has attracted much attention as a means to modify their magnetic and structural properties. This ability to tailor magnetic properties in a controlled manner can be exploited as a tool for nanoscale patterning of thin film systems [20, 21]. In some magnetic systems, irradiation can cause sufficient changes in magnetic properties to provide the opportunity to magnetically pattern structures without incurring any topographical changes in the sample [2]. This has many important technological applications from advances in magnetic data storage to magnetic sensor elements [22].

The effects of ion irradiation on a range of magnetic materials have been widely investigated. It has been shown that basic magnetic properties such as coercivity [4, 23] and local anisotropy direction [24] can be altered in NiFe (permalloy) films, whilst exchange bias materials experience changes in bias field strength and direction [25, 26, 27]. For materials exhibiting perpendicular magnetic anisotropy such as Co/Pt multilayers, ion irradiation resulted in a transition from perpendicular to in plane magnetisation, with sufficiently large doses rendering the material paramagnetic [28, 29]. These effects were then used to pattern the film [30]. In addition to the magnetic changes that are induced by ion irradiation, very high ion doses can sputter material from a sample, a technique often employed to create topographically patterned media [31].

There are various mechanisms by which the changes in material properties are produced. In multilayer systems, such as Co/Pt films and exchange bias systems

consisting of a bilayer sandwich containing a ferromagnetic and an antiferromagnetic layer , interfacial mixing between the layers induced by irradiation is thought to be the cause [32]. Both systems are particularly sensitive to the quality of the interfaces between the multilayers, so a reduction in this quality by irradiation induced roughness or mixing will be detrimental to the properties of the system [33]. In exchange bias systems a change in the exchange bias field strength and direction is observed at comparatively low doses [26, 34, 35]. Structural investigations show a broadening of the interfaces and the introduction of texture within the film layers [36].

Many investigations into the effect of ion irradiation on the properties of permalloy (NiFe) have been carried out. Permalloy is a very commonly used magnetic material [22], and as such, the ability to modify and control its magnetic and structural properties has attracted much interest. Commonly a focused ion beam (FIB) instrument with a Ga^+ source is used, however a wide range of other sources including He^+, Ar^+, Xe^+, C^+, Ni^+, O^+ and Si^+ have also been investigated. For a review see [37]. Ozkaya et al carried out a systematic study on the effects of Ga^+ ion irradiation on thin uncapped permalloy films [23]. It was found that with increasing ion dose there was a loss in uniaxial anisotropy and an increase in coercivity. This increase is most likely due to the increased stress in the irradiated region causing domain wall pinning at the boundary of the irradiated region, and thus resulting in a higher value of coercivity. Considerable grain growth from $\sim$5 - 50nm was also observed within a dose range of 3×10^{14} to 3×10^{14} ions cm^{-2}. The induced grain growth was further investigated by Park et al [38], over concerns about the use of FIB irradiation for developing recording heads via pole trimming. In a study by Kaminsky et al [4], ion irradiation of permalloy with a NiCr cap layer was found to reduce the coercivity in the irradiated regions, at a sufficiently high dose rendering them non-ferromagnetic at room temperature. It is possible that the increased grain size that accompanies irradiation can contribute to the decrease in coercivity. With larger grains there are fewer barriers or grain boundaries in a given area, making domain movement an easier process.

In other investigations the effect of irradiating permalloy with ions such as Ni^+ and Cr^+ has been reported. The implantation of Ni into thin NiFe layers has been shown to control layer magnetisation, saturation magnetisation and local anisotropy [37]. With increasing Ni^+ dose a magnetic dead layer is formed resulting in a reduction of the total magnetisation. As a further consequence, the increase in concentration of Ni^+ in the layer causes a shift in the stoichiometry,

and a reduction in the saturation magnetisation of the layer. Implanting with Cr^+ creates alloys of NiFeCr, such that with increasing Cr^+ dose, a steady reduction in magnetic moment and coercivity is observed [39]. At a dose which corresponds to a concentration of 20% Cr^+ in the alloy, the material is found to be non-ferromagnetic [40]. Another technique which resulted in effectively reducing the magnetic moment in a permalloy film was the deposition of a Ta cap and seed layer [41, 42]. The concentration of Ta present in the NiFe layer was increased by annealing the layer to affect thermally driven interdiffusion. A 12% Ta concentration was sufficient to reduce the magnetic moment to zero [41].

The effects of ion irradiation in thin film systems need not be experienced by the system as a whole, but can be laterally restricted leading to patterning through localised modification of the magnetic properties. Patterning with high spatial resolution can be achieved by the use of a FIB system [43, 44], where exact control of the ion beam movement eliminates the need for masks [45]. Magnetic structures created by FIB irradiation and other patterning techniques are discussed in section 1.6, whilst the irradiation method used during this work is described in detail in chapter 2.

1.6 Controlling domain walls in magnetic structures

Spintronics, a term referring to 'spin-based electronics', is an emergent technology which exploits the spin of an electron as well as its charge [46]. It is predicted that future spintronics devices will use magnetic domain walls to store information [47, 48], and so a thorough understanding of domain wall dynamics and how magnetic moments can be manipulated is key for further development. A comprehensive review on the fundamental principles of spintronics is available in reference [49]. Important issues for domain wall spintronics are reliable domain wall nucleation, control of domain wall location and the ability to pin and de-pin the wall at pre-defined locations.

Various domain wall trap (DWT) geometries have been devised with a view to investigating these properties [50, 51]. Brownlie et al. [52] have shown that domain walls could be trapped and moved within a nanowire with carefully chosen end shapes. These ends were designed to act as an energy barrier to the domain wall to prevent it from moving out of the wire. The concept of trapping walls has

been further developed by the introduction of notches [53, 54, 55] and anti-notches [56, 57] to the wire, which can pin the domain walls at pre-defined locations. These investigations have shown that the interaction of the domain wall with the pinning site and subsequent depinning fields are dependant on a number of factors such as domain wall type, the chirality of the wall, as well as the particular geometry of the pinning site.

Other investigations have focused on gaining a greater degree of control over the chirality of the domain wall that is formed or injected into the wire [58]. The geometry of a domain wall injection pad has been optimised to support a single vortex magnetisation state, the chirality of which can be controlled by magnetising the structure in a particular direction. A domain wall of known chirality can then be injected into the wire by application of a field along the wire. These recent results [52, 58] have motivated some of the work in chapter 5 of this thesis, where domain wall traps and nanowire structures were fabricated by FIB.

Domain walls are also known to offer a source of resistance to electrical current flow in magnetic material. Known as domain wall magnetoresistance (DWMR) it manifests as a change in resistance from a uniformly magnetised piece of magnetic material to a different value when magnetic domains and hence domain walls are present. However, there is some discussion over the nature of the DWMR contribution as both positive [59, 60, 61] and negative [62, 63, 64] values have been reported.

Structures which can support a high density of domain walls at pre-defined locations could prove useful in furthering investigations into the nature and origin of DWMR. In [43], a series of alternating long and short wires were patterned by FIB, in which the formation of an array of domains supporting anti-parallel magnetisation was possible. However, the structure was dependant on the reversal of the surrounding film to aid the anti-parallel alignment of the domains. This prompted an attempt to create a magnetically isolated structure which could support high domain wall densities, the results of which are presented in chapter 4.

1.7 Summary

In this chapter the properties of ferromagnetic thin films have been discussed. This has included a description of the various energy terms which contribute to the total energy of a magnetic system and which dictate its micromagnetic behaviour. In section 1.5, the effects of ion irradiation on the structural and magnetic properties of a variety of magnetic thin films has been detailed. This is particularly relevant to the work presented in chapters 3 and 6, where the effects of Ga^+ ion irradiation on permalloy films with metallic cap layers and on Co/Pd multilayers with perpendicular magnetic anisotropy are described. Finally in section 1.6, magnetic structures in which magnetic domain wall properties such as nucleation, propagation and location can be controlled are reviewed. Such structures have provided much of the motivation for the work described in chapters 4 and 5 of this thesis. An outline of the aims and objectives of this thesis follows.

Chapter 2 primarily describes the experimental procedures used throughout this work. The two deposition methods used, thermal evaporation and DC sputtering are described, along with a comprehensive description of the transmission electron microscope (TEM) and the different imaging techniques used. Particular attention is paid to Lorentz imaging which was used extensively to study the magnetic properties of the systems before and after irradiation, and the behaviour of the magnetic elements created. The focused ion beam (FIB) is also described with a detailed explanation of the patterning technique implemented which was specifically designed for use with magnetic materials that are sensitive to ion irradiation. Various simulation packages were used to predict the effects of Ga^+ ion irradiation on multilayer systems, as well as the micromagnetic behaviour of fabricated elements, and are described here.

In chapter 3, the effects of ion irradiation on a number of thin film systems consisting of a permalloy layer of varying thickness, and one or more non-magnetic layers are studied. Structural and magnetic characterisation by TEM was carried out prior to and subsequent to irradiation with a 30kV Ga^+ ion beam. The aim of studying the irradiation effects is to determine critical doses at which the magnetisation in the samples undergoes significant changes, such that this information can be used in subsequent chapters to pattern magnetic structures.

In chapter 4, results concerning the magnetisation reversal behaviour of a 'zigzag' structure are presented. The structure was designed to take advantage of the

fact that magnetisation in a soft magnetic film such as permalloy is strongly correlated to the edge shape. Modification of the structure by the introduction of irradiated delineation regions across the sample was introduced to allow the magnetisation to form an array of domains with alternating magnetisation. An element supporting such a magnetic state could potentially be used for domain wall magnetoresistance studies.

In chapter 5 irradiation of magnetic structures is again carried out, but this time on magnetic wires to create defect or pinning sites. In other investigations involving domain walls in wires, the artificial pinning sites introduced have been geometrical, whereas irradiated pinning sites are inherent to the wire and do not require any physical changes to the structure. With the continued reduction in the size of magnetic structures this could prove to be a novel way to control the propagation and location of domain walls in wires.

The effects of irradiation on Co/Pd multilayers with perpendicular magnetic anisotropy are investigated in chapter 6. Irradiation causes magnetic systems with perpendicular magnetisation to undergo a transition from out-of-plane magnetisation to in-plane, but so far there have been no studies to investigate how this transition occurs, i.e whether the magnetisation rotates gradually from out of plane to in plane with increasing dose or whether it occurs in a single step. A simple grid pattern was devised and irradiated onto the perpendicularly magnetised sample at a range of doses, so that magnetic states with both in-plane and out of plane magnetisation could be observed. A combination of differential phase contrast microscopy and simulations of integrated magnetic induction are used to attempt to determine the orientation of the magnetisation within irradiated regions.

Chapter 7 contains conclusions about the experimental work carried out and details potential future work that could be performed.

Bibliography

[1] G. Dearnaley, Annu. Rev. Mater. Sci. **4**, 4 (1974).

[2] C. Chappert *et al.*, Science **280**, 1919 (1998).

[3] B. D. Terris *et al.*, Appl. Phys. Lett. **75**, 403 (1999).

[4] W. M. Kaminsky *et al.*, Appl. Phys. Lett. **78**, 1589 (2001).

[5] D. Jiles, *Introduction to magnetism and magnetic materials* (Chapman and Hall, 1998).

[6] P. Weiss, J. Phys. **6**, 661 (1907).

[7] W. Heisenberg, Z. Physik **49**, 619 (1928).

[8] C. Kittel, Rev. Mod. Phys. **21**, 541 (1949).

[9] H. Hoffmann, IEEE Trans. Mag. **4**, 32 (1968).

[10] K. J. Harte, J. Appl. Phys. **39**, 1503 (1968).

[11] R. P. Cowburn, J. Phys. D.: Appl. Phys. **33**, R1 (2000).

[12] J. Fidler and T. Schrefl, J. Phys. D.: Appl. Phys. **33**, R135 (2000).

[13] Chikazumi, (Wiley, 1966).

[14] A. Hubert and R. Schafer, *Magnetic domains: the analysis of magnetic microstructures* (Springer, 1998).

[15] J. E. E. Huber, D. O. Smith, and J. R. Goodenough, J. Appl. Phys. **29**, 294 (1958).

[16] R. Ploessi, J. N. Chapman, A. M. Thompson, J. Zweck, and H. Hoffmann, J. Appl. Phys. **73**, 2447 (1993).

[17] H. M. Rosenberg, *The Solid State - Third Edition* (Oxford Science Publications, 1989).

[18] E. P. Wohlfarth and E. C. Stoner, Phil. Trans. Roy. Soc. **599**, A240 (1948).

[19] M. Prutton, *Thin ferromagnetic films* (Butterworth, 1964).

[20] J. Fassbender, D. Ravelosona, and Y. Samson, J. Phys. D: Appl. Phys. **37**, R179 (2004).

[21] S. Blomeier *et al.*, Eur. Phys. J. B **45**, 213 (2005).

[22] G. A. Prinz, J. Magn. Magn .Mat. **200**, 57 (1999).

[23] D. Ozkaya, R. M. Langford, W. L. Chan, and A. K. Petford-Long, J. Appl. Phys. **91**, 9937 (2002).

[24] S. I. Woods, S. Ingvarsson, J. R. Hirtley, H. F. Hamann, and R. H. Koch, Appl. Phys. Lett. **81**, 1267 (2002).

[25] S. Blomeier *et al.*, J. Mag. Mag. Mat. **0**, 1 (2004).

[26] D. McGrouther, J. N. Chapman, and F. W. M. Vanhelmont, J. Appl. Phys. **95**, 7772 (2004).

[27] A. Mougin *et al.*, Phys. Rev. B **63**, 060409 (2001).

[28] R. Hyndman *et al.*, J. Appl. Phys. **90**, 3843 (2001).

[29] C. T. Rettner, S. Anders, J. E. E. Baglin, T. Thomson, and B. D. Terris, Appl. Phys. Lett. **80**, 279 (2002).

[30] P. Warin *et al.*, J. Appl. Phys. **90**, 3850 (2001).

[31] T. Devolder *et al.*, Appl. Phys. Lett. **74**, 3383 (1999).

[32] T. Devolder, Phys. Rev. B **62**, 5794 (2000).

[33] R. Hyndman *et al.*, J. Mag. Mag. Mat. **240**, 50 (2002).

[34] A. Mougin *et al.*, J. Appl. Phys. **89**, 6606 (2001).

[35] J. Fassbender *et al.*, Phys. Stat. Sol. A **189**, 439 (2002).

[36] Y. G. Wang, D. McGrouther, S. McVitie, M. McKenzie, and J. N. Chapman, J. Appl. Phys. **100**, 073901 (2006).

[37] J. Fassbender and J. McCord, Appl. Phys. Lett. **88**, 252501 (2006).

[38] C. M. Park and J. A. Bain, J. Appl. Phys. **91**, 6830 (2002).

[39] J. Fassbender, J. von Borany, A. Mucklich, K. Potzger, and W. Moller, Phys. Rev. B **73**, 184410 (2006).

[40] L. Folks *et al.*, J. Phys. D.: Appl. Phys. **36**, 2601 (2003).

[41] M. Kowalewski *et al.*, J. Appl. Phys. **87**, 5732 (2000).

[42] G. H. Yu, T. Yang, F. W. Zhu, M. H. Li, and W. Y. Lai, J. Phys. D.: Appl. Phys. **36**, 4 (2003).

[43] D. McGouther and J. N. Chapman, Appl. Phys. Lett. **87**, 022507 (2005).

[44] D. Atkinson, J. Phys.: Conf. Series **17**, 33 (2005).

[45] B. D. Terris *et al.*, J. Appl. Phys. **87**, 7004 (2000).

[46] C. H. Marrows, Adv. Phys. **54**, 585 (2005).

[47] S. S. P. Parkin, United States Patent **6834005** (2004).

[48] S. S. P. Parkin, Int. J. Mod. Phys. B **01**, 117 (2008).

[49] I. Zutic, J. Fabian, and S. D. Sarma, Rev. Mod. Phys. **76**, 323 (2004).

[50] R. D. McMichael and M. J. Donahue, IEEE Trans. Mag. **33**, 4167 (1997).

[51] R. D. McMichael, J. Eicke, M. J. Donahue, and D. G. Porter, J. Appl. Phys. **87**, 7058 (2000).

[52] C. Brownlie, S. McVitie, J. N. Chapman, and C. D. W. Wilknson, J. Appl. Phys. **100**, 033902 (2006).

[53] C. C. Faulkner *et al.*, J. Appl. Phys. **95**, 6717 (2004).

[54] I. V. Roshchin, J. Yu, A. D. Kent, G. W. Stupian, and M. S. Leung, IEEE Trans. Mag. **37**, 2101 (2001).

[55] M. Klaui *et al.*, Appl. Phys. **87**, 102509 (2005).

[56] C. Sandweg *et al.*, J. Appl. Phys. **103**, 093906 (2008).

[57] D. Petit, A. Jausovec, D. Read, and R. P. Cowburn, J. Appl. Phys. **103**, 114307 (2008).

[58] D. McGrouther, S. McVitie, and J. N. Chapman, Appl. Phys. Lett. **91**, 022506 (2007).

[59] S. Lepadatu and Y. B. Xu, Phys. Rev. Lett. **92**, 127201 (2004).

[60] J. F. Gregg *et al.*, Phys. Rev. Lett. **77**, 1580 (1996).

[61] R. Danneau *et al.*, Phys. Rev. Lett. **88**, 157201 (2002).

[62] G. Tatara and H. Fukuyama, Phys. Rev. Lett. **78**, 3773 (1997).

[63] L. Gao *et al.*, J. Mag. Mag. Mat. **272**, 1301 (2004).

[64] K. Hong and N. Giordano, J. Phys.: Condens. Matter **10**, L401 (1998).

Chapter 2

Instrumentation and experimental techniques

2.1 Introduction

Many different experimental and computational techniques were employed during this work in order to understand the effects of ion irradiation on magnetic thin films and the behaviour of nano-scale magnetic elements fabricated by focused ion beam (FIB). A description of all stages of experiment from sample preparation through to characterisation by transmission electron microscopy (TEM) is given in the following sections. The techniques used to deposit the NiFe thin films and the Co/Pd multilayer thin film samples investigated in this thesis are described in section 2.2. In section 2.3 the basic principles of TEM and modes of operation are presented, whilst the Lorentz mode techniques used to investigate the magnetic structure of the materials are detailed in section 2.4. Following this in section 2.5, the principles of the focused ion beam system (FIB) are described, along with an explanation of how patterning magnetisation with ion irradiation is achieved. Simulations of ion irradiation effects and of the micromagnetic behaviour of magnetic elements were a very useful tool, and the programs used are outlined in section 2.6.

2.2 Thin film deposition

To be able to use TEM to study magnetic thin films, the films themselves must be electron transparent. For a 200kV microscope they should ideally be less than 100nm thick, but this is also dependant on the atomic weight of the material. The substrates onto which the films studied here are deposited are depicted in figure 2.1. These electron transparent membranes consist of 35nm Si_3N_4, supported

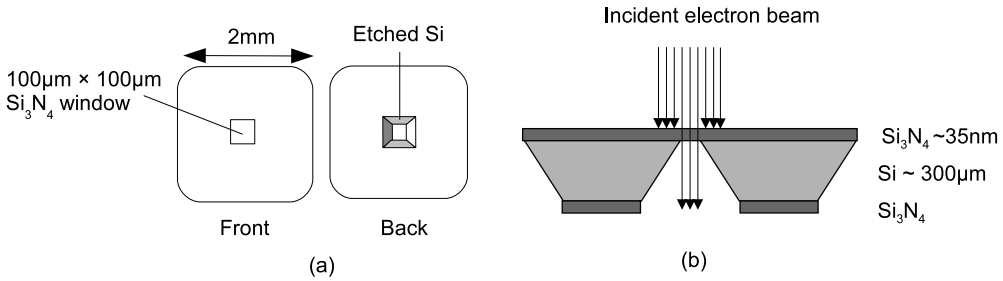

Figure 2.1: (a) Front, back and (b) cross-sectional schematics of single Si_3N_4 TEM membrane substrate.

on a Si frame with a 100μm × 100μm electron transparent window [1]. The membrane substrates are made by Kelvin Nanotechnology Ltd (KNT) based in the Department of Electronics and Electrical Engineering at the University of Glasgow. Use of the membranes gives the electron transparency required of the substrate as well as providing a high quality, flat surface for film deposition. The two most common methods for depositing thin films are thermal evaporation and sputtering. Both methods were used for the samples that have been investigated and are outlined in the following sections.

2.2.1 Thermal evaporation

The thermal evaporation system in the department in Glasgow is depicted in figure 2.2. This system was used to deposit 10nm and 20nm NiFe films with Al and Au cap layers. The chamber is evacuated down to a base presure of 2×10^{-6} torr, reducing the risk of contamination from other materials, and ensuring a direct route for the metallic vapour from source to target. Inside this, a ceramic coated tungsten wire crucible containing an amount of the material to be deposited is connected between two electrical contacts. It is possible to load two crucibles at the same time so that multilayer systems of different materials may be deposited without breaking the vacuum. The substrate is placed in a holder directly above

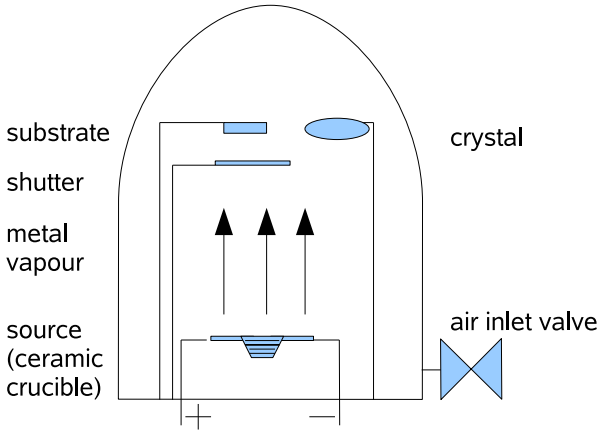

Figure 2.2: Thermal evaporation system.

the crucibles at a distance of ∼20cm, with a shield in place between the deposition source and the substrate. A steadily increasing current is passed through the crucible, heating the material within it until evaporation of the material occurs. At this point the current is left constant, allowing a constant rate of vapour to be released from the material which travels directly towards the substrate. Once any surface oxide is removed from the material, and a constant deposition rate is achieved, the shutter is removed from beneath the substrate, exposing it to the vapour. After the desired amount of material has been deposited, the shutter is replaced.

The amount of material being deposited is monitored by a crystal thickness monitor. A quartz crystal undergoes mechanical oscillation at a known frequency. This too is exposed to the metallic vapour, incurring a change in mass and therefore a change in the resonant frequency. The measured change in frequency can be calibrated and directly related to the thickness of material deposited. A calibration or control sample is always included in the deposition, so that the deposited thickness may be measured and checked directly by means of atomic force microscopy (AFM).

2.2.2 DC sputtering

DC sputtering is the main alternative to thermal evaporation for the deposition of high quality, polycrystalline thin films. The Co/Pd multilayer films discussed in Chapter 6, were deposited using DC Sputtering by Dr. Justin Shaw at NIST, Boulder, Colorado, USA. A schematic of a typical DC sputter system is shown in figure 2.3.

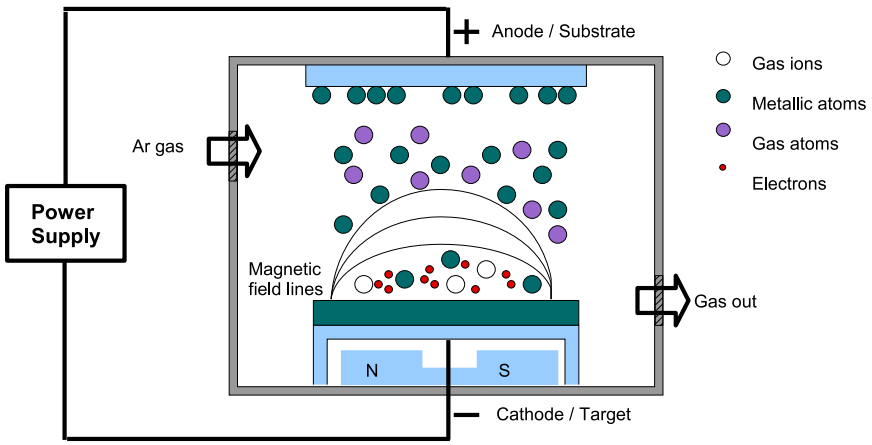

Figure 2.3: Schematic of parallel plate DC magnetron sputtering system.

The target material and substrate are held on the cathode and anode respectively, with the entire system held under vacuum. An inert gas, typically argon, is bled into the sputter chamber and a large voltage is applied between the two electrodes. Electrons from the cathode ionise the gas atoms generating a plasma. These ions are then accelerated towards the cathode, where atoms are ejected from the target on impact. The sputtered atoms are deposited onto exposed surfaces in the chamber and build up to form thin layers of the target material. The film thickness is controlled by the length of time the substrate is exposed during the process and the distance of the substrate from the target. To enhance the performance of the sputter coater, a magnetron is often placed above the target to produce a magnetic field which will trap electrons in the vicinity of the target. This increases the gas ionisation density, leading to an increased sputter rate and a more efficient system. An rf mode may also be implemented when working with insulating targets. This prevents charge build up on the target by varying the voltage bias at a high rate during deposition. Most systems now have multiple targets that may be chosen without breaking the vacuum, so that multilayer systems can be grown in a controlled environment.

2.3 Transmission electron microscopy (TEM)

The Rayleigh criterion for light microscopy states that the smallest distance, δ, that may be resolved depends on the wavelength, λ, of the light source

$$\delta = \frac{0.61\lambda}{\mu sin\beta} \tag{2.1}$$

where μ is the refractive index of the viewing medium and β is the semi-angle of collection of the magnifying lens. This makes the resolution of a light microscope at best $\sim$ 300nm [2], which is much larger than the length scales of many fundamental properties of materials and structures that we are interested in today.

In 1925 de Broglie postulated that the electron had wave-like properties with a wavelength far less than the wavelength of light, and the concept of a microscope using electrons as a source of illumination was soon realised. The first electron microscope was built in 1933 by Ruska and Knoll, and these were in regular production by the year 1939. Since then electron microscopes have undergone intense continuous development to increase the maximum resolution and reduce abberations, so that in some cases magnification can be increased several million times providing sub-angstrom resolution [3].

We can relate the wavelength of the electron to the acclerating voltage of the microscope

$$\lambda = \frac{h}{p} = \frac{h}{(2m_0eV)^{\frac{1}{2}}} \tag{2.2}$$

where h is Planck's constant, p is the momentum of the electron, m_0 the rest mass of the electron, e the charge on the electron and V the accelerating voltage of the microscope. In a modern TEM the accelerating voltage is typically $\sim$ 100-300keV, which causes the electrons to be accelerated to speeds greater than half the speed of light, c. Therefore equation 2.2 must be modified to take into account the relativistic correction [4]

$$\lambda = \frac{h}{[2m_0eV(1 + \frac{eV}{2m_0c^2})]^{\frac{1}{2}}}. \tag{2.3}$$

The electron microscopes used during this research have an accelerating voltage of 200kV which corresponds to an electron wavelength of 2.51pm.

2.3.1 The TEM

2.3.1.1 Electron sources

There are two main types of sources used to generate electrons for an electron microscope: thermionic sources and field emission sources [5]. The two microscopes used in this work, an FEI T20 and a Philips CM20, use a thermionic and a field emission source respectively.

A thermionic source is resistively heated to overcome the work function of the material and allow electrons to escape from the tip. They are commonly made from either Tungsten filaments or lanthanum hexaboride (LaB_6) crystals which both have the necessary high melting point and low value of work function [5]. In the FEI T20, a LaB_6 crystal is bonded to a metallic filament which is resistively heated, indirectly heating the crystal, until emission occurs at 1700K. A wehnelt cylinder, positioned between the source and the accelerator stack, controls the emission and focuses the electrons to a crossover point, before they are accelerated down the column by the anode. The crossover point is an image of the source and acts as the object for the illumination system which consists of the condenser lenses.

In a field emission gun (FEG) the source is made the cathode with respect to 2 anodes. The first anode generates an intense electric field at the tip allowing the electrons to tunnel out from the tip, whilst the second anode accelerates the electrons to their accelerating voltage. The crossover is formed from the combination of fields from both anodes. These sources are often tungsten needles formed into a sharp point. Field emission sources operate under UHV conditions to keep the tip in pristine condition, however build up of contaminants can still occur. Thermally assisted FEG's are held in a slightly poorer vacuum but are moderately heated to evaporate any contaminants. This also aids emission by helping the electrons to overcome the work function. Schottky emitters are FEG's which are coated with zirconia (ZrO_2) to help reduce the work function and enhance emission. The Philips CM20 is fitted with such a source.

In both types of electron gun, a virtual source is formed at the crossover point. The diameter of the crossover is an important parameter, as it determines the size of electron probe that can be formed further down the column, and in turn, the suitability of the source to a particular use. The brightness, β of the gun is

controlled by the characteristics of the virtual source,

$$\beta = \frac{4i_e}{\pi d_0 {\alpha_0}^2} \tag{2.4}$$

where i_e is the cathode emission current, d_0 is the diameter of the virtual source, and α_0 the angular convergence. The virtual source size of a field emission source is of the order of 100 times smaller than that of a thermionic emitter. Its small source means that the beam is highly spatially coherent and has much reduced energy spread. This makes a FEG particularly suitable to Lorentz imaging where it is necessary to have a small coherent beam with an angular convergence significantly less than the Lorentz deflection angle. Thermionic sources are found to be better suited to routine TEM work where large areas of the sample need be illuminated without loss of intensity on the viewing screen.

2.3.1.2 The electron column

The electron column houses a series of magnetic lenses and apertures which are used to control the mode of operation of the microscope, a schematic of which is shown in figure 2.4. It is held under high vacuum, $\sim 10^{-7}$ torr to reduce scattering events and contamination. All of the lenses in the column are magnetic lenses, only the gun lens is electrostatic.

A magnetic lens consists of a core of soft magnetic material such as iron, known as the pole piece, with a hole drilled through it, the bore. There are usually two pole pieces in a single lens separated by a gap. A coil of wire surrounds each pole piece causing a magnetic field to be produced in the bore when a current is passed through the wires. The strength of the magnetic field controls the path of the electron in the column and in turn can be controlled by changing the strength of the current in the wires. Resistive heating in the wires is an unavoidable side effect, therefore magnetic lenses must be water cooled.

The condenser lenses are the first lenses that the electron beam encounters on leaving the gun. The C1 lens forms a demagnified image of the crossover, while the C2 lens alters the intensity of the illumination by controlling the angular convergence. Beneath the condenser lens system is the condenser aperture strip which consists of a series of apertures typically ranging from 20μm to 200μm. Selection of a smaller aperture restricts the amount of electron intensity transmitted, but gives a beam with greater coherence.

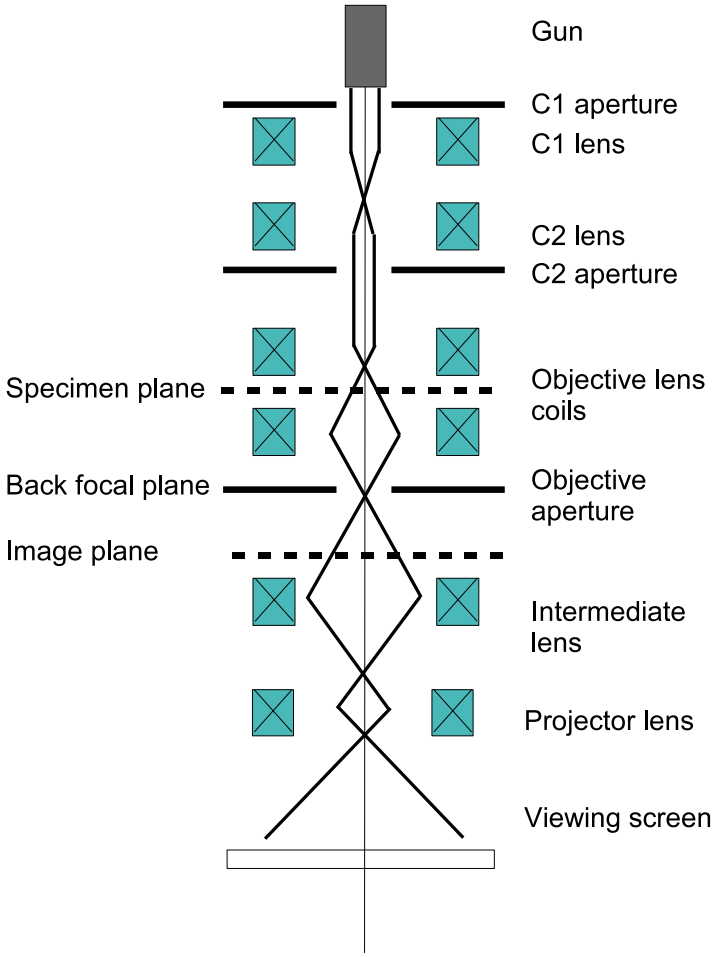

Figure 2.4: Schematic of TEM column showing the position of the magnetic lenses and apertures used for image formation.

After leaving the condenser lens system, the beam enters the objective lens and is incident upon the sample. In most TEM's the specimen is situated between the upper and lower objective lens pole pieces where in some cases it is immersed in a field of up to 2 Tesla. For the microscopes used in this work, the typical objective lens field is of the order of 1T, which is still more than sufficient to destroy any magnetic information which may be stored on a sample. However, as is discussed in more detail in section 2.4, the objective lens can be switched off to create a field-free environment for the sample. The objective lens is the primary imaging lens and forms the first intermediate image. The intermediate and projector lenses then project a magnified image from the objective image plane in bright field mode or back focal plane in diffraction mode onto the viewing screen. Images are recorded by using a CCD (charge coupled device) which is exposed by lifting the viewing screen. A scintillator plate converts the electron image into a light image which is then transferred to the surface of the pixellated CCD through a fibre optic plate. The image data is read out directly to a computer which allows

real time viewing and processing. Photographic film is still commonly used to record diffraction patterns to avoid the intense spots burning the CCD.

Some imaging and analytical techniques require the microscope to be operated in scanning TEM (STEM) mode. A mini-condenser (or twin) lens is used when the microscope is operating in STEM mode to focus the electron beam to a probe at the specimen. The electron beam is then rastered across the specimen by using two sets of deflection coils which keep the motion of the beam parallel to the optic axis.

2.3.2 Structural characterisation

Two of the fundmental procedures of a TEM are the formation of an image and electron diffraction pattern. Information about the grain size and shape in samples can be obtained from TEM images, whilst the diffraction pattern can provide details about the sample composition and texture. Both these techniques are used to characterise the structural properties of the as-deposited and irradiated films in chapter 3, as well as the fabricated magnetic structures in chapters 4 and 5.

2.3.2.1 Diffraction

Electrons incident on a sample are scattered by a variety of elastic and inelastic scattering interactions and emerge at various angles. Some are incident on crystallographic planes at the Bragg angle, satisfying Bragg's Law,

$$n\lambda = 2dsin\theta \tag{2.5}$$

where n is an integer, λ is the wavelength of the electrons, d is the spacing of the lattice planes and θ is the emergent angle of the electrons [6]. These electrons will emerge in phase with electrons from neighbouring planes resulting in constructive interference of significant intensity. The diffraction pattern is formed in the back focal plane of the microscope, as shown in the schematic in figure 2.5(a). It can be viewed in diffraction mode by adjusting the post-specimen lenses so that the back focal plane of the objective lens acts as an object plane for the intermediate lens and a magnified image of the back focal plane is projected onto the viewing screen.

In a polycrystalline sample all possible directions of the crystallite are present and a concentric ring pattern is produced. The rings are continuous if the grains of the material are small, or discontinuous if the grains are large. When tilting a non-textured sample, the diffraction pattern will remain constant. However, when tilting a textured sample, i.e. one in which there is a preferred orientation of the crystallites, the intensity within the rings will vary and arcs will be formed in the ring pattern.

2.3.2.2 Bright field & dark field imaging

To form an image of the sample rather than a diffraction pattern, the intermediate lens is set so that the object plane is the image plane of the objective lens. Images formed using the bright central diffraction spot are known as bright field images as shown in figure 2.5(b). Contrast in the bright field image is due to the variations in electron scattering across the sample. The main scattering mechanism in the polycrystalline thin films investigated is Bragg diffraction from the crystallites. Therefore, dark regions in the bright field image correspond to grains that satisfy the Bragg condition. The level of image contrast can be enhanced by inserting an objective aperture, as it prevents scattered electrons from a range of Bragg angles from contributing to the final image.

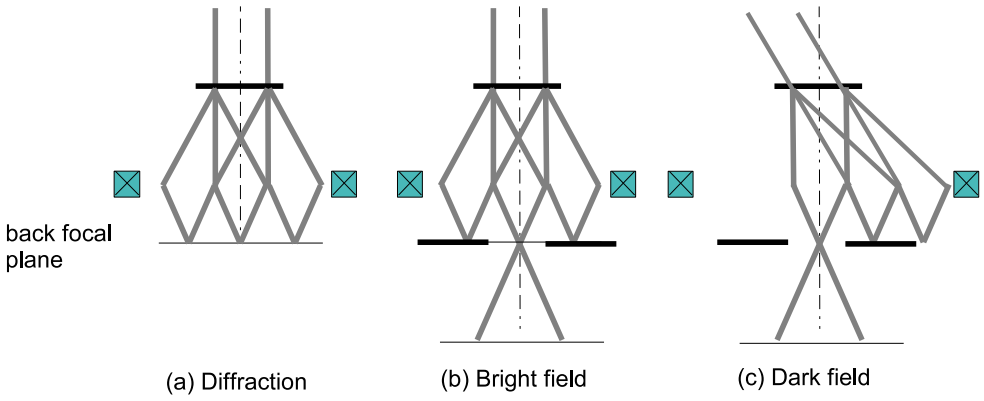

Figure 2.5: Schematic of (a) diffraction, (b) bright field and (c) dark field imaging modes.

Displacing the aperture from the optic axis will select only diffracted beams and will form a dark field image on the screen. However, in this method the electrons are off-axis so the image suffers from aberrations and can be difficult to focus. A dark field image can also be formed by tilting the beam so that the desired diffracted electrons travel down the optic axis avoiding the aberrations. More relative contrast can be attained in a dark field image when compared to the

corresponding bright field image, however there are fewer electrons contributing to the image and the overall signal is lower. Dark field imaging is easier when the sample has large single crystals, so that electrons may be taken from an individual diffraction spot. Polycrystalline samples with ring diffraction patterns are not well suited to dark field imaging and so was not often used in the course of this work. Bright field imaging and diffraction were the main techniques used for the structural investigations of the thin films in this thesis.

2.4 Magnetic imaging

All magnetic characterisation of the samples in this thesis was performed on a Philips CM20 TEM/STEM which has been optimised for Lorentz microscopy [7]. In a conventional TEM the sample is situated between the upper and lower objective lens pole pieces where it can be immersed in fields of up to 1T. A field of this magnitude would be more than enough to destroy any magnetic information stored in most samples. In the CM20, the objective lens can be switched off creating a field-free environment for the sample. The objective lens may also be used as a source of magnetic field by passing a current through the coils. Other modifications have been implemented on the microscope including a widened gap between the objective lens pole pieces, and two Lorentz lenses situated above and below the pole pieces. The wider gap allows enough space for specially designed TEM rods to be tilted through large angles, whilst the Lorentz lenses act as the imaging lenses so that the sample may be held in a field free environment without significant degradation of the final image.

2.4.1 Lorentz microscopy

Magnetic materials possessing an in plane component of magnetisation will cause a deflection in a beam of electrons passing perpendicularly through it. The Lorentz force, $\mathbf{F}_L$ can be expressed classically [8, 9]

$$\mathbf{F}_L = -e(\mathbf{v} \times \mathbf{B}) \tag{2.6}$$

where e is the electron charge, $\mathbf{v}$ is the velocity of the electrons, and $\mathbf{B}$ is the magnetic induction of the sample. Assuming that the arrangement of magnetic sample and electron beam is as shown in figure 2.6, the deflection will be in the

± x-direction through an angle $\beta_L(x)$ given by

$$\beta_L(x) = \frac{e\lambda}{h} \int_{-\infty}^{\infty} B_y(x,z)dz \tag{2.7}$$

where λ is the de Broglie wavelength, h is Planck's constant, and B_y is the y component of magnetic induction. For a specimen of thickness t, with uniform in-plane magnetisation and saturation magnetic induction B_s, the above expression can be simplified to

$$\beta_L = \frac{eB_s t\lambda}{h}. \tag{2.8}$$

Typical values of Lorentz deflections range from 1-100μrad, which are significantly smaller than the 10mrad typical of Bragg deflections.

This classical approach is sufficient to qualitatively illustrate most principles of Lorentz microscopy. However, Lorentz microscopy can also be considered from a quantum wave-optical approach which is necessary to extract quantitative information from the technique. In this approach the deflection is equivalent to a phase shift, ϕ, experienced by the electrons when passing through the sample. By the theory of Aharonov and Bohm [10] the phase shift is given by

$$\phi = \frac{2\pi eN}{h} \tag{2.9}$$

where N is the magnetic flux enclosed by the paths of two electron rays. For a plane wave incident on the thin film considered above, the phase shift between beams travelling through points x_1 and x_2 is given by

$$\phi(x_2 - x_1) = \frac{2\pi et}{h} \int_{x_1}^{x_2} B_y dx. \tag{2.10}$$

Thus, a ferromagnetic film acts as a pure phase object to the electron beam, and it can be seen that the magnitude of the phase shift is proportional to the integrated induction along the electron trajectory.

2.4.1.1 Fresnel mode

The Fresnel mode of Lorentz microscopy is a very useful technique for obtaining information on the magnetic state of a sample. It is quick and easy to implement and as such is one of the most commonly used modes for magnetic investigations. Oppositely magnetised domains will deflect the electron beam in opposite direc-

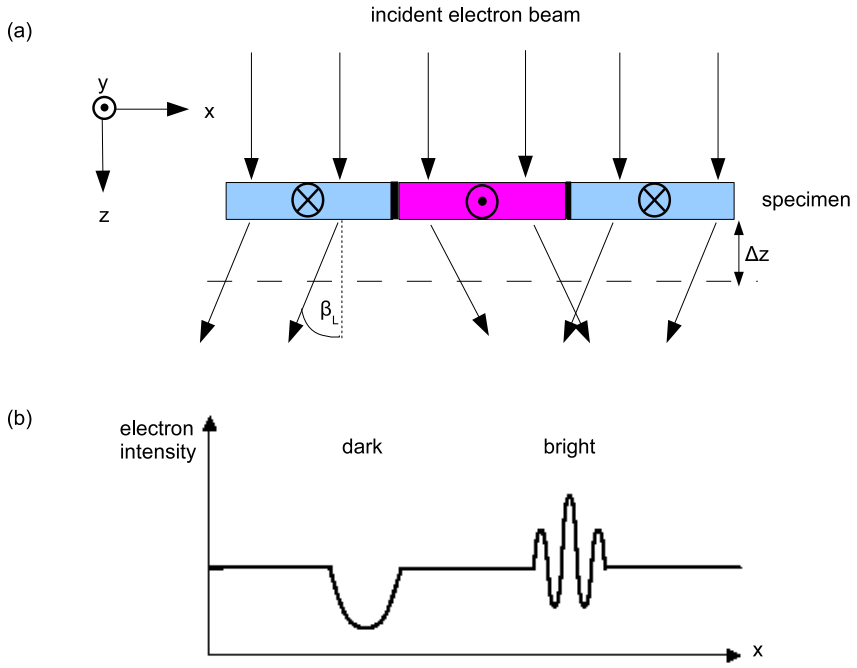

Figure 2.6: Schematic ray diagram for Fresnel image formation (a) Deflection of electrons beam from oppositely magnetised domains, (b) Intensity distribution at a plane displaced Δz from the sample.

tions, giving regions where the exiting beams are convergent (bright bands) and divergent (dark bands) as illustrated in figure 2.6. De-focussing of the imaging lenses has the effect of raising or lowering the focal plane of the image so that the distribution of electron intensity at that displacement can be viewed [11]. The amount of defocus used must be carefully chosen to suit the sample and the experiment. A large defocus will increase the level of contrast, but will reduce the resolution of the final image, whereas smaller defocus can make it increasingly difficult to observe magnetic features.

When using Fresnel mode to image small magnetic structures, electrostatic phase contributions arising from variations in the mean inner potential are sometimes very large and can almost mask the Fresnel contrast. For this reason, and the limited resolution, Fresnel microscopy is unsuitable for imaging magnetic elements with dimensions <200nm. However, it is particularly useful for the observation of magnetic behaviour in continuous films, such as those described in this thesis.

In a polycrystalline sample, magnetisation ripple is often seen within the near-uniform background of the image. Ripple is due to the random distribution of the individual easy axes of the crystallites, and is known to lie perpendicular to the mean direction of magnetisation within that domain [12]. Thus, the mag-

netisation ripple can be used to orient the sample such that the applied field is parallel to either the easy or hard axis.

2.4.1.2 Differential phase contrast

Differential phase contrast (DPC) [13] is a scanning transmission electron microscope (STEM) technique which is performed in the CM20 microscope. There is a direct relationship between the magnetic induction in the sample and the measured signal which allows quantitative measurements of induction to be made.

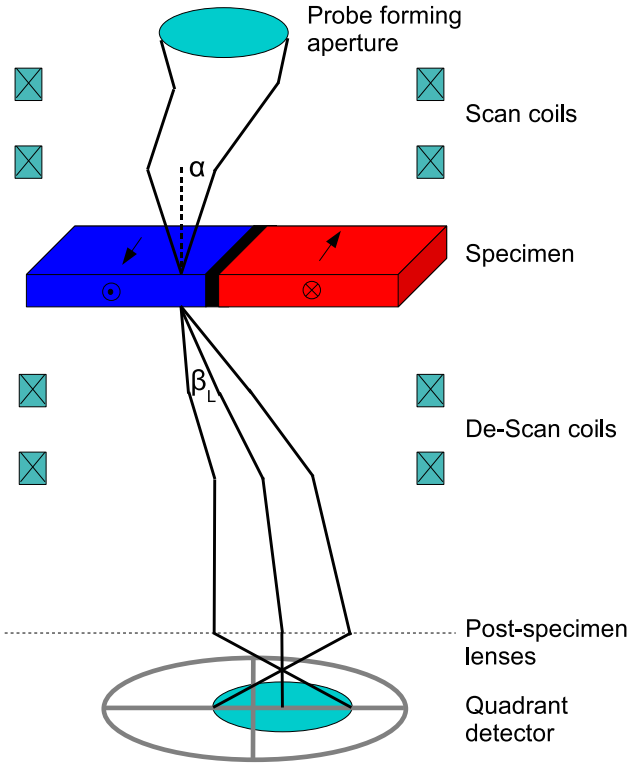

Figure 2.7: Illustration of DPC imaging mode.

Figure 2.7 shows a schematic of the DPC imaging mode outlined here. The electron beam is focused into a small probe and scanned across the sample by two sets of deflection coils which keep the beam parallel to the optic axis. On transmission through the sample, the beam emerges as a cone of illumination, which after passing through the de-scan coils, is projected onto a segmented detector in the far-field. In the absence of a magnetic sample, the beam will pass undeflected through the sample and will lie concentric with the detector. A magnetic sample will cause the beam to be deflected by the Lorentz force which is perpendicular to both the induction and the beam direction, and will be off-set

from the centre of the detector, as illustrated in figure 2.7. The difference signal from the quadrants of the detector gives a measure of the beam deflection which in turn is proportional to the integrated magnetic induction. Summing all the signals from the detector will give an equivalent bright field image of the sample in perfect registration with the difference images, allowing direct correlation between magnetic and structural information.

2.4.1.3 Magnetising experiments

Using Lorentz microscopy it is possible to study the dynamic behaviour of a magnetic sample as well as static magnetic states. To do this magnetic fields are applied to the sample in-situ by weakly exciting the objective lens and by using the Lorentz lenses to image. The magnitude and direction of the vertical field, H, can be altered by changing the size of current and the direction of current flow through the coils respectively. When the specimen is untilted, no component of the field is experienced in the plane of the sample. By tilting the sample through θ, as shown in figure 2.8, an in-plane component is induced in the sample and is given by

$$H_{in} = Hsin\theta. \tag{2.11}$$

The corresponding perpendicular component is given by

$$H_{out} = Hcos\theta. \tag{2.12}$$

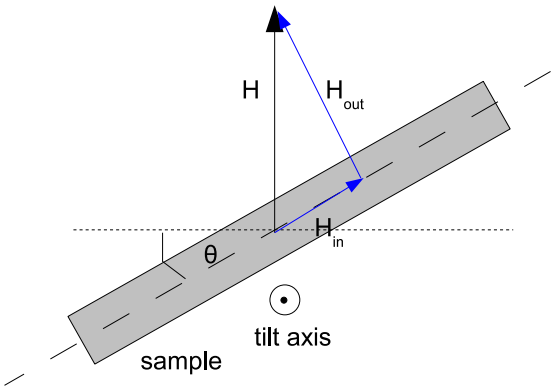

Figure 2.8: Generation of an in-plane H_{in} and out-of-plane H_{out} components of magnetic field by tilting the sample in an objective lens vertical magnetic field.

For the soft permalloy films that were investigated, an objective lens field of 30 Oe was sufficient to cycle the film through its hysteresis loop. This corresponds

to a maximum in-plane field of ∼12 Oe with an out-of-plane component of ∼25 Oe when the sample is tilted through 30°. The strong in-plane anisotropy of the continuous film prevents the out-of-plane component of magnetic field from pulling the magnetisation out of plane. Thus a magnetic sample can be taken through a complete magnetisation cycle by tilting the sample in the presence of a magnetic field.

A similar procedure can be carried out for a sample exhibiting perpendicular magnetisation. When a sample is perpendicularly magnetised there is no in-plane magnetic induction, and an electron beam will pass through undeflected as shown in figure 2.9(a). This results in an image with no magnetic information. However,

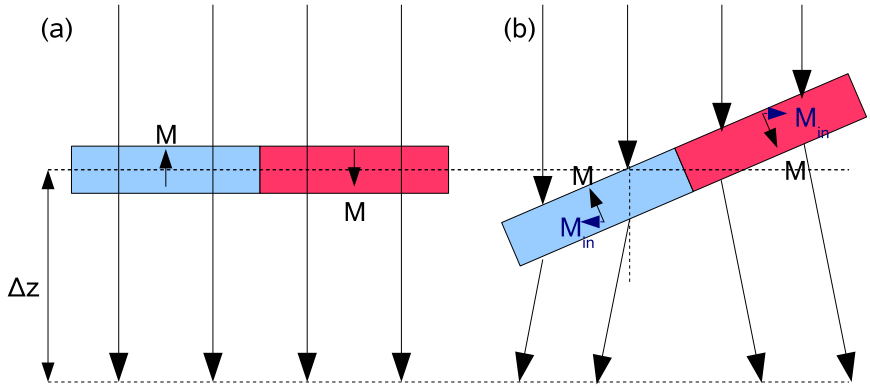

Figure 2.9: Imaging a sample with perpendicular magnetic anisotropy (a) untilted sample with undeflected electron beam, (b) tilted sample with component of magnetic induction perpendiclar to the beam resulting in deflection of the beam and magnetic contrast.

on tilting the sample there is now a component of the magnetic induction in the plane of the film (perpendicular to the beam). This causes a deflection in the incident electron beam resulting in an image with magnetic contrast, as in figure 2.9(b). The typical coercivity of the Co/Pd films with perpendicular magnetic anisotropy used for this work is of the order of 700 Oe. In order to observe the magnetic behaviour throughout a full hysteresis loop it is necessary to tilt the sample and then gradually increase the objective lens current. To reverse the perpendicular magnetisation direction, a magnetic field must be applied in the opposite direction by reversing the direction of current flow in the objective lens.

2.5 Focused ion beam (FIB)

The focused ion beam is a very versatile system and has a diverse range of uses across the scientific and industrial communities. They are most commonly used as a tool for milling and are employed in tasks such as TEM cross-section sample preparation [14] and trimming of read/write head pole pieces [15]. They also have the ability to deposit material, usually Pt or W, by gas ion injection allowing areas of a sample to be protected during sample preparation or to lay down conductive tracks during integrated circuit editing [16].

In this work, a FIB has been used as a tool to irradiate and pattern magnetic thin films. Its use as a tool for the modification of materials has been widely investigated with many researchers looking to specifically tailor magnetic properties of thin films. In this section the FIB and FIB/SEM instruments are described along with an explanation of how the irradiation dose is calculated. The patterning technique used was developed at Glasgow, and has been specifically designed with magnetic materials in mind. This technique is detailed in Section 2.5.3.

2.5.1 The FIB instrument

Two different FIB systems were utilised during the course of this PhD work. In the early stages an FEI Strata 200XP [17] machine was used, until it was replaced by an FEI xT Nova NanoLab 200 SEM/FIB [18]. The former was a conventional FIB system, whilst the latter is a DualBeam FIB/SEM system. Magnetic patterning was carried out in both systems however there are many advantages of a FIB/SEM to this work, which are detailed in section 2.5.2.

The Focused Ion Beam is in many ways similar to a scanning electron microscope (SEM), except that the beam rastered over the material surface is an ion beam instead of an electron beam. High resolution imaging and machining of a sample requires a highly focused probe, which in turn requires to be formed from as small a source as possible. A gallium liquid metal ion source (LMIS) [19, 20] is the most popular source in commercial FIB systems, although there is a range of other materials available, vastly increasing the number of potential applications of FIB. The Ga^+ LMIS consists of a spiral wound Gallium reservoir and a tungsten needle. By applying a fixed potential to the extraction electrode a strong electric field is produced at the tip of the needle, drawing the Ga coating at the tip of

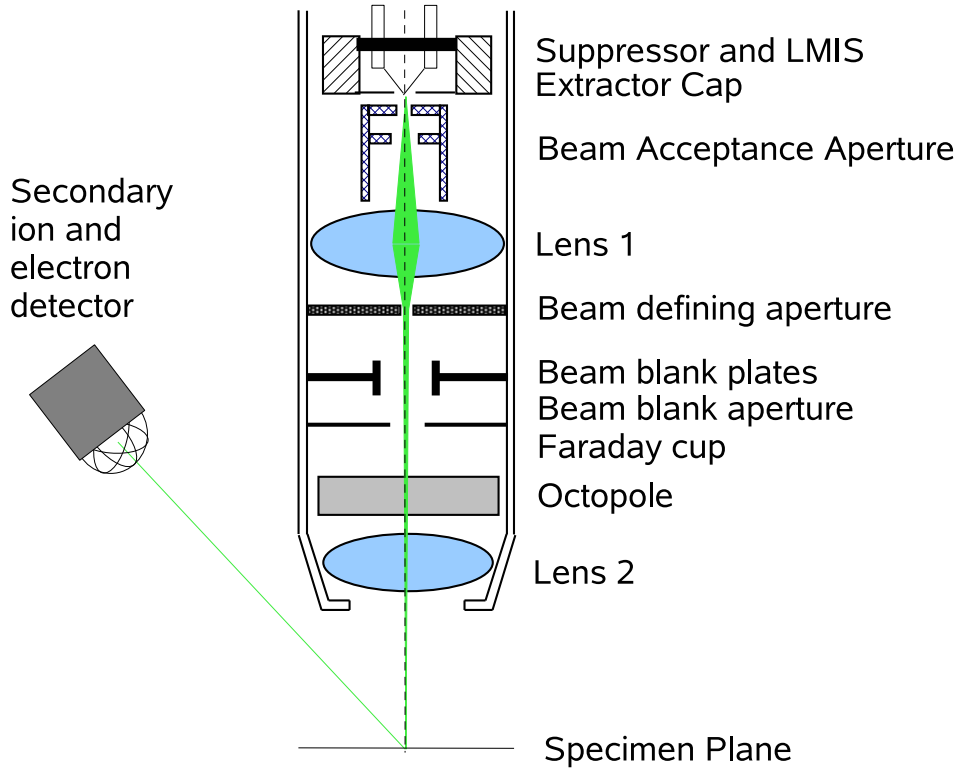

Figure 2.10: Schematic of the LMIS and ion column.

the needle into a Taylor cone with a tip radius of 5nm. The emission current is typically 2.2μA.

The ions emitted from the source then enter the ion column which is held under vacuum, 2x10^{-6}mbar, to avoid interference of the beam with atmospheric gas molecules. A schematic of the ion column can be seen in figure 2.10. The column contains two electrostatic lenses (a condenser and an objective lens) which focus the 30kV beam onto the surface of the sample. Beam currents range from 1pA to 20,000pA with corresponding profiles (FWHM) of 6nm to 350nm [18]. The beam current is chosen to suit the priorities of the task in hand such as spatial resolution or milling rate, whereas during irradiation the beam current is typically chosen so that the beam profile corresponds to the pixel spacing of the pattern to be irradiated. The octupole above the second lens gives control over the astigmatism of the beam, whilst the deflector plates control the scanning motion of the beam. Both secondary ions and electrons can be collected to form an image by selection of the polarity and voltage of the detector.

2.5.2 DualBeam FIB

The FEI DualBeam FIB is the most recent addition to the equipment in the Kelvin Nano-Characterisation centre and was heavily used during the latter parts of the project. The DualBeam consists of an electron column with a Sidewinder Ion column mounted at an angle of 52°. During operation of the ion beam,

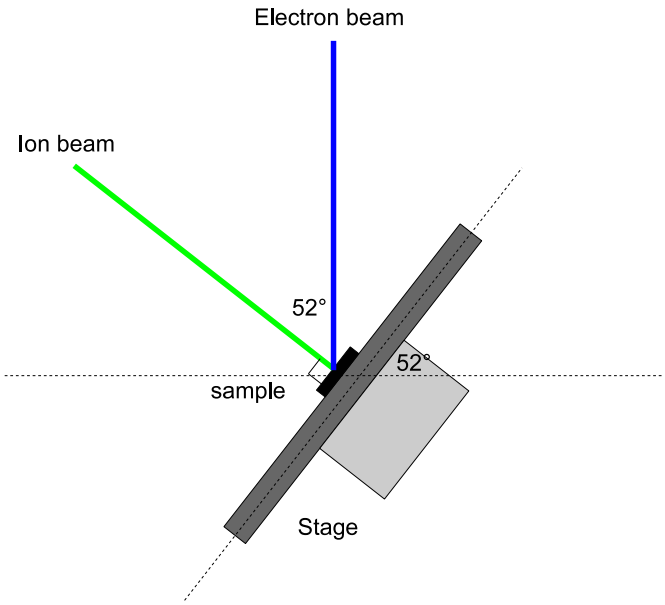

Figure 2.11: Schematic diagram showing the relative orientation of the ion beam and electron beam to the sample during patterning.

the stage is tilted through 52° so that the sample surface is perpendicular to the incident ion beam, as illustrated in figure 2.11. For use in SEM mode, the stage is left untilted so that the electron beam as the main imaging beam is perpendicular to the sample surface. The sidewinder column was specifically chosen as it has several useful advantages over the Magnum column which is standard on this type of instrument. The Sidewinder column gives a well defined ion probe at large probe currents, allowing more accurate rapid removal of material, and also the ability to form small ion probes down to 2 keV energy, allowing final polishing to remove surface damage from cross-sectioned samples.

The addition of the electron column is exceedingly useful when patterning magnetic samples, which are very susceptible to changes induced by the ion beam. Simply imaging with the ion beam is enough to cause damage or property modification in a magnetic sample. This makes accurate placement of patterns on an electron transparent window a difficult task when only an ion beam is available. Previously this problem was tackled by either scribing a line on the surrounding

substrate as a visible guide to the location of the window, or by repetitive patterning which can be time consuming. At best a precision of $\sim$50μm or half the width of the window was achievable. However, using the electron beam it is possible to view the sample without causing any damage or alteration in the magnetic sample. Using a sufficiently high accelerating voltage, the electron transparent window is easily visible as demonstrated in figure 2.12.

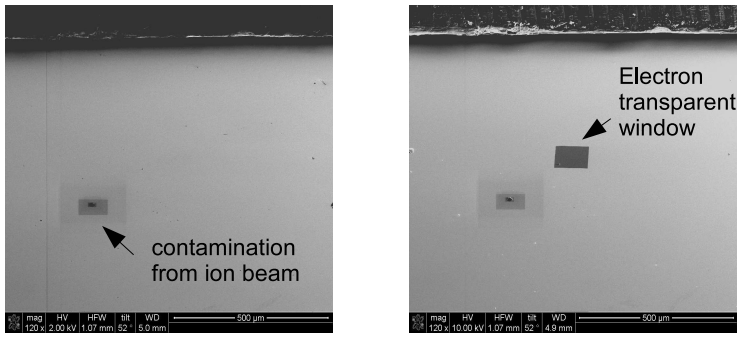

Figure 2.12: Image of TEM substrate taken at with electron beam at(a)5kV energy and then at (b)10kV energy where the TEM window is clearly visible.

An important part of the alignment procedure is to set-up the coincidence point of the two beams, to ensure that both the ion and electron beams are incident upon the same point. When this is achieved, accurate pattern registration of $<$1μm can be achieved.

This particular model of dual beam FIB has 2 modes for electron imaging. Mode 1 or search mode is for general imaging and can be used simultaneously with the ion beam to provide live imaging of the patterning process. Whilst both the SEM and FIB generate secondary electrons, the secondary electron yield per primary electron for FIB is roughly double that for the SEM. This means that the electron beam current must be larger than the ion beam current so that it may be detected above the FIB induced signal. Mode 2 is known as immersion mode as the sample is immersed in the magnetic field from the final ultra high resolution (UHR) lens. This gives much higher angular convergence, allowing finer probes to be produced and higher resolution SEM images to be obtained. The simultaneous ion and electron beam imaging cannot be used in immersion mode as the magnetic field of the immersion lens causes a large deflection of the ion beam. A diagram showing the formation of the electron probe in search and immersion modes is shown in figure 2.13.

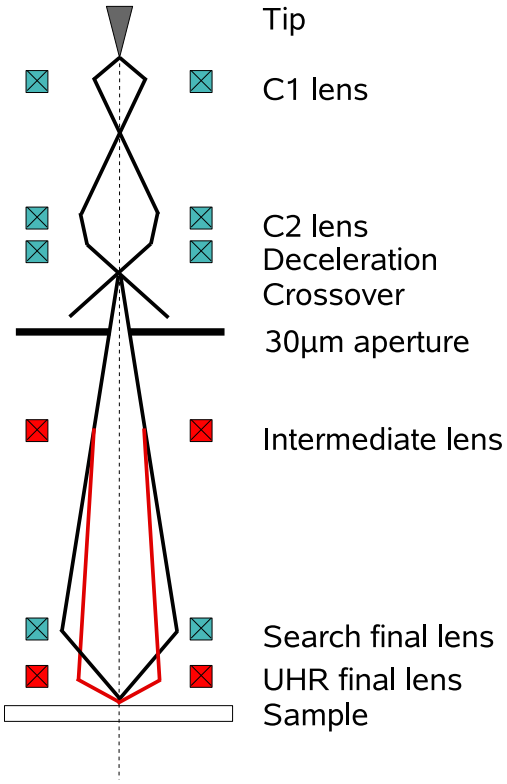

Figure 2.13: Schematic showing the path of the electron beam in search mode shown in black and immersion mode, shown in red.

2.5.3 FIB irradiation

Focused ion beam systems were primarily designed as a tool for sputtering and milling of material. Since their introduction they have been found to be extremely useful in many areas of research, development and industry [15, 16, 21, 22]. Ion irradiation of magnetic materials is one such use, but it is not straightforward to implement as the system was not designed for the task. Irradiation dose in ions cm^{-2} is not a parameter that can be directly input to the FIB, and must therefore be controlled indirectly by a number of other variables available to the user. A summary of the main parameters connected with irradiation - pixel overlap, dwell time and sputter rate, follows.

The pattern to be irradiated is divided up into a known number of pixels, which is either defined by the user as part of the input file, or is the number of pixels on the FIB patterning screen. For irradiation purposes the pixel overlap is set to 0%, as shown in figure 2.14. This is to ensure that each pixel receives the same dose and that the irradiation effects are homogeneous. The beam current is typically chosen so that the beam diameter (FWHM) matches the pixel size, d.

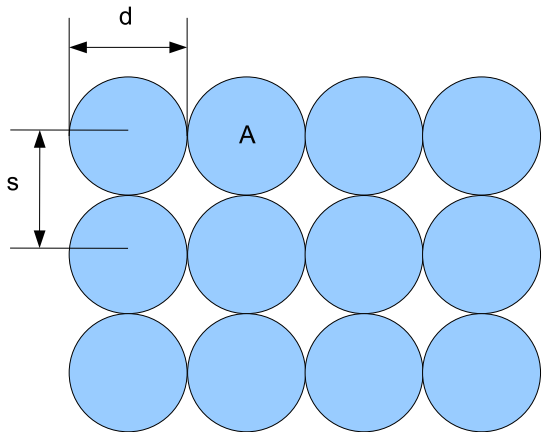

Figure 2.14: Schematic of irradiation with 0% overlap, where d and s are equal and are the pixel size and pixel spacing respectively.

The time that the beam dwells on each pixel in the pattern is defined by the dwell time parameter. The dwell time per pixel is a parameter that can be directly controlled by the user and will depend on the total dwell time for irradiation. For longer dwell times, multiple passes per pixel can be made. This results in better pattern definition than by using a single pass with long dwell time [22, 23]. The number of passes is calculated from the ratio of total dwell time / dwell time per pixel. Typical dwell times per pixel range from several μs at a dose of 1×10^{13} ions cm^{-2} to several hundred μs for doses of 1×10^{16} ions cm^{-2} and above. The result is that total pattern times can vary from less than 1s to several minutes, depending on both the dose and the size of the pattern.

The sputter rate is used to calculate the total milling time per pixel for a certain material, for a particular depth and beam current. It is a measure of the volume of material that may be sputtered per nA per second, and is a constant for a given material. It is a parameter that is utilised primarily for milling materials but which can be customised so that sensible depth values can be entered to directly assign the dose. The total dwell time is given by

$$t = \frac{Az}{SI} \tag{2.13}$$

where A the beam area in μm^2, z is the milling depth of each pixel in μm and S the sputter rate in μm^3 nA^{-1}s^{-1}, and I the beam current in nA.

It is known that irradiation dose may be calculated using the expression

$$D = \frac{tI}{eA} \tag{2.14}$$

where D is dose in ions cm^{-2}, e is the charge on the Ga^{+} ion. Therefore the total dwell time for a particular irradiation dose can be written as

$$t = De\frac{A \times 10^{-8}}{I \times 10^{-9}}. \tag{2.15}$$

By rearranging the equation 2.14 for total dwell time per pixel for irradiation and equating it with equation 2.15, an expression for irradiation dose can be obtained which is independent of beam current and area and is expressed in terms of variables that are at the users disposal.

$$D = \frac{z}{10eS} \tag{2.16}$$

For convenience the sputter rate was chosen to have a value of 1000 when performing irradiation. With this value for S a dose of 1×10^{16} ions cm^{-2} corresponds to the input of milling depth z=16μm.

2.5.3.1 Patterning method

Patterning is controlled in one of two ways depending on the intricacy of the pattern and the nature of the experiment. Firstly the in-built scripting language can be used for simple patterns where movement of the beam will not adversely affect the resulting structure. Either a serpentine or raster scan can be selected for this application, as depicted in figure 2.15(a-b). However, when creating magnetic nano-structures the motion of the beam as it irradiates the material must be controlled, otherwise modification of material that should remain unaffected may occur. This can be due to the lag in beam blanking time or fly back of the beam as it returns to its starting position. Raster or serpentine scans can also result in rough edges which will be detrimental to the definition of the pattern.

Some particularly complex structures cannot be created using the range of basic shapes available, so it is possible to input a bitmap image of the structure to the FIB to define it. But again this does not give the user enough control over the beam direction and edge roughness.

To overcome this externally generated stream files containing the x, y location and dwell time of every point to be irradiated, are used. These provide greater control over the motion of the beam and ensure that every point receives the same

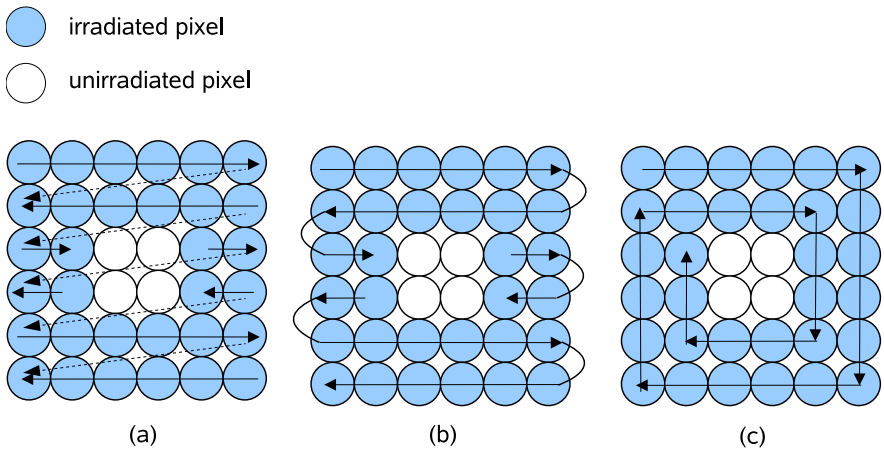

Figure 2.15: Schematic diagram showing the path of the ion beam during (a) a raster scan (b) a serpentine scan and (c) using a stream file generated by the 'edgestream' program

dose. A custom program called 'edgestream' uses a vector scanning strategy to trace out shape edges rather than rastering, as shown in figure 2.15(c), and orders the co-ordinates to control the beam. This program also allows the pattern to be irradiated in several stages or cuts. This is necessary for larger patterns in order to overcome the maximum number of points that can be read by FIB and also to reduce the effects of stage drift on the definition of the pattern. For the NovaNanoLab 200 SEM/FIB, drift is quoted at 10nm min^{-1}, which is comparable to the pixel size used for patterning. Therefore the first cut is generally small so that the patterning time is less than 1 minute. Subsequent cuts can be larger as any drift that occurs then will not affect the quality of the pattern definition. It is also necessary to wait for several minutes after the last stage movement to allow the stage to settle before patterning commences.

2.6 Simulations

Fabrication of magnetic thin films, subsequent pattering and investigations can be a time consuming and expensive process. Therefore it is sensible to attempt to simulate the outcome of the experiment as a guide to what may be expected, and as an aid to analysis of the experimental results. Several packages are available which can be used to simulate many aspects of this work. The programs and codes used are described in the following sections.

2.6.1 Stopping range of ions in matter (SRIM)

During the irradiation of a magnetic thin film, ions penetrate the magnetic sample modifying its structural and magnetic characteristics. Much of this research involves the irradiation of thin films of permalloy with a non-magnetic cap layer. When such a sample is subject to irradiation, the incident ions will not only directly alter the magnetic layer, but will cause mixing of atoms at the interface between the magnetic and non-magnetic layers, a process that is thought to play a significant role in the modification of magnetic thin films by FIB [24, 25].

The Stopping Range of Ions in Matter (SRIM) [26] package allows simulation of the irradiation process to be carried out. The penetration of any atomic ion, with an energy between 500eV to 2GeV, into a bulk or multilayer target may be simulated. Any target compound may be selected by choice of target atoms and stoichiometry, and can consist of up to 8 layers of various thickness and composition.

Statistical Monte Carlo algorithms are used to calculate the final 3D distribution of the ions as well as data concerning the ions energy losses. The ions are allowed to make jumps between collisions with the results being averaged over the gap between them. Loss of incident ion energy in nuclear interactions is considered in the screened Coulomb interactions which occur during ion-atom collisions. Here exchange and correlation interactions between overlapping electron shells are modelled. Ion energy loss via electronic process is also modelled by calculation of such effects as the electron and plasmon excitation.

During the calculation a cascade plot for every incident ion is produced. A screen shot taken during the calculation is shown in figure 2.16.

Cascades are a result of primary and secondary target atom knock-ons. When an incident ion collides with a constituent atom, it will impart some energy to it. If the energy received by the atom is greater than its binding energy then it will be displaced from its position and can go on to strike other atoms. This chain of events is known as a collision cascade. In many cases the energy imparted to an atom is not sufficient for displacement, so the atom will relax through vibration and dissipation of energy through phonons.

Data output concerning both the incident ion and the target material is calculated. Of particular interest here is data involving the range of the incident ions

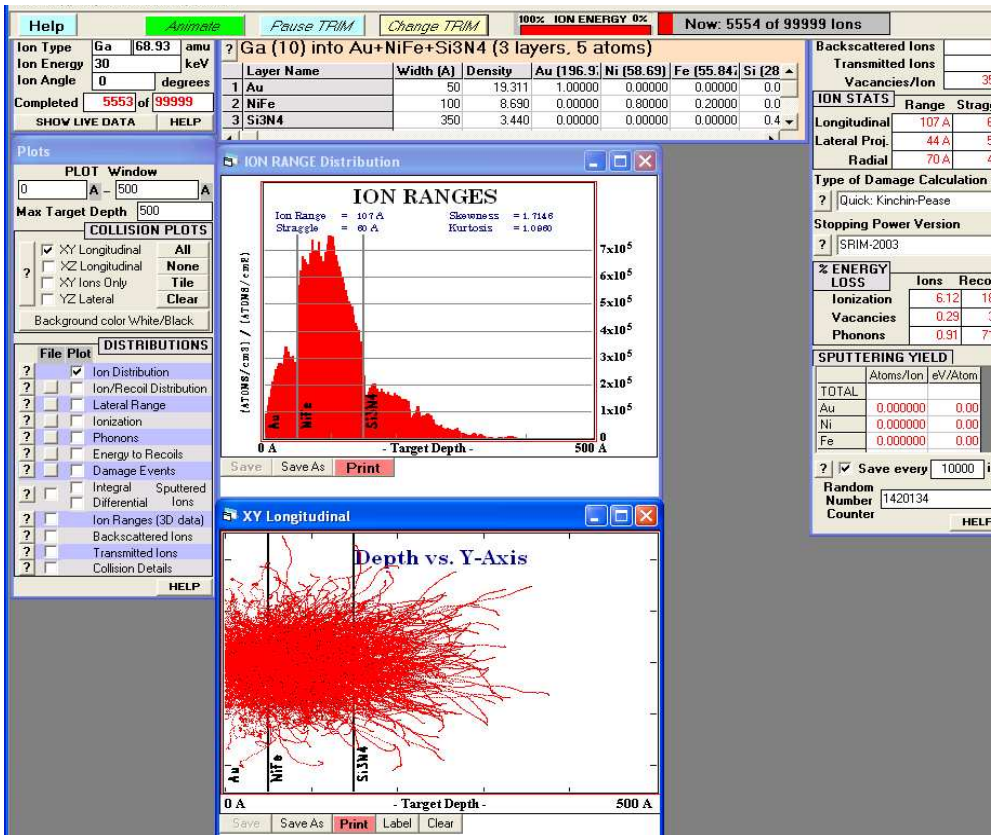

Figure 2.16: Screen shot from a SRIM simulation showing the range and trajectory of the incident ions.

within the target material and any mixing of atoms at the interfaces between the layers of the target.

Some weaknesses in the data produced by the program stem from the fact that the calculations assume the target material to be amorphous. As permalloy is a polycrystalline sample, any variation in atom binding energy with respect to the crystallography of the sample and ion channelling along particular crystallographic axes are neglected.

2.6.2 Tridyn

Previous codes such as SRIM do not account for the modification of the target substance during irradiation. This is suitable for simulating the effect of low irradiation doses, but at high doses there can be large scale modifications of the target.

The Tridyn code [27] is based on TRIM (Transport of Ions in Matter), one of the

programs in the SRIM simulation package described in section 2.6.1, and uses the binary collision approximation (BCA) model for ballistic transport. As well as computing the range profile for the incident ions, the program will simulate the dynamic change of thickness and composition for multicomponent targets. Ballistic effects such as incident ion implantation and reflection, sputtering and ion mixing are calculated for a target at zero temperature.

The calculation can be carried out for any ion at any incident angle. The ion energy is limited by the BCA to ∼10eV at low energies, whereas at high energies, the limit is determined by computation time and so is less suitable for MeV energies and above. The energy of the ion beam used in this work is 30kV and sits well within these limits.

The target can be defined as bulk material or as a multilayer system, but is limited to a total of 5 elements. This meant that some approximations had to be made during the calculations, such as the Si_3N_4 substrate being defined as pure Si. The target layers as well as any layers deposited during irradiation are also assumed to be amorphous.

An advantage of this program over SRIM is the control given to the user over the ion dose. The user can define the dose in ions cm^{-2} and the number of particle histories to be considered. Each particle is an increment of the dose and the output can be saved at several points during the calculation.

The main use for this program during this research was to simulate the depth profiles of each element in the target as a function of the incident ion dose. This gave a good indication of the amount of mixing that occured between the layers due to a particular dose, and is used in chapter 3.

2.6.3 Micromagnetic simulations

The Object Orientated Micromagnetic Framework (OOMMF) [28] is a micromagnetic modelling package developed at the National Institute of Standards and Technology (NIST). It allows the user to simulate possible magnetisation configurations that will be supported in a particular nanomagnet, as a consequence of the various energy terms in the system. Anisotropy, applied field and initial magnetisation states can be varied and shaped elements can be modelled. A 3D version is also available for use in modelling structures where changes in

magnetisation in the z direction need to be considered, such as in layered materials.

The program determines the effective field at every point in a 2D mesh, followed by calculation of the magnetisation by solving the Landau-Lifshitz equation

$$\frac{d\mathbf{M}}{dt} = -\gamma \mathbf{M} \times \mathbf{H}_{eff} - \frac{\alpha}{M_S} \mathbf{M} \times (\mathbf{M} \times \mathbf{H}_{eff}) \tag{2.17}$$

where γ is the electron gyromagnetic ratio, $\mathbf{M}$ is the magnetisation, with $\mathbf{M}_S$ the saturation magnetisation, $\mathbf{H}_{eff}$ is the effective field and α is the damping coefficient. The first term in the equation involves the precession of the magnetisation vector around the effective field direction, whilst the second term is the damping term.

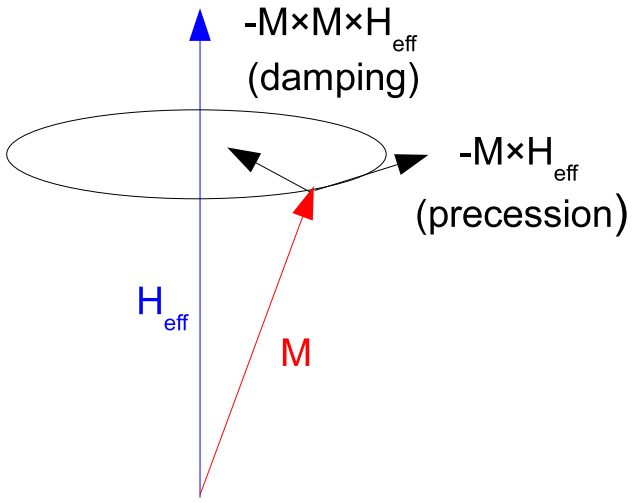

Figure 2.17: Procession of magnetisation around effective field direction.

With each spin iteration, the equation is re-evaluated until an equilibrium value is reached. This may be specified by the torque $\frac{d\mathbf{M}}{dt}$ falling below a critical value, or by use of a maximum simulation time or iteration count. This process is repeated with each step-wise increase of the applied field.

Although the results may be considered a fairly reliable guide between theory and experiment, there are a number of assumptions and compromises made in the calculation that must be taken into account when analysing the results. An ideal simulation would take into account every atomic moment in the sample. Realistically this is not possible owing to constraints provided by available time and computing power. The problem is broken down to a manageable size by

defining cells of uniform magnetisation. Cell size is an important factor in the outcome of the simulation. The cells used in the simulations shown in chapters 4 and 5 of this work have 5nm sides as this is close to the exchange length for permalloy. On a length scale shorter than this, the magnetisation may be expected to be uniform making it a suitable choice. Cell size also has practical implications regarding the length of time required for the simulation run.

Another of the assumptions made in the program results from the use of the square cells to define the structure. These mosaic like representations form geometrically perfect elements with straight edges and uniform thickness. In reality elements will not have perfectly defined edges or uniform thickness due to the limitations of the fabrication process [29]. They may also contain defects. Irregular shaped structures or those containing curves can also be difficult to model accurately using this method, although recent developments by the creators of the OOMMF package have taken steps to tackle this issue [30].

In addition to this, the calculation does not take into account the contributions that either thermal effects or time dependence have on the magnetisation states of the structure. A final point to note is that when the simulation is being carried out, the magnetic field is applied in steps, rather than the steady increase or decrease that is applied in TEM experiments. The field steps may be decreased by the user to impose a more realistic situation, but would again, be detrimental to the time required for calculation.

2.6.4 Fresnel image calculation

In this section a technique is described which is used to calculate the magnetic phase, and create the corresponding DPC and Fresnel images. These can be particularly useful as a guide to the contrast that can be expected in experimental images and also in helping to understand observed magnetic configurations.

To recall, Lorentz imaging involves the deflection of the electron beam, which is given by

$$\beta = \frac{e\lambda}{h} \int_{-\infty}^{\infty} (\mathbf{B} \times \hat{\mathbf{n}}) dl \tag{2.18}$$

where e is the magnitude of charge on the electron, λ is the electron wavelength, h is Planck's constant, $\mathbf{B}$ is the magnetic induction and $\hat{\mathbf{n}}$ is the unit vector parallel to the electron beam. The integration is performed along a line, l, parallel to

the optic axis. Deflection is caused by induction components perpendicular to the electron beam trajectory. If we consider the quantum mechanical approach, the electron beam experiences a phase shift as it passes through the magnetic material which is given by

$$\phi(r) = \frac{-e}{\hbar} \int_{-\infty}^{\infty} (\mathbf{A} \cdot \hat{\mathbf{n}}) dl \tag{2.19}$$

where $\hbar$ is Planck's constant divided by 2π and $\mathbf{A}$ is the magnetic vector potential [10]. The form of the magnetic vector potential is given by

$$\mathbf{A}(\mathbf{r}) = \frac{1}{4\pi} \iiint \frac{\nabla \times \mathbf{B}(\mathbf{r}')}{|r - r'|} d^3\mathbf{r}'. \tag{2.20}$$

Mansuripur described a technique which uses the magnetic vector potential to calculate the phase changes imparted to the electron beam in Lorentz microscopy [31]. In differential phase contrast microscopy an in focus image is built up as the beam is rastered across the sample. Contrast in the final DPC image is generated by a segmented detector which converts phase changes into intensity variations. By taking the 2D derivative of the phase, equation 2.19, perpendicular to the electron beam, we derive a quantity which is proportional to the integrated induction.

$$\nabla_{\perp}\phi(r) = \frac{-e}{\hbar} \int_{-\infty}^{\infty} (\nabla \times \mathbf{A}) \times \hat{\mathbf{n}} dl \tag{2.21}$$

as $\bigtriangledown \times \mathbf{A} = \mathbf{B}$ we can write

$$\nabla_{\perp}\phi(r) = \frac{-e}{\hbar} \int_{-\infty}^{\infty} (B \times \hat{\mathbf{n}}) dl. \tag{2.22}$$

Therefore we can say that the DPC image is related to integrated magnetic induction perpendicular to the beam, which indicates that the differential phase produces a map of the deflection angle.

Fresnel imaging is generally considered to be non-linear, but under certain conditions it can be linearly interpreted and used in a quantitative manner. In the linear regime the Fresnel image intensity is proportional to $\nabla^2\phi$ where

$$I(r, \Delta) = 1 - \frac{\Delta\lambda}{2\pi} \nabla_{\perp}^2 \phi(r) \tag{2.23}$$

where Δ is the defocus distance and $\nabla_{\perp}^2$ is the Laplacian relating to the in plane

co-ordinates [32].

Reference [32], shows that beginning with equation 2.23 shown above, the intensity of a Fresnel image at small defocus Δ, for a thin film normal to the beam with no magnetisation variation through the thickness can be written as

$$I(\mathbf{r}, \Delta) = 1 - \Delta \frac{e\mu_0 \lambda t}{h} (\nabla \times \mathbf{M(r)}).\mathbf{z}. \tag{2.24}$$

This reveals that the image intensity can be calculated from knowledge of the microscope parameters and the out of plane component of the magnetisation curl when the linear imaging conditions are applicable. The spatial frequencies in the image determine the extent that this equation can be applied for a given defocus. For the images in this thesis the resolution may be determined by the width of a magnetic domain wall. Therefore for in a 200keV TEM, defocus values of $\ll 200\mu$m should allow for linear imaging.

The scripts used to calculate the phase and Fresnel images use the fast Fourier transform (FFT) in the Digital Micrograph software package and were written by Dr. Stephen McVitie and Gordon White of Glasgow University. Using the FFT algorithm requires the images to be have sides N=2^n where n is an integer. Input images were padded out with zeros to fit this size. This was also useful as it allows stray field around the edges of the elements to be observed.

To calculate the Fresnel image, we require a phase image and an amplitude image. The phase is calculated using the process detailed in Mansuripur [31]. The x, y and z components of the magnetisation can be obtained from an OOMMF simulation or by creating three separate images each representing one component of the magnetisation. This process also calculates the integrated magnetic induction for that configuration. In the simplest case we can neglect amplitude modulation and can make it equal to 1 everywhere. However, in some cases the amplitude and hence electrostatic phase from changes in the mean inner potential must be included. To include simply the amplitude, we can make a mask of the element being simulated, with a value of 1 in the patterned region and 0 everywhere else. To get the electrostatic phase, we calculate

$$\phi_e = \pi \frac{Vt}{\lambda E} \tag{2.25}$$

where V is the inner potential of the material, 21V for permalloy, t is the sample thickness, λ is the electron wavelength, and E is the electron accelerating voltage.

Multiplying this by the mask created, we obtain an amplitude input image which includes the electrostatic phase.

Initally the electron wave is assumed to be in phase with uniform amplitude, $ae^{i\phi}$. To calculate the exit wave, the Fourier transform is taken of the electron wave and multiplied by the transfer function based on a Lorentz lens in a FEI Tecnai TEM operating at 200kV with spherical aberation term C_s=8000mm and λ=2.51pm. The image wave is then calculated by taking the inverse Fourier transform of the exit wave and is multiplied by its complex conjugate to give the intensity.

Bibliography

[1] B. Khamsehpour, C. D. Wilkinson, J. N. Chapman, and A. B. Johnston, J. Vac. Sci. Technol. **14**, 3361 (1996).

[2] M. W. Davidson and M. Abramowitz, Optical Microscopy, National High Mag Field Lab, FL, USA (1999).

[3] S. J. Pennycook *et al.*, Proceedings for 2003 International Conference on Characterisation and Metrology for ULSI Technology **683**, 627 (2003).

[4] L. Reimer, *Transmission Electron Microscopy* (Springer-Verlag, 1984).

[5] D. B. Williams and C. B. Carter, *Transmission Electron Microscopy* (Kluwer Academic / Plenum Publishing, 1996).

[6] H. M. Rosenberg, *The Solid State - Third Edition* (Oxford Science Publications, 1998).

[7] J. N. Chapman, A. B. Johnston, L. J. Heyderman, S. McVitie, and W. A. P. Nicholson, IEEE Trans. Mag. **30**, 4479 (1994).

[8] J. N. Chapman, J. Phys. D.: Appl. Phys. **17**, 623 (1984).

[9] J. N. Chapman and M. R. Scheinfein, J. Mag. Mag. Mat. **200**, 729 (1999).

[10] Y. Aharonov and D. Bohm, Phys. Rev. B **115**, 485 (1959).

[11] H. W. Fuller and M. E. Hale, J. Appl. Phys. **31**, 238 (1960).

[12] H. Hoffmann, IEEE Trans. Mag. **4**, 32 (1968).

[13] J. N. Chapman, P. E. Batson, E. M. Waddell, and R. P. Ferrier, Ultramic. **3**, 203 (1978).

[14] R. M. Langford and A. K. Petford-Long, J. Vac. Sci. Technol. **A19**, 2186 (2001).

[15] T. Koshikawa, A. Nagai, A. Yokohama, T. Hoshino, and Y. Ishizuki, IEEE Trans. Mag. **34**, 1471 (1998).

[16] G. L. Gorman *et al.*, IEEE Trans. Mag. **33**, 2824 (1997).

[17] *FEI Strata 200XP Operation Manual, PN21021-B.*

[18] *XT Novananolab User Manual 4022 262 52351.*

[19] J. Meingallis, J. Vac. Sci. Technol. **B5**, 469 (1987).

[20] J. Orloff, Rev. Sci. Instrum. **64**, 1105 (1993).

[21] A. A. Tseng, J. Micromech. Microeng. **14**, R15 (2004).

[22] A. A. Tseng, Small **10**, 924 (2005).

[23] C. A. Volkert and A. M. Minor, MRS Bulletin **32**, 389 (2007).

[24] Y. G. Wang, D. McGrouther, S. McVitie, M. McKenzie, and J. N. Chapman, J. Appl. Phys. **100**, 073901 (2006).

[25] T. Devolder, Phys. Rev. B **62**, 5794 (2000).

[26] *SRIM software by J. F. Ziegler freely available from www.srim.org.*

[27] *TRIDYN FZR User Manual, W. Moller and M. Posselt, 2002.*

[28] M. J. Donahue and R. D. McMichael, NISTIR 6376, National Institute of Standards and Technology, Gaithersberg, MD (1999).

[29] C. Brownlie, *A TEM investigation of controlled magnetic behaviour in thin ferromagnetic films*, PhD thesis, University of Glasgow, UK, 2007.

[30] M. J. Donahue and R. D. McMichael, IEEE Trans. Mag. **43**, 2878 (2007).

[31] M. Mansuripur, J. Appl. Phys. **69**, 2455 (1991).

[32] S. McVitie and M. Cushley, Ultramic. **106**, 423 (2006).

Chapter 3

Effect of Ga^+ ion irradiation on permalloy multilayers

3.1 Introduction

Previous experiments have shown that the irradiation of permalloy thin films can effectively modify the magnetic and structural properties of the film [1, 2, 3]. In multilayer samples such as Co/Pt and exchange bias samples, irradiation has been used to tailor magnetic properties by induced mixing of layers in the system [4, 5, 6]. In this chapter magnetic thin film systems containing permalloy and one or more non-magnetic metal layers are used to investigate how effectively a combination of irradiation and interlayer mixing can modify the properties of the system.

Simulations of the penetration of the Ga^+ ions into the multilayer system and induced alloying are also shown. The as-deposited microstructural and magnetic properties of the thin film systems are presented, followed by results showing changes induced in these properties by irradiation. These effects are investigated for a range of ion doses, different magnetic layer thickness and non-magnetic metal cap layers. A discussion of results and comparison of the two different sample structures is given in section 3.5.

Specimen ↓ / Deposition order →	Layer 1	Layer 2	Layer 3
Bilayer 1	10nm $Ni_{80}Fe_{20}$	5nm Al	
Bilayer 2	10nm $Ni_{80}Fe_{20}$	5nm Au	
Bilayer 3	20nm $Ni_{80}Fe_{20}$	5nm Al	
Bilayer 4	20nm $Ni_{80}Fe_{20}$	5nm Au	
Trilayer 1	5nm Al	10nm $Ni_{80}Fe_{20}$	5nm Al
Trilayer 2	5nm Au	10nm $Ni_{80}Fe_{20}$	5nm Au

Table 3.1: Composition and layer thickness of magnetic systems investigated.

3.1.1 Magnetic thin film systems

The magnetic material investigated in this study is permalloy, a nickel iron alloy with a $Ni_{80}Fe_{20}$ composition. A simple, versatile material, permalloy is commonly used in a range of electromagnetic and thin film applications. It is a polycrystalline material with low anisotropy and as such, it does not possess any strong crystallographic easy axes. However, an easy axis can easily be established by depositing the film in the presence of an applied magnetic field. Indeed, even when no applied field is present during deposition, stray fields from nearby electrical equipment, or even the Earth's magnetic field, may influence deposition enough to establish a weak anisotropy in the film. The thin films used in this project were deposited by thermal evaporation and DC sputtering in the absence of any applied field, making the local environment the largest contributing factor to any induced anisotropy.

Two sets of samples were studied and are summarised in Table 3.1. Bilayer samples were deposited in Glasgow University by thermal evaporation, whilst trilayer samples were deposited at the University of Leeds using the DC sputter method. A schematic of the structures is shown in figure 3.1.

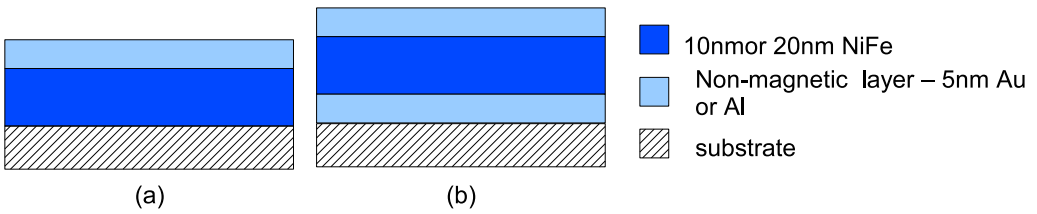

Figure 3.1: Schematic diagram showing the layer structure of the bilayer and trilayer samples.

The aim of the work in this chapter is to achieve solely magnetic patterning of permalloy systems with little or no topographic changes. The presence of the non-magnetic cap layer is to allow mixing of the magnetic and non-magnetic layer to

occur during the irradiation process. This is thought to enhance modification of the properties of the magnetic layer by introducing impurities or defects into the layer as well as changing the amount of irradiation induced damage[7] compared to uncoated films. In the trilayer structure, a layer of Al or Au is deposited on either side of the NiFe layer, as shown in figure 3.1. This structure allows interfacial mixing from both sides and potentially causes the NiFe layer to undergo magnetic and structural changes at a lower dose than with the equivalent single layer. Aluminium and Gold were chosen as the non-magnetic layers as a result of SRIM simulations (discussed in section 3.1.2), so as to be able to compare the effect of the atomic mass of the non-magnetic layers on the resultant magnetic and physical properties of the thin film system.

3.1.2 Simulations

Two different simulation packages, SRIM and Tridyn (discussed in chapter 2) were used in this chapter to help choose suitable materials for multilayer systems and to help understand the irradiation induced changes. In the first instance, SRIM simulations were used to assess the suitability of different materials as the non-magnetic layers. The depth to which the Ga^+ ions penetrate the bilayer can be calculated and the mode of energy loss and manner of stopping is determined. For 30kV Ga^+ ions, nuclear interactions with atoms in the multilayer is the main energy loss mechanism, leading to displacement and mixing of the atoms [8].

Aluminium and gold were chosen for the simulations to see the effect of the mixing atoms of different atomic mass into the magnetic layer. Figure 3.2(a) shows the simulated distribution for 30keV Ga^+ ions stopping in the 5nm Al/10nm NiFe bilayer. From the distribution it can be seen that some ions penetrate through the entire thickness of the permalloy layer and into the substrate, with only a small fraction being stopped by the aluminium layer. The Ga^+ ion profile within the NiFe layer shows that a large number of ions are stopped in this region suggesting that modification of the magnetic and structural properties throughout the entire thickness of this layer is likely to occur, either through the creation of defects or mixing with the Al atoms across the interface.

In figure 3.2(b), showing the irradiation of the 5nm Al/20nmNiFe sample, a similar distribution of ions are stopped in the Al layer, and the first 10nm of the NiFe layer as was seen in figure 3.2(a). The concentration of ions stopping in the NiFe layer then falls off, with only a very few ions penetrating the complete

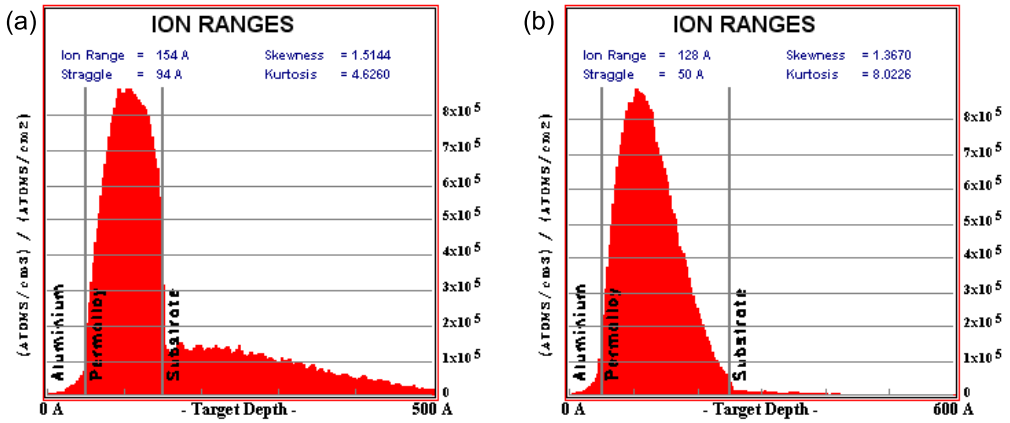

Figure 3.2: SRIM simulated stopping distances for 30kV Ga^+ ions in Al/NiFe bilayers, combination 1 & 3 in table 3.1.

depth and stopping in the substrate. From this we can infer that modification of the magnetic material due to mixing will occur more evenly throughout the 10nm NiFe layer, whereas the 20nm layer may experience more modification of properties in the top half than in the bottom half.

The same simulations were carried out using gold as the non-magnetic layer, and are shown in figure 3.3. Here a larger fraction of the ions stop in the gold layer than the aluminium layer, which is in accordance with the higher scattering cross-section of Au. It is also likely that the Ga is more efficient at transferring energy to the Al atoms being that they are of similar atomic weight. This means that there are fewer ions to go on to modify the properties of the magnetic layer in the samples with the Au layers. However, of the ions that do penetrate through to the permalloy layer, a similar response to the thickness of the layer is seen as with the aluminium sample. In the 10nm NiFe sample, figure 3.3(a), there is a significant ion concentration throughout the thickness of the layer. This concentration profile is replicated in the first half of the 20nm NiFe layer, followed by a decrease in the second half of the layer, figure 3.3(b). This again suggests that for the thicker permalloy samples, the overall effect of modification will be less than in the samples with thinner layers of permalloy. These results also suggest that of the two sets of samples, the systems with Al as the non-magnetic layer will more effectively modify the magnetic layer due to the larger number of ions that pass through and stop in that region.

Figure 3.4(a) and (b) show the SRIM simulations for the Al and Au trilayer samples respectively. In the top non-magnetic layers in both 3.4(a) and (b) the Ga^+ ion profile is the same as for the corresponding bilayer systems as expected.

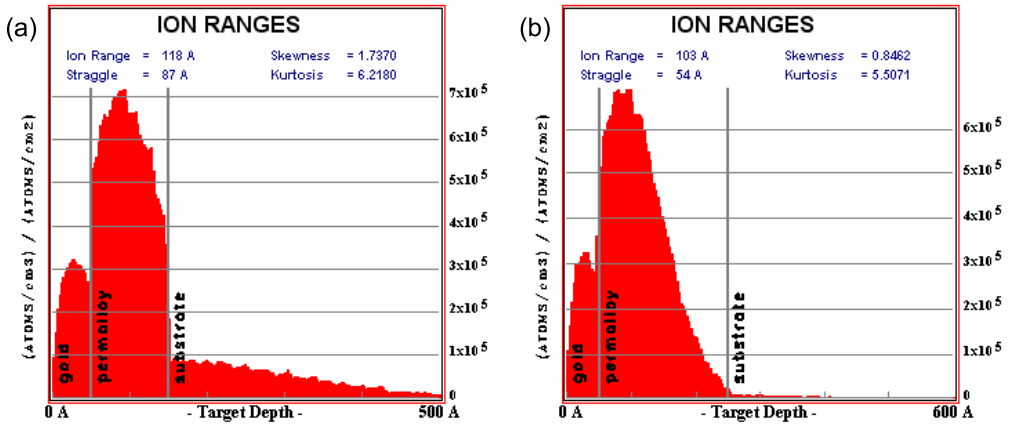

Figure 3.3: SRIM simulated stopping distances for 30kV Ga^+ ions in Au/NiFe bilayers, combinations 3 & 4 in table 3.1.

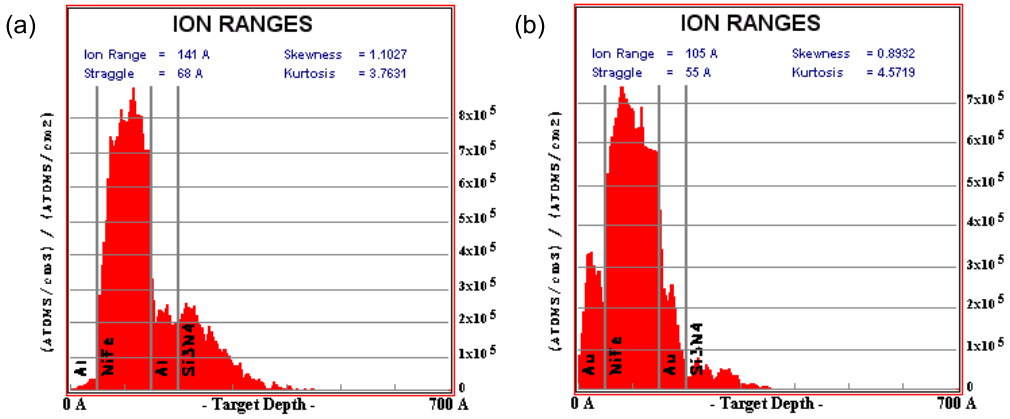

Figure 3.4: SRIM simulated stopping distances for 30kV Ga^+ ions in (a) Al/NiFe/Al and (b) Au/NiFe/Au trilayers, combinations 5 & 6 in table 3.1.

However, at the second interface with the lower non-magnetic layer, there is a significant difference in the Ga^+ distribution. This is not unexpected as the presence of the extra non-magnetic layer means that many of the Ga^+ ions will be stopped in this layer rather than penetrating through to the substrate. This suggests that with ions penetrating the entire way through both trilayers, there will be mixing of the atoms in the layers at both interfaces, in turn allowing more effective modification of the material properties at lower ion doses.

3.2 Properties of the multilayer systems in the as-deposited state

The bright field and Fresnel modes of electron microscopy have been used to investigate the physical microstructure and magnetic behaviour of the multilayer systems in the as-deposited state and subsequent to irradiation with a 30keV Ga^+ ion beam. Throughout this section, the 20nmNiFe/5nmAu sample, bilayer 3 in table 3.1, is used to illustrate the results as it is representative of the character and behaviour of the other multilayers. Particular details from the other bilayers are tabulated and discussed where appropriate.

3.2.1 Structural properties of the as-deposited state

Shown in figure 3.5 is a bright field image and diffraction patterns taken of the 20nm NiFe/5nm Au bilayer prior to irradiation. The Digital Micrograph package was used to take measurements of grain diameter. This was achieved by using the histogram to display intensity traces across a number of grains. Grains appear in the histogram as regions of low intensity allowing accurate measurements of their diameter to be made. Multiple grain size measurements were made for each sample. A mean grain size for this sample was found to be 5.2±1.3nm, and was consistent across all 4 bilayer samples. The error in these values was calculated from the standard deviation of the measurements made.

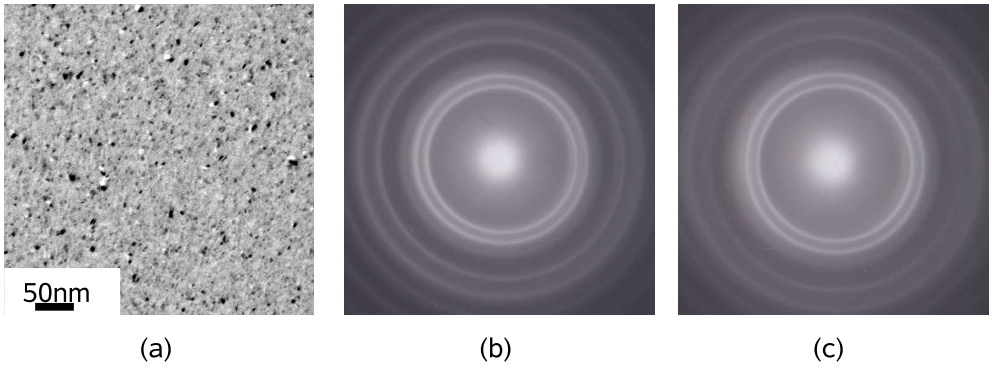

Figure 3.5: (a) Bright field image (b) untilted diffraction pattern (c) diffraction pattern tilted through 30 degrees of 20nm NiFe/5nm Au in the as-deposited state.

In figure 3.5(b), which shows the diffraction pattern for the 20nm NiFe/5nm Au sample, it can be seen from the clear rings that the film has polycrystalline

structure. On tilting the sample through 30° no change in the diffraction pattern was seen (fig. 3.5(c)), indicating that there is no preferred orientation of the grains in the sample. Again, this sample is illustrative of the properties of the 3 other bilayer films, which all show the same polycrystalline and untextured structure.

The procedure outlined above was carried out for the two trilayer samples consisting of 5nm Au/10nm NiFe/5nm Au and 5nm Al/10nm NiFe/5nm Al. The sample with Au layers was consistant with the bilayer samples, showing a mean grain size of ∼5nm and an untextured polycrystalline structure. However, on examining the Al trilayer samples, figure 3.6(a), unexpected changes in diffraction contrast were clearly visible and appear in the image as a change in greyscale contrast in a diagonal band from top right to bottom left. Diffraction analysis confirmed that the area on the left hand side of the image was untextured, whereas a diffraction pattern formed from the right hand side of the image showed texture.

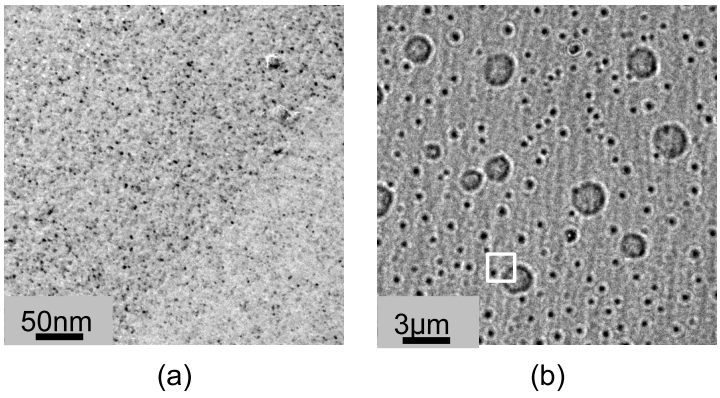

Figure 3.6: (a) Bright field TEM image of grain structure in Al/NiFe/al system (b) Fresnel mode image of Al/NiFe/Al system showing delaminated regions of material. Image (a) is taken across the edge of one of the bubbles indicated by the white box in image (b).

A lower magnification Fresnel image was also taken of the magnetic state of this sample, figure 3.6(b), where in addition to smaller regions of contamination or dirt, which could not be removed by cleaning, large 'bubbles' of material were seen. The image in figure 3.6(a) is taken across the edge of one of these bubbles, indicated by the white box on figure 3.6(b). This difference is thought to be due to delamination of the Al film from the substrate. The reason for delamination is unclear, however it is possibly caused by residual contamination on the substrate which would promote oxidisation of the Al and make it less likely to adhere well to the substrate.

Attempts were made at depositing the Al sandwich structure in the thermal

evaporator in Glasgow. First observations indicated that this had been successful, and easy and hard axis reversals were recorded. However, on patterning the sample with the ion beam, the Al/NiFe/Al multilayer again delaminated from the substrate. This is visible in the Fresnel image shown in figure 3.7, where bubbles of material are clearly seen in the 3×10^{14} and 1×10^{15} ions cm^{-2} dosed regions. As such this multilayer combination was not used in any further study.

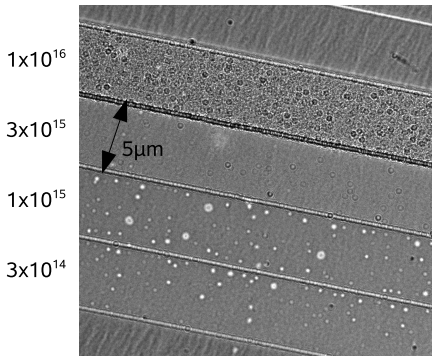

Figure 3.7: Fresnel image of Al/NiFe/Al sample deposited by thermal evaporation showing local delamination and the formation of 'bubbles' after irradiation. Note that there is no clear relationship between the density of delaminated bubbles and the irradiation dose.

3.2.2 Magnetic properties of the as-deposited state

The magnetic properties of the multilayers before and after irradiation have been investigated using the Fresnel mode of Lorentz microscopy. It was also important to determine the direction and strength of any intrinsic anisotropy present in the samples, as it may influence the magnetic behaviour of patterns created in the material.

Firstly the samples were rotated in the holder through 180° with magnetic reversal sequences taken at different orientations so as to ascertain whether any anisotropy was present. In both the Au and Al capped samples the magnetisation ripple aligned with a preferred direction at remanence, indicating that there was indeed an easy axis. The evolution of the magnetisation distribution has been studied for two orthogonal directions of applied field, i.e along directions which displayed typical easy and hard axis behaviour. Images at various fields during the magnetisation reversal are shown for both directions with the applied field and magnetisation direction indicated by the red and white arrows respectively.

Again, bilayer combination 3, 20nm NiFe/5nm Au has been selected as being

representative of the multilayer combinations, with individual values of coercivity and anisotropy fields for the individual samples itemised in table 3.2.

3.2.2.1 Easy axis behaviour

Lorentz microscopy images showing the easy axis reversal of sample bilayer 3 are shown in figure 3.8. The field was applied by tilting the sample through ±30° at 1° intervals. The sample tilt was then converted into a field value via the calibration relation

$$H = (1.214I - 12.545)sin\theta \tag{3.1}$$

where H is the applied field on Oe, I is the objective lens current in mA, which for these samples was 30mA and θ is the angle through which the sample is tilted. Using this relation a change in tilt angle of 1° is equivalent to changing the applied field by 0.4Oe. As the applied field was taken from -12.9 Oe to +1.4 Oe, figure 3.8(a-c), the magnetisation ripple contrast and wavelength increased. A domain wall, not captured on the camera, swept through effecting the reversal of the film between images (c) and (d). An image of the sample after reversal is shown in figure 3.8(d), where the change in magnetisation direction between figures 3.8(c) and (d) is highlighted by the reversal of the ripple contrast. The film was then saturated in the direction of the applied field 3.8(e), where a reduction in the ripple contrast (quantified below) is apparent. The field direction is reversed, figure 3.8(f,g), and again an increase in the ripple contrast is observed, until reversal of the film occurs in figure 3.8(h) at -2.1 Oe. The field was then increased to -14.9, figure 3.8(i,j) to saturate the magnetisation in this direction and complete the reversal. The outward and return cycles are consistent and give a value of coercivity of 1.9 Oe.

Assuming that M $\propto \cos\theta$, where θ is the angle between the net magnetisation and the direction of the applied field, the Fresnel images can be used to determine the net moment in the sample at a particular point during the reversal. This information in turn can be used to plot M-H loops for the material. The hysteresis loop plotted using the information in the sequence in figure 3.8 is shown in figure 3.9. The coercivity of the sample was calculated using the relation

$$H_c = \frac{H_+ - H_-}{2} \tag{3.2}$$

where H_+ and H_- are the outward path and return path switching fields respec-

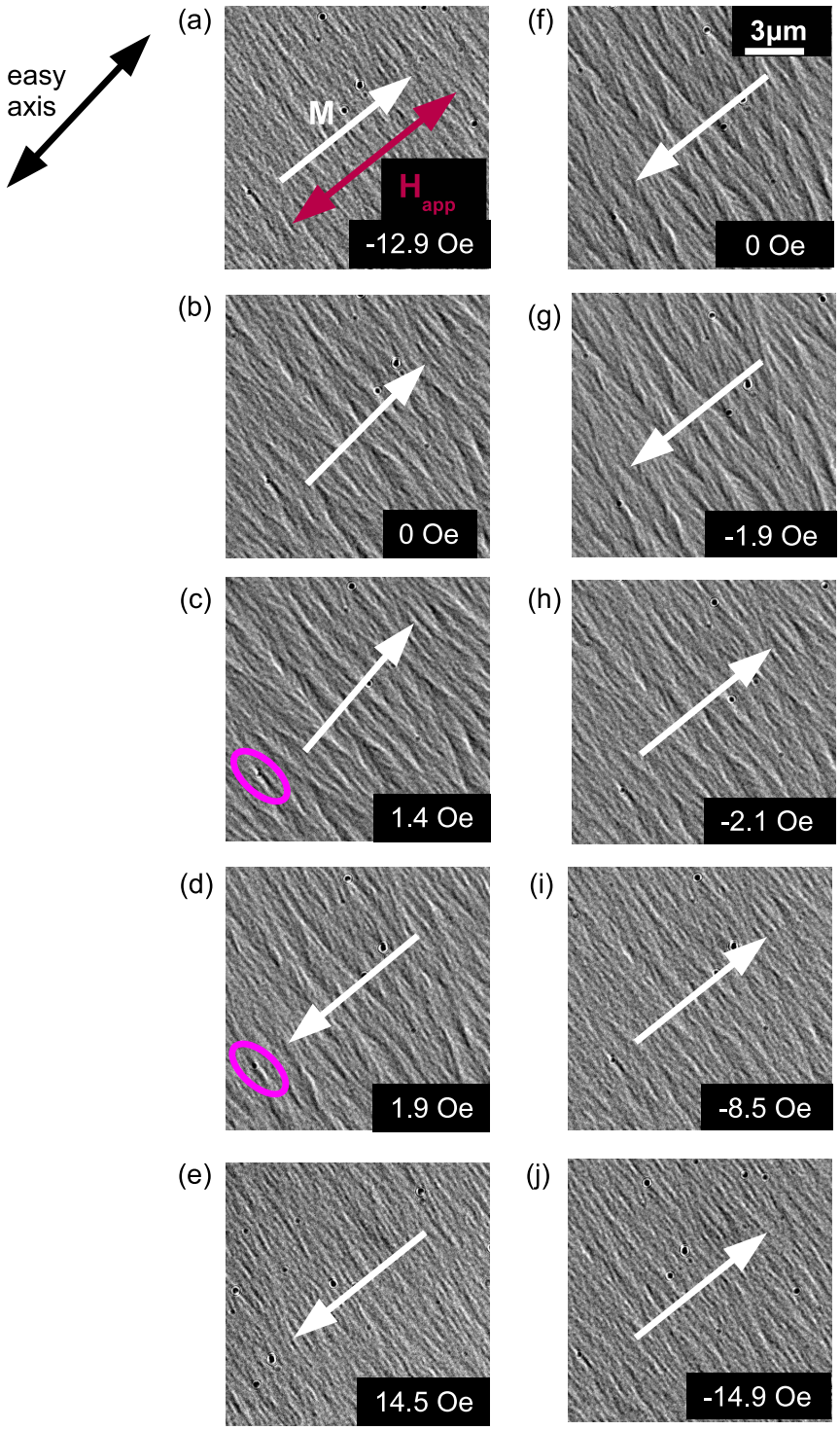

Figure 3.8: Fresnel image sequence of 20nmNiFe/5nmAu easy axis reversal with red arrow indicating the direction of applied field and the white arrows the magnetisation direction. The contrast is observed to switch between (c) and (d), see for example the encircled ripple.

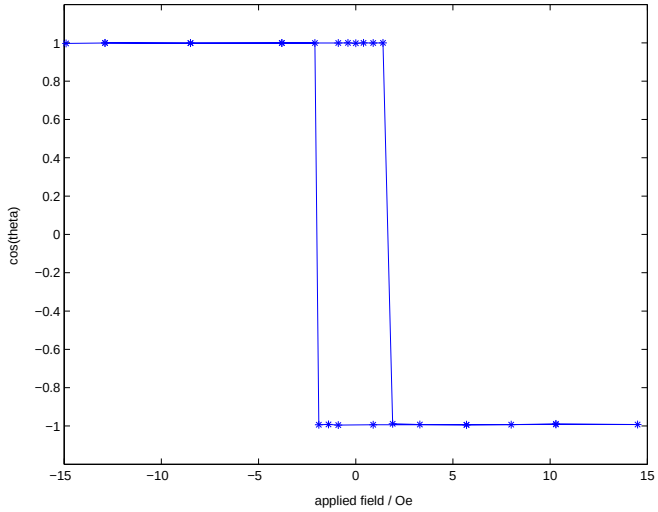

Figure 3.9: Hysteresis loop calculated from images of 20nmNiFe/5nmAu easy axis reversal.

tively. H_+ and H_- are determined by observation of the magnetic contrast in the images to see at which point it reverses, as indicated in figure 3.8 (c) and (d). All the samples were analysed by the same method and a table showing the outward and return switching fields and calculated coercivities for the four bilayer samples are shown in table 3.2. The values of coercivity were consistant, varying between 1.5 and 2.5 Oe. The Au trilayer sample showed self-consistant reversal behaviour, but with a lower value of coercivity of 0.6 Oe.

Variation in magnetisation ripple is evident throughout the reversal sequence. These changes are due to competition between the anisotropy in the sample and the applied field. The ripple magnitude has been calculated from the image sequence in 3.8, using the method detailed in [9], where it has been shown that the ripple magnitude is equal to the root mean square dispersion angle of the ripple, δ, divided by the average ripple wavelength, Λ.

The calculated magnetisation ripple is plotted against applied field and is shown in figure 3.10. During an easy axis reversal, the applied field, H, and anisotropy, H_k, act along the same axis. At high field values, both H and H_k act together to reduce dispersion resulting in a small ripple magnitude. As the field is applied in the opposite direction, there is an increase in Lorentz deflection due to the opposing directions of H and H_k, so the ripple magnitude increases. When the film reverses, there is a sharp decrease in ripple magnitude, as now the anisotropy and applied field are acting in the same direction. The ripple magnitude continues to decrease until the film is saturated in that direction.

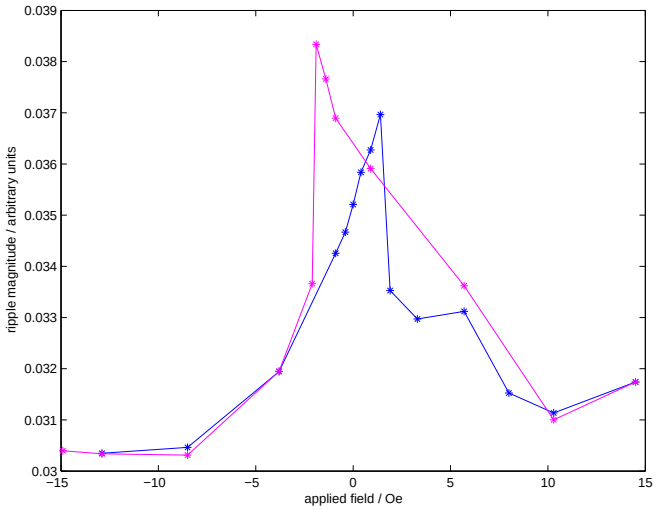

Figure 3.10: Variation in ripple magnitude during easy axis reversal of 5nm Au/20nm NiFe.

3.2.2.2 Hard axis behaviour

Bilayer 3 sample was then rotated through 90° so that the hard axis was aligned with the direction of the applied field. The hard axis reversal of the 20nm-NiFe/5nmAu sample is shown in figure 3.11. Both the outward, figure 3.11(a-e), and return paths, figure 3.11(f-j) were consistent with the magnetisation reversal occurring by coherent rotation. The hysteresis loop deduced from this sequence is shown in figure 3.12, and shows typical hard axis behaviour.

The applied field value required to rotate the magnetisation from the hard axis to the easy axis is known as the anisotropy field, and has a value of ∼5 Oe for this sample. Anisotropy values for the other samples range from 4-5 Oe in the bilayer samples and 2.5 Oe in the Au trilayer sample and are included in table 3.2. All the samples displayed hard axis reversal behaviour that was consistant with the example shown.

The magnetisation ripple variation, shown in figure 3.13, displays typical hard axis behaviour and can be explained by considering the competing effects of anisotropy and applied field.

The hard axis of the film is at 90° to the easy axis, and as such anisotropy in the film, H_k, in the hard axis direction is large. If a very strong field, H, is applied, then the ripple magnitude will be small, since the applied field dominates over anistropy. As the applied field along the hard axis is reduced, H and H_k become comparable and this competition will result in strong ripple contrast. As the field is further reduced, the magnetisation rotates towards the easy axis and H_k

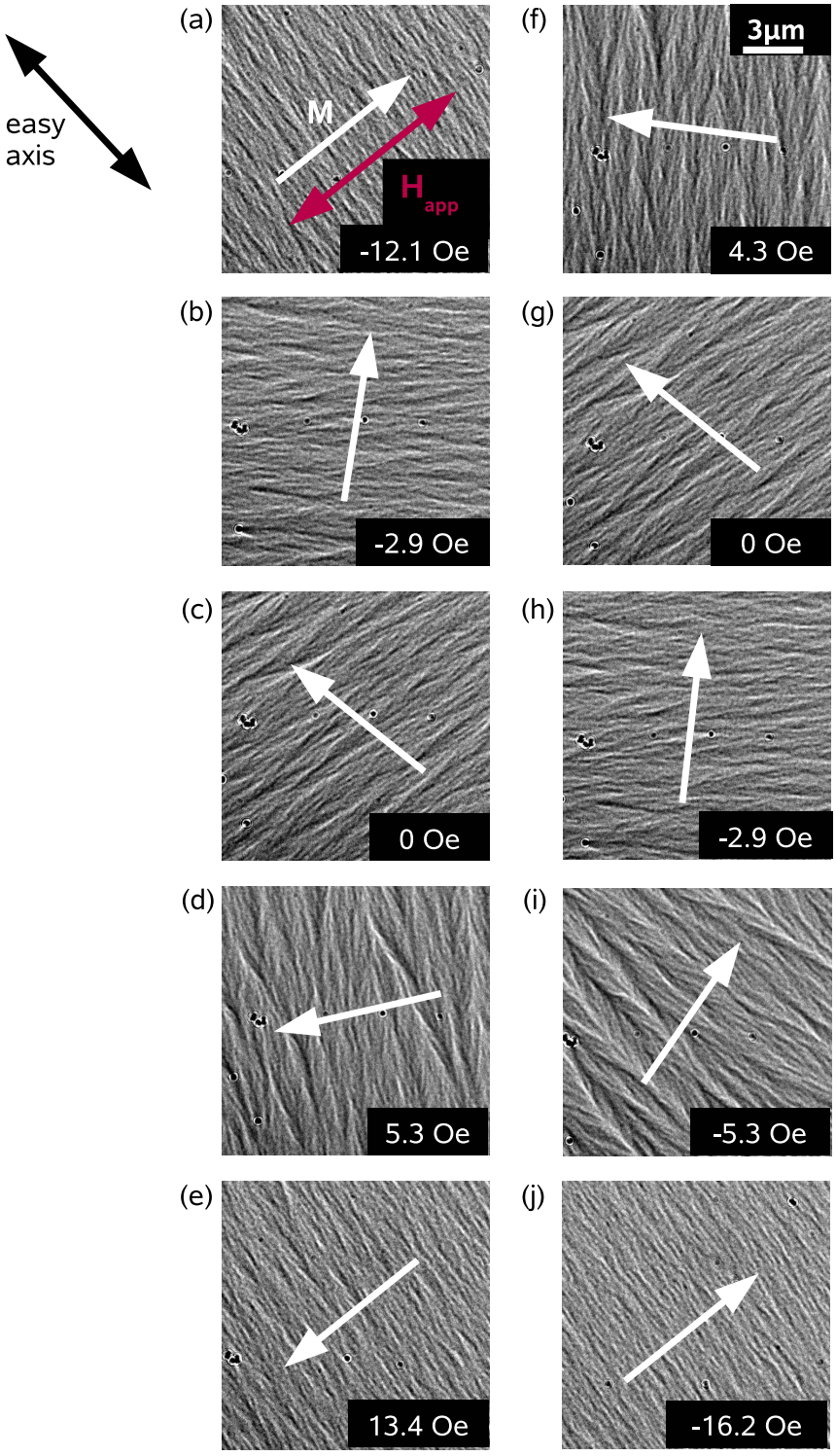

Figure 3.11: 20nmNiFe/5nmAu hard axis reversal with the red arrow indicating the axis of applied field and the white arrows indicating the magnetisation direction.

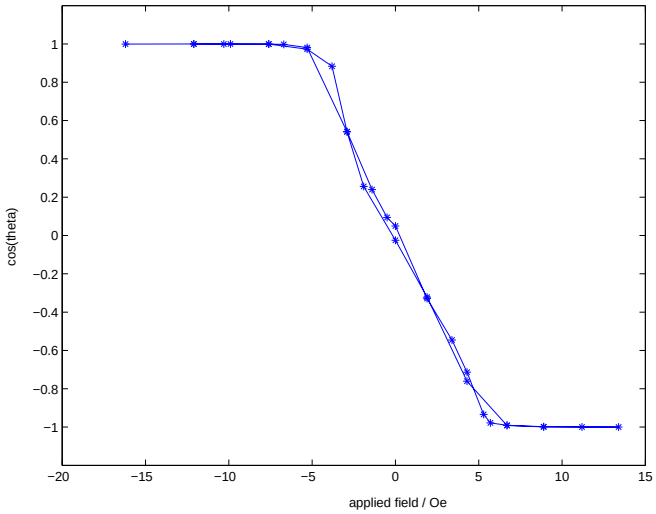

Figure 3.12: Hysteresis loop calculated from images of 20nmNiFe/5nmAu hard axis reversal.

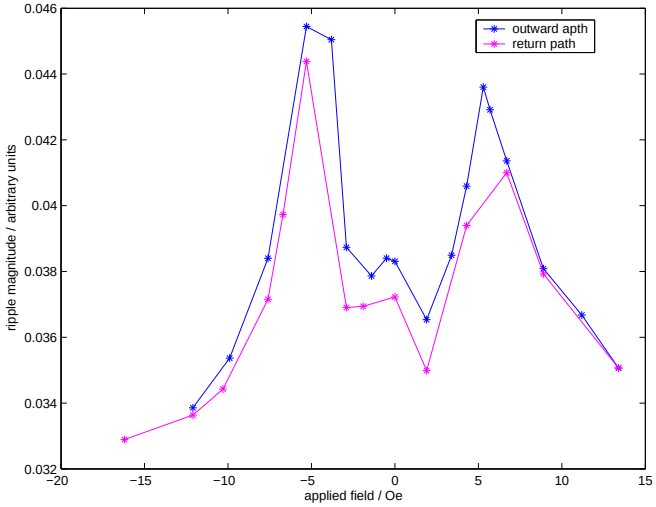

Figure 3.13: Variation in ripple magnitude during hard axis reversal of 5nm Au/20nm NiFe.

begins to dominate. Thus, ripple contrast appears reduced and we obtain the characteristic plot shown in figure 3.13.

Table 3.2 details the individual switching fields, coercivities and anisotropy fields found for each of the samples. The error in the outward and return switching fields results from the reading uncertainty in the measured tile angle of ±0.5° which corresponds to ±0.2Oe. The anisotropy field was measured from the hard axis reversal plot, hence the error here is slightly greater. The reversal behaviour for each of the samples was consistent and little variation in values of coercivity and anisotropy field was observed.

Specimen	Outward switching field / Oe	Return switching field / Oe	Coercivity / Oe	Anisotropy field / Oe
10nm $Ni_{80}Fe_{20}$/5nm Al	2.2± 0.2	-1.75± 0.2	1.95± 0.3	5± 2
10nm $Ni_{80}Fe_{20}$/5nm Au	1.65± 0.2	-2± 0.2	1.8± 0.3	4± 1.5
20nm $Ni_{80}Fe_{20}$/5nm Al	2.3± 0.2	-2.7± 0.2	2.5± 0.3	4± 1.5
20nm $Ni_{80}Fe_{20}$/5nm Au	1.65± 0.2	-1.35± 0.2	1.5± 0.3	4± 1.5
5nm Au / 10nm $Ni_{80}Fe_{20}$/5nm Au	0.4± 0.2	-0.8±0.2	0.6±0.2	2.5±1.5

Table 3.2: Experimental switching fields, coercivity and anisotropy field for each of the multilayer systems studied.

These values were found to be reproducible for both the easy and hard axes.

3.3 Irradiation method

In order to investigate the effects of ion irradiation, a dose test pattern, based on that used in previous irradiation work [8], was devised. A schematic of the pattern is shown in figure 3.14. The horizontal and vertical lines were patterned with a dose of 3×10^{16} ions cm^{-2} in order to outline the pattern so that it was easily visible in TEM and also to magnetically isolate the adjacent regions from each other and from the surrounding continuous film. This dose was chosen as a result of irradiation effects observed in both [1, 8]. The width and dose of these lines was altered to suit the material combination being studied, but was typically between 100 and 500nm wide and of the order of 1×10^{16} ions cm^{-2}. A range of doses covering several orders of magnitude were investigated. The 1nA ion beam was used for all patterning described in this chapter.

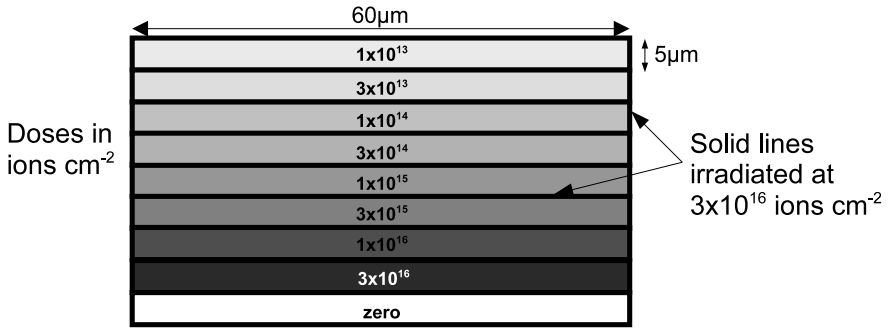

Figure 3.14: Schematic of dose test pattern used to investigate effects of Ga^+ ion irradiation.

3.4 Irradiation induced alteration on the properties of the multilayer systems

Each of the five multilayer samples were irradiated with a dose test pattern as described in the previous section. Again, bright field and Fresnel imaging was used to investigate the structural and magnetic properties of the samples and how they varied with irradiation dose.

3.4.1 Effect of ion irradiation on the physical microstructure

3.4.1.1 Grain analysis

A bright field image was taken of each of the dose regions in each sample and the grain size analysed again using the Digital Micrograph program. In each bilayer sample studied there is little deviation in the grain size from the unirradiated value of 5nm until a dose of 1x10^{15} ions cm^{-2} is reached. Beyond this value considerable grain growth occurs. However, there is a difference in the grains formed in the Al and Au samples, so they shall be discussed separately.

Figure 3.15 shows images of the grain structure in the 20nm NiFe/5nmAl sample. No significant changes are seen below a dose of 3×10^{14} ions cm^{-2}, figure 3.15(a,b). At 1×10^{15} ions cm^{-2}, figure 3.15(c) the onset of grain growth is observed, with some grains increasing in size from 5nm to ∼20nm. On further increasing the dose to 1×10^{16} ions cm^{-2}, rapid grain growth is seen, figure 3.15(d), which continues up to a dose of 3×10^{16} ions cm^{-2}, where the average grain size is ∼30-40nm. In this sample the grain shape is maintained over the range of irradiation doses.

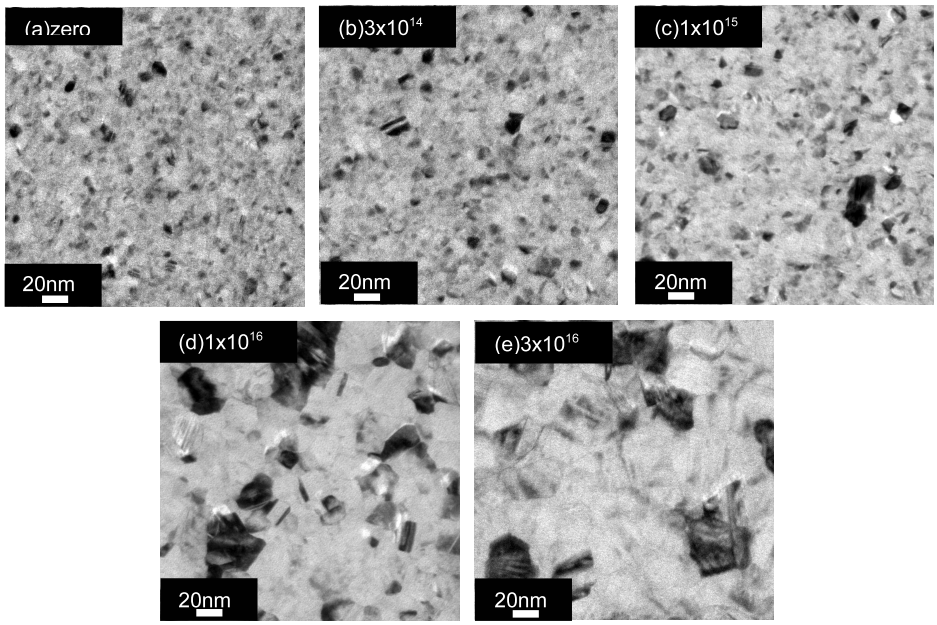

Figure 3.15: Bright field images of grain structure with increasing dose in 5nm Al/20nm NiFe.

In figure 3.16, bright field images of the grains in dosed regions of the 20nm Au/5nm Au sample are presented. Again, no considerable change in grain size or shape occured in regions irradiated with doses of up to 3×10^{14}, figure 3.16(a-b). At 10^{15} ions cm^{-2}, figure 3.16(c),some of the grains have increased in size to 10-20nm. Also visible in the image are narrow dark regions, which appear at first to be due to a change in grain morphology. However, this is not the case and they are most likely arise from changes in diffraction contrast within individual grains. These changes are probably due to stacking faulting or twinning in the Au [10] which have occurred as a result of the irradiation. The grains continue to grow with increasing dose, figure 3.16(d), until at a dose of 3×10^{16} ions cm^{-2} some very large grains averaging $> \sim 60$nm are seen, figure 3.16(e). Note the change in scale bar on images 3.16(d-e).

Figure 3.17 shows bright field images of the grain structure over a range of irradiation doses for the 5nm Au/10nm NiFe/5nm Au sample. Again, no significant changes were seen up to a dose of 3×10^{14} ions cm^{-2}, figure 3.17(a). A change in grain size and shape was observed at 1×10^{15} ions cm^{-2}, 3.17(b) which was consistant with the changes seen in the Au bilayer samples. The twins are again visible, with lengths varying between 5 and 20nm. However the effect is more pronounced in this sample due to the presence of the two Au layers. Increasing the dose to 3×10^{15} ions cm^{-2}, figure 3.17(c), further increases in grain size and change of grain shape was observed. The grains appear more elongated but are

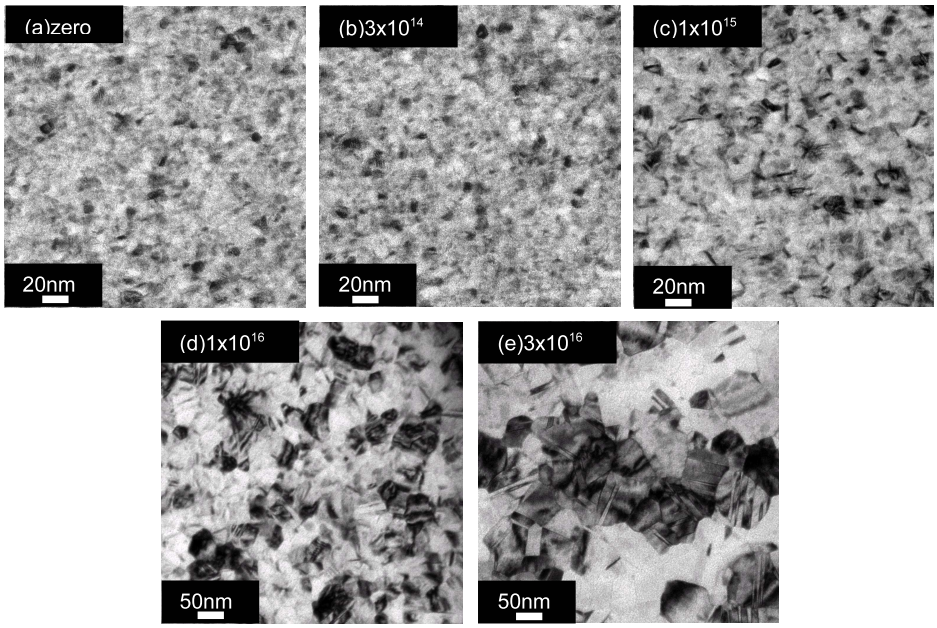

Figure 3.16: Bright field images of grain structure with increasing dose in 5nm Au/20nm NiFe, note the change in magnification in images (d) and (e)

very irregular and hard to quantify with no common axis to measure. At 1×10^{16} ions cm^{-2} substantial milling of the sample is observed, figure 3.17(d,e), with only small islands of permalloy remaining. Similar milling effects were observed in both the 5nm Al/10nm NiFe and 5nm Au/10nm NiFe samples.

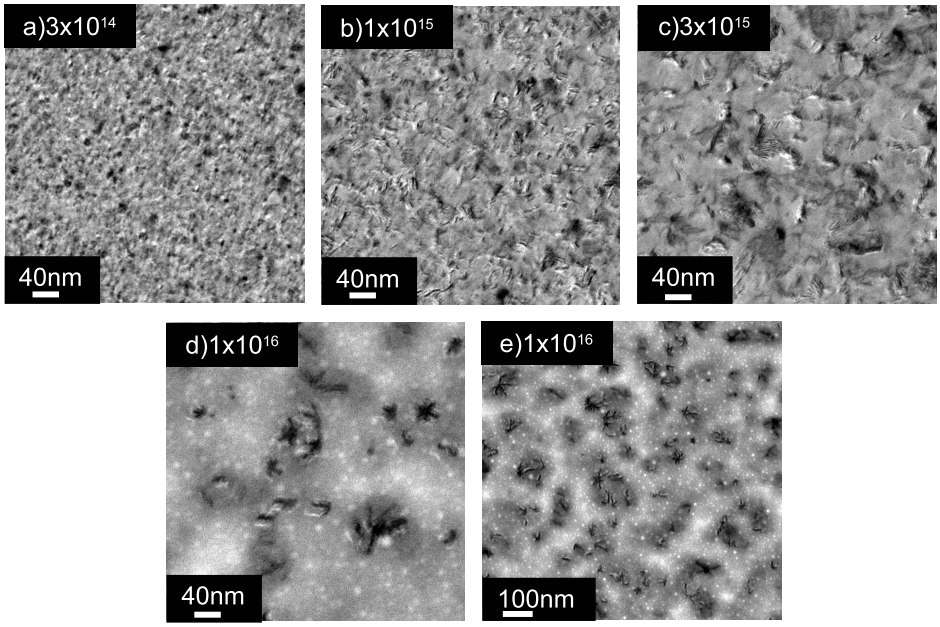

Figure 3.17: Bright field images of grain structure with increasing dose in 5nm Au/10nm NiFe/5nm Au

A summary of these results is presented in the graph of average grain size against

dose in figure 3.18. The error bars displayed on the graph give an indication of the range of grain sizes present within a particular dose region. Only data concerning the bilayer samples is included on the graph, as previously mentioned it was not possible to make accurate measurements of grain size in the Au trilayer samples due to the random variation in grain structure. It should also be noted that at 3×10^{16} ions cm^{-2} there are only grain size values for the two samples with 20nm thick permalloy layers. At this dose the samples with 10nm thick permalloy had been milled too much for the actual grain structure to be measured. Irradiation induced milling of the samples is discussed in the following section.

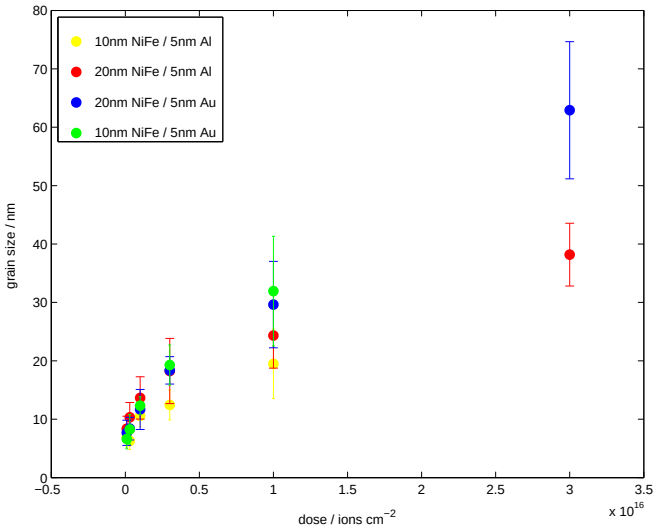

Figure 3.18: Mean increase in grain size as a result of 30kV Ga^+ ion irradiation for each of the bilayer samples

3.4.1.2 Irradiation induced milling

The milling depth as a function of dose was measured for each sample using AFM and is shown in table 3.3. For doses of 3×10^{14} ions cm^{-2} and less no change was measured in any of the samples, so only values for 1×10^{15} ions cm^{-2} and above are shown.

As expected milling depth increasing with dose. By a dose of 1×10^{16} ions cm^{-2} all of the bilayer samples had experienced milling of between 2 and 3.7nm, meaning that only the top non-magnetic layer had been milled. At the heaviest dose of 3×10^{16} ions cm^{-2} the samples with 20nm NiFe had experienced 6nm of material milled from the surface, whilst the samples 10nm thick NiFe layers had been milled to a depth of 10nm. These measurements indicate that in the 10nm NiFe

Specimen ↓ / Dose / ions cm^{-2}	1×10^{15}	3×10^{15}	1×10^{16}	3×10^{16}
10nm NiFe/5nm Al	1	1	2	10
20nm NiFe/5nm Al	1.4	1.7	3	6
10nm NiFe/5nm Au	1.6	2	2	10
20nm NiFe/5nm Au	1	1.6	2.5	6
5nm Au/10nm NiFe/5nm Au	1	2.5	3.7	20

Table 3.3: Milling depth in nm with increasing dose for each magnetic thin film system studied.

samples, the entire cap layer and half the thickness of the NiFe is milled away. For the 20nm samples, again the cap layer has been milled, but only 1nm of the magnetic layer has been affected, leaving an uncompromised layer of permalloy.

3.4.2 Effect of ion irradiation on magnetic properties

Initially, the dose test pattern shown in figure 3.14 with a single line border of 3×10^{16} ions cm^{-2}, and a dose range of 1×10^{13} to 3×10^{16} ions cm^{-2} was used to irradiate the bilayer samples. However, initial TEM observations on the 20nm NiFe / 5nm Au sample showed that different dose regions of the bilayer samples were still magnetically connected to each other and to the surrounding film. This is demonstrated in the Fresnel image shown in figure 3.19(a), where it is clear to see the magnetisation ripple extend from one region to another across the heavily irradiated boundary.

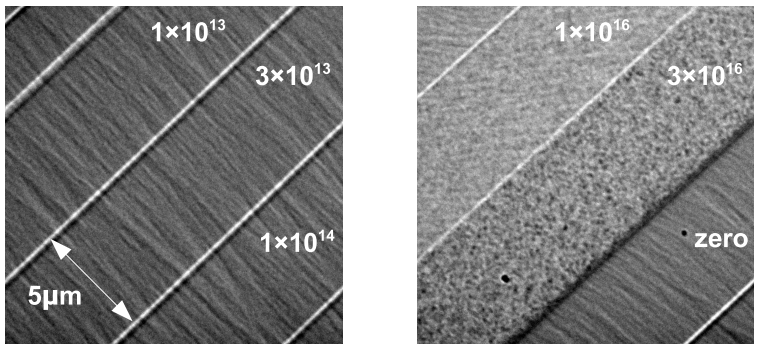

Figure 3.19: Fresnel images showing dosed regions 5nm Au/20nm NiFe sample irradiated separated by a single line of 3×10^{16} ions cm^{-2}. (a) Magnetisation ripple is continuous over the delineation lines, whereas (b) the extended region irradiated with 3×10^{16} ions cm^{-2} has been rendered non-magnetic.

However it was also observed that in the extended 3×10^{16} ions cm^{-2} dose region,

figure 3.19(b), that no magnetisation ripple was present, and magnetic contrast at the edges of the region did not change on tilting the sample. This is indicative that the material had been rendered non-magnetic at this dose. The difference in resultant effects between large and small areas irradiated with the same dose and patterning conditions, most likely arises from the overlap of the tails of the ion beam. A 1nA beam was used to pattern the dose test regions which has a Gaussian profile with a FWHM of 35nm. In a single line, the tails will only overlap in one direction, i.e. the x-direction, as shown in figure 3.20(a). When a larger area is being patterned, the beam moves in a raster fashion and results in overlapping of the beam tails in both the x and y-directions, fig 3.20(b). This can cause the larger dose region to experience a slightly higher dose than the single line. It is also reasonable to assume that even if the narrow line was non-magnetic, magnetisation in the regions either side could remain coupled across it.

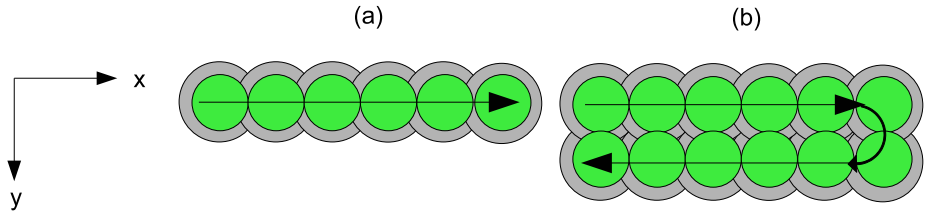

Figure 3.20: Schematic showing the overlap of the tails of the ion beam as it patterns (a) a single line and (b) an extended area. Green area shows the individual pixels to be irradiated whilst the grey area indicates the area irradiated by the tails of the ion beam.

With this in mind, the dose test pattern was modified to include larger delineation regions of 500nm. This ensured that each dose region was magnetically isolated from both the surrounding film and adjacent dose regions.

3.4.2.1 Reversal of regions irradiated at 1×10^{13} - 1×10^{14} ions cm^{-2}

Figure 3.21 shows the Fresnel image sequence of the magnetisation reversal of the 20nm NiFe/5nm Au sample, irradiated with 1×10^{13}, 3×10^{13} and 1×10^{14} ions cm^{-2}. It should be noted at this point that the thick white band seen in the top right hand corner of each of the images is due to a tear in the substrate and is not to be confused with the 'black-white' contrast referred to throughout this description.

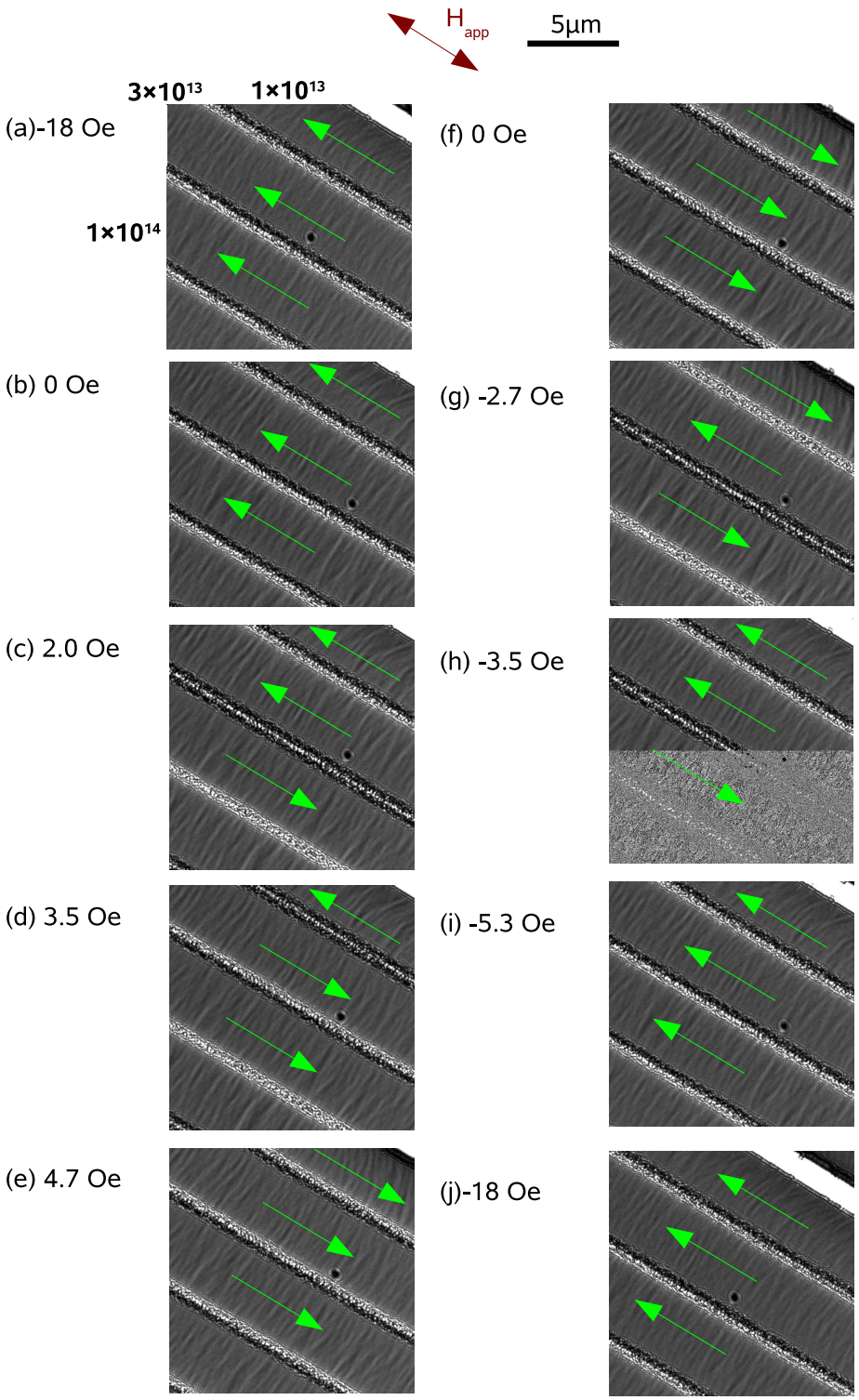

Figure 3.21: Magnetisation reversal behaviour of 20nm NiFe/5nm Au sample for regions receiving doses of 1×10^{13}, 3×10^{13} and 1×10^{14}ions cm^{-2}. Green arrows indicate the direction of magnetisation in the irradiated regions, determined from the contrast of the intermediate lines as discussed in the text.

At the boundaries of the dose regions, strong black-white contrast can be seen. This strong contrast is a consequence of the deflection experienced by the electrons which pass through the near-uniformly magnetised dose regions, due to the Lorentz force. Those electrons which are incident on the nonmagnetic delineation line pass through undeflected. This effect is depicted in the schematic diagram in figure 3.22. If adjacent domains are magnetised in the same direction, then the electrons passing through the domains will be deflected in the same direction resulting in regions of increased and decreased intensity at the edges of the delineation lines. From this diagram it is clear to see that if the direction of magnetisation in the dosed regions is reversed, then the contrast at the edges of the delineation region will also be reversed.

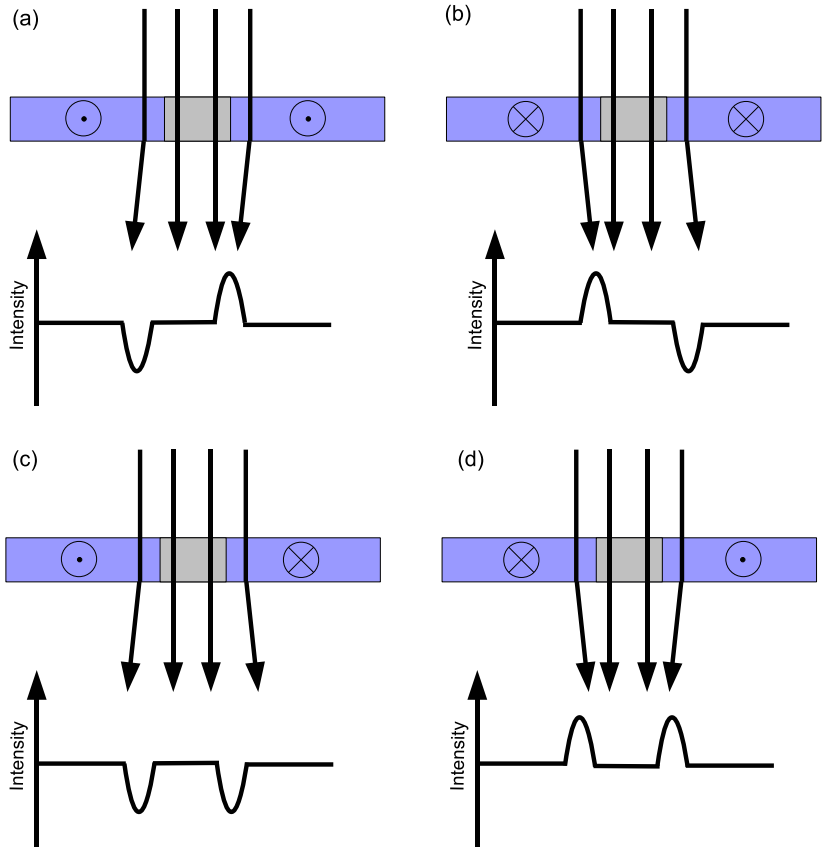

Figure 3.22: Schematic showing the magnetic contrast in Lorentz microscopy due to differing orientations of adjacent magnetic regions (blue) on either side of a non-magnetic delineation region (grey).

This contrast provides useful information about the magnetisation direction in each dose region, especially when looking at regions irradiated with higher doses where the magnetisation ripple magnitude has decreased. An additional point to note is the strong white line in the centre of the delineation region, clearly seen

in figure 3.21(c). This is a result of increased transmitted electron intensity due to milling which has ocurred in that region. It does not provide any information on the magnetic state of the sample.

At zero field, figure 3.21(b), the net moment is lying parallel to the long axis of the structure. This is determined from the orientation of the magnetisation ripple which is known to be perpendicular to the mean magnetisation direction. Additionally, looking from the top of the image downwards, the edge contrast is black-white, i.e. black above and white beneath.

As the field is increased, an increase in the magnetisation ripple magnitude is seen in all three regions. At a value of 2.0 Oe, fig 3.21(c), the 1×10^{14} ions cm^{-2} region has reversed, which is indicated by the change in contrast at the edges from black-white to white-black. On further increasing the field to 3.5 Oe, 3.21(d), a domain wall was visible in the 3×10^{13} ions cm^{-2} region which swept through and affected the reversal. The 1×10^{13} ions cm^{-2} region did not switch until a field of 4.7 Oe was applied, figure 3.21(e). The applied field is then increased to +15 Oe in order to ensure that the entire sample is saturated. During the reverse cycle, the field is initially relaxed to zero, fig 3.21(f), where an increase in the ripple magnitude is observed. This observation is made by eye, as the change is easy to see when observing the reversal in real time during the experiment. Again, the 1×10^{14} ions cm^{-2} region reversed first, at a field of -2.7 Oe, figure 3.21(g). Further decreasing the field saw the 1×10^{13} ions cm^{-2} region reverse at -3.5 Oe, 3.21(h), whilst a field of -5.3 Oe (i) was required to reverse the magnetisation in the 3×10^{13} ions cm^{-2} region. The field was taken back to -18 Oe, figure 3.21(j) to complete the reversal sequence.

The switching fields for these dose regions varied somewhat for the outward and return cycles. Equation 3.1 was used to calculate values of coercivity for each of these regions which are shown in table 3.4.

3.4.2.2 Reversal of regions irradiated at 3×10^{14} - 3×10^{15} ions cm^{-2}

In the intermediate range, for doses from 3×10^{14} to 3×10^{15} ions cm^{-2}, the effect of irradiation on the magnetisation of the 20nm NiFe/5nm Au sample began to become apparent. Between doses of 3×10^{14} and 3×10^{15} ions cm^{-2}, a significant decrease in magnetisation ripple magnitude is observed. This is most clearly seen in the zero field images 3.23(b) and (g), where ripple contrast is greatest. This

reduction in magnetic ripple contrast indicates that there is a reduction in the net magnetic moment in these regions when compared to the regions with lower or zero dose.

In fig. 3.23(a), the magnetisation is aligned with the applied field along the long axis of the pattern. As with the low dose sequence, the progress of the reversal can be followed by observing the black white contrast at the edges of the dose regions. Initially all regions have black-white contrast when looking from the top of the image to the bottom. The applied field is increased from -18 Oe through remanence to +2 Oe, figure 3.23(a-c), where at a field value of +2.0 Oe, both the 3×10^{14} and 3×10^{15} ions cm^{-2} regions reverse. The 1×10^{15} ions cm^{-2} region required a field of 4.0 Oe, figure 3.22(e) to be applied before the magnetisation direction switched. The return cycle, figures 3.23(f-j), was consistent with the outward cycle for the 3×10^{15} ions cm^{-2} region which switched again at -2 Oe. The 1×10^{15} ions cm^{-2} region also switched at -2 Oe, while the 3×10^{14} ions cm^{-2} region reversed at -2.7 Oe. The coercivities of these regions have been calculated from the images and are shown in table 3.4 at the end of section 3.4.

3.4.2.3 Reversal for doses $> 1\times10^{16}$ ions cm^{-2}

The magnetisation reversal of the high dose region of the 20nm NiFe/ 5nm Au sample, 1×10^{16} and 3×10^{16} ions cm^{-2}, is shown in figure 3.24. In the 1×10^{16} ions cm^{-2} region, no magnetisation ripple is visible at any point during the reversal cycle. However, by observing the reversal of the contrast at the edges of the region, it can be seen that it remains magnetic. The outward, figure 3.24(a-e), and return paths, figure 3.24(f-i), are consistent with the magnetisation switching at $\pm$7.3 Oe. This is a large increase in coercivity compared to the zero dose regions which switched at $\pm$2.5 Oe.

The 3×10^{16} ions cm^{-2} region appears much brighter than the surrounding areas and has some grain structure visible in the interior of the region. The increased intensity is a result of the decreased thickness of the sample due to milling, whereas the contrast in the interior is due to increased grain size and surface roughness. By close examination of the edge contrast, it can be seen that the contrast remains constant and does not reverse, indicating that the region is now non-magnetic. This was checked by sweeping the magnetic field up to very high fields to ensure that the unchanging contrast was not just due to a further increase in coercivity. Values of coercivity from the all four bilayer samples are

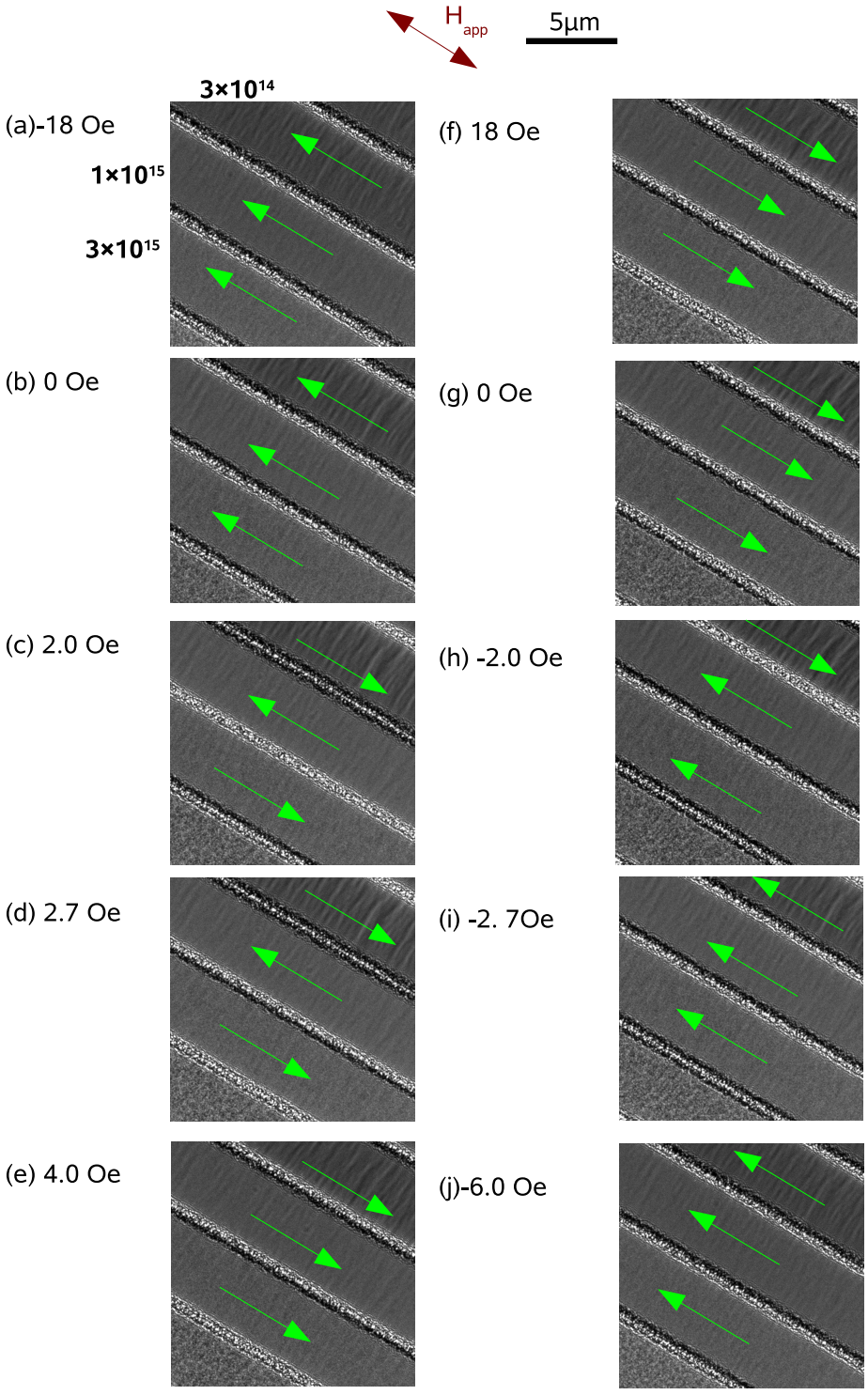

Figure 3.23: Magnetisation reversal behaviour of 20nm NiFe/5nm Au sample for regions receiving doses of 3×10^{14}, 1×10^{15} and 3×10^{15}ions cm^{-2}. Green arrows indicate the direction of magnetisation in the irradiated regions, determined from the contrast of the intermediate lines as discussed in the text.

summarised in table 3.4, which appears at the end of this section.

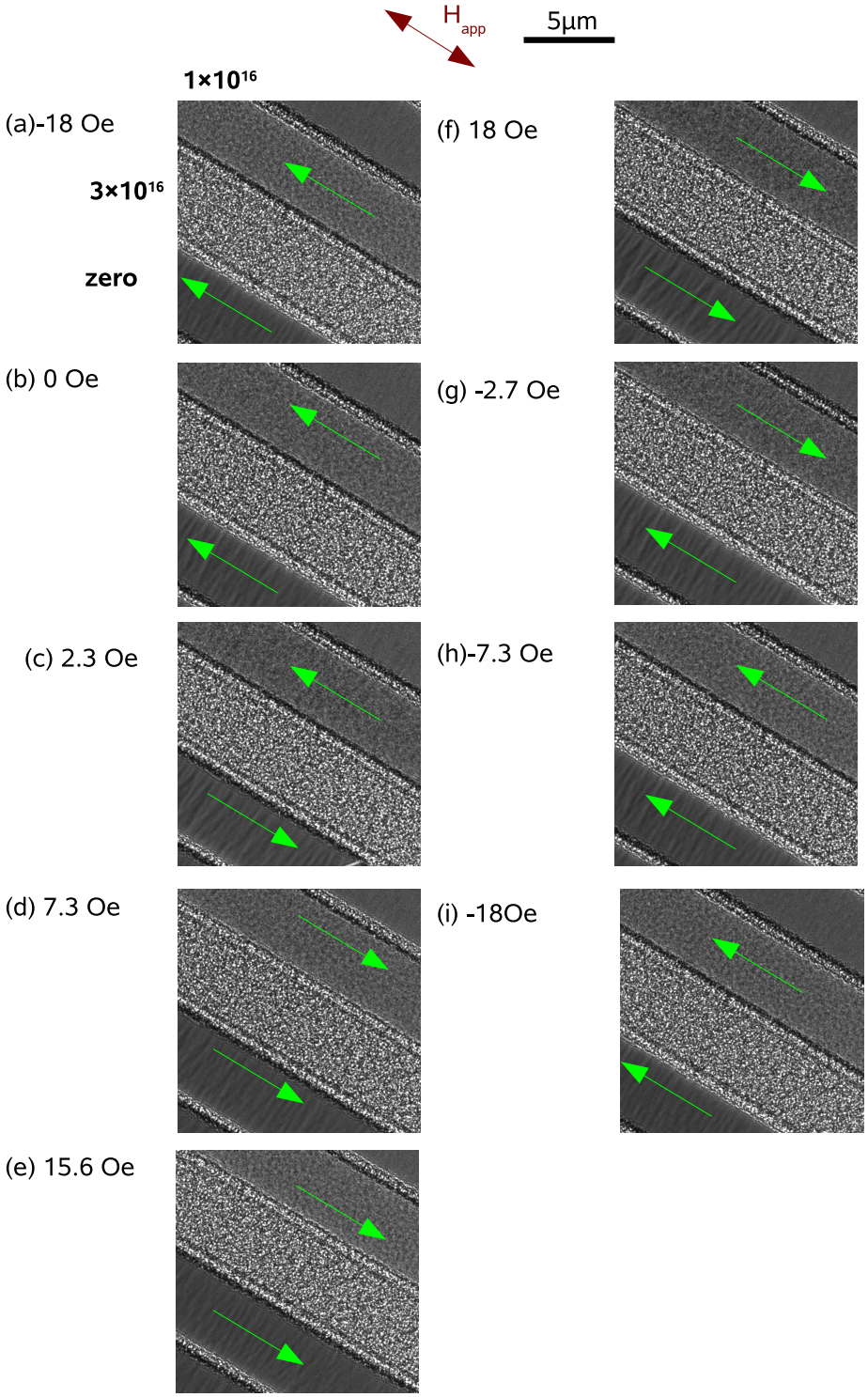

Figure 3.24: Magnetisation reversal behaviour of 20nm NiFe/5nm Au sample for regions receiving doses of 1×10^{16} and 3×10^{16} ions cm^{-2}. Green arrows indicate the direction of magnetisation in the irradiated regions, determined from the contrast of the intermediate lines as discussed in the text.

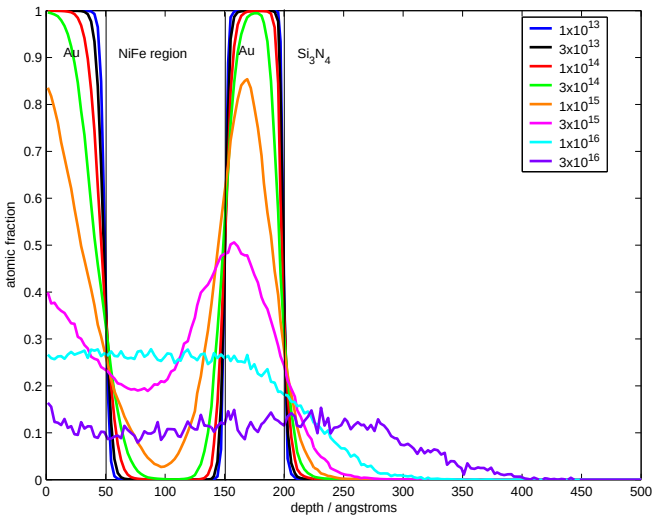

Figure 3.25: Tridyn simulation of Au concentration profiles with varying dose. All doses stated are measured in ions cm^{-2}

3.4.2.4 Effect of irradiation on the magnetic properties of trilayer system

In order to determine a suitable dose range to investigate for the trilayer system, simulations were carried out using the Tridyn program outlined in chapter 2.6.2. One of the main advantages of the TRIDYN code is that the concentration profiles of each element across the multilayer are recalculated after each ion impact, producing a dynamic simulation of the effect of ion irradiation induced mixing. Simulations can be carried out for a particular dose and proved to be particularly useful in helping to assess how effective the extra non-magnetic layer would be over a range of doses. Initially, the atom concentration profiles are in the form of a 'top-hat' function. As the irradiation dose is increased, these profiles gradually broaden and there is overlap of atoms across the interfaces, with the transfer of material in both 'forward' and 'backward' directions.

Figure 3.25 shows the profile of Au throughout the multilayer for doses between 1×10^{13} and 3×10^{16} ions cm^{-2}. This plot shows that for the Au trilayer sample, a dose of 1×10^{16} ions cm^{-2} yielded a consistant concentration of between 25-30% throughout the extent of the NiFe region. A dose of 3×10^{15} ions cm^{-2} also showed a significant concentration of Au atoms, at least 20%, throughout the NiFe layer thickness. However this profile was not as consistent as the one calculated for the 1×10^{16} ions cm^{-2} dose, with ~20% in the top half of the NiFe region, rising to ~50% near to the second gold layer. Previous work has shown that lesser concentrations than this, ~12% Ta [11], and 20% Cr [12] have been successful in

rendering NiFe paramagnetic , so it is likely that a 20% concentration of Au in the NiFe layer will significantly modify its magnetic properties.

In the experiments presented in chapter 3.4, it was found that 3×10^{15} ions cm^{-2} was not able to render the bilayer non-ferromagnetic. However it appears that at this dose the trilayer sample will have sufficient Au to undergo significant changes. A tridyn simulation, shown in figure 3.26, was carried out to observe a direct comparison between the Au concentration in the bilayer and trilayer samples at a dose of 3×10^{15} ions cm^{-2}.

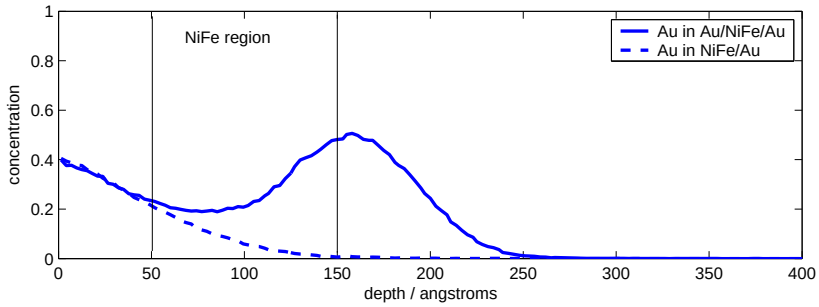

Figure 3.26: Tridyn simulation showing the concentration of Au atoms throughout the Au bilayer and Au trilayer samples.

In the NiFe region of 50-150$\mathring{A}$ no Au was originally present in either sample. The difference in concentration throughout the layers is clear and it would appear that a significant amount of mixing comes from the additional Au layer that is present in the trilayer sample, with a concentration of at least ~20% Au across this area. In fact, there is a greater concentration of Au in the second half of the NiFe layer compared to the top half, indicating that mixing from the second gold layer has a significant effect on the properties of the magnetic layer. The graph showing the single metal layer revealed that the concentration of Au throughout the thickness of the NiFe layer is not consistent, starting at a concentration of ~20% and falling away quickly to 5% in the top half of the layer, explaining why a higher dose was needed to render the layer non-magnetic.

Based on the results of these Tridyn simulations, the dose test pattern was modified to account for changes occuring in the system at lower doses. The dividing lines used here were patterned with a single line of 1×10^{16} ions cm $^{-2}$, and the larger regions were patterned with a range of 1×10^{13} to 1×10^{16} ions cm $^{-2}$.

The magnetisation reversal of regions irradiated with doses of 1×10^{13} to 3×10^{14} ions cm^{-2} is shown in figure 3.27. Initially, the pattern is magnetised such that

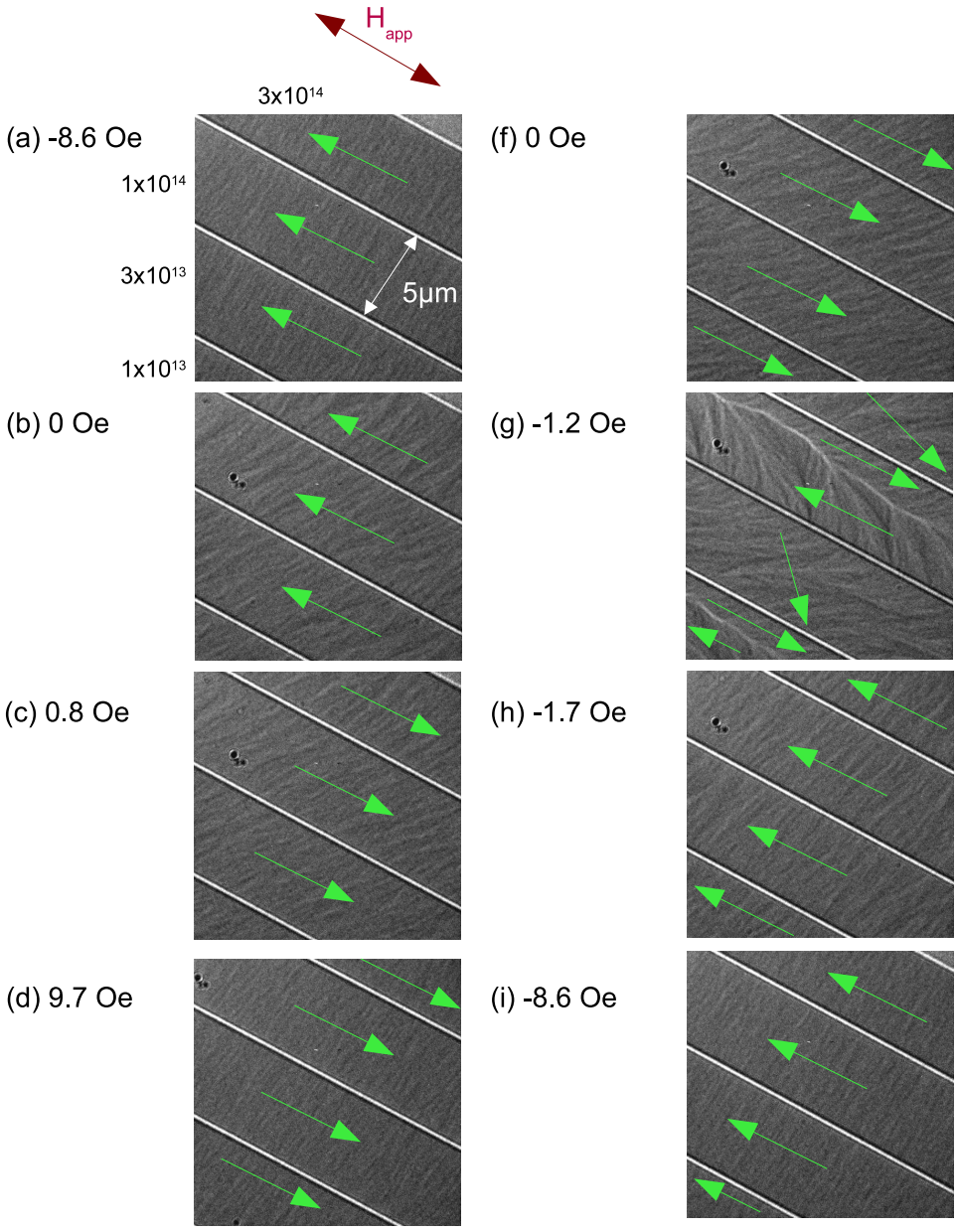

Figure 3.27: Magnetisation reversal behaviour in Au/NiFe/Au multilayer for regions receiving doses of 1×10^{13}, 3×10^{13}, 1×10^{14} and 3×10^{14} ions cm^{-2}.

the magnetisation lies parallel to the delineation lines, and the contrast is black-white when looking from the top of the image to the bottom, figure 3.27(a). On the outward cycle, an increase in magnetisation ripple magnitude is seen as the applied field is increased from -8.5 Oe to 0 Oe, figure 3.27(b). The magnetisation in all three regions switches at a value of 0.8 Oe, indicated in figure 3.27(c). The field was then increased to 9.7 Oe, figure 3.27(d) to saturate the film, where a decrease in magnetisation ripple is seen. On the return cycle, it can be seen that at zero field, the magnetisation ripple has begun to rotate and the magnetisation is no longer lying parallel to the long axis of the pattern, figure 3.27(e). This indicates that the dose test pattern is offset from the easy axis by several degrees. In image 3.27(f), at -1.7 Oe, the magnetisation is reversed in all the regions and again the field is increased to -8.6 Oe, shown in figure 3.27(g) to saturate the magnetisation in this direction. In this dose range irradiation has no measureable effect on the magnetic properties.

In figure 3.27, magnetisation ripple contrast and intensity remain constant with increasing dose. However, in figure 3.28, where the material is irradiated with 1×10^{15}, 3×10^{15} and 1×10^{16} ions cm^{-2}, changes in both magnetic contrast and transmitted intensity are clearly visible. In figure 3.28(a) a field of -8.6 Oe is applied and the magnetisation is aligned along the dose pattern. No magnetisation ripple contrast is visible in any of the irradiated regions, so it is necessary to look to the black-white contrast at the edges to determine when the magnetisation in a particular region switches, or if, in fact, it has remained magnetic at all. As the contrast at the edges of each region in figure 3.28 is faint, a line trace has been taken across the boundary and the resulting intensity graph displayed in figure 3.29.

Figure 3.29, shows image 3.28(b) and (c) respectively and the intensity profiles from the area indicated on each image. A change in intensity at the edges of the 1×10^{15} ions cm^{-2} region between figure 3.29(b) and (d) is visible indicated by the regions marked bright and dark on the profiles. This shows that the magnetisation, although significantly reduced, has switched at 1.7 Oe. On examination of the edges of the 3×10^{15} and 1×10^{16} ions cm^{-2} regions, there is no change in intensity level at this value of applied field. The field was then increased to 11.5 Oe, so as to ensure that there had not simply been an increase in coercivity at these irradiation doses. No change in intensity was witnessed even at 40 Oe. This, coupled with the lack of any magnetic contrast within the region, suggests that they are non-magnetic. On the return cycle, the magnitude of the applied

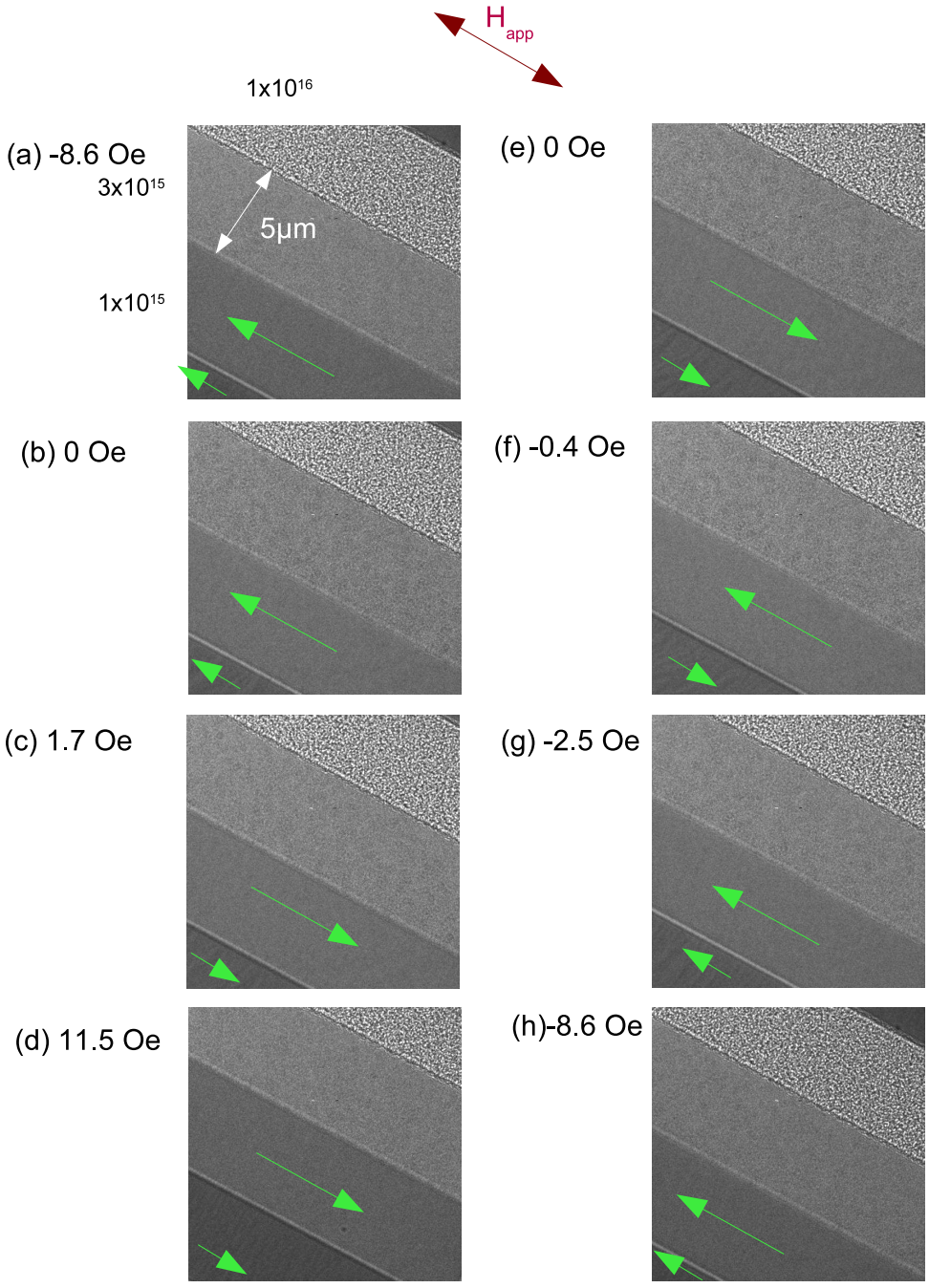

Figure 3.28: Magnetisation reversal behaviour in Au/NiFe/Au multilayer for regions receiving doses of 1×10^{15}, 3×10^{15} and 1×10^{16} ions cm^{-2}.

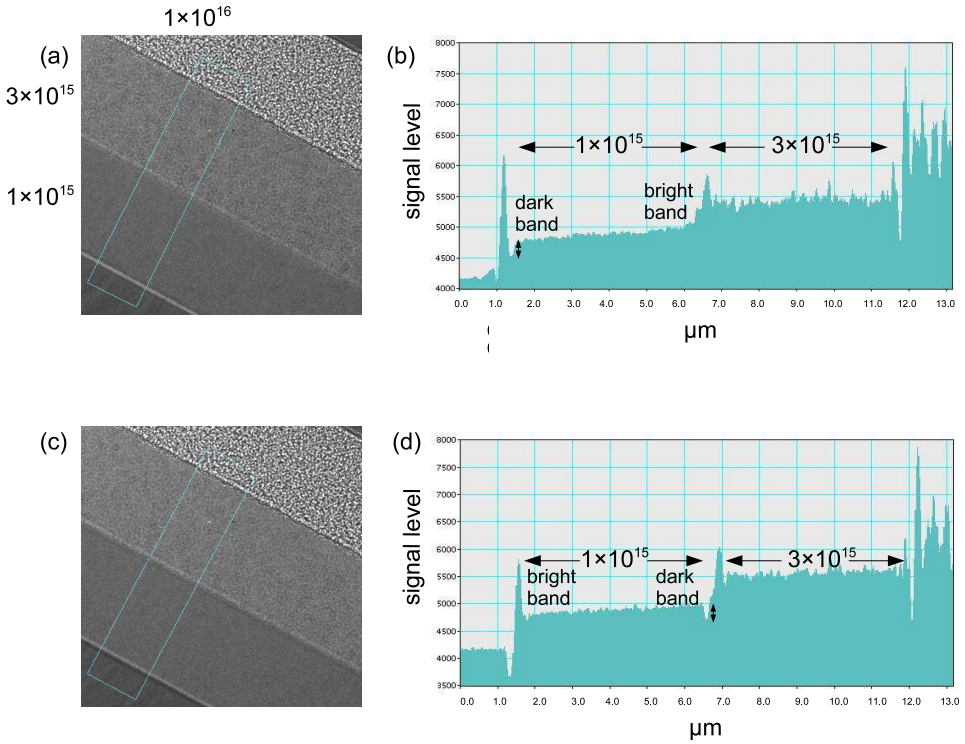

Figure 3.29: Profile of 1×10^{15} and 3×10^{15}ions cm^{-2} irradiated region before and after switching of magnetisation direction.

field is reduced to zero, figure 3.28(e), and the 1×10^{15} ions cm^{-2} region is seen to switch at a field of -0.4 Oe in figure 3.28(f). To saturate the structure in the original direction and complete the reversal, the field was decreased to -8.6 Oe, figure 3.28(g,h).

3.4.2.5 Summary of effects on magnetic behaviour

Table 3.4 shows the coercivity for each dose region in each of the four bilayer samples and the Au/NiFe/Au trilayer sample using data extracted from their reversal sequences. Only the 20nm NiFe/5nm Au and the Au/NiFe/Au sequences have been shown here, as they are illustrative of the properties of the other systems.

A reduction in the magnetic ripple contrast was seen in all samples as the dose was increased to 1×10^{15} ions cm^{-2} and above, indicating that a reduction in mean magnetic moment or intrinsic anisotropy had occured. At doses of 3×10^{15} ions cm^{-2} and below, statistical variation dominates the data in all the samples and no clear dose dependant effect on the coercivity is observed. The only clear increase

Dose/Specimen	10nm NiFe/5nm Al	20nm NiFe/5nm Al	10nm NiFe/5nm Au	20nm NiFe/5nm Au	5nm Au/10nm NiFe/5nm Au
zero	3.6	2.9	2.52	2.15	1.25
1×10^{13}	3.6	3.5	3.6	4.1	1.25
3×10^{13}	3.6	5.35	2.8	3.1	1.25
1×10^{14}	3.6	4.75	3.6	3.65	1.25
3×10^{14}	3.6	4.4	3.15	3.35	1.25
1×10^{15}	4.8	4.75	2	2	1.1
3×10^{15}	5	4.75	4.1	2.35	non-FM
1×10^{16}	non-FM	12.45	non-FM	7.3	non-FM
3×10^{16}	non-FM	non-FM	non-FM	non-FM	non-FM

Table 3.4: Values of coercivity for dosed regions in each of the systems studied. Dose is measured in ions cm^{-2}, whilst coercivity values are measured in Oe.

in coercivity was observed at 1×10^{16} ions cm^{-2} in the 5nm Al/20nm NiFe and 5nm Au/20nm NiFe, where increases to 12.45 Oe and 7.3 Oe respectively, were seen. At this same dose both the 10nm NiFe bilayers had been rendered non-magnetic, whereas it was found that a dose of 3×10^{16} ions cm^{-2} was required to render the bilayers with 20nm NiFe non-magnetic. The Au trilayer sample underwent this change at a lower dose of 3×10^{15} ions cm^{-2}.

3.5 Discussion

The Fresnel mode of Lorentz microscopy has been used to investigate the magnetic properties of NiFe thin film systems with non-magnetic layers, in the as-deposited state and after irradiation with a Ga^+ ion beam, whilst bright field imaging was used to investigate the structural properties.

In the as-deposited state, the four bilayer samples were found to have reasonably constant magnetic and structural properties. The coercivities of the samples varied by only 1 Oe, from 1.5 to 2.5 Oe. The anisotropy field of the samples, found by investigation of the hard axis magnetisation reversal, again were found to be in the range of 4 to 5 Oe. This showed that in spite of the low intrinsic anisotropy of NiFe, and lack of any influence during deposition, that a preferential magnetisation direction was established in each of the samples, the cause of which is likely to be due to the local environment at the time of deposition. Analysis of the grain size using the Digital Micrograph package showed a grain size of $\sim$5nm which

was common to each of the bilayer samples. Diffraction patterns showed a polycrystalline structure with no texturing. The 5nmAu/10nm NiFe/5nmAu trilayer sample showed similar structural properties to the bilayers in the as-deposited state. The magnetisation reversal of the easy and hard axes proceeded in the same manner but the coercivity and anisotropy fields were found to be 0.6 Oe and 2 Oe respectively, which are approximately half of the measured values for the bilayers. Due to differences in the deposition technique and location between the bilayer and trilayer samples, we cannot directly tell whether differences in magnetic properties are due to the change in the layer structure or the deposition conditions, but it is likely that the permalloy in the trilayer is slightly thinner. However, the aim of this chapter was not to compare the properties of the unirradiated films, but to investigate the effect of ion irradiation on each individual system.

Ion irradiation experiments were carried out on all four of the bilayer samples, using a dose range of 10^{13} to 3×10^{16} ions cm^{-2}. The onset of grain growth in the samples occurred at 1×10^{15} ions cm^{-2}. This was significant in all the samples investigated and covered a range from 5nm in the as-deposited state to more than 50nm at the highest dose of 3×10^{16} ions cm^{-2}. This increase in mean grain size is consistent with that observed by Ozkaya et al. [1], where the effect of Ga^+ ion irradiation on 30nm NiFe was investigated. In this case grain size was seen to increase to $\sim$20nm at 1×10^{15} ions cm^{-2} and $\sim$50nm at 1×10^{16} ions cm^{-2} which is a more rapid increase than seen in the bilayer samples investigated here. The results shown here indicate that the thickness of the permalloy layer does not appear to influence the rate of grain growth within the sample. The most likely reason for the difference in growth rate is that in the case of the bilayer samples, the ions have to first traverse the non-magnetic metal layer before they can directly influence the magnetic permalloy layer. As shown in the SRIM simulations, some of the Ga^+ ions are stopped in the non-magnetic layer, as well as causing displacement of the non-magnetic metal atoms. This results in fewer atoms being available to modify the magnetic layer when compared to only the permalloy layer. Throughout the dose range all of the samples retained their polycrystalline structure and did become amorphous as has been seen in other irradiated samples [6, 12].

As expected, the milling depth increases with increasing dose. However, it had also been expected that there would have been a difference in the amount of milling experienced by the Al capped samples and the Au capped samples due

to the difference in sputter rate of the materials, but this was not observed. Au has a sputter rate of $1.5\mu m^3 nC^{-1}s^{-1}$, whereas the value for Al is $0.3\mu m^3 nC^{-1}s^{-1}$, which reflect the scattering cross section and atomic mass for each material. This would suggest that for a given dose, the amount of milling that occured would be around 5 times greater for Au than Al, but this was not found to be the case. A possible explanation is that as the experiment was set up for irradiation with a sputter rate value of $1000\mu m^3 nC^{-1}s^{-1}$ (see chapter 2.5.3), and not for milling where the conditions would be optimised for the material to be milled.

In each of the bilayers, regions irradiated at relatively low doses, 1×10^{13}, 3×10^{13}, 1×10^{14} and 3×10^{14} ions cm^{-2} showed little variation from the as-deposited sample. The coercivities of the low dose regions were found to be consistantly higher than the coercivity of the continuous film. Albeit a small increase, it can be explained by the fact that the dose regions have been isolated from the continuous film, and patterned into long rectangular elements, thus introducing a shape anisotropy. Being a soft magnetic film, the magnetisation will prefer to lie along the long axis of the shape, and will require a larger applied field to switch the magnetisation direction. Small fluctuations in the outward and return switching fields led to a random variation in coercivity of these regions and no clear dose dependant effect was observed. At these doses no alteration of the magnetisation or physical microstructure was detected using the TEM techniques employed here.

Between 3×10^{14} and 1×10^{15} ions cm^{-2} a reduction in magnetic moment was observed and was visible in the Fresnel images as a reduction in the magnetisation ripple contrast. This trend continued with increasing dose until the samples were rendered non-magnetic at 1×10^{16} ions cm^{-2} and 3×10^{16} ions cm^{-2} for the samples with 10nm and 20nm of permalloy respectively. However, no significant increase in coercivity was seen, with the exception of at a dose of 1×10^{16} ions cm^{-2} in both the 20nm NiFe samples, which was attributed to increased surface roughness due to irradiation induced milling. This is in contrast to reports where an increase in coercivity in NiFe is observed due to domain wall pinning [1] at the irradiated region, but in agreement with [13] where moment reduction and no increase in coercivity was seen. The reduction in moment could be explained had there been a reduction in the total thickness of the magnetic layer due to irradiation induced milling of the sample surface. However in these samples a maximum depth of 3nm had been milled at a dose of 1×10^{16} ions cm^{-2}, meaning that the 5nm cap layers had not been compromised and no milling of the NiFe layers had occurred. This

indicates that the reduction in moment is due to the effects of irradiation on the sample.

The lack of change in the coercivity of the samples is unexpected when considering the significant increase in the grain size. With larger grains there are fewer grain boundaries which should make domain movement easier, and result in an overall lower coercivity. Variation in coercivity of each of the samples is very slight with a difference of ∼2 Oe at most over the dose range 1×10^{13} to 3×10^{15} ions cm^{-2}. The only occasion of an increase in coercivity was seen at a dose of 1×10^{16} ions cm^{-2} in both of the 20nm NiFe samples. However this is most likely due to increased surface roughness as a result of milling of the sample surface. At this same dose the 10nm NiFe samples had become non-magnetic. An increase in dose to 3×10^{16} ions cm^{-2} was required to render the 20nm NiFe samples non-magnetic. This is consistant with results presented in [1, 2], where it is shown that 1×10^{16} ions cm^{-2} is able to render NiFe films of up to 15.5nm thickness non-magnetic, but not sufficient to render 30nm NiFe films non-magnetic.

Similar trends in both magnetic and structural modifications were observed in the 5nm Au/10nm NiFe/5nm Au sample, but these occurred at different doses than in the corresponding bilayer systems. The onset of structural changes began at 1×10^{15} ions cm^{-2} when an increase in grain size was seen. Changes in magnetic properties became immediately apparent at this dose with no magnetic ripple present in the Fresnel images, and at a dose of 3×10^{15} ions cm^{-2} the material has been rendered non-magnetic which is lower than the 1×10^{16} ions cm^{-2} required to realise this effect in the 10nm NiFe bilayer samples. Tridyn calculations, figure 3.26, showed that there is a significant difference in the concentration profile of Au throughout the system at a dose of 3×10^{15} ions cm^{-2}, which led to the trilayer being rendered non-ferromagnetic whilst the bilayer retained a net moment. As in [7] it is likely that the modifcation at the top Au layer is due to short range motions of the atoms resulting in increased interfacial roughness and some mixing, whereas at the lower NiFe/Au interface alloying of the two layers occurs.

This chapter has identified key doses at which significant changes in magnetic properties occur in each of the thin film systems investigated, and found that the trilayer system is much more sensitive to irradiation. In the following two chapters, this information is used to magnetically pattern different magnetic elements in which magnetisation may be controlled.

Bibliography

[1] D. Ozkaya, R. M. Langford, W. L. Chan, and A. K. Petford-Long, J. Appl. Phys. **91**, 9937 (2002).

[2] W. M. Kaminsky *et al.*, Appl. Phys. Lett. **78**, 1589 (2001).

[3] S. I. Woods, S. Ingvarsson, J. R. Hirtley, H. F. Hamann, and R. H. Koch, Appl. Phys. Lett. **81**, 1267 (2002).

[4] R. Hyndman *et al.*, J. Appl. Phys. **90**, 3843 (2001).

[5] J. Fassbender, D. Ravelosona, and Y. Samson, J. Phys. D: Appl. Phys. **37**, R179 (2004).

[6] D. McGrouther, J. N. Chapman, and F. W. M. Vanhelmont, J. Appl. Phys. **95**, 7772 (2004).

[7] T. Devolder, Phys. Rev. B **62**, 5794 (2000).

[8] D. McGrouther, *Effects of Focused Ion Beam Irradiation on Thin Ferromagnetic Films*, PhD thesis, University of Glasgow, 2004.

[9] A. Gentils, J. N. Chapman, G. Xiong, and R. P. Cowburn, J. Appl. Phys **98**, 053905 (2005).

[10] D. B. Williams and C. B. Carter, *Transmission Electron Microscopy* (Kluwer Academic / Plenum Publishing, 1996).

[11] M. Kowalewski *et al.*, J. Appl. Phys. **87**, 5732 (2000).

[12] J. Fassbender, J. von Borany, A. Mucklich, K. Potzger, and W. Moller, Phys. Rev. B **73**, 184410 (2006).

[13] C. M. Park and J. A. Bain, J. Appl. Phys. **91**, 6830 (2002).

Chapter 4

Patterning ferromagnetism by FIB for the creation of high density domain structures

4.1 Introduction

The ability to control the formation, location and behaviour of magnetic domain walls in thin films has many potential applications, as well as providing insight into their fundamental properties [1]. In particular, gaining control over the density of domain walls that are formed in a continuous magnetic thin film or magnetic element would be advantageous in investigations involving domain wall magneto-resistance (DWMR) [2] and to the development of domain wall based spintronic devices [3, 4].

In this chapter results concerning the magnetic behaviour and structural characteristics of magnetic elements designed to support multiple domains are presented. The reasoning behind the shape of the magnetic element is discussed, followed by micromagnetic simulations which investigate the different magnetic states that can be supported by the structure. Physical and magnetic characterisation has been carried out using different TEM techniques. In section 4.4.1, the physical characterisation of the structures using bright field TEM is shown and the irradiation effects as well as the quality of the structures that can be created is discussed. Section 4.4.2 details the magnetic characterisation of the fabricated elements by DPC microscopy. A discussion follows in section 4.5, where the re-

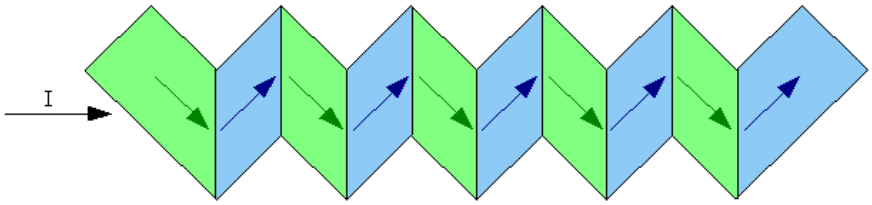

Figure 4.1: Schematic of zigzag wire with angle of magnetisation varying along the length of the element. Also shown, the direction of current flow in the wire.

sults of the simulations and experiemental work is considered, as well as further possibilities for continuing the work on these structures.

4.1.1 Control of magnetisation direction in magnetic structures

Previous studies have shown that magnetic elements with structured edges have a strong influence on the magnetisation processes which occur within the element [5], a fact which has been exploited in work involving magneto-resistive sensors. A 'zigzag' shaped wire has been devised in which the angle of magnetisation is found to vary along the element and is strongly related to the edge shape [6]. The domain structures within the wire can be controlled by applying a magnetic field parallel to the length of the wire. A current passed along the long axis of the wire, as indicated in figure 4.1, will experience a resistance which will vary as a function of this applied field. With this geometry the wire can be used as a single axis magnetic field sensor.

However, as the dimensions of the repeat unit are decreased, the sensitivity of the system is reduced as there is less deviation of the magnetisation direction from the long axis of the wire. This effect can be significantly reduced by breaking the exchange coupling between adjacent regions [7]. This concept is investigated in this chapter, with a view to creating structures where domains with anti-parallel alignment and not just varying magnetisation directions are the aim.

Such structures have also been used to investigate resistivity due to domain walls in the wires [8, 9]. As mentioned in chapter 1, a domain wall offers a source of resistance to current flow passed perpendicular to it. Due to the similarities in magnetic geometry of a spin valve, where anti-parallel alignment of two ferromagnetic layers leads to the giant magnetoresistance effect, and a domain wall separating two regions of oppositely aligned magnetisation, it has been postu-

lated that a magnetoresistive effect should occur for a domain wall [10]. These similarities are illustrated in figure 4.2.

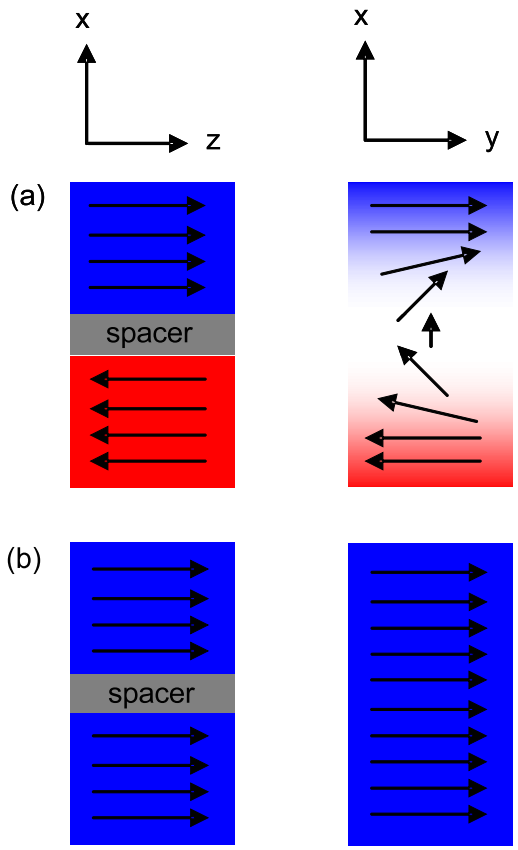

Figure 4.2: Schematic illustration of the similarity between the magnetic geometry of a GMR spin valve and a magnetic domain wall. (a) The spin valve in its antiferromagnetically aligned state which corresponds to the presence of a domain wall. (b) The spin valve in its ferromagnetically aligned state corresponding to the absence of the domain wall in the ferromagnet.

It has been shown to be possible to measure this effect in Co [10] and FePd [11, 12] films where stripe domain configurations are formed in zero applied field. This technique however does not give control over the location and density of domain walls that are formed. Magnetic nano-wires with constrictions have also been used to observe electron scattering due to domain walls by taking resistivity measurements in the presence and absence of a domain wall pinned at the constriction [13, 14]. A disadvantage of this arrangement is that it is only possible to create one or two isolated domain walls. To obtain large measurements of DWMR it would be necessary to create a structure where multiple domain walls could be present.

This prompted work by McGrouther et al [2, 15], who attempted to increase the density with which domain walls could be packed. CoFe films were ferromagnet-

ically patterned into a series of alternating parallel long and short wires. The longer wires remained magnetically connected to the surrounding film causing them to reverse their magetisation direction at a lower field than the isolated short wires. In this state, the pattern supported a series of domains with anti-parallel alignment. However, as described, the formation of this state relied upon the reversal of the surrounding continuous film. Ideally an independant magnetic structure in which a high density of domain walls at predefined locations could be created is desirable, and this is the intention of the work described in the rest of this chapter.

4.2 The 'zigzag' element concept

In order to create an array of magnetic domains supporting anti-parallel alignment, the structure shown in figure 4.3 was devised. As in reference [6], these structures take advantage of the strong correlation between edge structure and magnetisation direction.

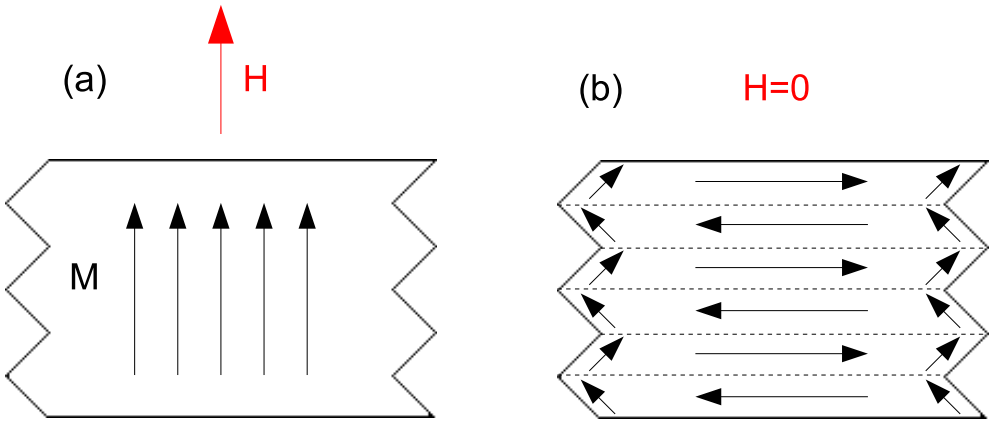

Figure 4.3: Schematic showing geoemtry of zigzag element. (a) Arrows indicate direction of magnetisation when an applied field is acting along the short, or hard, axis of the element. (b) Showing the formation of anti-parallel domains when the applied field is relaxed to zero. Arrows indicate the direction of magnetisation, whilst the dotted lines show the location of domain walls.

On application of a field along the short, or hard, axis of the structure, figure 4.3(a), the magnetisation of the structure should become saturated along this direction. When the field is relaxed to zero, figure 4.3(b), the edge structure is expected to dominate the magnetic behaviour and, as in the hard axis reversal of a continuous film, the element will split into oppositely magnetised domains. The

zigzag structure is designed as a wide strip rather than a narrow wire to increase the length of the domains and hence the domain walls which will separate them. This will aid potential transport measurements which could be made on this type of sample (see chapter 7). Other benefits of this design is that it is easily scalable, the number and size of the domains being varied by simply changing the dimensions and number of 'zigzag' repeats.

4.3 Micromagnetic simulations of domain states in the 'zigzag' element

Micromagnetic simulations were carried out using the OOMMF program described in chapter 2.6, to investigate the magnetic configurations that could be supported in the zigzag elements.

Initially the zigzag structure shown in figure 4.3 was modelled, with dimensions of $1\times0.6\mu$m. The input material parameters chosen were for permalloy, i.e. exchange stiffness constant of 1.3×10^{-11}J/m and saturation magnetisation of 8.6×10^{6}A/m. Magnetocrystalline anisotropy was set to zero and a cell size of $5\times5\times10$nm^3 was used. Relaxation of the magnetisation followed Landau-Lifshitz behaviour with the damping coefficient, α, set to 0.5. A hard axis field (along short axis) of 2000 Oe was applied to saturate the element along this direction, and was then relaxed to zero. The magnetisation vector maps in figure 4.4 show the relaxation process. Here it is clear that the long edges of the structure dominated the magnetic behaviour as the majority of the element is magnetised parallel to the long edge. Near to the zigzag feature ends, the magnetisation locally aligned with the pattern, but the two ends were proved to be too far apart to influence the formation of an anti-parallel domain structure.

The limitations of OOMMF have been discussed in detail in chapter 2, and must be carefully considered when comparing theoretical and experimental results. OOMMF cannot account for changes in magnetic properties within the sample. In FIB fabricated samples it is known that the region around the edges is also subject to irradiation by the tails of the ion beam. As a result of this, permalloy samples, such as those used here can experience changes in exhange coupling, saturation magnetisation and coercivity. All of these variables are potential sources of discrepancy between the simulation and experiment. Changes in coercivity could provide nucleation sites for the material to reverse at a lower field than

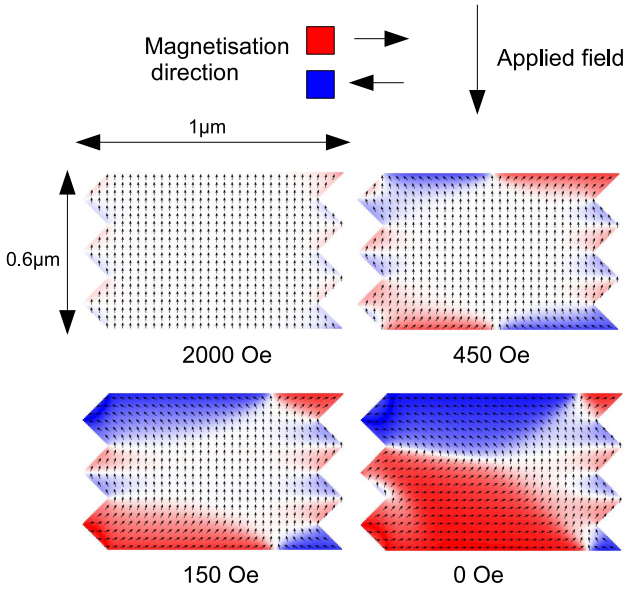

Figure 4.4: Simulated hard axis reversal of the zigzag element.

expected, whilst any difference in saturation magnetisation will require a change in the magnitude of applied field required to saturate the material. The potential for changes in exchange coupling are particularly important in the structures discussed in the following sections where irradiated regions are included across the structure. The main difference here is that the in OOMMF these regions are simulated by simply removing them from the calculation, essentially rendering that region of the sample non-magnetic, instead of just changing the magnetic properties.

4.3.1 Introduction of de-coupling lines

From the initial simulations it is apparent that some modification of the zigzag element is required to attain the desired anti-parallel alignment of domains. A line defect was introduced between opposite pairs of pointed ends as shown in figure 4.5, in an attempt to break the exchange coupling between potential domain regions. In an experiment this would be done by irradiating along the indicated line with a dose that is known to alter the magnetic properties of the magnetic film. For the purposes of the simulation, 5nm rows of cells were removed, essentially rendering those regions non-magnetic and disrupting the exchange coupling between adjacent strips. The simulated reversal is shown in figure 4.6.

A hard axis field of 2000 Oe was applied along the hard axis of the structure to

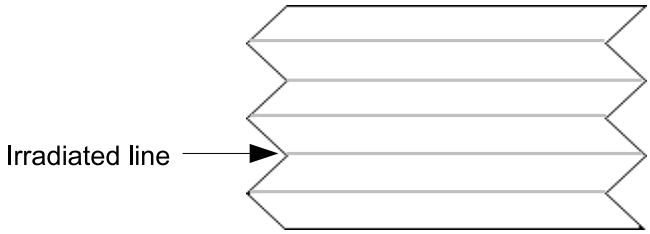

Figure 4.5: The zigzag structure with the grey lines indicating the positions of the irradiated de-coupling lines.

saturate the magnetisation in this direction. This field was then relaxed to zero and the simulation predicted that an array of domains supporting anti-parallel magnetisation would form. The element was then saturated in the opposite direction and on returning to zero applied field, anti-parallel aligned domains were again formed.

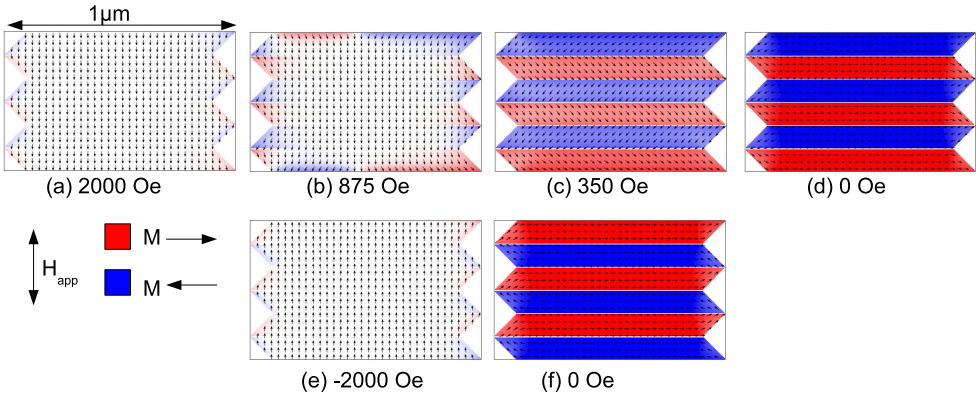

Figure 4.6: Simulated reversal of zigzag element with a 5nm wide row of pixels removed to simulate the irradiated lines between opposite points.

As previously mentioned the cell size used for the OOMMF simulations was 5nm. As such this provided a limit as to the narrowest line that could be removed from the simulation. However, the best resolution of the 10pA beam used for patterning is ∼10nm. This means that at best the modified line would measure 10nm, but in reality the tails of the beam and subsequent grain growth will likely extend the limits of the region that was intended to be irradiated. However, as the simulations predicted that the anti-parallel alignment of domains could be formed with only a 5nm region of modified material, it follows this will also be true for wider irradiated lines. It is also useful to be able to scale the number of domains that can be created. It is reasonable to assume that if the dimensions of the pattern and end structure remain the same, that increasing the number of repeats in the pattern will not affect the resultant magnetic state.

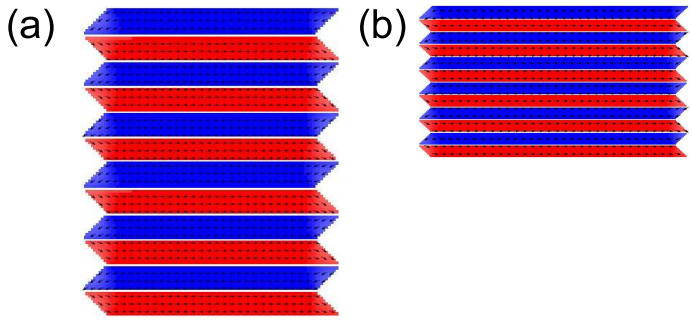

Figure 4.7: (a) An extended array of domains with anti-parallel alignment created by increasing the number of zigzag repeats to the structure. (b) High density array of domains created by halving the width of the domain regions.

A higher density of domain walls can also be achieved by reducing the dimensions of the repeated pattern, essentially by introducing more repeats into the same space, without changing the aspect ratio of the ends. Both these situations are demonstrated in figure 4.7. In figure 4.7(a) the simulated remanent state is shown for a zigzag element that has been increased in length by including more zigzag repeats. The length or number of repeats in the pattern has had no effect on the resultant magnetic state and an extended array of domains supporting anti-parallel magnetisation is formed. Figure 4.7(b) shows the variation of packing density of the domains in the structure. The aspect ratio of the ends has not changed, but the width of the domains is half of the original, essentially allowing double the number of domains to be fitted in the same space. Again, this variation in the element geometry will support anti-parallel alignment of domains.

4.4 Ion beam fabricated zigzag elements

Zigzag patterns were defined by FIB irradiation using the edge stream program described in chapter 2.5. An ion beam of 10pA was used for both defining the pattern and introducing the modified lines. In the previous experiments in chapter 3, in which the effect of irradiation dose on the permalloy systems was determined, a 1nA beam was used. However, the calculation used to determine the irradiation parameters, equation 2.16, is independant of beam current, so as long as care is taken to match the ion beam FHWM to the pixel size inthe pattern, the resultant irradiation effects are unchanged. The dose used to create the line defects is varied in order to investigate the extent of modification that is required to allow domains with anti-parallel alignment to be formed. A pattern of dimensions

$2\times1.2\mu$m was created on 10nm NiFe/5nm Al samples. At the time this work was carried out the 10nm NiFe/5nm Al samples were most readily available and were chosen for this reason. The dimensions of the OOMMF simulations presented in the previous section are smaller than the experimental structures to reduce computational time. The physical structure was observed using bright field imaging, whilst the magnetic behaviour was investigated using the DPC mode of Lorentz microscopy.

4.4.1 Physical characterisation of structures

A dose of 3×10^{16} ions cm^{-2} was chosen to define the zigzag patterns. From measurements in chapter 3, this dose is known to mill to a depth of around 10nm in the 10nmNiFe/5nmAl system. This would allow structures that were both physically and magnetically isolated from the surrounding film to be created, and would provide a direct comparison to the structures simulated by the OOMMF program. Throughout this chapter, all structures are defined with 3×10^{16} ions cm^{-2} and only the dose used to pattern the line defects across the structure is varied.

Initially, the lines were also created with a 3×10^{16} ions cm^{-2} dose. A montage of bright field images of this zigzag pattern is shown in figure 4.8.

It can be seen from the increased intensity surrounding the element that this dose has milled the surrounding film and the delineation regions. An intensity profile was taken across one of the milled lines and was averaged over the region in the blue box in image 4.8(b). The profile is shown in image 4.8(c) from which the width of the line is measured as $\sim$25nm. Some large grains which have not been milled away are still visible along the lines. Around the contour of the structure a region of increased grain size can be seen. This is due to grain growth induced by irradiation from the tails of the beam as it defined the pattern. These images also show the high quality of the patterns that can be created by this method. Edge roughness of the structures is of the order of the grain size.

Doses of 1×10^{16}, 3×10^{15} and 1×10^{15} ions cm^{-2} were also used to pattern the lines across the milled structures so as to investigate the effect of dose on the ability of the structure to form the desired anti-parallel state, and to reduce the amount of milling experienced by the sample in the lines. Bright field images of these structures are shown in figure 4.9.

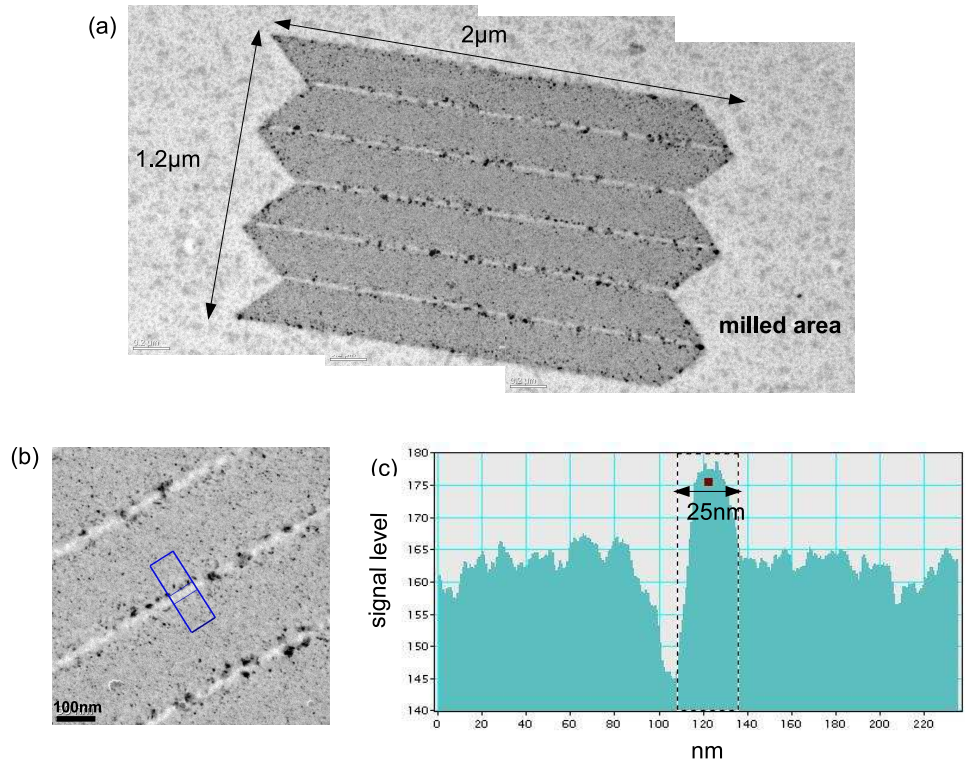

Figure 4.8: (a) Montage of bright field images showing the entire zigzag structure. Both surrounding area and delineation region irradiated with 3×10^{16} ions cm^{-2}. (b) Higher magnification image of the delineation lines, and (c) intensity profile averaged across the region in the box on image (b).

In figure 4.9(a) and (b), a zigzag structure with 1×10^{16} ions cm^{-2} lines is shown. From results in chapter 3, we expect grain growth for this dose to be between 30nm and 40nm, which is consistant with the high concentration of large grains seen within these irradiated lines. However, as shown in figure 4.9(b), the width of these irradiated lines is ∼70nm, almost 3 times the width of the milled lines. It had been expected that owing to the lower dose, the width of the 1×10^{16} ions cm^{-2} irradiated lines would be narrower. It is possible that this is due to a slight difference in ion beam focus from when the 3×10^{16} ions cm^{-2} line structure was patterned. A simple occurence such as a small stage movement can cause a change in the height of the sample and in turn affect the focus of the beam. While every effort was made to ensure accurate focus of the beam, it is a slightly subjective procedure. There is no method for measuring the optimum focus other than by imaging at high magnification (>25k x) which rapidly erodes the sample.

All of the structures shown in figure 4.9 were patterned at the same time under the same patterning conditions, so any differences in line width, grain growth or magnetic behaviour (as discussed in the following section) can be attributed to

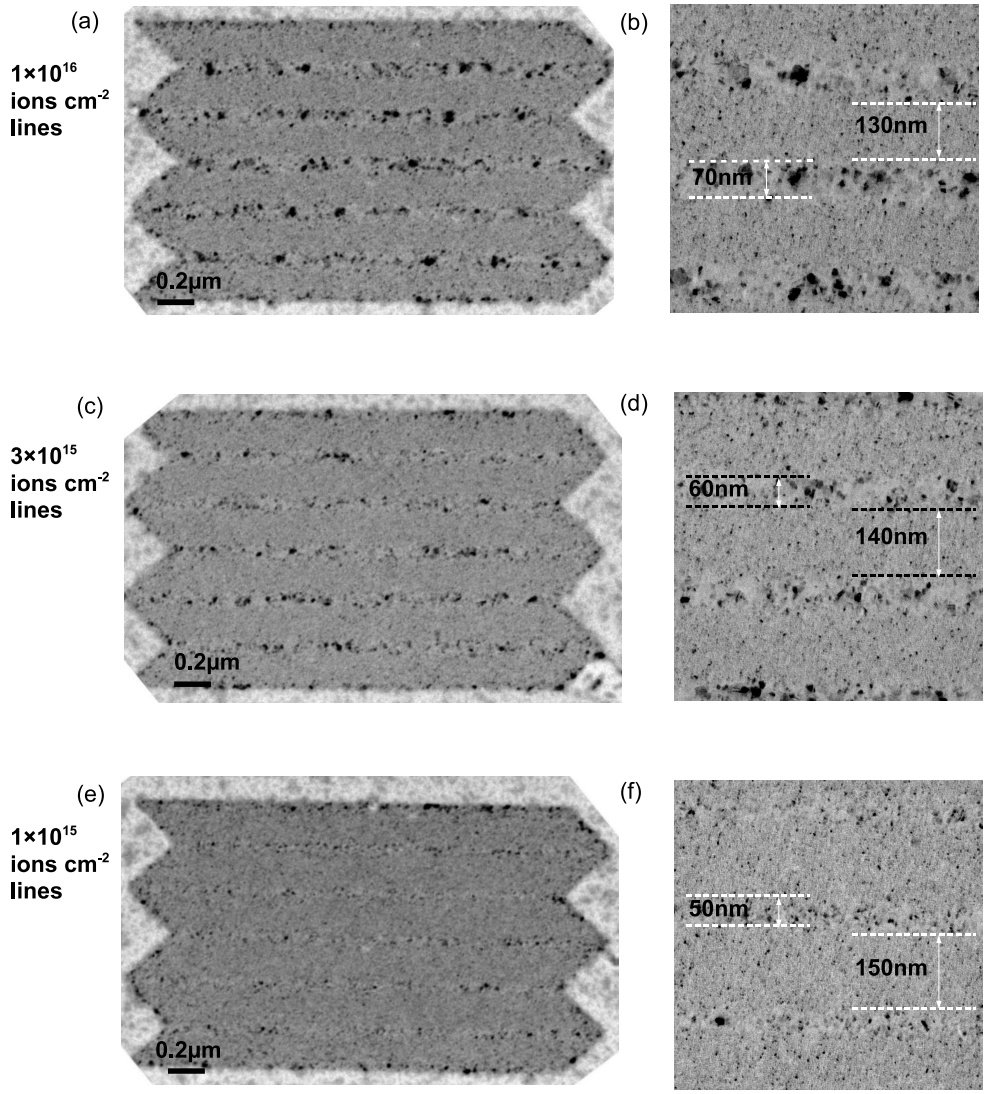

Figure 4.9: Bright field images of zigzag structure with lines irradiated at (a,b) 1×10^{16} ions cm^{-2}, (c,d) 3×10^{15} ions cm^{-2} and (d,e) 1×10^{15} ions cm^{-2}

the effect of the dose used to pattern the lines.

Figures 4.9(c) and (d) show the zigzag structure with 3×10^{15} ions cm^{-2} lines. The line width and width of the domain were measured and found to be 60nm and 140nm respectively. This is a decrease in line width of 10nm from the lines irradiated at 1×10^{16} ions cm^{-2}. This trend is continued with a further 10nm decrease in line width measured in the 1×10^{15} ions cm^{-2} sample, figure 4.9(e) and (f), where the line and domain are found to be 50nm and 150nm respectively. It is also clear to see that the amount of grain growth in the line regions is greatly reduced as the dose is decreased, and that no evidence of milling is seen in any of these dosed lines.

4.4.2 Magnetic characterisation

Differential phase contrast microscopy has been used here to provide detailed information about the local direction of magnetic induction in the zigzag samples. Figure 4.10 shows the magnetisation reversal of the zigzag element with 3×10^{16} ions cm^{-2} lines where. This is the same sample presented in figure 4.8 where milling has occured in the delineation lines. These images are sensitive to the component of magnetic induction parallel to the long axis of the structure, as indicated by the white double headed arrow. The direction of the applied field is indicated by the black arrow. In the images, when the local induction lies parallel or anti-parallel to the mean direction of sensitivity, then the pixels appear dark or bright, i.e. when the domains are magnetised along the easy axis. If the local induction direction lies parallel to the direction of sensitivity, then zero component exists and an average grey value is observed.

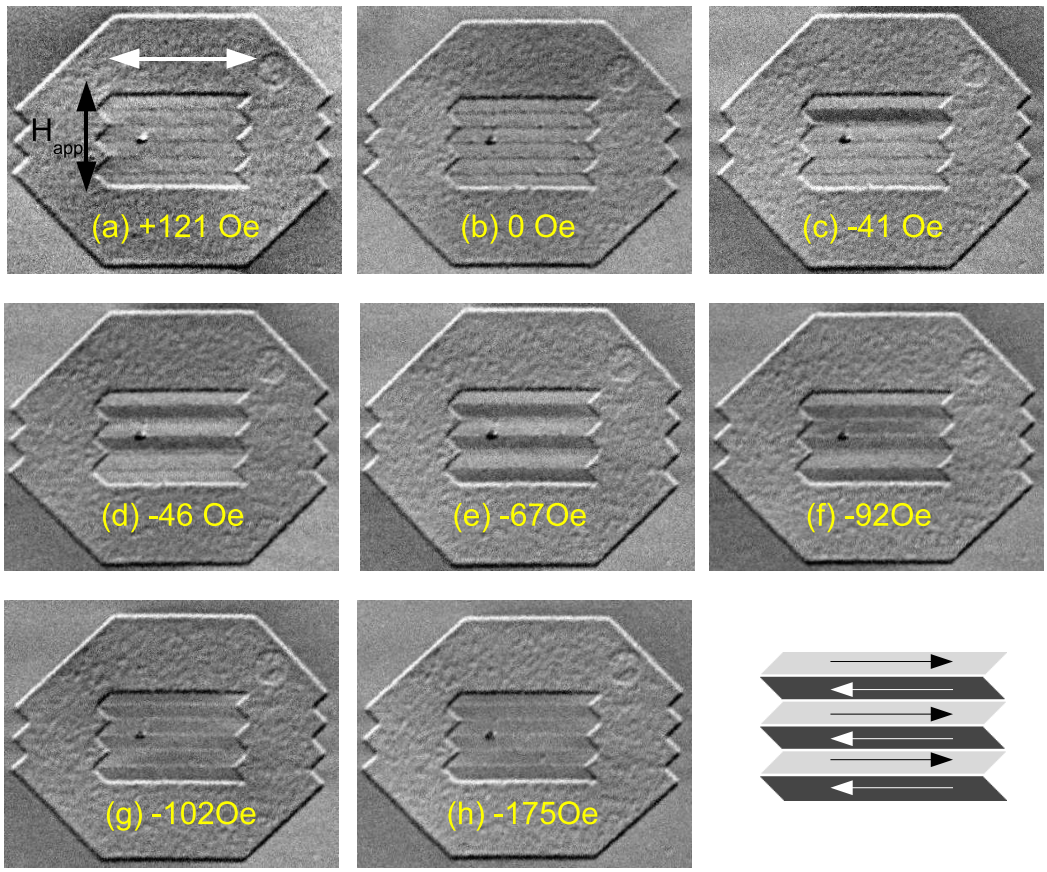

Figure 4.10: DPC sequence of the reversal of the element created with 3×10^{16} ions cm^{-2} surrounding and lines, sensitive to the magnetic induction parallel to the long axis of the element as indicated by the red arrow. Direction of the applied field is shown by the white arrow.

Initially the element was saturated with an applied field of +2000 Oe as in the

OOMMF simulations, but observations made as the field was cycled showed that it was only necessary to apply a field of ∼200 Oe in order to saturate the element. The reversal sequence in figure 4.10(a) shows the element saturated along the hard axis by a field of +121 Oe. On relaxing the field to zero, 4.10(b), the magnetic state of the element did not immediately form an array of domains supporting anti-parallel alignment, as was predicted in the OOMMF simulations. The direction of the applied magnetic field was reversed, and had reached a value of -41 Oe when a single domain reversed, figure 4.10(c). Following this, the direction of magnetisation in a second domain reverses, 4.10(d), whilst the complete anti-parallel state does not form until a field of -67 Oe is applied, figure 4.10(e). This step-wise reversal of domains is also contrary to prediction made by OOMMF where all domains were shown to reverse simultaneously with a domain wall sweeping from one end of the domain region to the other. At -92 Oe a further domain region had reversed, figure 4.10(f), followed by the final two domains at -102 Oe, figure 4.10(g). In this image it can be seen that the second lowest domain in the structure has not fully reversed at this stage, but has been caught mid-reversal. The rest of the domain quickly reversed after this image was taken. Finally the structure was saturated with a field of -175 Oe.

Whilst this set of results show that the structure can support an array of domains with alternating magnetisation, the aim was to achieve this magnetic state by the introduction of regions of modified rather than milled material. Therefore the dose in the irradiated lines was reduced to 1×10^{16} ions cm^{-2}. Inital observations of these structures showed that the contrast was not as strong as in the images in figure 4.10, indicating that the magnetisation in the domains was not aligned fully parallel. Therefore, the orthogonal components of the DPC signal are also shown here so that any magnetisation directed along the hard axis of the structure can be observed.

Figure 4.11 shows the DPC image pair sequence for the reversal of the zigzag structure with 1×10^{16} ions cm^{-2} irradiated lines. For each image pair, the left hand image is sensitive to the component of induction along the easy axis of the structure, whilst the right hand image is sensitive to the orthogonal direction, as indicated by the white double headed arrows. A hard axis field, indicated by the blue arrow in figure 4.11, of -80 Oe was applied to saturate the element, figure 4.11(a,b). As the field was relaxed to 0 Oe, the magnetic domain regions aligned along the easy axis of the structure, but did not relax into anti-parallel alignment. There are three domains magnetised in each direction, but they are not in an

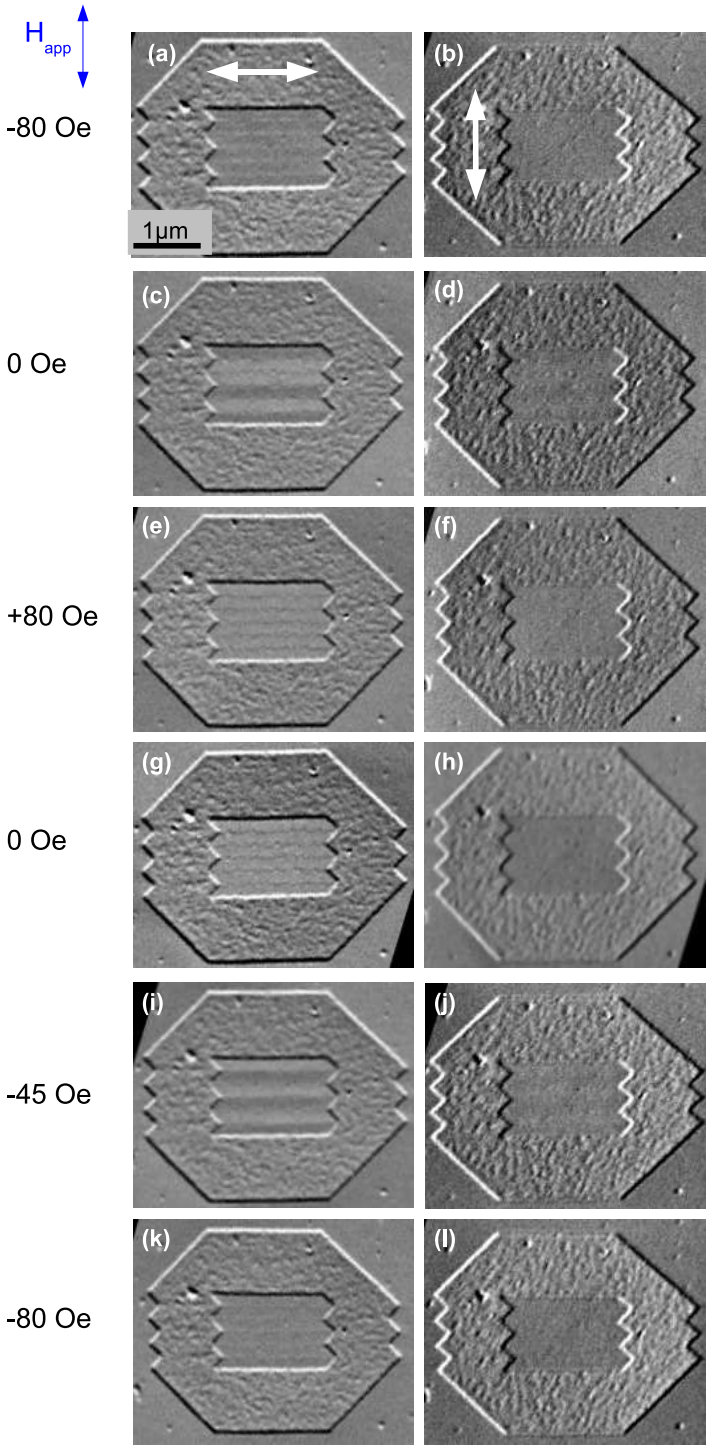

Figure 4.11: DPC reversal sequence of zigzag element with lines irradiated at a dose of 1×10^{16} ions cm^{-2}. White double headed arrows indicated the approximate direction of magnetic induction that each column of images is sensitive to.

alternating arrangement. In image 4.11(d) it can be seen that the contrast is not uniform, but mirrors the domain pattern in figure 4.11(c). This is indicative that there is a component of magnetisation in this direction and explains why contrast in the orthogonal component is reduced. Increasing the field to +80 Oe, 4.11(e,f), saturates the element in the opposite direction. On the return cycle no domains have been reversed as the structure is relaxed at remanence. A step-wise reversal of domains was then seen as the field was reduced to -45 Oe, figure 4.11(i,j), where alternating alignment of the domains is formed. In figure 4.11(k,l) at -80 Oe, magnetisation in all the domains regions has reversed. The reversal sequence was repeated several times and the formation of the alternating domain state was only seen on the return cycle. Intensity profiles taken from images 4.11(i,j) are shown in figure 4.12. The difference signal for the easy axis component is approximately 5 times greater than that for the hard axis.

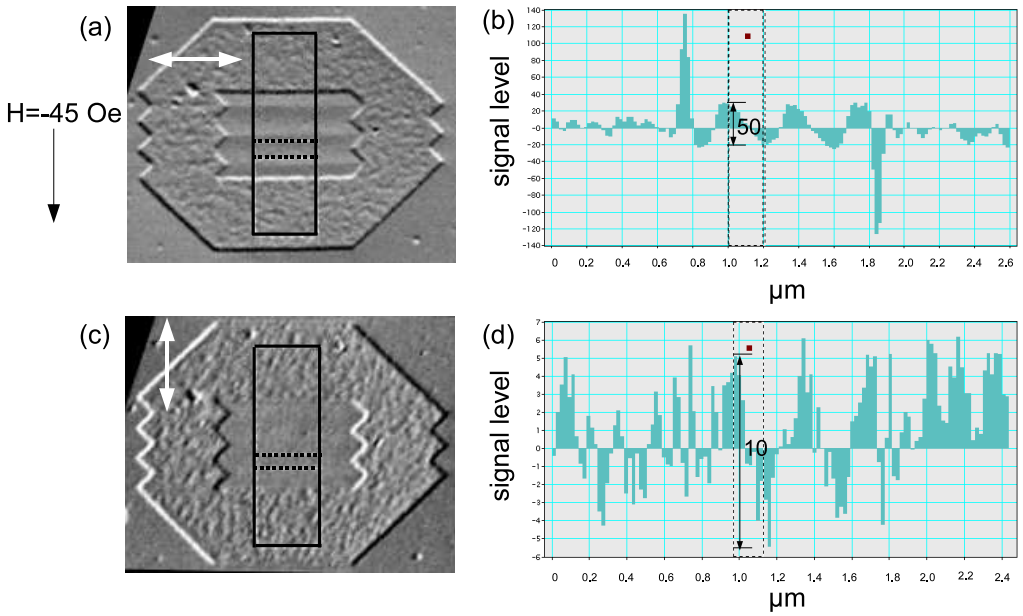

Figure 4.12: DPC images of zigzag element with 1×10^{16} ions cm^{-2} lines, supporting alternating domains. White arrows indicate the direction of magnetic induction each image is sensitive to. Corresponding intensity profiles from the selected area, shown in (b,d), show the relative difference in signal strength between orthogonal components.

The dose used to pattern the de-lineation regions was further reduced to 3×10^{15} and 1×10^{15} ions cm^{-2} to try and find the minimum disruption or modification that was required in the delineation region to allow the alternating domain pattern to form.

Shown in figure 4.13 is the zigzag structure with 3×10^{15} ions cm^{-2} irradiated lines. In 4.13 (a-d), the orthogonal components of magnetisation of the structure

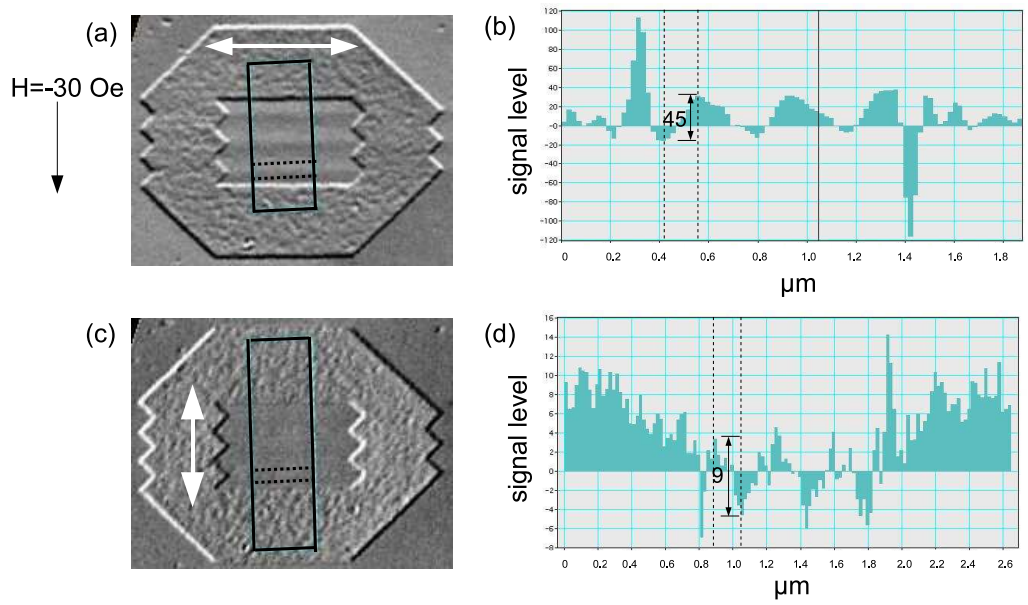

Figure 4.13: DPC images of zigzag structure with 3×10^{15} ions cm^{-2} lines at -30 Oe, showing domains with alternating magnetisation direction. White double headed arrows indicate the direction of magnetic induction to which the image is sensitive. Intensity profiles from the selected areas, shown in (b,d), show the relative difference in signal strength between orthogonal components.

with 3×10^{15} ion cm^{-2} lines are shown, along with the corresponding intensity profiles. These images were taken at a field of -30 Oe where it can be seen that a state with alternately magnetised domains has been formed. As in the previous results there remains a component of magnetisation directed along the hard axis, which is small compared to that for the easy axis, but it clearly visible in the profile 4.13(d). Again, the structure did not form an anti-parallel state at zero field. In contrast to the other reversal sequences shown, this structure formed the desired anti-parallel state at -30 Oe on both the outward and return cycles. Both times the magnetic state is the same, which is different from that shown in the simulations where the direction of magnetisation in the domains is reversed. However, this is not unexpected, as the element will have no memory of the magnetic state and will not have any preference as to which arrangement of domains it will form.

In figure 4.14, the structure has been irradiated with lines of 1×10^{15} ions cm^{-2}. A line of this dose proved to be unable to cause sufficient decoupling between adjacent regions to allow anti-parallel aligned domains to form, but this was not unexpected as even in a larger area it did not have a significant effect on the magnetic properties of the film. As can be seen in figure 4.14, the magnetisation locally varies at the edges of the sample. The edge structure and irradiated lines

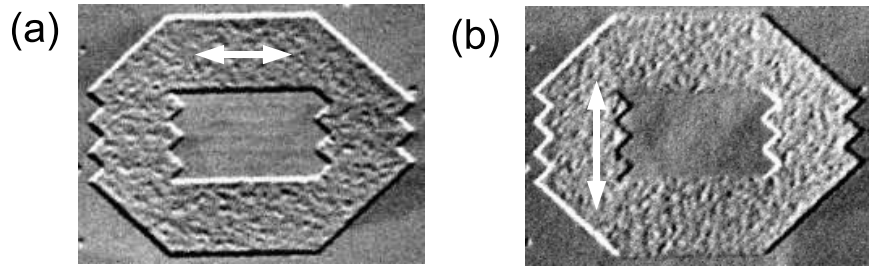

Figure 4.14: DPC images of zigzag structure irradiated with 1×10^{15} ions cm^{-2} lines. White double heases arrow indicate the direction of magnetic induction to which the image is sensitive.

influence the magnetisation in the local vicinity, but the effect does not extend across the entire element.

4.5 Discussion

In this chapter it has been shown that magnetic elements with zigzag structured edges are able to support alternately magnetised domains and that by using irradiation it is possible to control the position and density of the domain boundaries.

The zigzag element was designed to benefit from the fact that the magnetisation of a patterned element will tend to align with the edges of the structure due to induced shape anisotropy. Simulations showed that in order to form an array of domains supporting anti-parallel magnetic alignment it was necessary to modify the structure by the inclusion of irradiated lines which spanned the structure between opposite pairs of pointed ends. Without these lines, the structure behaved much like a single element with only regions closest to the structured edges being influenced.

The 10pA Ga^+ ion beam was used to fabricate the structures in samples consisting of a 10nm NiFe/5nm Al. An ion dose of 3×10^{16} ions cm^{-2} defined the zigzag pattern creating physically and magnetically isolated structures. Grain growth was seen around the edges of the structure which was due to irradiation from the tails of the ion beam as the structure was created. An increase in mean grain size from 5nm - $\sim$10nm was observed, which is consistent with the edges of the structure receiving a dose of 3×10^{14} ions cm^{-2}.

Initially the delineation lines were also milled so as to be as close to the simulation circumstances where it was only possible to represent the removal of material rather than the modification of material properties. The presence of larger grains

along the edges of these lines is consistant with the effects of high irradiation doses on this sample, and it is likely that what is seen are the remains of even larger grains that have subsequently been milled away. The variation in grain size within lines of differing doses is also consistent with observations in chapter 3. However, it was not expected that the width of the milled line would be narrower than the irradiated lines due to the much higher dose and longer patterning time required. The difference is most likely due to better patterning conditions on the day that the milled structures were created. There may also have been a change in the ion beam profile itself. The zigzag structures with irradiated lines were made some time after the original milled structure. With use over time, the apertures which control the ion beam current become eroded and gradually the amount of current in a particular beam will increase.

When measuring the width of the milled line, only the completely milled region was included and not grain growth on either side of the line. Measurements of the irradiated line took into account all irradiation induced effects, i.e. from where visible grain growth began and finished. When this was done with the milled lines, the width almost doubles to 40nm. However, this is still lower than the 70nm, 60nm and 50nm measured for the 1×10^{16}, 3×10^{15} and 1×10^{15} ions cm^{-2} lines, making the change in patterning conditions the most likely source of the discrepancy. In spite of this, it is encouraging that the lowest dose capable of realising an array of alternately magnetised domains, 3×10^{15} ions cm^{-2}, had a measured line width of $\sim$50nm, which is approaching the estimated size of $\sim$30nm for the core of a Néel wall. This means that with improvements in the ion beam focus and patterning conditions the width of patterned lines could be reduced to 30nm and provide a more accurate representation of a domain wall.

Differential phase contrast microscopy was used to investigate the magnetic behaviour of the structures which allowed the magnetic induction parallel to the long axis of the structure to be mapped. The aim of introducing the irradiated lines in the structures was to influence the magnetisation to form an array of anti-parallel aligned domains magnetised along the easy axis of the structure. With 3×10^{16} lines this was achieved by simply milling the line and therefore physically as well as magnetically isolating the adjacent domain regions. This effectively broke the exchange coupling between neighbouring regions. With lower doses of 1×10^{15} and 3×10^{15} ions cm^{-2}, the magnetic layer was not compromised, and so any influence on the magnetic behaviour of the sample can be attributed to modification of the magnetic properties in the irradiated line. It is known from

results in chapter 3, that a dose of 1×10^{16} ions cm^{-2} was sufficient to render this system non-magnetic in an extended area, but magnetisation in the sample remained connected across a single line of this dose. This shows that it is not necessary to completely magnetically isolate the adjacent domain regions in order for them to form domains with alternating magnetisation. This result is further confirmed by the fact that lines of 3×10^{15} ions cm^{-2} allowed the desired magnetisation state to be formed, but as shown in chapter 3 this dose was not sufficient to render the system non-magnetic. However, a reduction in the magnetic moment of the sample was observed at 3×10^{15} ions cm^{-2} and it is likely that this effect has occurred within the irradiated lines. It is possible that this has caused a reduction in the exchange coupling across this area allowing the domain regions to act independantly of each other and relax into an alternating array.

The anti-parallel alignment of domains was only realised in the structure with milled delineation lines. Structures with lower doses in the lines were only able to support domains with varying magnetisation directions. From looking at the intensity profiles of the magnetic induction in both orthogonal directions, the easy axis component was ∼4 times greater than the hard axis component, so we can interpret that the structure is predominantly magnetised along the easy axis. This would mean that the domain boundaries are not what we would class as 180° walls, but as lower angle walls as they do not separate domains of opposite magnetisation, as illustrated in figure 4.15.

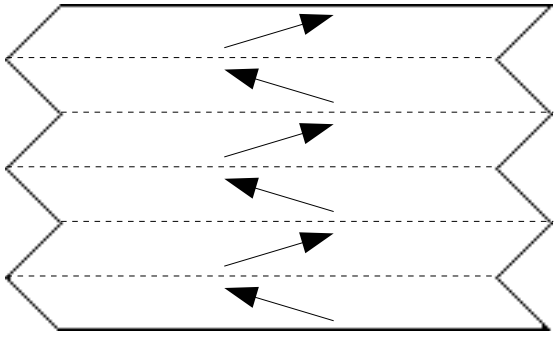

Figure 4.15: Schematic of zigzag element showing the likely orientation of magnetisation when domains are alternately aligned.

Several discrepancies were observed between the magnetisation reversal behaviour seen experimentally and that predicted by the OOMMF simulations. Firstly the zigzag structures did not relax to the anti-parallel state at zero field. This was unexpected as at zero field, the anisotropy in the shape should influence the magnetisation to lie along the easy axis of the structure, and having no memory

of its previous state, the domains should align anti-parallel. The most probable reason for this is due to a misalignment of the field with the hard axis of the element. This would lead to a preference for one direction of magnetisation over the other, thus requiring a field to be applied in the opposite direction to switch the magnetisation. Aligning the field with any feature is always subject to a small error and is even harder to do when imaging in DPC mode as the sample is not viewed in real time. Initially, Fresnel imaging of the sample was carried out. During these experiments it was observed that the anti-parallel state was formed at zero applied field, confirming that it is possible. These results were not shown as electrostatic effects were very strong and the magnetic state was not easy to determine, whereas DPC images clearly showed the results.

A slight modification of the structure itself may also be useful to help ensure that the domains relaxed along the easy axis of structure at zero field. The schematic in figure 4.16 shows the zigzag structure as it was patterned (black line) and with higher aspect ratio ends (red line). The more pointed ends would have a stronger influence on the magnetisation which would be directed closer to the easy axis of the structure.

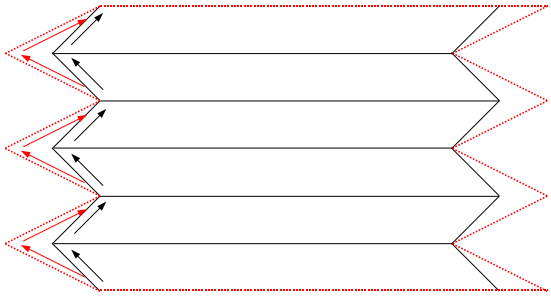

Figure 4.16: Schematic showing the variation in end shape which could aid the formation of the desired anti-parallel domain state. Arrows indicate the direction of magnetisation at the ends.

The structures also showed a step wise or domain by domain reversal process. This was in contrast to the prediction made in the micromagnetic simulations where the domains reversed simulataneously. It is possible that this is due to the increased line width of the experimental structures over the simulated structures and that the domain segments are rather more independent of each other than predicted. However, this gradual reversal process could prove to be useful in that it allows there to be a known number of domains aligned parallel or anti-parallel at a given time. Domain wall magnetoresistance measurements could therefore be made over a varying number of domain walls within a single sample by simply varying the applied field value.

The domain walls that are created in these structures are what could be termed 'pseudo-domain walls', as they only mark the edges of domains and are not necessarily domain walls. A further development that could be made would be to see if it would be possible to create a structure where magnetisation could be influenced enough to allow the formation of domain walls between the pointed ends without including an irradiated region the entire way across the structure. This was done using a similar structure to those already shown but with the de-lineation marks only protruding into the element at the edges. It was thought that by aiding the formation of extended regions of anti-parallel alignment at the ends, that the domain walls may form in the intervening region to complete the gap. This would allow more accurate measurements of domain wall resistance to be made if such structures were to be used for this purpose.

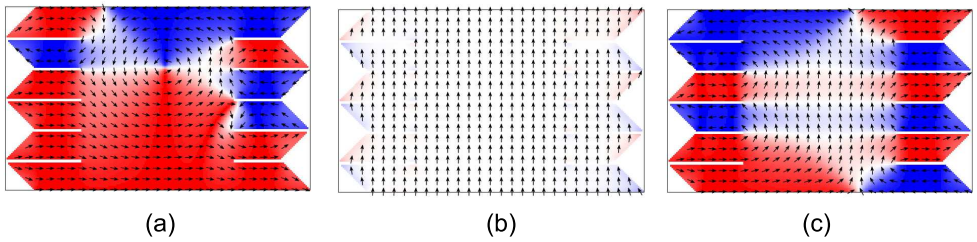

Figure 4.17: Zigzag element with partial delineation regions. (a) Shows the intial relaxed state of the element, (b) the element saturated along the hard axis and (c) the element at zero field, showing low angle domains.

As can be seen in figure 4.17 and 4.18, simulations have been carried out with different lengths of line extending into the element from the pointed ends. In 4.17 (a), the areas local to the points have been influenced by the edge and partial delineation mark, but as the end of this is reached, the magnetisation behaves as in a regular rectangular element and a vortex is formed. After the structure has been saturated in 4.17(b), we can see that in 4.17(c), the end structure has again influenced the magnetisation and within the limits of the partial delineation region, individual domains are formed. However, in the centre of 4.17(c) two regions magnetised along the long axis of the element are visible. There is some slight variation in the direction of the magnetisation suggesting that some influence of the end shape is felt across this region. In figure 4.18, the simulation was carried out with delineation marks protruding further into the central region of the element.

Again, this shows that prior to saturation of magnetisation in the hard axis direction, a random magnetic configuration was formed in the element. After saturation, 4.18(b), the element relaxed to a state where regions in between the

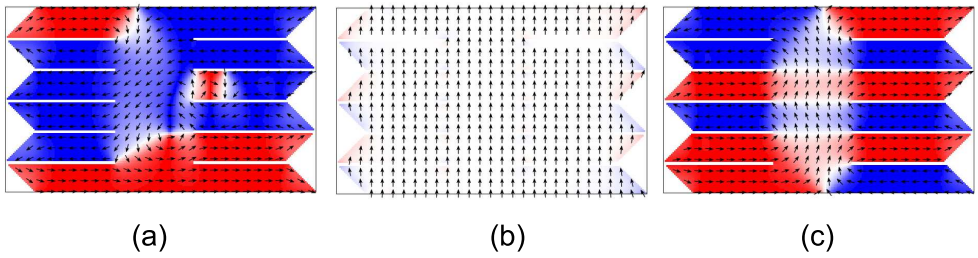

Figure 4.18: Simulated reversal of element with delineation regions extending further into the element at (a) initial relaxed state, (b) saturated along the hard axis and (c) relaxed to zero field and showing the formation of some some low angle domains in the central region.

delineation marks aligned anti-parallel to each other, 4.18(c). In the central region where there are no marks, there was only a partial influence and similar to the previous simulation, some slight variation in magnetisation direction is seen.

Therefore it is concluded that it is necessary to include a delineation region which extends across that entire element in order to achieve uniform domains supporting anti-parallel alignment.

Bibliography

[1] R. Weiser, U. Nowak, and K. D. Usadel, Phys. Rev. B **69**, 064401 (2004).

[2] D. McGouther and J. N. Chapman, Appl. Phys. Lett. **87**, 022507 (2005).

[3] S. S. P. Parkin, Int. J. Mod. Phys. B **01**, 117 (2008).

[4] D. A. Allwood *et al.*, Science. **309**, 1668 (2005).

[5] M. Herrmann, S. McVitie, and J. N. Chapman, J. Appl. Phys. **87**, 2994 (2000).

[6] F. C. S. da Silva *et al.*, Appl. Phys. Lett. **85**, 6022 (2004).

[7] M. Donahue, F. da Silva, and D. P. Pappas, Micromagnetic and analytic study of small zigzag sensors, in *49th Conference on Magnetism and Magnetic Materials: November 7-11, 2004, Jacksonville, Florida*, 2004.

[8] T. Taniyama, I. Nakatani, T. Namikawa, and Y. Yamazaki, Phys. Rev. Lett. **82**, 2780 (1999).

[9] J. L. Tsai, S. F. Lee, Y. D. Yao, and C. Yu, J. Appl. Phys. **91**, 7983 (2002).

[10] J. F. Gregg *et al.*, Phys. Rev. Lett. **77**, 1580 (1996).

[11] M. Viret *et al.*, Phys. Rev. Lett. **85**, 3962 (2000).

[12] R. Danneau *et al.*, Phys. Rev. Lett. **88**, 157201 (2002).

[13] U. Ebels, A. Radulescu, Y. Henry, L. Piraux, and K. Ounadjela, Phys. Rev. Lett. **84**, 983 (2000).

[14] S. Lepadatu and Y. B. Xu, Phys. Rev. Lett. **92**, 127201 (2004).

[15] D. McGrouther, *Effects of Focused Ion Beam Irradiation on Thin Ferromagnetic Films*, PhD thesis, University of Glasgow, 2004.

Chapter 5

Domain wall trap structures with irradiated pinning sites

5.1 Introduction

Domain walls in ferromagnetic nanoelements are currently the subject of much interest due to their potential uses in metallic spintronics devices [1], magnetic logic [2, 3, 4] and magnetic data storage [5, 6], where information is conveyed by the propagation and controlled motion of domain walls in patterned magnetic structures. As such a greater understanding of the fundamental physical properties of domain walls, propagation of walls and the interaction with pinning sites is required.

In section 5.2, the fabrication of magnetic domain wall traps by focused ion beam is discussed and intital results on the behaviour of these structures is presented. The introduction of irradiated pinning sites to the domain wall traps is also shown. The success of the inital results led to the magnetic nanowire structure discussed in section 5.3 being developed, so that the interaction of domain walls with the irradiated pinning sites could be further investigated. Micromagnetic simulations are shown to support the work in this section. Section 5.4 contains conclusions and a discussion of the work presented in this chapter.

5.1.1 Domain walls in wires

As a first step it is necessary to be able to create domain walls in wires. Different methods have been used to achieve this depending on the geometry of the magnetic entity. Domain walls can be injected into wires using different methods depending on the geometry of the structure. Some wires have larger injection pads at one end to provide an area where the domain wall can nucleate and then be injected into the wire [7, 8, 9]. In domain wall trap structures a domain wall is established by applying a saturating field perpendicular to the long axis of the wire and then relaxing the field to zero [10, 11], whereas domain walls are formed in ring structures when it is placed in a uniform magnetic field for any orientation[12]. The structure of the domain walls that are formed in wires is highly dependant on the width of the wire and the thickness of the magnetic film. A refined phase diagram was calculated by Nakatani et al [13], giving the preferred wall type for a given wire width and film thickness, and is shown in figure 5.1.

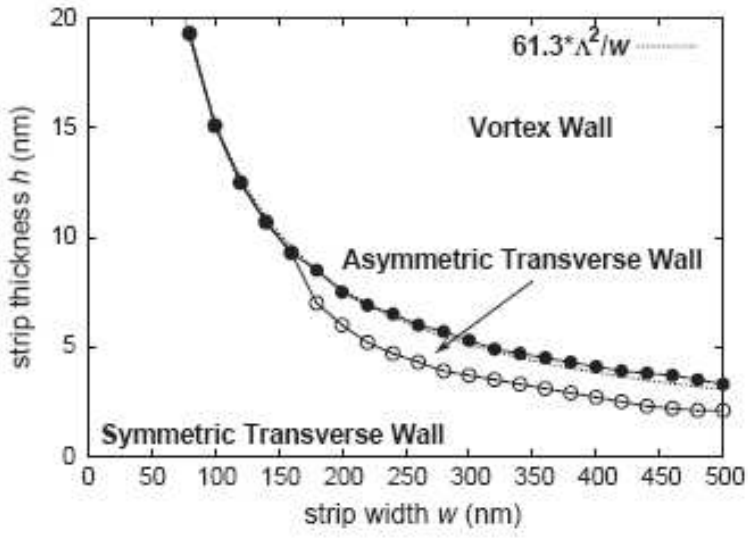

Figure 5.1: Phase diagram of the domain wall structure in strips of Permalloy. The preferred wall type is determined for strips of varying width and thickness. *Taken from Y. Nakatani et al, Journal of Magnetism and Magnetic Materials, 290-291, (2005) 750-753.*

Figure 5.2 shows schematic diagrams of the domain wall structures predicted by the phase diagram. The vortex domain wall packet comprises three wall sections and can have clockwise or counter clockwise rotation of the magnetisation around the core. The transverse domain wall has two wall sections and the central domain has its moment perpendicular to the wire. The third wall type is the

asymmetric transverse domain wall where the central domain has a component of magnetisation both perpendicular and parallel to the length of the wire. Also shown are the equivalent domain wall configurations if the magnetisation in the wire is tail to tail. The magnetic wires that are investigated in this chapter are made from 10nm thick permalloy and have widths of 300nm and 500nm, making the vortex structure the preferred domain wall type.

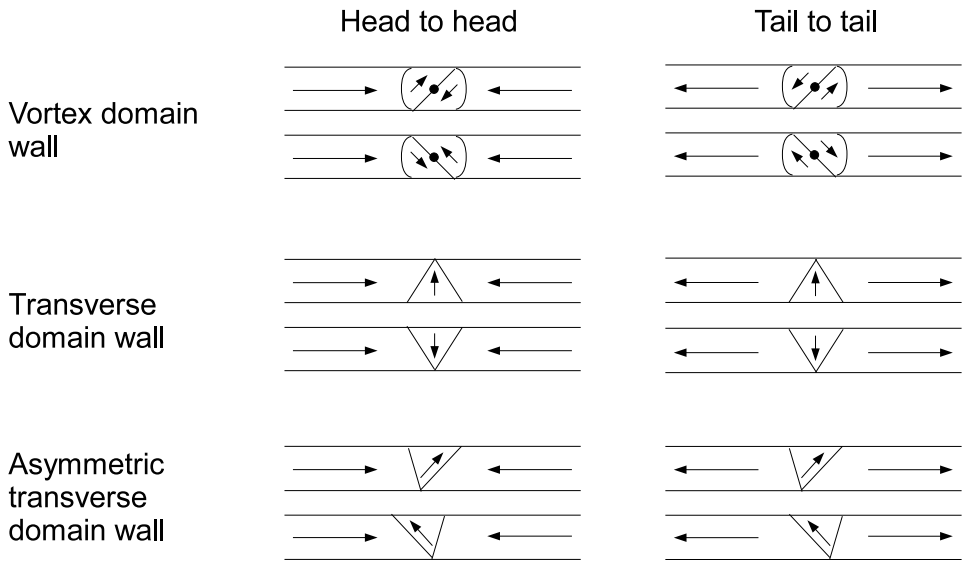

Figure 5.2: Simplified schematic of head to head and tail to tail domain walls with vortex, transverse and asymmetric transverse configurations.

Once created, it is possible to move the domain wall within the structure by the application of an applied field parallel to the length of the wire, as depicted in figure 5.3. It has also been shown to be possible to move domain walls using electrical currents through the spin torque effect. [14, 15, 16, 17].

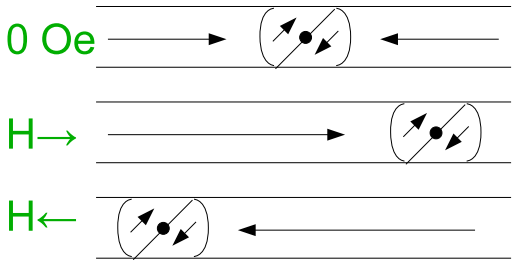

Figure 5.3: Schematic showing the motion of a vortex domain wall under the influence of magnetic field applied along the long axis of the wire.

In addition to being able to form domain walls and to move them within these structures, it is also important to study the interaction of magnetic domain walls with pinning sites. These can be used to control the behaviour of the domain

walls by providing well defined, stable locations as well as being used to confine the wall propagation. Unintentional pinning sites can often result from defects in the material or pattern, which are hard to control and become increasingly important as the dimensions of structures are reduced. With recent improvements in lithography and FIB etching techniques it is now possible to artificially engineer pinning sites [18, 19, 20, 21, 22, 23]. Various pinning site geometries have been studied in the form of constrictions and protrusions at the edges of the wires. These act as potential barriers or potential wells to the domain wall and impede its propagation along the wire. These sites essentially trap the domain wall at a predefined location until the potential energy feature can be overcome by applying a large enough de-pinning field. Some examples of the geometries which have been investigated are shown in figure 5.4.

Figure 5.4: Schematic diagram of the notches and anti-notches that have been investigated as potential domain wall pinning sites.

This approach has proven to be successful in its aim, however as magnetic structures continue to reduce in size, creating well defined geometrical pinning sites will become much more difficult. Variations in the fabricated sites will become comparable in size to the edge roughness and will also be limited by the lithographic or milling techniques used. A possible alternative to this is to use ion irradiation to modify the magnetic properties of selected areas along the length of the wire. These areas will act as inherent pinning sites to the wire without any need to modify the shape. In this chapter different nanowire geometries were used to investigate the interactions of walls of different chirality with irradiated regions orientated at 45° and 90° to the long axis of the wire.

5.2 Creation of domain wall trap structures by focused ion beam

The domain wall trap structure was first proposed by McMichael et al [10] as a way of reducing the coercivity and improving the reproducibility of switching of submicron magnetic elements. Once a domain wall is established within the

trap it can be moved reproducibly between the ends, switching the direction of magnetisation within the centre region, at a much lower field than required by a single element where nucleation of the wall is necessary.

This work was further developed by Brownlie et al [11], where the structure shown in figure 5.5 was devised. The end shapes are designed to act as an energy barrier to the wall to confine it to the central wire. A domain wall can be created and moved in such a structure by use of a pair of orthogonal fields, one applied to the hard axis of the structure and then relaxed to zero to create the domain wall, and the other to the easy axis to move the wall between the ends of the wire. The geometry of the ends ensure that each region becomes oppositely magnetised as the magnetostatic energy is minimised when the magnetisation lies parallel to the edges.

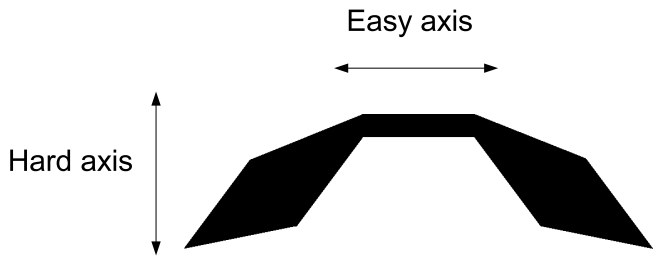

Figure 5.5: Schematic diagram of the geometry of the domain wall trap structure.

For this work, these structures have been modified slightly by increasing the length of the central wire, so as to allow enough space to include irradiated pinning sites at regular intervals along the wire. It was also necessary to characterise the behaviour of structures made by FIB, as e-beam lithography had been used for all previous fabrication [11]. All elements shown in this chapter have been patterned from 5nm Au/10nm NiFe/5nm Au films. This magnetic system was chosen for these experiments due to the comparatively low does of 3×10^{15} ions cm^{-2} that is required to render it non-magnetic (as discussed in chapter 3), as well as there being a reliable source of samples to allow the experiments to be carried out on a consistent set of samples. Again the structures have been patterned using the 10pA Ga^+ ion focused ion beam by the 'vectorfib' method described in chapter 2.5.

A domain wall trap structure created by irradiation with 3×10^{15} ions cm^{-2} is shown in figure 5.6. This dose is known to render the Au trilayer non-ferromagnetic, and as can be seen from the images was able to isolate the magnetic structure, which behaved independently of the surrounding film.

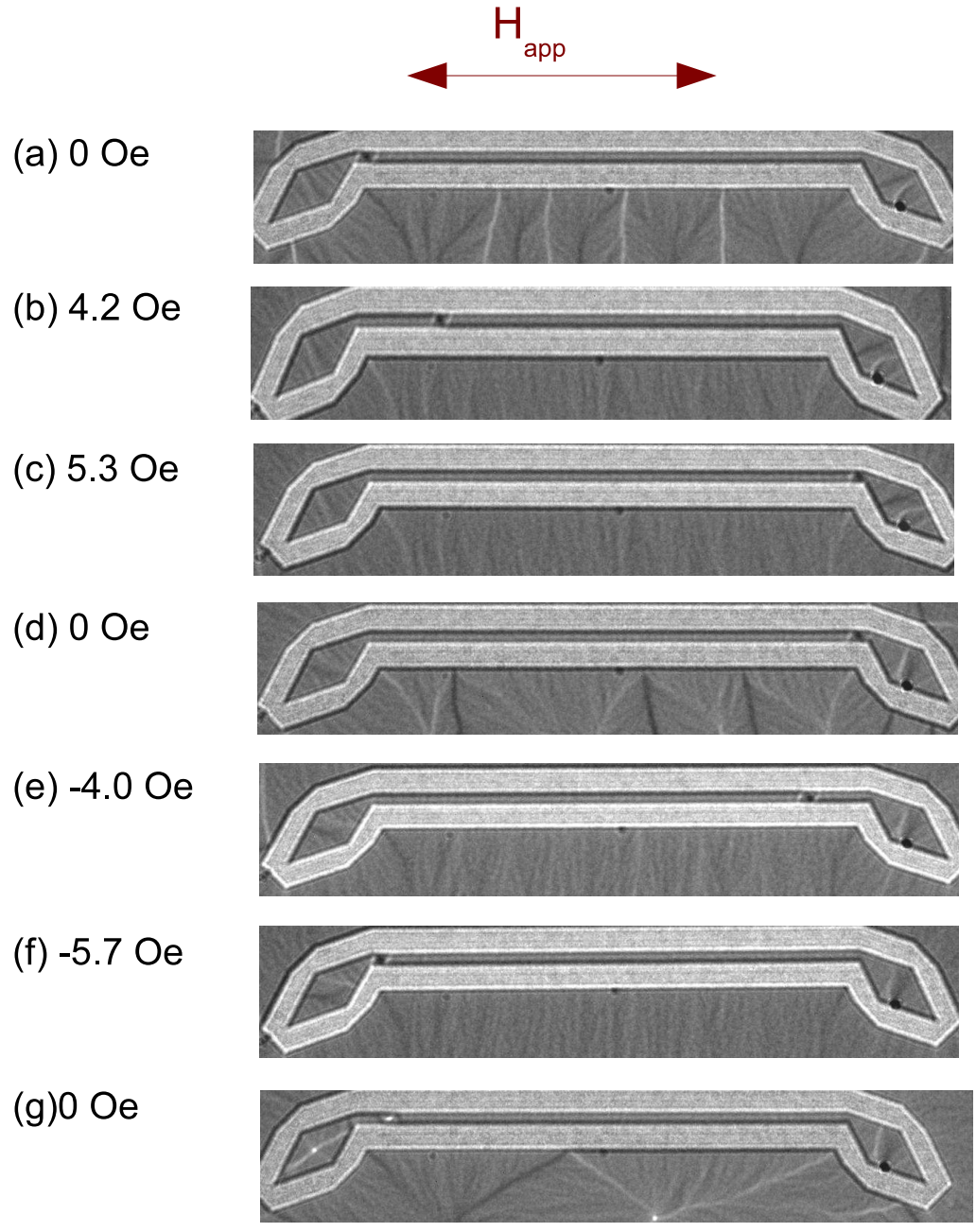

Figure 5.6: Images of domain wall trap patterned with 3×10^{15} ions cm^{-2} showing the motion of a vortex domain wall under the influence of magnetic field applied along the long axis of the wire.

Initially, a magnetic field was applied along the hard axis of the structure and on relaxing this field to zero, a vortex domain wall formed in the wire. The sample was then rotated through 90° in the TEM such that the magnetic field was aligned along the easy axis of the wire, indicated by the red arrow in figure 5.6. As can be seen in figure 5.6(b-c), the magnetic field was increased along the easy axis causing the domain wall to move from one end to the other. Contrast at the edges of the wires can be used as a reference for the direction of magnetisation in the wire. On applying a field in the opposite direction figure 5.6(d-f), the domain wall begins to move back in the original direction at -4 Oe and reaches the other end of the wire at -5.7 Oe.

On applying a hard axis field in the opposite direction a vortex domain wall with a white core was formed, as shown in figure 5.6(g). This could also be moved reproducibly between the ends of the wire by a field of 6 Oe.

5.2.1 Domain wall traps with irradiation induced pinning sites

5.2.1.1 Vertical irradiated pinning sites

Domain wall trap structures such as those presented in the previous section were again fabricated by a focused ion beam dose of 3×10^{15} ions cm^{-2}. This time single lines of 1×10^{15} ions cm^{-2} were patterned perpendicularly to the length of the wire, as depicted in the schematic in figure 5.7.

Note that the white circles in the images are markers at the top and bottom of the irradiated lines so that their position could easily be identified in the TEM. A vortex domain wall was set up in the wire by application of a large hard axis field, figure 5.7(b) and then moved along the wire by applying an easy axis field. It is clear to see that by a field value of -6.2 Oe, figure 5.7(c), the wall has moved along the wire unimpeded by two of the pinning sites. The magnitude of the applied field was further increased to -8.5 Oe (d) and the domain wall moved straight past the final pinning site with no interaction or pinning to complete the reversal of the wire.

Another set of wires were patterned on the same sample but with an increased dose used to pattern the perpendicular lines. The dose used was increased from 1×10^{15} ions cm^{-2} to 3×10^{15} ions cm^{-2} to see if the higher dose caused enough

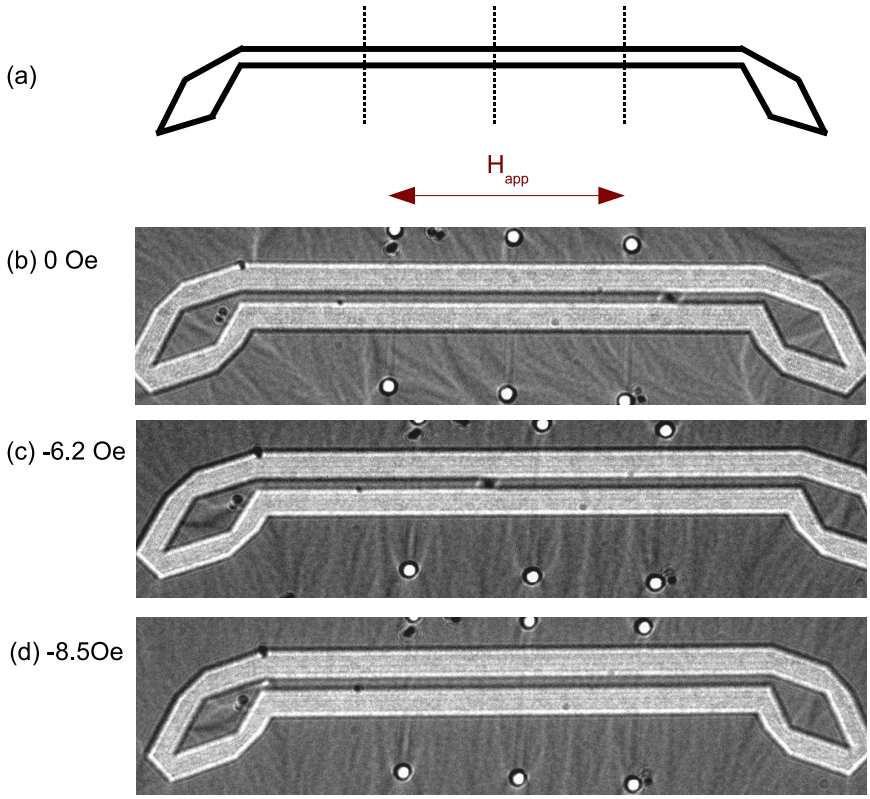

Figure 5.7: (a)Schematic diagram showing the position of the irradiated lines. (b-d)Reversal of domain wall trap structure with perpendicular lines irradiated at 1×10^{15} ions cm^{-2}

modification of that region of the wire to act as a pinning site. The reversal of this structure is shown in figure 5.8, along with schematic diagram indicating the magnetisation within the wire.

A hard axis field was applied and then relaxed to zero to form the vortex domain wall in the wire. The structure was then rotated through 90° to align the wire with the applied field, figure 5.8(a). The vortex domain wall remained at the end of the wire until a field of -8.6 Oe was applied, figure 5.8(b). At this point it began to propagate along the wire and was pinned at the first irradiated line that it encountered. It appears that the core of the domain wall packet has moved through the pinning site so that domain wall packet is pinned at the site. At -12Oe shown in figure 5.8(c), it can be seen that the domain wall packet has become slightly extended as the core tries to move along the wire while right hand side remains pinned at the irradiated line. A field of -14.7 Oe is required to depin the wall and complete the reversal of the wire (d).

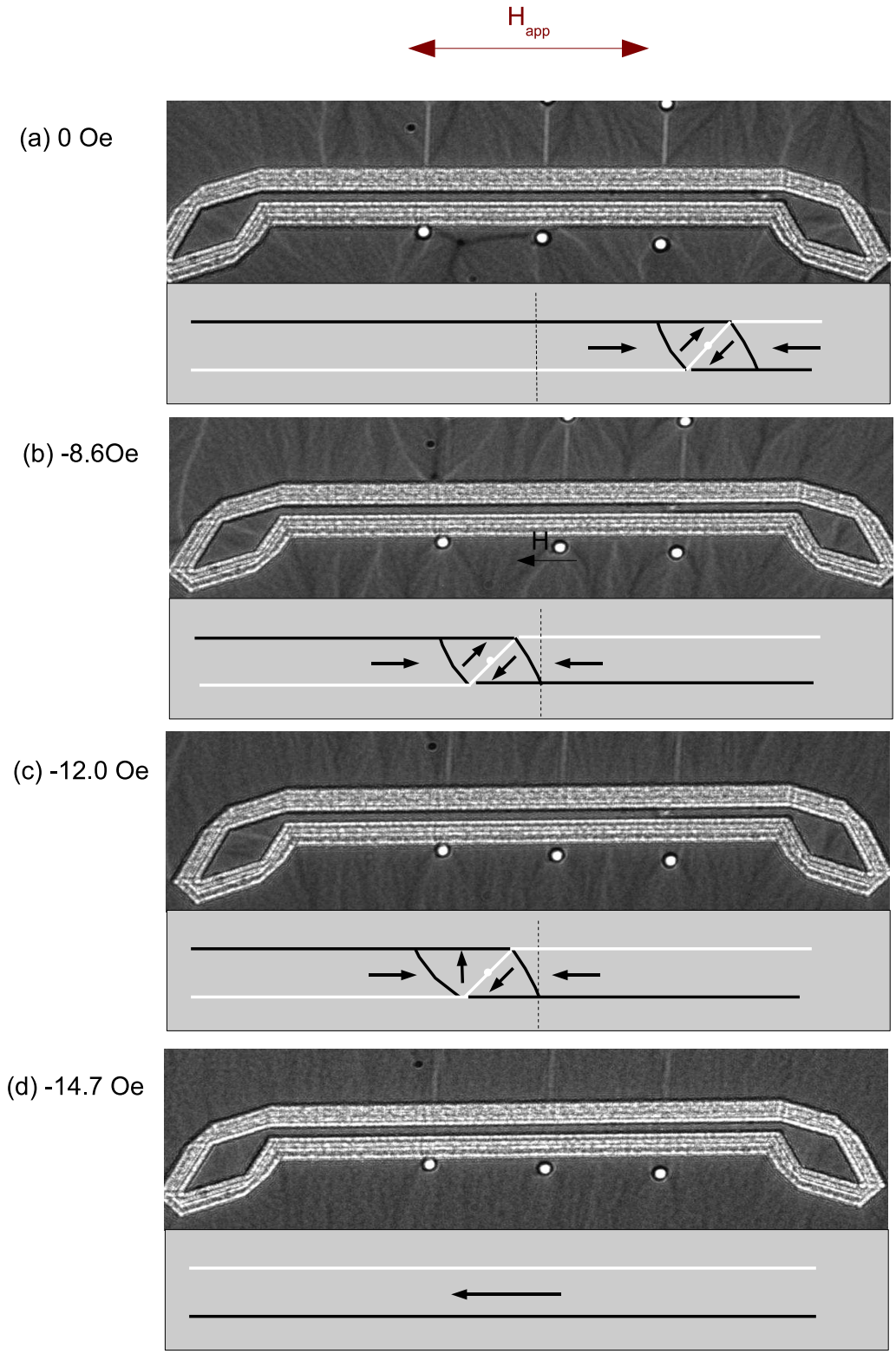

Figure 5.8: Reversal of domain wall trap structure with perpendicular lines irradiated at 3×10^{15} ions cm^{-2}. Schematic diagrams illustrate the domain wall structures.

5.2.1.2 Variation of the orientation of irradiated pinning sites

Pinning of vortex domain walls using a vertical irradiated line was shown to be successful, but effective pinning was sought at a lower dose. Therefore varying the orientation of the line rather than dose was considered as a means of overcoming this. It can be seen from the diagram in figure 5.9 that the central wall in a vortex domain wall is orientated at ∼45° to the horizontal of the wire. In the following experiments the angle of the irradiated line was changed to 45° as it may be more energetically favourable for the central section of the domain wall packet to pin at these sites.

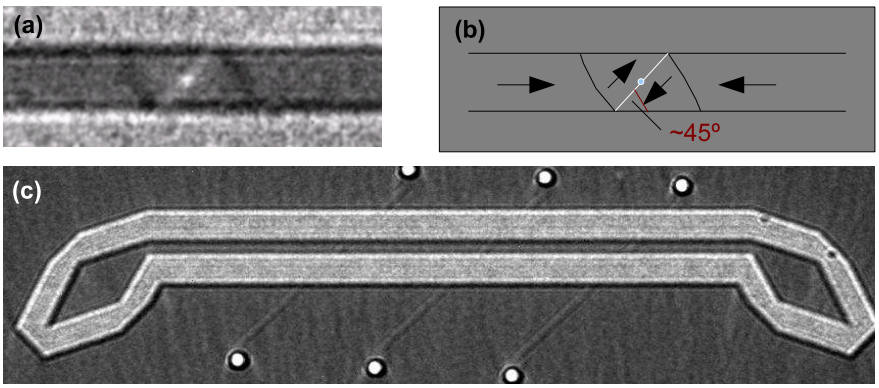

Figure 5.9: (a) Fresnel image showing the structure of a vortex domain wall in a wire, (b) Schematic diagram of a vortex domain wall with arrows indicating the direction of magnetisation and the 45° angle that the central line makes with the edge of the wire, and (c) a Fresnel image of a domain wall trap showing the position of three lines irradiated at an angle of 45° to the length of the wire.

Shown in figure 5.10 is a domain wall trap structure with 1×10^{15} ions cm^{-2} lines irradiated at 45°. It can be seen in figure 5.10(a) that a vortex with a white core was established in the wire. In figure 5.10(b) a field of 5.8 Oe has been applied along the wire, and the domain wall began to propagate along the wire. Without further increase in the applied field, the domain wall then moves to and is pinned at the first pinning site in the wire. It remains stable at this site, until at a field of 15.3 Oe, when a second domain wall is seen at the next pinning site, figure 5.10(d). This is a tail to tail domain wall with a black core and is injected into the wire due to the reversal of the other end of the wire. A field of 19 Oe is required to annihilate the two walls and reverse the magnetisation in the wire, figure 5.10(e).

This result has shown that a line irradiated at a similar angle to the core of a vortex domain wall was able to pin a vortex domain wall, whereas a vertical irradiated line of the same dose was not. The domain wall is also much more

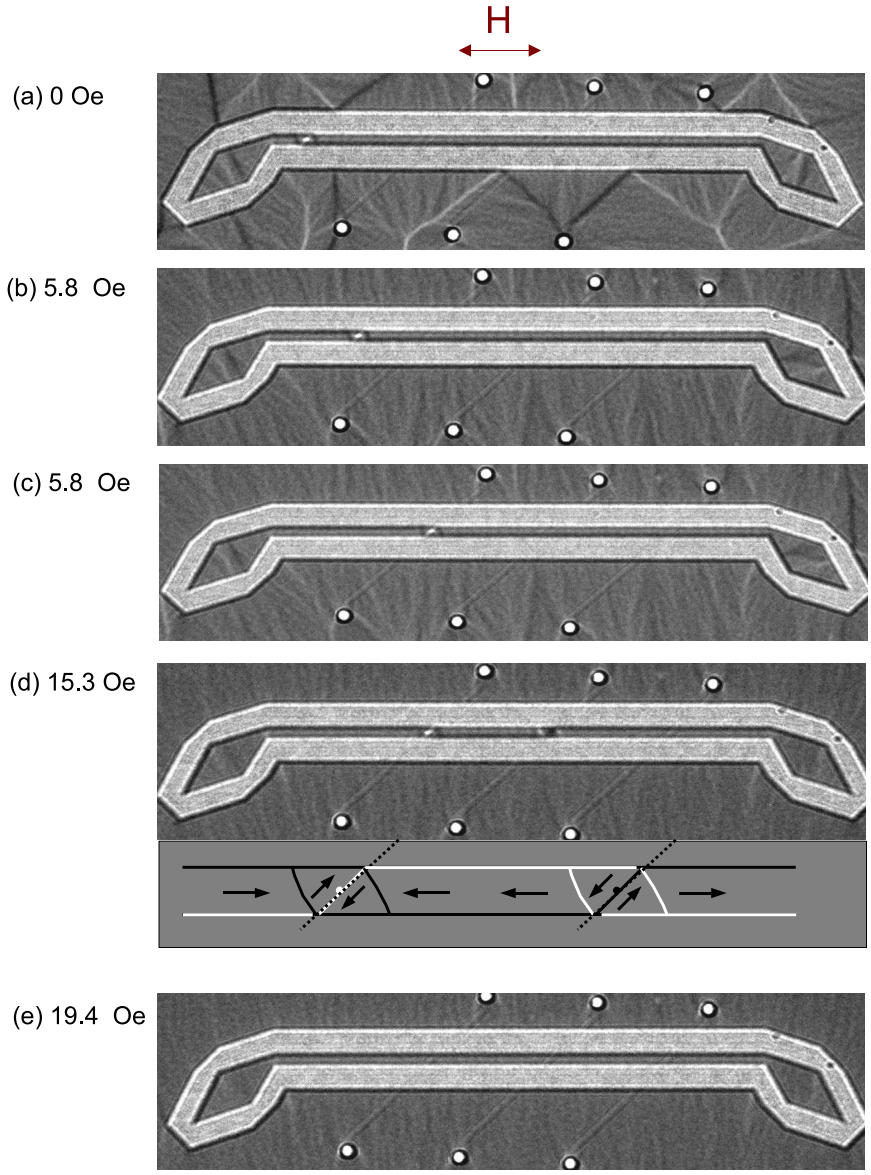

Figure 5.10: Reversal of domain wall trap structure with lines irradiated at 45° with a dose of $1{\times}10^{15}$ ions cm^{-2}

stable at this site and remains pinned at this site over a range of 15 Oe compared to 6 Oe for the vertical lines.

However, from the results shown above it is not clear whether or not the line has imposed on the structure of the domain walls which are pinned at it. In figure 5.10(c) we see a black vortex domain wall with counter clockwise rotation of magnetisation reverse the wire from the other end. From the magnetisation arrangement in the wire it is also possible that this wall could have had a white vortex with clock-wise rotation. This would mean that on arriving at the irradiated pinning site the domain wall transformed into one that fitted with the

pinning site.

However, if this was not the case, then it leaves a question regarding the interaction of a domain wall with an unfavourably aligned pinning site. There are many potential situations which could arise, as illustrated in the schematic in figure 5.11.

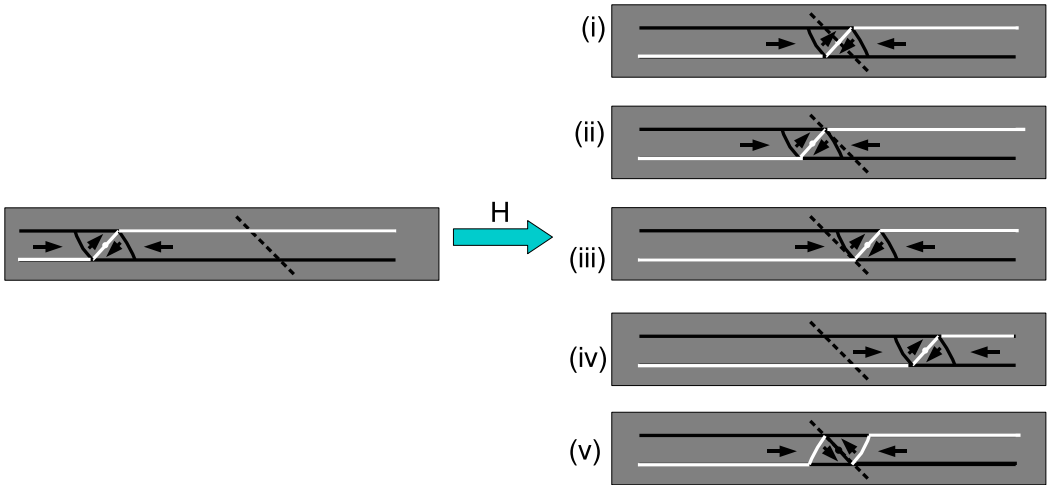

Figure 5.11: Schematic diagram illustrating the possible interactions of a domain wall and irradiation site with a symmetry mismatch.

It is possible that the domain wall could pin at the irradiated line with the centre of the domain wall packet centred on the line, or that it could pin at either side as was the situation with the vertical line. Another option shown in figure 5.11 (iv) is that the wall will simply pass through the pinning site unaffected. Figure 5.11(v) shows the transformation of the domain wall to fit with the irradiated region.

Investigations were then carried out to observe the interaction of domain walls with opposite chiralities with differently orientated irradiated pinning sites. To do this a greater degree of control over the chirality of the vortex domain wall created in the wire was required. Methods for achieving this are discussed in the following section.

5.3 Magnetic nano-wires with ellipse injection pads

In the domain wall trap structures described in the previous section, it is necessary to apply orthogonal fields in order to create and then move the domain wall. It is

possible to influence the type of wall that is formed by offsetting the applied field from the hard axis of the wire. This can be an awkward and time consuming process, as alignment with the field is always subject to a small error. Other investigations have shown that a degree of control over the chirality of the vortex wall can be obtained, by the addition of a large ellipse shape injection pad in which a vortex domain structure can be formed [24]. A bright field TEM image of such a structure is shown in figure 5.12(a). Application of a saturating field along the wire and relaxing it to zero caused a vortex state to be set up in the injection pad. The vortex cores observed in the pad can appear black or white depending on the sense of rotation of magnetisation around the core. Results of these experiments showed that in general when a black vortex was setup in the pad, a vortex domain wall with a black core was injected into the wire and pinned at a notch. A similar situation was observed for injection from a white vortex vortex, as shown in schematic in figure 5.12. The sense of rotation of the magnetisation around the vortex is dependant on the direction of magnetisation in the wire.

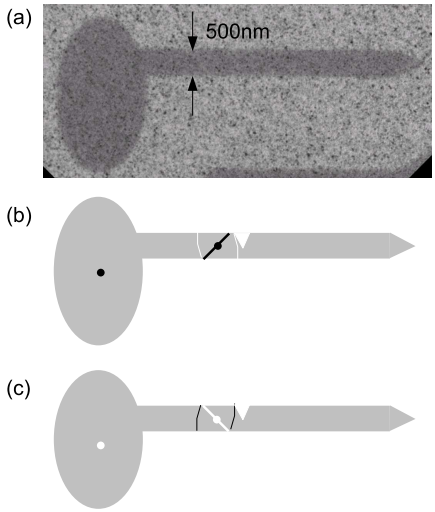

Figure 5.12: (a) Bright field image of a nanowire attached to a large ellipse shape injection pad, fabricated by FIB irradiation. (b,c) Schematic showing the domain walls pinned at a notch in a nanowire having been injected from ellipse injection pads supporting vortex domains of opposite chirality.

Simulations were carried out on wire with ellipse injection pads to observe the pinning behaviour when an irradiated region rather than a notch was used. As in chapter 4, the irradiated region was simulated by excluding it from the simulation, as shown in figure 5.?, essentially rendering that region of the structure non-magnetic. As previously stated, it was expected that a black vortex would inject a vortex domain wall with a black core and vice versa for a white vortex. However,

as can be seen in the simulations in figure 5.13 this is not necessarily the case when irradiated lines are used as the pinning sites. In figure 5.13(a) and (c) the magnetisation distributions calculated by OOMMF are shown for each vortex rotation, alongside the calculated Fresnel images (b) and (d).

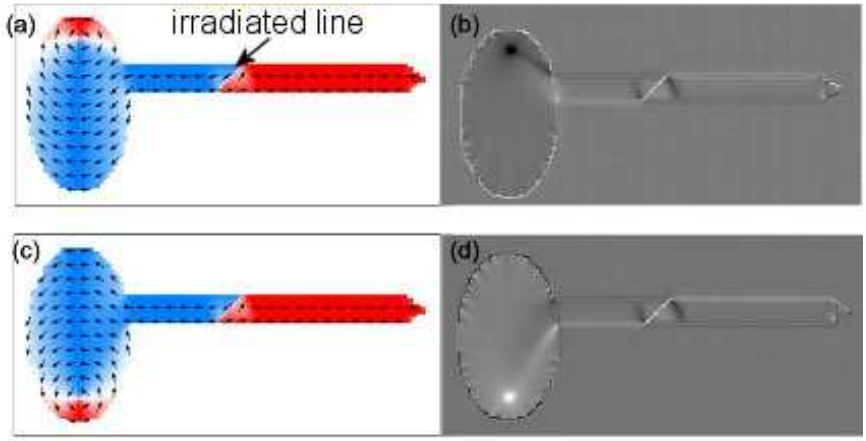

Figure 5.13: (a)+(c) OOMMF simulations showing the pinning of domain walls of the same chirality from opposite magnetic vortices. (b)+(d) corresponding Fresnel image simulations.

In 5.13 (a) a black core is seen in the injection pad whilst a vortex domain wall with a white core is pinned at the line. In figure 5.13(b) a white vortex core is observed in the injection pad and a domain wall with a black vortex core is seen pinned in the wire. This indicates that the simulated irradiated line has an influence on the structure of the incident domain wall.

To further investigate this, simulations were carried out using the same chirality of vortex but different orientations of the irradiated line. The resultant magnetisation configurations and simulated Fresnel images are shown in figure 5.14. A schematic diagram illustrating the origin of the different contrast is also shown. Both these simulations were seeded using the same magnetisation state, consisting of a counter clockwise vortex in the injection pad and the wire magnetised to the left. We would expect that in such an arrangement, both injection pads would inject the same chirality of vortex domain wall and we would therefore see two identical walls pinned at the lines. Again, this is not what is observed and domain walls of different chiralities are seen pinned at the differently orientated lines.

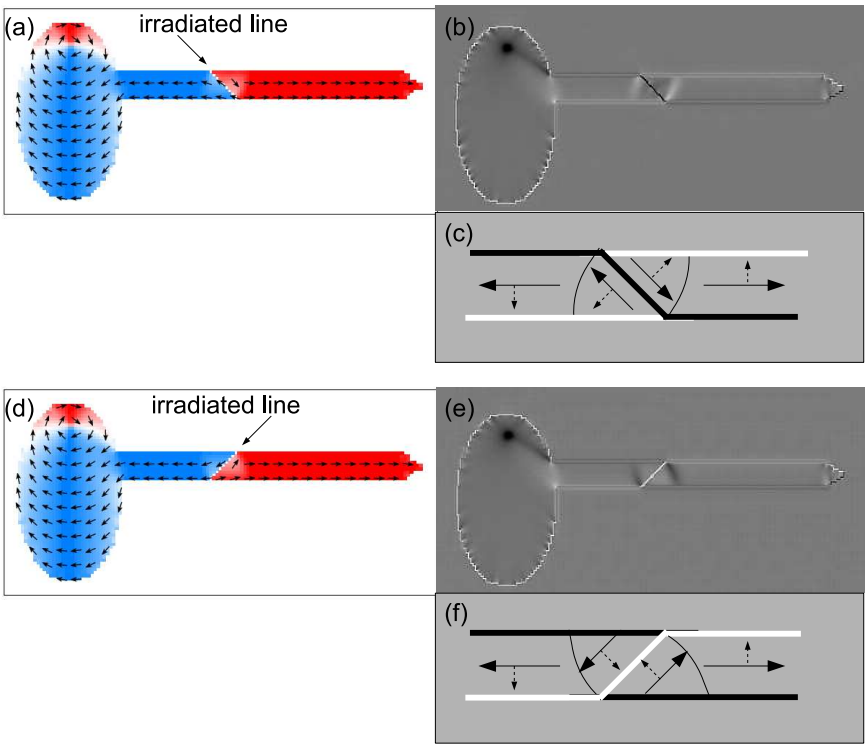

Figure 5.14: (a)+(d) OOMMF simulations showing pinning of domain walls at oppositely orientated pinning sites. (b)+(e) Corresponding Fresnel image calculations, with schematics showing the origin of the magnetic contrast shown in (c)+(f). The small dotted arrows in the schematic denotes the direction of the Lorentz deflection which causes the regions of increased and decreased intensity.

5.3.1 Experimental structures

Structures similar to those simulated in the previous section but with longer wires were patterned with a dose of 3×10^{15} ions cm^{-2}. This time irradiated lines were patterned at a dose of 1×10^{15} ions cm^{-2} at angles of $\pm45°$ to the length of the wire.

Initally a white vortex was set up, and the different situations observed are shown. Figure 5.15 shows the injection of a domain wall from a white vortex into a wire with irradiated lines at $+45°$. At zero field, the vortex in the injection pad is slightly higher than the centre of the pad. As the magnitude of the applied field is increased the vortex moves towards the bottom of the pad. A domain wall with a white core is injected into the wire at a field of 13.2 Oe and pins at the irradiated line. A field of 23.3 Oe is required to depin the wall from the wire and reverse the remainder of the wire, which is less than the field necessary to expel the vortex from the injection pad.

The field was again relaxed to zero, as shown in figure 5.16(a), and a field applied

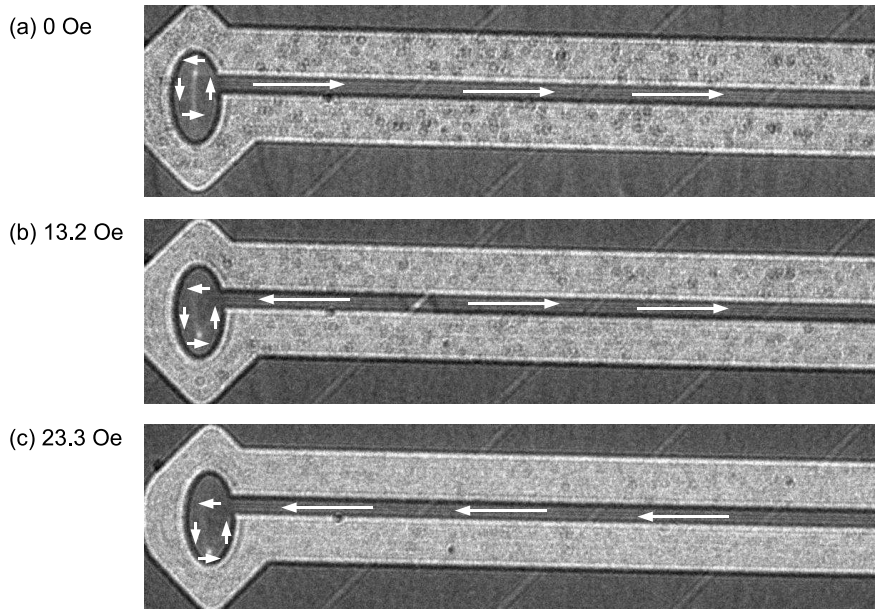

Figure 5.15: Fresnel image sequence of the injection of a domain wall from a white vortex state into a magnetic wire with 1×10^{15} lines at $+45°$. The wire is initially magnetised to the right.

in the opposite direction. A domain wall was injected at -8.8 Oe and passed through the first two irradiated lines and pinned at the third line. The wall then depinned from the site at -14.7 Oe.

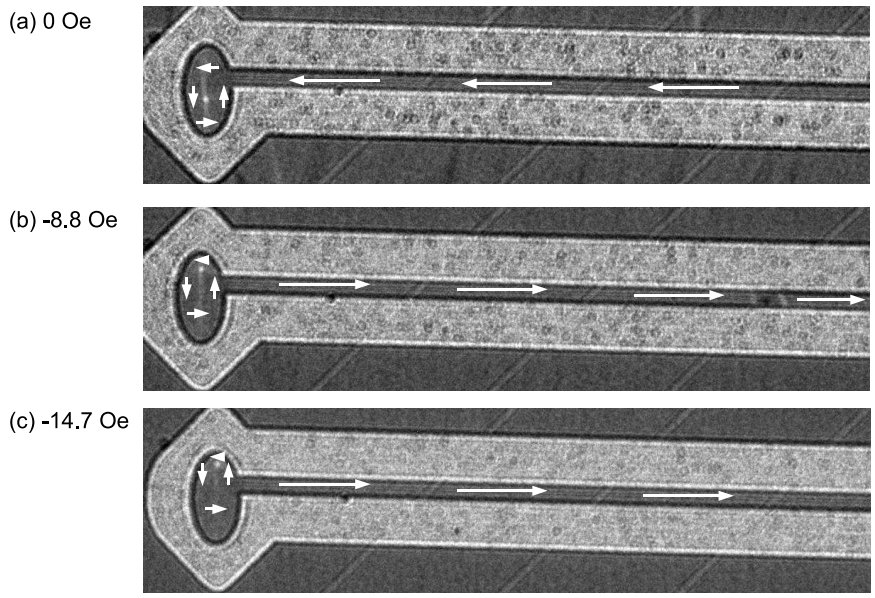

Figure 5.16: Injection of a domain wall from a white vortex state into a magnetic wire with 1×10^{15} lines at $+45°$. The wire is initially magnetised to the left.

In figure 5.17, the same procedure as outlined above was carried out on a structure with the irradiated line orientated at-45°. The injection field is found to be 11.8 Oe when a domain wall with a black core was injected and pinned in the wire.

This time the wire began to reverse from the other end and a second domain wall is pinned at the third pinning site. At 20.5 Oe the walls annihilate and the wire is reversed.

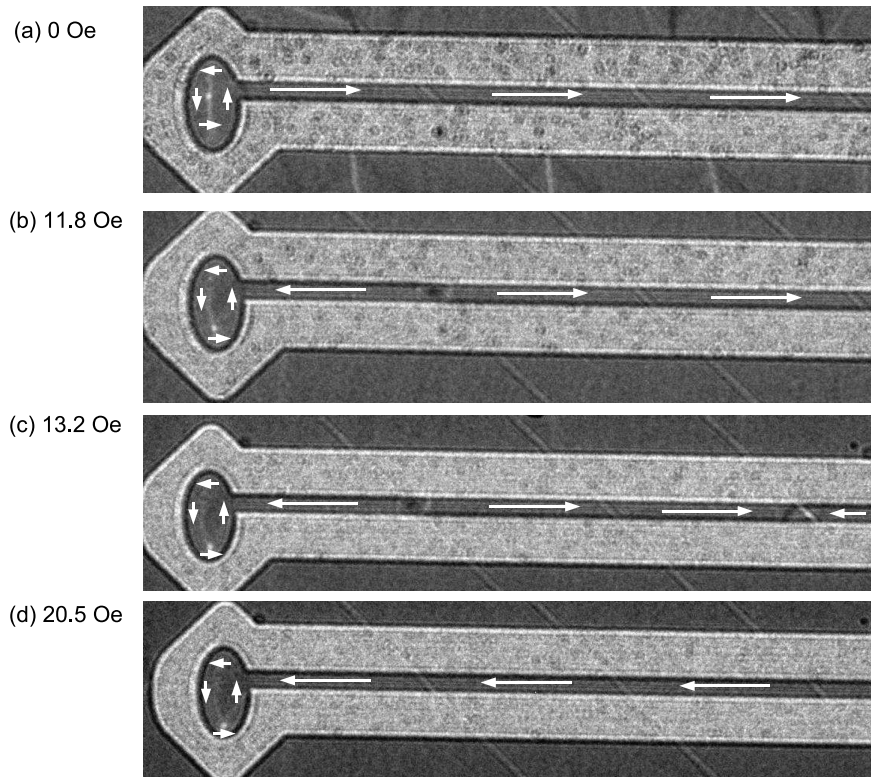

Figure 5.17: Injection of a domain wall from a white vortex state into a magnetic wire with 1×10^{15} lines at -45°.

Following this the structures were saturated to drive the white vortex out of the injection pad. On relaxing the field to zero a black vortex was formed in the injection pads of the structures. Figure 5.18 shows the reversal of a wire structure in this magnetic state with lines irradiated at -45°. Again the vortex sits just off centre of the ellipse pad, and with the application of a magnetic field, is driven towards the bottom of the pad. At -4.4 Oe a domain wall is injected into the wire. Unlike the other results presented so far, this wall depins at a field of -10.3 Oe and then gets pinned a second time at the next irradiated line. The wall is finally depinned and the wire is completely reversed at -14.6 Oe.

In figure 5.19 and 5.20, the wire structure has lines irradiated with a dose of 1×10^{15} ions cm^{-2} at +45°. Figure 5.19 (a-c) shows the outward cycle from 0 to -14.6 Oe. A black vortex wall is injected and pinned at -5.8 Oe and depinned at -14.6 Oe.

The final reversal sequence shows the return cycle following figure 5.20. Here a

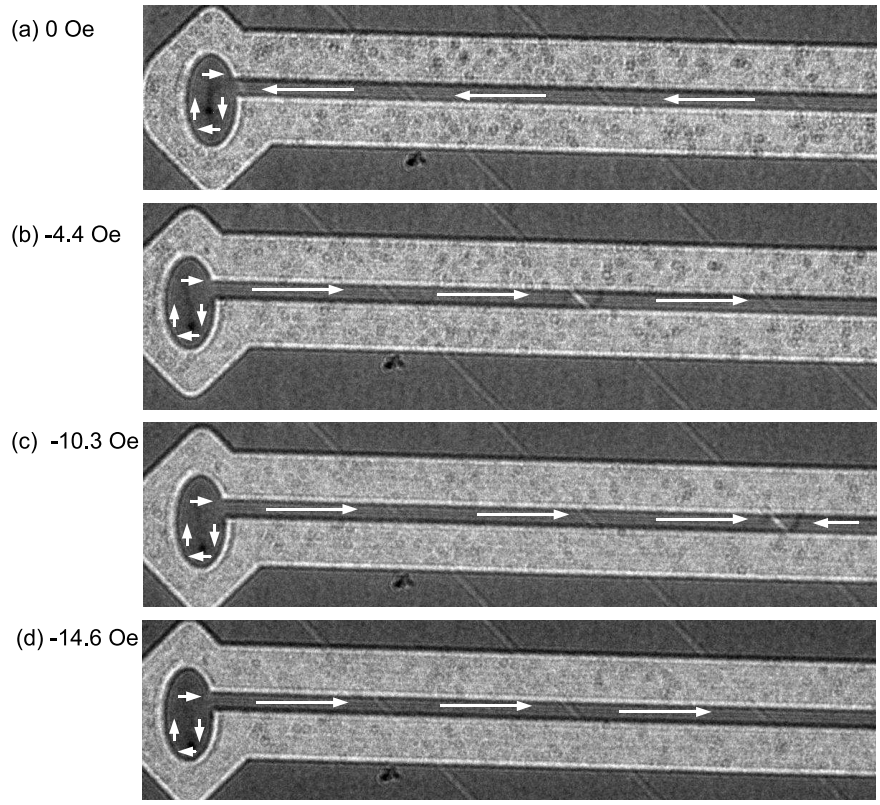

Figure 5.18: Injection of a domain wall from a black vortex state into a magnetic wire with 1×10^{15} lines at -45°. The wire is initially magnetised to the left.

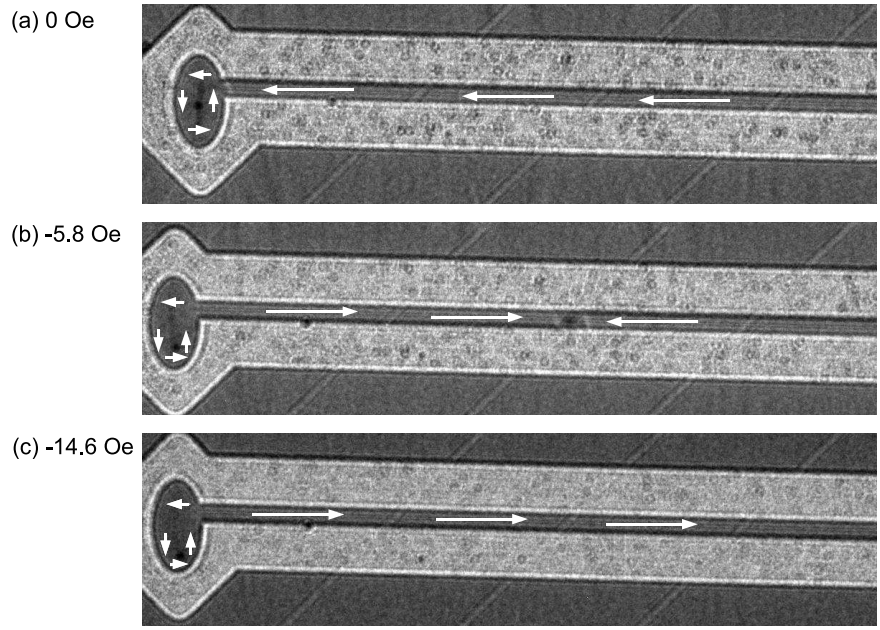

Figure 5.19: Injection of a domain wall from a white vortex state into a magnetic wire with 1×10^{15} lines at +45°. The wire is initially magnetised to the left.

white vortex domain wall is injected into the wire at 14.6 Oe (b), where it pins at the final irradiated line. A field of 20.5 Oe is required to depin the wall and

reverse the wire.

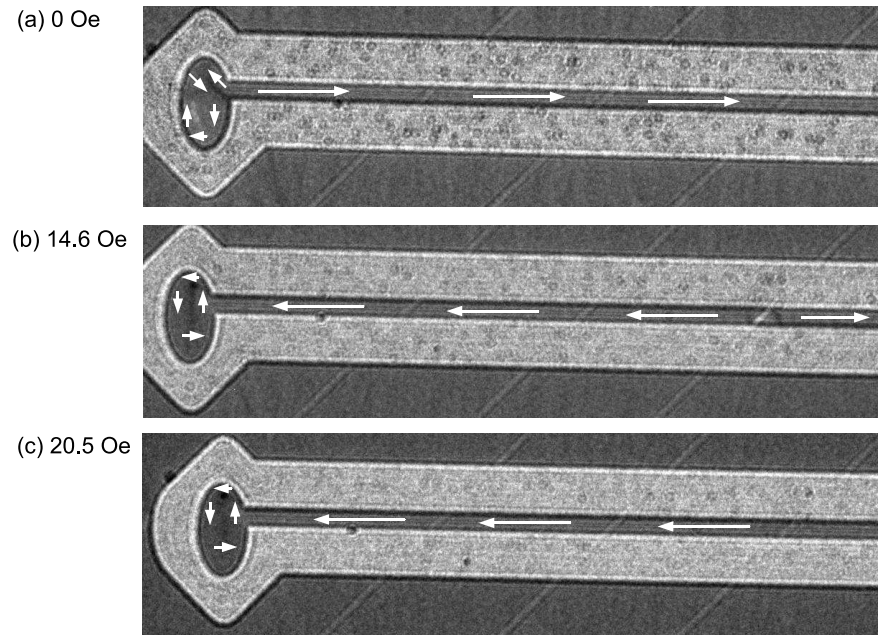

Figure 5.20: Injection of a domain wall from a white vortex state into a magnetic wire with 1×10^{15} lines at +45°. The wire is initially magnetised to the right.

During these experiments two possible configurations were not seen, namely a white vortex injecting a white vortex domain wall into a -45° pinning site and a black vortex injecting a black vortex domain into a -45° pinning site. However, there is no reason why these states should not occur and it is likely due to an oversight when considering the possible number of configurations that these were not recorded during the experiment. It should be noted that in more than 20 observations of the reversals of these wires, there were only 4 occurences of the domain wall sweeping through the wire without being pinned at one of the pinning sites.

5.4 Discussion

The magnetic behaviour of domain wall traps made in permalloy by FIB is very similar to those made by e-beam lithography, in that it is possible to set up a domain wall and then reproducibly move it between the ends of the structures. The main difference is that the propagation fields of the walls are much lower than in these experiments, less than 10 Oe in both cases compared to several 10's Oe in the e-beam structures [11]. However, the thin film systems investigated

in each case are not identical, with the irradiated samples having the additional non-magnetic layer. For a direct comparison of propagation fields and other properties of the wire it would be necessary to replicate identical patterns by the two methods on samples with the same composition which are deposited at the same time. However, the observed trend is consistent with predictions that nanoscale wires made by FIB patterning may have lower propagation fields. This is thought to be due to irradiation induced changes at the edges of the wires by the tails of the ion beam as patterning is carried out. In permalloy, irradiation can weaken the moment and change the coercivity, which could aid the propagation of domain walls along the wire. It is likely that the effective smoothing of the wire due to patterning by irradiation will also have an effect on the propagation field.

The inclusion of irradiated lines along the length of the wires allowed domain walls to be pinned at predefined locations. The dose required to do this varied with the orientation of the lines with respect to the length of the wire. When vertical lines were patterned, domain walls in the wire were only pinned when the dose was 3×10^{15} ions cm^{-2} or greater. It is expected that this dose would pin the domain wall as it is capable of rendering the system non-ferromagnetic. When the line was patterned at an angle similar to that of the core of a vortex domain wall, the dose required to pin the domain wall was 1×10^{15} ions cm^{-2}. This shows that varying the angle of the irradiated line causes a change in the energy landscape for the domain wall. It appears to be more energetically favourable for the domain wall to pin at a site which relates to the magnetisation distribution of the domain wall. It was also seen that the domain wall which pinned at the angled site, remained pinned over a larger field than the wall pinned at the vertical site. This was even in spite of the vertical site having been created with a heavier dose which will have caused increased modification of the properties of the wire.

Following from this, it was postulated that if the vortex domain wall met with an irradiated line orientated in the opposite direction to the core of the domain wall, the symmetry mismatch would mean that it would either not pin at the site at all or that it would not be as stable. However, this was not observed in any of the experiments carried out. Each time a domain wall was pinned at an irradiated site the direction of the vortex core matched the direction of the irradiated line, regardless of the original chirality of the incoming wall. This strongly suggests that in order to reach an energy minimum the magnetisation in the domain wall will rotate to align with the irradiated line. The dose used to pattern the lines

is not sufficient to render the line non-magnetic, but does cause a reduction in magnetic moment. The central wall of the domain wall packet has the highest energy of the packet, as it is a 180° wall. The irradiated pinning sites have lower moment and hence sit in a lower energy state, and so it is going to be energetically favourable for the central wall to align with the site to lower its energy.

The reliability and reproducibility of this result presents a novel method for creating domain walls of known chirality at predefined locations. This could have direct applications in the field of spintronics, and in particular in race track memory proposed by Parkin et al [6], where a method of controlling the position of domain walls in the system is required.

Bibliography

[1] C. H. Marrows, Adv. Phys. **54**, 585 (2005).

[2] D. A. Allwood, G. Xiong, and R. P. Cowburn, Appl. Phys. Lett. **85**, 2848 (2004).

[3] D. A. Allwood, G. Xiong, and R. P. Cowburn, Appl. Phys. Lett. **89**, 102504 (2006).

[4] G. Xiong, D. A. Allwod, M. D. Cooke, and R. P. Cowburn, Appl. Phys. Lett. **79**, 3461 (2001).

[5] S. S. P. Parkin, United States Patent **6834005** (2004).

[6] S. S. P. Parkin, Int. J. Mod. Phys. B **01**, 117 (2008).

[7] L. Thomas, C. Rettner, M. Hayashi, A. Doran, and A. Scholl, Appl. Phys. Lett. **87**, 262501 (2005).

[8] D. Atkinson *et al.*, Nat. Mater. **2**, 85 (2003).

[9] A. Yamaguchi *et al.*, J. Magn. Magn. Mat **92**, 077205 (2004).

[10] R. D. McMichael, J. Eicke, M. J. Donahue, and D. G. Porter, J. Appl. Phys. **87**, 7058 (2000).

[11] C. Brownlie, S. McVitie, J. N. Chapman, and C. D. W. Wilknson, J. Appl. Phys. **100**, 033902 (2006).

[12] M. Laufenberg *et al.*, Appl. Phys. Lett. **88**, 052507 (2006).

[13] Y. Nakatani, A. Thiaville, and J. Miltat, J. Mag. Mag. Mat **290**, 750 (2005).

[14] V. K. Dugaev *et al.*, Phys. Rev. B **74**, 054403 (2006).

[15] L. Gan, S. H. Chung, K. H. Aschenbach, M. Dreyer, and R. D. Gomez, IEEE Trans. Mag. **36**, 3047 (2000).

[16] M. Hayashi *et al.*, Phys. Rev. Lett. **96**, 197207 (2006).

[17] E. B. Myers, D. C. Ralph, J. A. Katine, R. N. Louie, and R. A. Buhrman, Science **285**, 867 (1999).

[18] D. Petit, A. Jausovec, D. Read, and R. P. Cowburn, J. Appl. Phys **103**, 114307 (2008).

[19] C. Sandweg *et al.*, J. Appl. Phys. **103**, 093906 (2008).

[20] M. Klaui *et al.*, Appl. Phys. **87**, 102509 (2005).

[21] Y. Labaye, L. berger, and J. M. D. Coey, J. Appl. Phys. **91**, 5341 (2002).

[22] I. V. Roshchin, J. Yu, A. D. Kent, G. W. Stupian, and M. S. Leung, IEEE Trans. Mag. **37**, 2101 (2001).

[23] C. C. Faulkner *et al.*, J. Appl. Phys. **95**, 6717 (2004).

[24] D. McGrouther, S. McVitie, and J. N. Chapman, Appl. Phys. Lett. **91**, 022506 (2007).

Chapter 6

Ion irradiation of perpendicularly magnetised Co/Pd multilayers

6.1 Introduction

In this chapter the effect of ion irradiation on perpendicularly magnetised Co/Pd films is investigated. Results of previous investigations have shown that the properties of Co/Pd and Co/Pt multilayers, also with perpendicular magnetic anisotropy, can be easily manipulated by ion irradiation and that patterning purely by modification of magnetic properties can be achieved [1, 2]. On irradiation of a perpendicularly magnetised thin film system, the magnetisation in the film undergoes a transition from perpendicular to in-plane and at sufficiently high doses can be rendered non-magnetic [3]. The origin of the reduction in perpendicular magnetic anisotropy is thought to be due to interfacial mixing across the layers [4]. Magnetic patterning of perpendicularly magnetised films can be carried out by either rendering chosen areas of the film non-magnetic leaving isolated magnetic elements, similar to the patterning method used in the previous chapters of this thesis, or by irradiating with a lower dose to create regions with an in-plane component of magnetisation surrounded by perpendicularly magnetised film.

However, in spite of the extent of previous investigations carried out, one aspect of the perpendicular to in-plane transition has not been fully understood. To date there have been no investigations to clarify whether the magnetisation rotates gradually from out of plane to in plane with increasing dose or whether it happens

in a single step at a critical dose.

6.2 Co/Pd multilayer system

The material investigated here is a Co/Pd multilayer sample, the layer structure of which is shown in figure 6.1. These films were deposited by Dr. Justin Shaw at NIST, USA, who also supplied the out of plane hysteresis loop shown in figure 6.2. From this loop it can be seen that the system has a switching field of between 600 and 700 Oe.

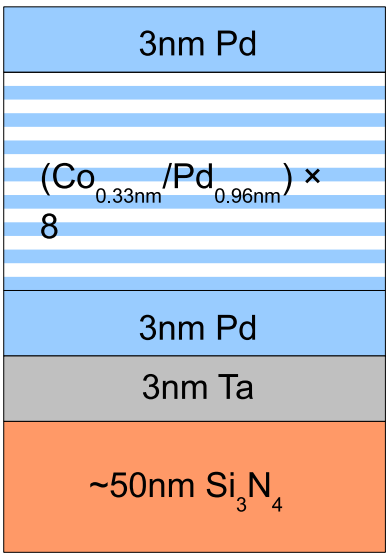

Figure 6.1: Schematic representation of the layer structure of the Co/Pd multilayer.

It has been reported that at a dose of 5×10^{12} ions cm^{-2}, Co/Pt films experience a reduction in coercivity [3]. Between a dose of 5×10^{12} and 1×10^{13} ions cm^{-2}, the magnetisation experiences a transition from perpendicular to in-plane orientation and finally at 1×10^{15} ions cm^{-2} is rendered paramagnetic. It has also been shown that patterning of both Co/Pt and Co/Pd films can be achieved by irradiating regions of the film such that perpendicularly magnetised regions are separated by those with in-plane magnetisation [5, 6, 7].

In order to investigate the effects of irradiation on the magnetism of Co/Pd multilayers, a simple grid pattern, such as that described in [5], was used, and is shown in figure 6.3. The lines of the grid are irradiated, whilst the squares of the grid are unchanged. Based on the results detailed above the grid lines were irradiated with a range of doses from 1×10^{13} to 3×10^{15} ions cm^{-2}, to allow

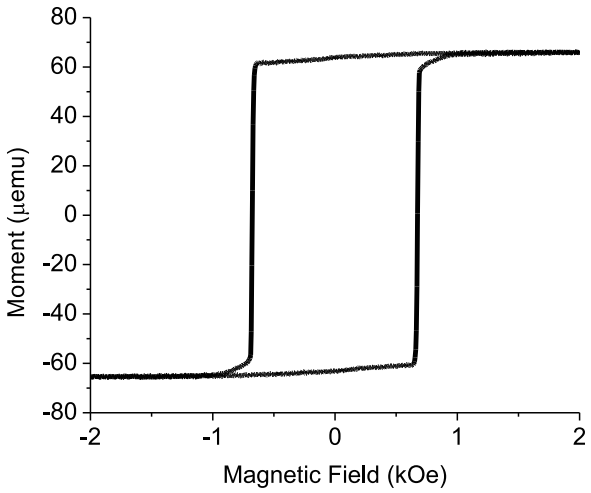

Figure 6.2: Out of plane hysteresis loop for Co/Pd

patterns with potentially varying in-plane magnetisation in the lines to be studied.

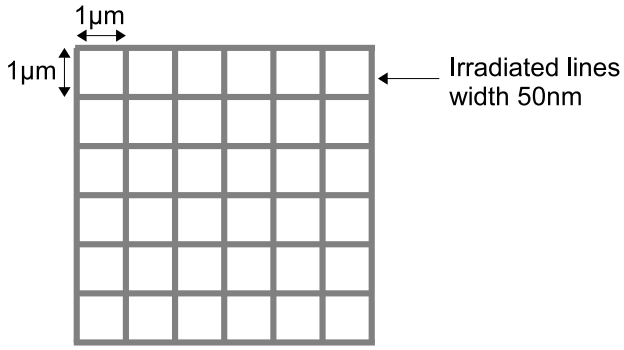

Figure 6.3: Schematic representation of the grids irradiated on Co/Pd samples.

The in-plane and out of plane magnetisation can be controlled independently by use of appropriate fields as described in [5] to create a range of magnetic configurations in the sample. The technique used for investigating the magnetisation in the irradiated grid patterns is described in the following sections.

6.3 Geometry of magnetisation in irradiated lines

Differential phase contrast microscopy can be used to map the integrated magnetic induction of a sample. Using this technique it should be possible to detect differences in magnetisation induced by the irradiation. These changes could be a result of a change in the angle of magnetisation with respect to perpendicular as the magnetisation rotates to in-plane orientation or due to an altered magnetic moment in the irradiated region.

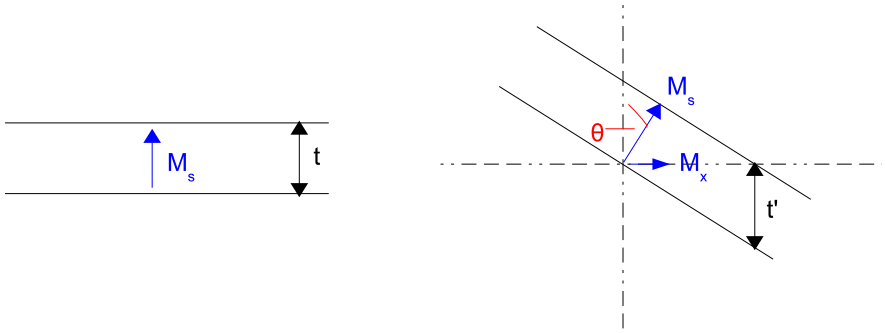

Figure 6.4: (a) Schematic showing a piece of perpendicularly magnetised material of thickness,t, at 0°, and (b) at an angle φ.

In order to determine if there is a change in magnetic direction or moment, we first consider the situation illustrated in figure 6.4(a), where we have a piece of material with perpendicular magnetic anisotropy. Here the integrated induction, B, is given by

$$\int_0^t B dx = \mu_0 M_s t \tag{6.1}$$

where M_s is the saturation magnetisation, and t is the thickness of the sample. When the sample is tilted through an angle θ, figure 6.4 (b), the component of magnetisation in the x direction becomes

$$M_x = M_s sin\theta \tag{6.2}$$

and the thickness through which the electron now has to travel is

$$t' = \frac{t}{cos\theta}. \tag{6.3}$$

This means that the integrated induction in the x-direction is now given by

$$\int_0^t B_x dx = \mu_0 M_x t' = \mu_0 M_s t.tan\theta. \tag{6.4}$$

We now consider the integrated induction in the sample subsequent to irradiation. We assume that the magnetisation is no longer orientated out of plane, but is at an angle φ to the normal. There are many different variables to consider such as the angle of magnetisation from the normal, the sample tilt, and the magnitude of the magnetic moment. For consistency any clockwise rotation or tilt from the normal of the sample is taken as positive, and counter clockwise rotation is taken as negative. Possible combinations of magnetisation direction and sample tilt are shown in figure 6.5.

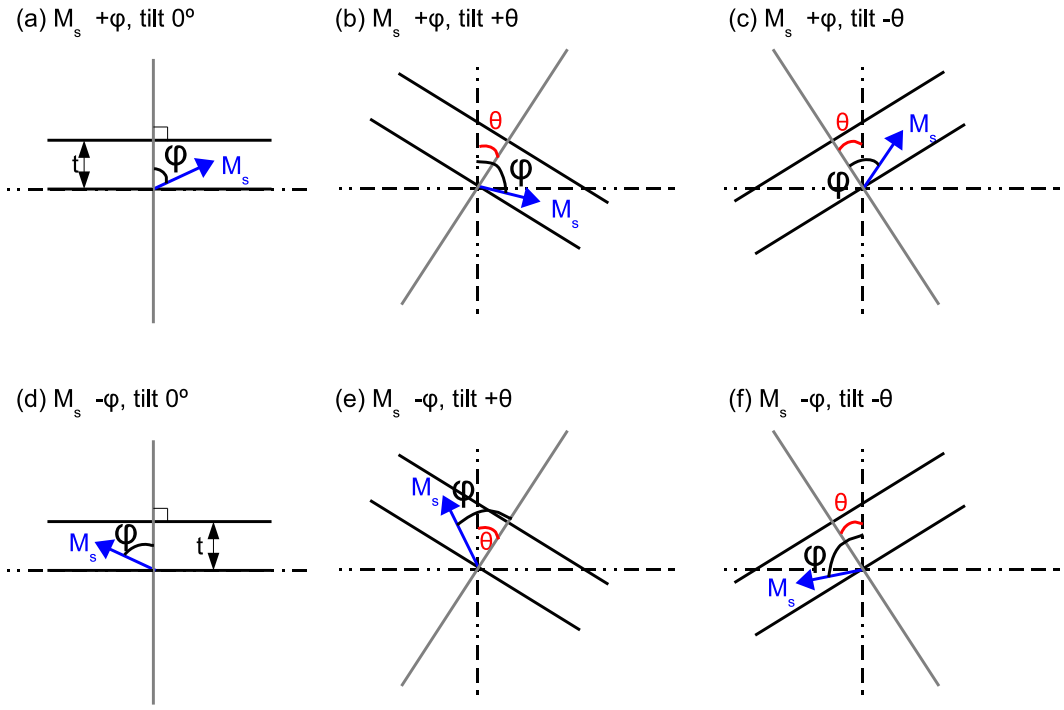

Figure 6.5: Schematic diagram showing magnetisation at an angle φ to perpendicular. (a-c) show the magnetisation at an angle $+\varphi$ with the sample tilt at 0, $\pm\theta$ and (d-f) show the magnetisation at an angle $+\varphi$ with the sample tilt at 0, $\pm\theta$. All angles measured clockwise from normal are assigned positive values, whilst counter clockwise angles are taken as negative.

As is clearly illustrated in the diagram, each of these situations will result in a different value of magnetic induction in the plane of the sample. It can now be seen that when magnetisation in the sample is tilted away from perpendicular through an angle φ, and the sample is tilted through an angle θ, the component

of magnetic induction in the x-direction becomes

$$B_x = \mu_0 M_s t \frac{sin(\theta + \varphi)}{cos\theta}. \tag{6.5}$$

If irradiation had caused the magnetisation to be rendered completely in plane, φ=±90°. To account for the possible change in magnetic moment due to irradiation we denote magnetisation in the modified line as M_L to distinguish it from the original magnetisation. This means equation 6.5 above is re-written as

$$B_x = \mu_0 M_L t \frac{sin(\theta + \varphi)}{cos\theta}. \tag{6.6}$$

By comparison of signals from known magnetic configurations, at known sample tilt θ it should be possible to extract information on M_L and φ for the sample.

6.4 Simulations of magnetic configurations in irradiated Co/Pd films

Simulations provide a useful guide to the signal variations that can be expected from DPC experiments from a known magnetic configuration. In this section simulations of grids with perpendicular magnetisation in the squares and lines of zero moment, perpendicular magnetisation and in-plane magnetisation are shown. At this point we assume that the magnitude of magnetic moment in the lines has not been altered.

6.4.1 Zero moment in irradiated lines

Simulations of integrated magnetic induction have been carried out using the method outlined in chapter 2.6.4. Shown in figure 6.6(a) is a schematic of the magnetisation in a sample with perpendicularly aligned squares and lines that are non-magnetic. Magnetic induction maps have been calculated at a sample tilt of $\theta = \pm 30°$, figure 6.6(b,d) and the intensity profiles averaged across the area in the box are shown, 6.6(c,e). The selected region goes from one perpendicularly magnetised square to another, across the non-magnetic region. The signal of interest is the difference signal between the non-magnetic line and the perpendicularly magnetised square. The size of signal between the perpendicular

and non-magnetic areas has a value of 5.72×10^{-9} Tnm, which is equivalent to $\mu_0 Mst\ \tan\theta$ (equation 6.4) for the sample. The relative magnitude of integrated induction is shown to be equal for both directions that the sample is tilted.

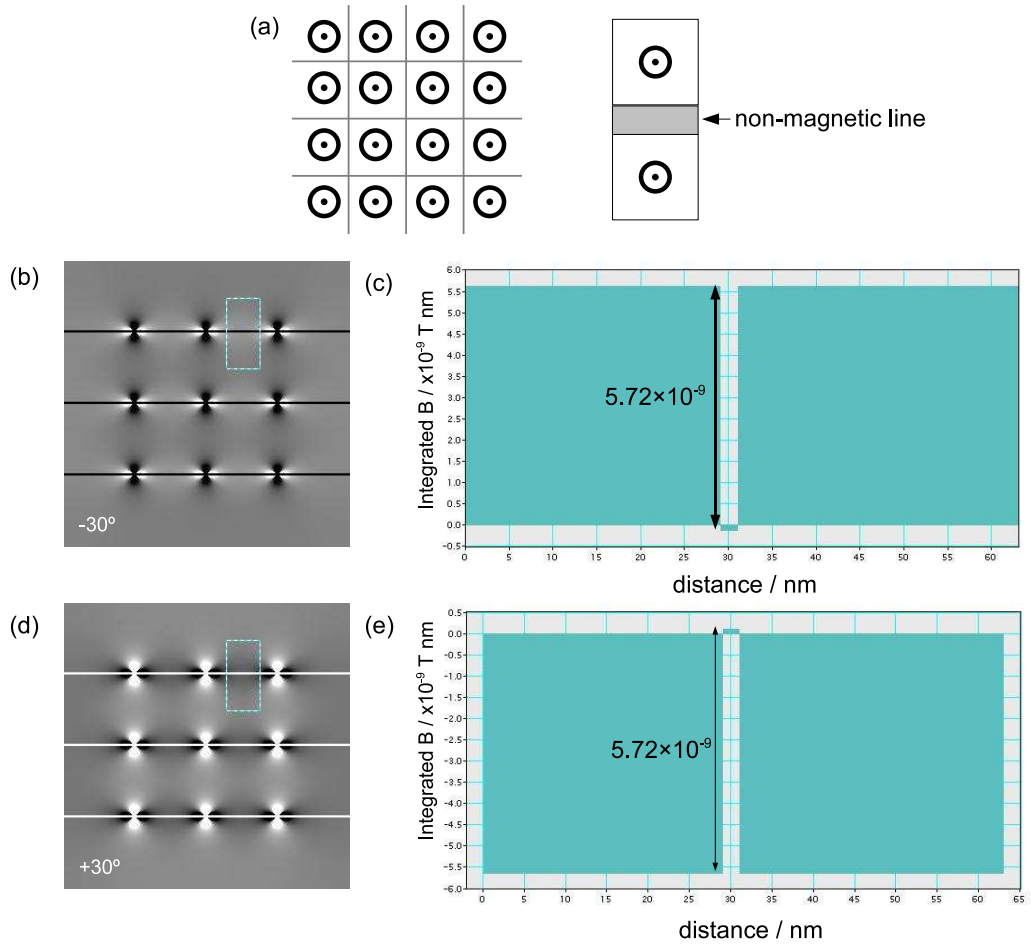

Figure 6.6: (a) Schematic diagram showing the patterned grid with perpendicularly aligned squares and non-magnetic lines. Simulated integrated induction in sample and corresponding intensity profile for this state at (b,c) -30° and (d,e) +30°.

Figure 6.7 also has no magnetisation component in the lines, as illustrated in the schematic in figure 6.7(a), but has alternately aligned perpendicular magnetisation in the squares. The magnetic induction has been calculated at a sample tilt of θ=±30°. The intensity profiles are taken across two alternately aligned perpendicularly squares and the non-magnetic region in between. These profiles show different characteristics to those where the perpendicular magnetisation is uniform, i.e. there is a variation in intensity over what is a uniform region of magnetisation. This is due to the effect of stray fields from neighbouring squares. The stray fields make accurate measurements of the difference signal harder, hence the θ=±30° signals vary slightly when we would expect them to be the same. However, it is a very small change, from 1.062×10^{-8} to 1.088×10^{-8}Tnm. We can

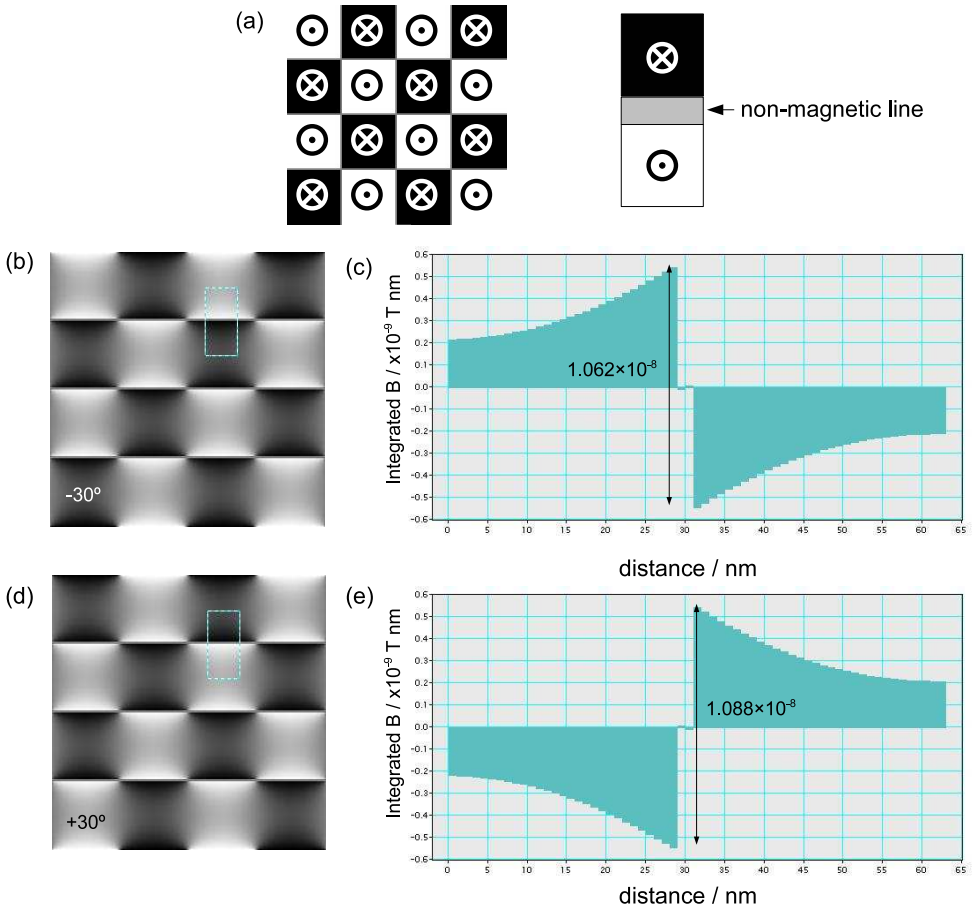

Figure 6.7: (a) Schematic diagram showing the patterned grid with alternating perpendicular magnetisation in the squares and non-magnetic lines. Simulated integrated induction in sample and corresponding intensity profile for this state at (b,c) -30° and (d,e) +30°.

see that it is approximately twice that for situation described in figure 6.6, of 5.72×10^{-9}Tnm. This is as we would expect as the signal now goes from $+M_s t \tan\theta$ to $-M_s t \tan\theta$, and therefore provides a measure of $2M_s t \tan\theta$ for the sample.

6.4.2 Irradiated lines with perpendicular magnetisation

Figure 6.8 shows a grid with perpendicularly aligned squares. In this case the lines are also perpendicularly magnetised, but in the opposite direction to the squares. A schematic of this magnetic arrangement is shown in figure 6.8(a). This situation would arise had the irradiated lines retained their perpendicular magnetic anisotropy and M_s but experienced a reduction in coercivity and so had reversed before the squares. Again, calculations have been carried out at $\theta=\pm30°$, figure 6.8(b,d). The difference signal between the oppositely magnetised lines and squares were measured from the corresponding intensity profiles, figure 6.8(c,e)

has a value of 1.15×10^{-8} Tnm. This again gives a measure of $2M_s t \tan\theta$ for the sample.

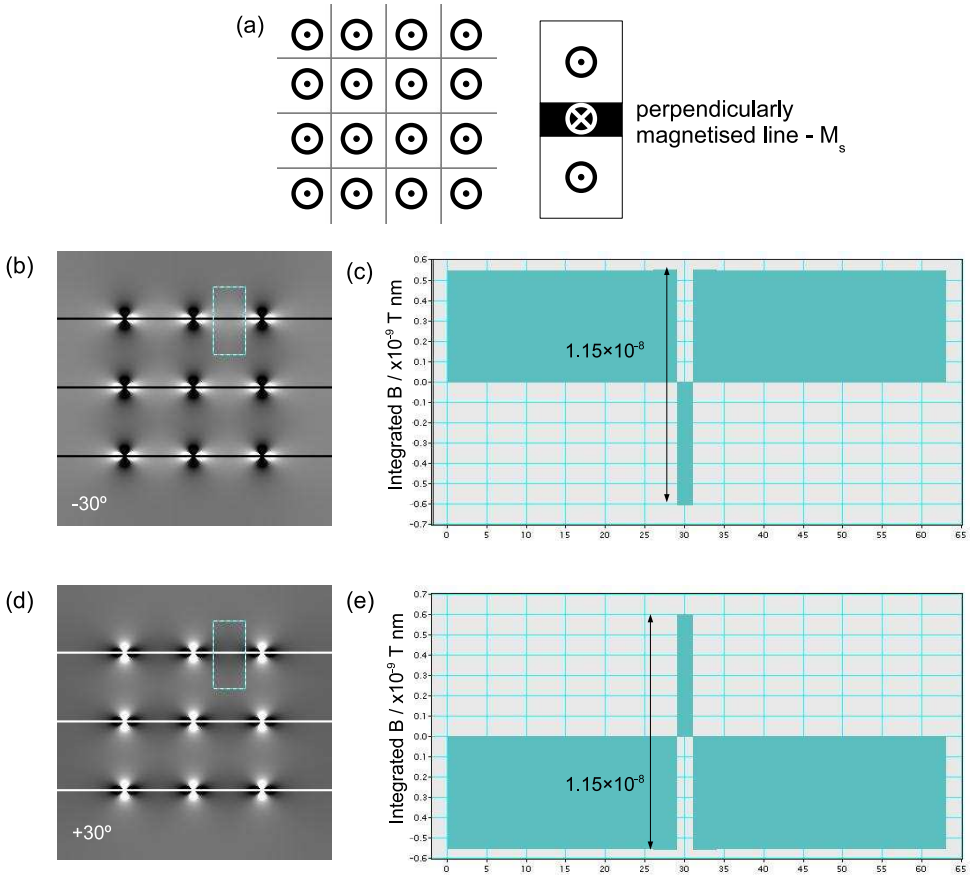

Figure 6.8: (a) Schematic diagram showing the patterned grid with perpendicularly aligned squares and perpendicular lines of opposite magnetisation direction. Simulated integrated induction in sample and corresponding intensity profile for this state at (b,c) -30° and (d,e) +30°.

Figure 6.9(a) shows an arrangement with alternating perpendicular magnetisation in the squares separated by perpendicularly magnetised lines. The integrated induction has been calculated for a sample tilt of $\theta=\pm30°$, and is shown in figure 6.9(b,d). The intensity profiles shown in 6.9(c,e) show similar characteristics to the equivalent situation with non-magnetic lines. The main difference is that in the region of the non-magnetic line the intensity is midway between the intensity from opposite squares, whereas here the line intensity is at the same level as the squares. Again the difference signals measured in this simulation show only a very small difference for $\theta=\pm$ 30° of between 1.085×10^{-8}Tnm and 1.13×10^{-8}Tnm.

From the simulations carried out so far we can conclude that it is possible to tell whether or not the magnetisation in the lines has been rendered non-magnetic due to irradiation. The squares have not been irradiated and so it is assumed

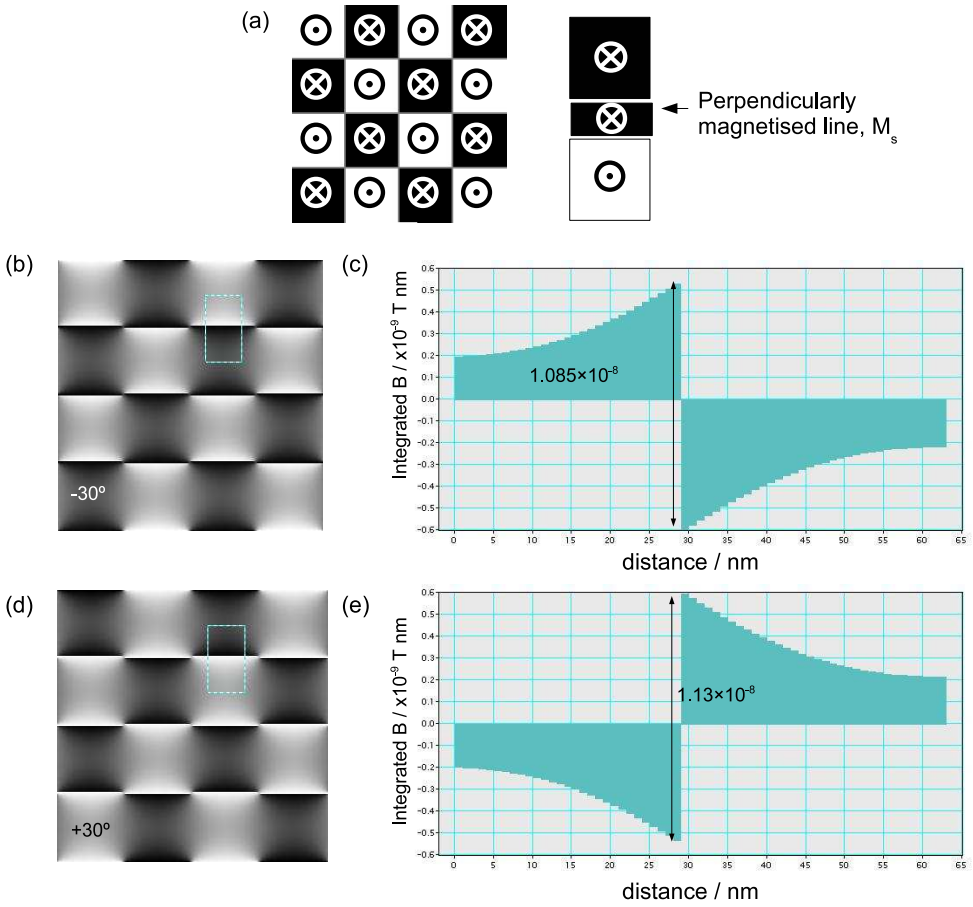

Figure 6.9: (a) Schematic diagram showing the patterned grid with alternating perpendicular magnetisation in the squares and perpendicular lines. Simulated integrated induction in sample and corresponding intensity profile for this state at (b,c) -30° and (b,c) +30°.

that they have not experienced any irradiation induced changes in coercivity or moment. As such the difference between two oppositely magnetised squares will be consistent and this measurement can be used as a reference during the simulations. If the lines are non-magnetic, then there will be a factor of approximately 2 difference between the measured signal when the squares are aligned parallel, and when they are aligned anti-parallel, as shown in figures 6.6 and 6.7. If the lines remain perpendicularly magnetised, the difference signal measured when the magnetisation in the squares is aligned parallel and anti-parallel remains constant, as is illustrated in figures 6.8 and 6.9. It would be possible to identify a reduction of the magnetic moment in the lines, as the size of the signal in the region of the line would be less than that of the squares. Differences in the expected signals from oppositely magnetised perpendicular squares with non-magnetic lines, perpendicular lines with M_s and with $0<M<M_s$ are shown schematically in figure 6.10.

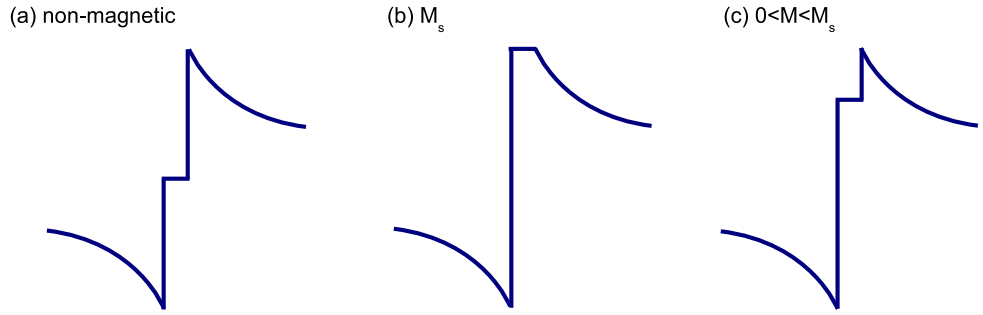

Figure 6.10: Schematic showing profile of induction signal for oppositely magnetised squares with (a) non-magnetic lines, (b) perpendicular lines and (c) perpendicular lines but with reduced M_s.

6.4.3 Irradiated lines with in-plane magnetisation

Now we consider the situation when the magnetisation in the lines has been rendered entirely in plane with unchanged M_s. The squares still have perpendicular magnetisation and original M_s. Figure 6.11(b,d) show the integrated induction of the sample when the squares are aligned perpendicularly and the lines are magnetised fully in-plane. The difference signals here, shown in figure 6.11(c,e), are equal on either side of zero tilt, which is what we expect when the magnetisation lies completely in-plane.

Finally, in figure 6.12, we have anti-parallel perpendicular magnetisation in the squares and in plane magnetisation in the lines. The simulated integrated induction is shown in 6.12(b,d), whilst the intensity profiles are shown in figure 6.12(c,e). Again the difference signals are equal either side of zero tilt, however, the intensity profiles are clearly different from any previous simulation. In 6.12 we can see the characteristic signal which arises from the oppositely magnetised squares, as in figures 6.7 and 6.9. However, also visible is an additional peak which is due to the induction from the in-plane magnetisation in the line. By taking these features into consideration, it is possible to distinguish between perpendicular and in-plane magnetisation by looking at a trace across two oppositely magnetised squares, as in figures 6.9 and 6.11.

This is true for the magnetisation being completely in-plane and having no reduction in M_s. Therefore the difficulty arises when the in-plane magnetisation has reduced moment. Depending on the extent of the reduction, the peak seen in the difference signal, as in figure 6.11, will also reduce and the profile will become similar to that for perpendicular magnetisation in the line.

Up until now the all the difference signals have been symmetric for a sample tilt

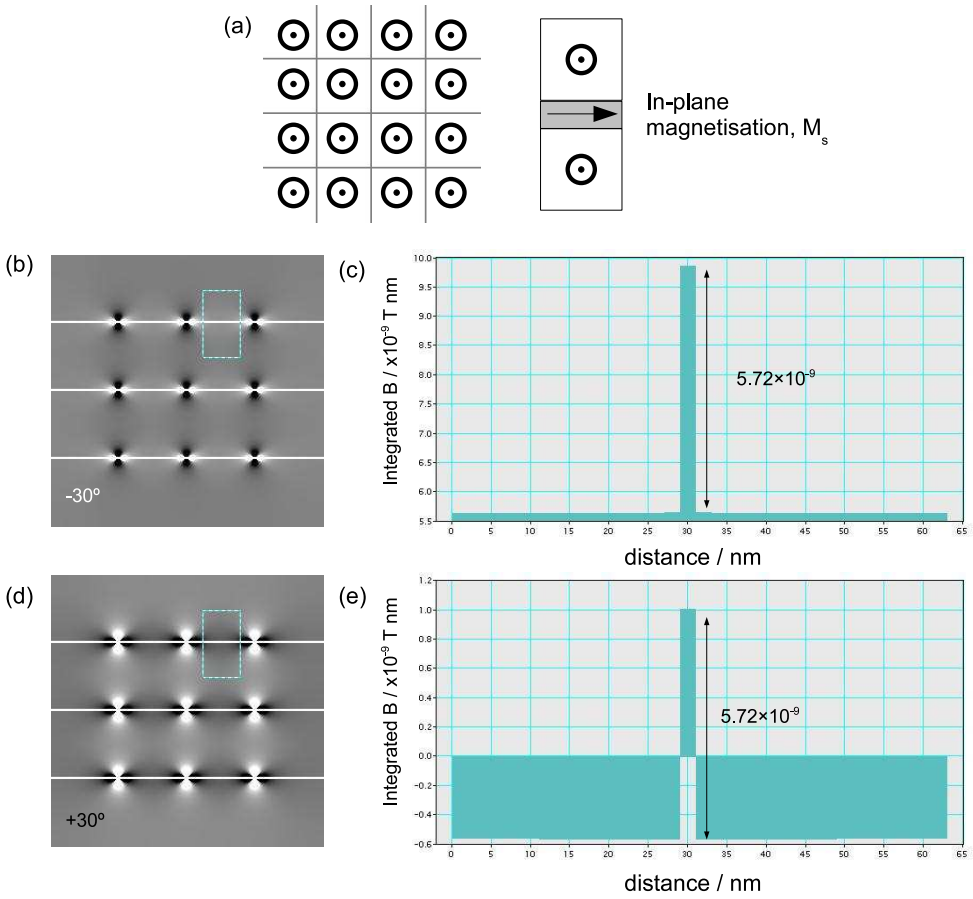

Figure 6.11: (a) Schematic diagram showing the patterned grid with aligned perpendicular magnetisation in the squares and in-plane magnetisation in the lines. Simulated integrated induction in sample and corresponding intensity profile for this state at (b,c) -30° and (d,e) +30°.

of $\pm\theta$. If the measured signals are not equal for $\pm\theta$, then we can conclude that the magnetisation is not fully in plane but at an angle φ, as depicted in the schematic in figure 6.5. If this is found to be the case, further analysis is required to be able to calculate the angle of rotation of the magnetisation and any potential change in M_s.

The rationale in carrying out all these simulations is to have a reliable guide as to the magnetic configurations that lead to observed images during magnetising experiments. These experiments are described in the following sections.

6.5 Experimental results

Initially the Fresnel mode of Lorentz microscopy was used so that an interesting magnetic state consisting of anti-parallel magnetisation in the squares, as well as

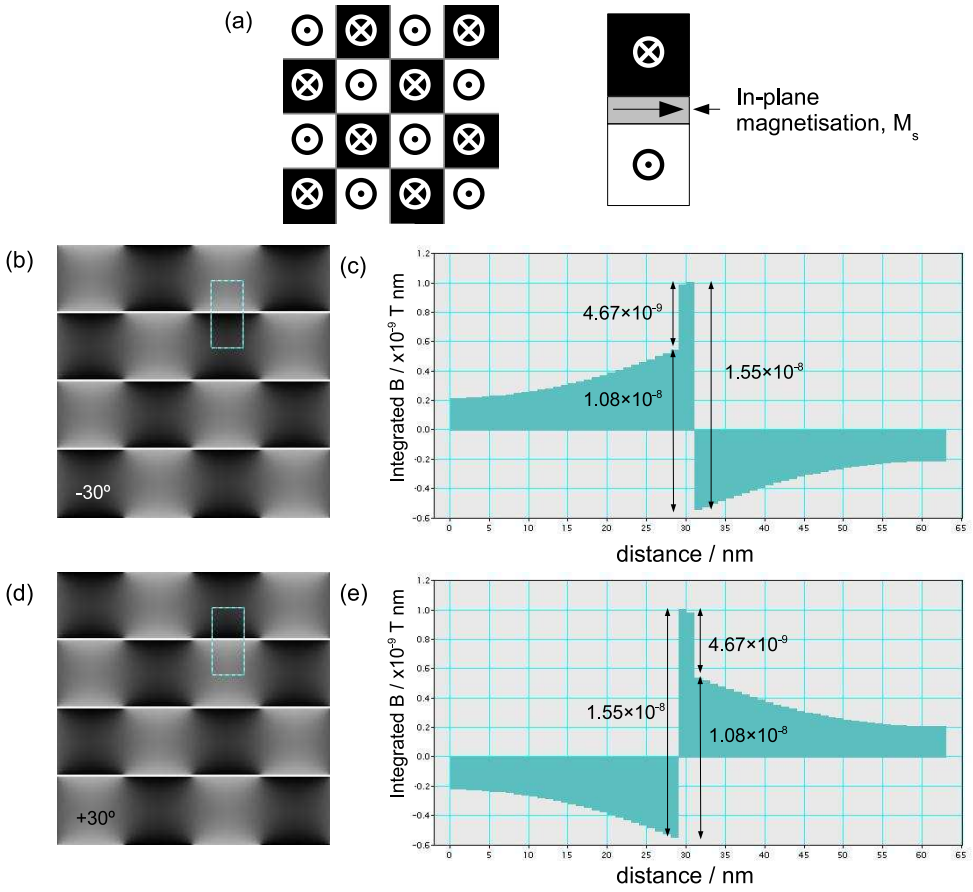

Figure 6.12: (a) Schematic diagram showing the patterned grid with aligned perpendicular magnetisation in the squares and in-plane magnetisation in the lines. Simulated integrated induction in sample and corresponding intensity profile for this state at (b,c) -30° and (d,e) +30°.

alternating in-plane magnetisation in the lines could be set up and observed. The desired magnetic state is shown schematically in figure 6.13. To achieve this state, a large perpendicular field, ∼6000 Oe is applied to saturate the magnetisation out of plane. As this field is returned to zero, the perpendicular magnetisation will remain unchanged whilst the irradiated lines will relaxed back in plane if they have a component of in-plane magnetisation. To obtain near-zero perpendicular magnetisation for the sample overall, it is necessary to apply a perpendicular field in the opposite direction so that the magnetisation in the squares will begin to reverse direction. To align the in plane magnetisation in the lines the specimen is tilted so as to create a component of the field in the plane of the sample.

Presented in figure 6.14 are Fresnel images of the grid pattern irradiated at 3×10^{13} ions cm^{-2}. The images are recorded after the sample was subjected to the alignment procedure outlined above. Images taken at θ=0, $\pm$30° are shown. It is expected that if the magnetisation is aligned perpendicularly, i.e. parallel to the

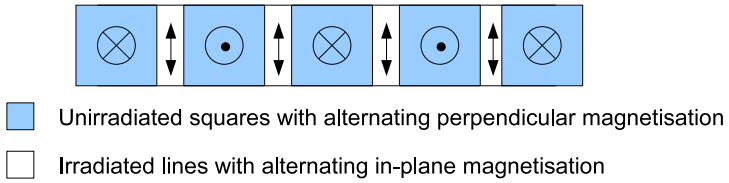

Figure 6.13: Schematic showing a single row of the irradiated grid supporting the ideal magnetic state for experiments, where alternating in plane magnetisation is present in the lines and alternating out of plane magnetisation in the squares.

electron beam, no Lorentz deflection will be seen in the images at zero tilt. However, Fresnel contrast would arise in the zero tilt images if there was any in-plane magnetisation. As can be seen in figure 6.14 at θ=0° there is no contrast due to the lines. In fact, the only contrast visible in these images is at the intersections of the lines which have experienced a slightly higher dose during irradiation of the pattern. These images are consistent with the magnetisation in the lines remaining perpendicularly magnetised.

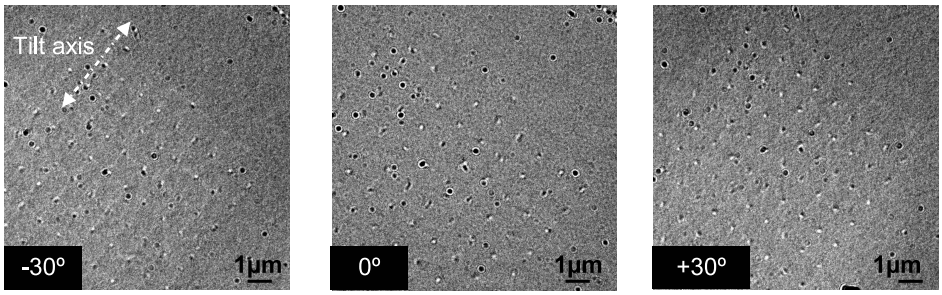

Figure 6.14: Fresnel images taken at different tilt angles of a grid irradiated at 3×10^{13} ions cm^{-2} at zero field.

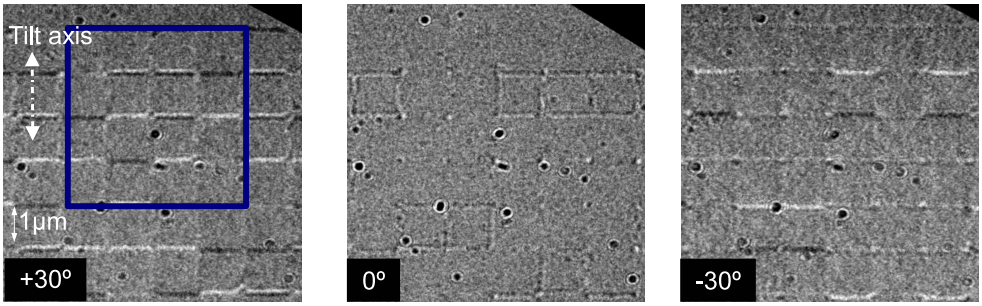

Figure 6.15: Fresnel image sequence showing the 3×10^{13} ions cm^{-2} with randomly orientated perpendicular magnetisation in the squares.

As the field was increased, the perpendicular magnetisation started to reverse in some of the squares, figure 6.15, as shown by the black/white lines. It was clear to see that the irradiation has had an effect on the magnetisation in the lines allowing the squares would not have to be able to behave independently.

On tilting the sample to θ=+30°, it is clear to see that the magnetisation is not in the same state as it was at θ=-30°, indicating that more of the perpendicular squares have switched.

For comparison, the reversal of a region of unirradiated film, and low dose regions is shown in figure 6.16, where irregularly shaped domains are formed.

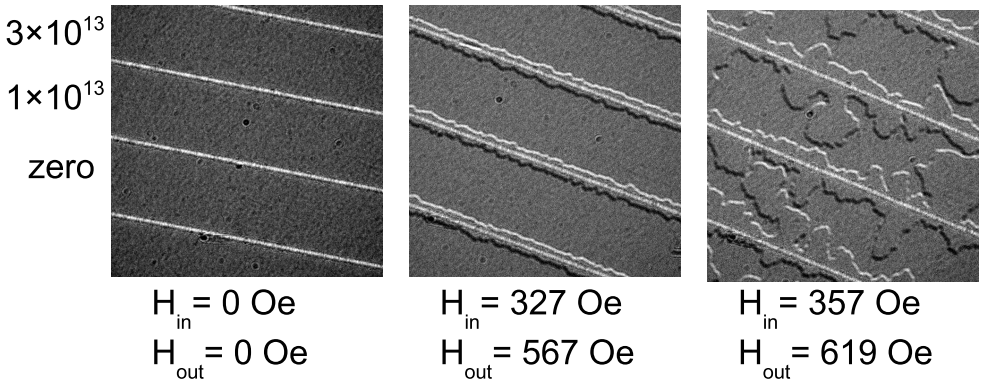

Figure 6.16: Fresnel images showing the reversal behaviour of the unirradiated film and low dose regions for varying applied field.

From these Fresnel image sequences it is possible to determine the magnetisation direction in the squares, but not in the lines. This is illustrated by the simulations in figure 6.17. From the selected area of 6.16(a), a grid pattern was created which represents the out of plane magnetisation, with the black and white squares representing oppositely magnetised squares. Using this grid, the Fresnel images shown in figure 6.17(b,c) were simulated. Figure 6.17(b) includes an in-plane component in the lines, and in figure 6.17(c) the lines are non-magnetic, yet there is no clear difference between the images.

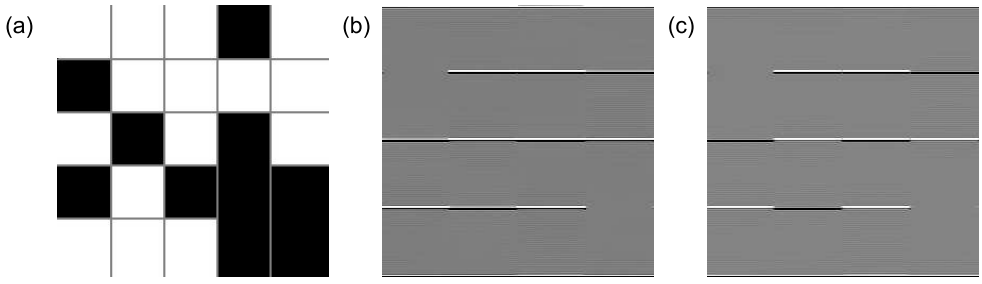

Figure 6.17: (a) Representation of the out of plane magnetisation in figure 6.16(a). Fresnel image simulated from the magnetisation distribution in (a) where (b) includes a component of magnetisation in the lines and (c) has non-magnetic lines.

However, the use of Fresnel imaging proved to be useful in identifying the conditions under which a varied magnetisation state could be achieved. It also showed

that this value of applied field, +800 Oe, was too close to the coercivity of the sample, and whilst tilting the sample from θ=+30° to θ=-30° more of the squares reversed. This is not ideal because as was explained in the previous section, it is necessary to have equivalent images at opposite tilt values so as to be able to draw conclusions about the in-plane magnetisation. Hence it is necessary to use DPC to extract this information.

6.6 DPC results

Prior to carrying out DPC experiments, the magnetic state of the sample was reset by following the procedure described earlier, but this time without increasing the field too close to the coercivity. Attempts were made to set the magnetisation in the lines and squares independently by use of appropriate fields. Achieving opposite magnetisation in the squares was fairly straightforward, but this was not managed for the lines in spite of repeated attempts to do so. Grids were patterned with higher doses in order to see if there was a stronger in-plane moment. However, grain growth in the lines and the associated increase in noise in the images made these even harder to interpret. In the following section the results are presented from samples irradiated with 1×10^{13} and 3×10^{13} ions cm^{-2}.

Figure 6.18 shows DPC images of a grid pattern irradiated with a dose of 3×10^{13} ions cm^{-2} and supporting randomly orientated perpendicular squares. No magnetic contrast is visible in the zero tilt image, 6.18(g). This would generally indicate that not only is there no in-plane component of magnetisation, but that the lines have been rendered non-magnetic. However, it is known from initial dose experiments on these samples, that the sample is not rendered non-magnetic until a dose of 3×10^{15} ions cm^{-2} is applied. It is likely that this dose instead of rotating the magnetisation direction to in-plane, has weakened the perpendicular coercivity of the line allowing it to reverse at a lower field than the unirradiated squares.

Due to the random orientations of the perpendicular squares we are able to make measurements from an area across two squares with the same magnetisation direction, region A, and two squares with opposite magnetisation, region B. Intensity profiles showing the difference signals across regions A and B, at θ=+30° are shown. Those taken at θ=-30° are shown in figure 6.18(e,f). The first observation made from these measurements is that they are not consistent with the

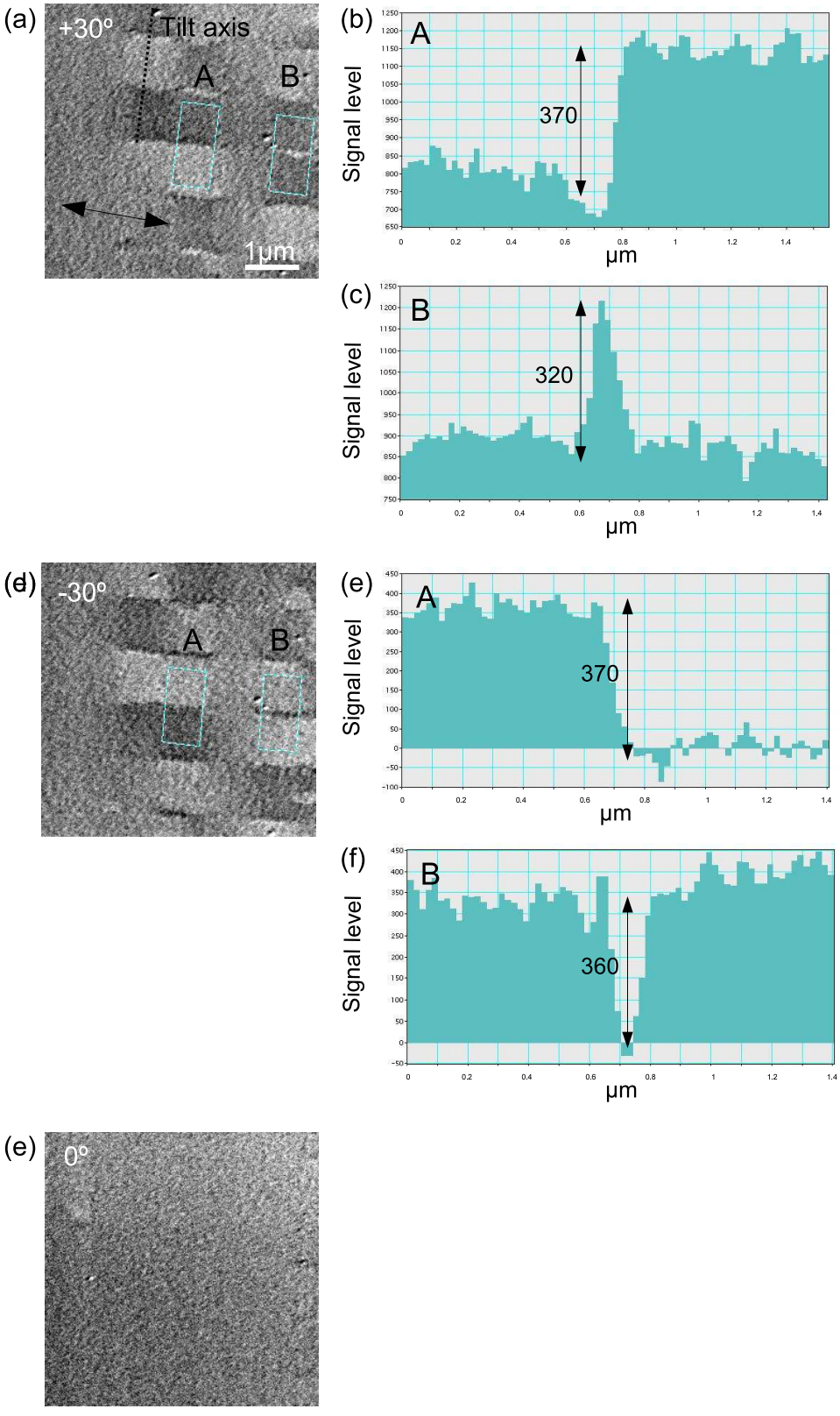

Figure 6.18: DPC images taken of grid irradiated with 3×10^{13} ions cm^{-2}

line being non-magnetic. This can be ruled out by directly comparing the signals from regions A and B. As was demonstrated in the simulations, figure 6.6 and 6.7, there would be a factor of 2 difference between the signals from A and B if the line had been non-magnetic. The signals measured are similar, ∼370 compared to ∼320, but are within the limits of the 25% error due to noise. The error is taken from the range of signals measured within the squares, which should be uniform. The signals are also symmetric on either side of zero tilt. This is consistent with the magnetisation in the lines retaining its perpendicular magnetisation, but experiencing a reduction in coercivity with respect to the unirradiated squares, as illustrated by the simulations in figures 6.8 and 6.9.

DPC results from another grid pattern irradiated with 1×10^{13} ions cm^{-2} are shown in figure 6.19 and 6.20. The images are taken from different parts of the same grid under the same imaging conditions. In the zero tilt image for this sample 6.19(e), some very faint magnetic contrast can be seen. This shows that there is some in-plane magnetisation in the lines. To determine whether the magnetisation is fully in plane or at an angle we must look at the difference signals across the line. Firstly we consider the difference signal across two aligned squares, 6.19 (a) and (c). The contrast in the images has reversed between +30° and -30°, although the intensity profiles shown in figures 6.19(b) and (d) show that the signal is not symmetric. This situation was not seen in any of the simulations carried out. However, from the schematic shown in figure 6.5 this is consistent with the magnetisation not being completely in plane, but an some angle φ to the normal of the sample.

To be able to use this to get some more useful information about the magnetisation in the line, we need to get a reference signal from two oppositely magnetised squares from the same grid. Such an arrangement is shown in figure 6.20.

The intensity profiles taken across two oppositely magnetised squares at $\theta=\pm30°$ are shown in 6.20(b,d) respectively. We can see that the signals measured are very similar, ∼160Tnm. It is not possible isolate the signal from the in-plane line and only the difference due to the oppositely magnetised squares is seen. The difference between $\theta=\pm30°$ is also symmetric. This is consistent with the magnetisation in the line being perpendicular and with no change in M_s. However, we know that there is an in-plane component from observations of the zero tilt images and the signal between aligned squares. Therefore it is likely that the signal due to the line is still there, but is indistinguishable from the difference signal between the squares.

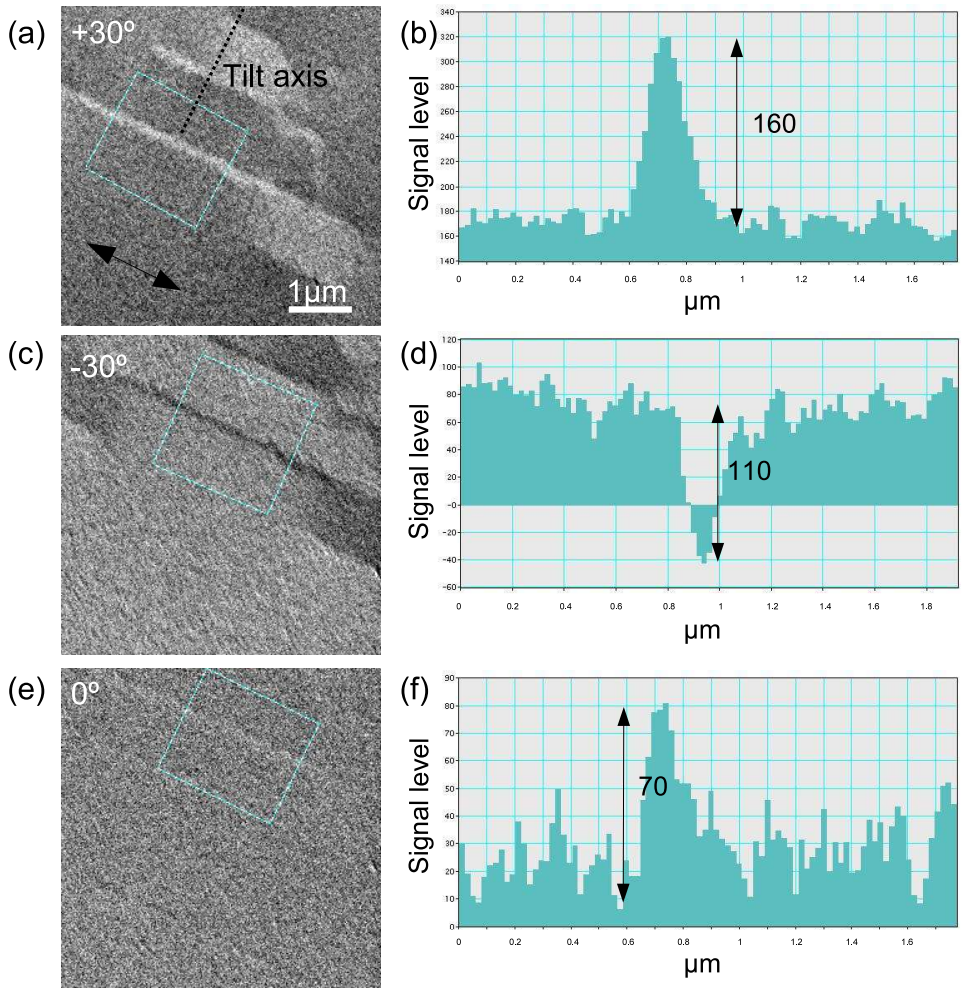

Figure 6.19: DPC images of the grid irradiated at 1×10^{13} ions cm^{-2}, at (a) 30°, (b) -30° and (c) 0°. The tilt axis is shown and the double headed arrow indicated the direction of magnetic induction that the image is sensitive to.

6.7 Conclusions

In this chapter the irradiation of Co/Pd multilayer films is carried out with the aim of investigating the perpendicular to in-plane transition that occurs. A grid pattern was devised and patterned for a range of doses in order to be able to witness the effect of irradiation on the extent to which the magnetisation is rendered in plane. Simulations of the integrated magnetic induction for a variety of possible magnetic configurations in the squares and lines were carried out, and from these several key trends were observed.

From the simulations carried out it was deemed possible to be able to determine if the magnetisation in the irradiated lines was non-zero, perpendicular but with reduced coercivity or lying completely in the plane of the film with original M_s,

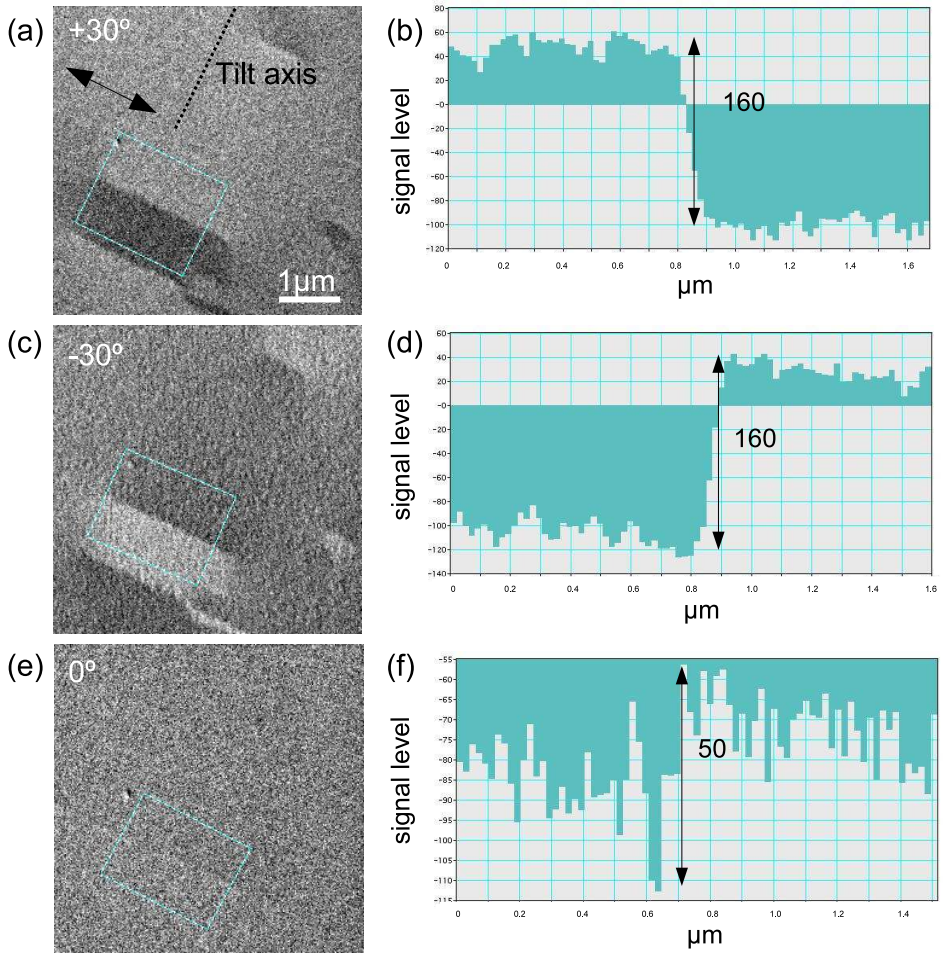

Figure 6.20: DPC images of the grid irradiated at 1×10^{13} ions cm^{-2}, at (a) 30°, (b) -30° and (c) 0°. The tilt axis is shown and the double headed arrow indicates the direction of magnetic induction that the image is sensitive to.

simply by comparing difference signals in the integrated induction maps. If the line was non-magnetic, then the difference signal between two squares with the same perpendicular magnetisation would be half that when the difference signal was measured between two squares with opposite perpendicular magnetisation. If the line was perpendicular, then the difference signals would be the same when measured over aligned squares and oppositely aligned squares. It is also possible to determine if the perpendicular line has suffered a reduction in moment. Finally, the line could be said to be in-plane if there was an additional peak in the signal over and above that of the difference signal between the two squares. This could only be determined from the simulation with 2 oppositely aligned squares.

It was observed that all of these signals were symmetric at $\theta=\pm\theta$. This was to be expected as the direction of the magnetisation in the zero, perpendicular and in-plane configurations could all be symmetrically tilted about the normal of the

film. An asymmetric signal is the signature of a line with magnetisation at an angle between perpendicular and in plane.

These calculations provided a much needed insight into difference signals that are characteristic of a particular magnetic state. They were also a useful guide as to the contrast that can be expected during DPC magnetising experiments.

The Fresnel mode of Lorentz microscopy was used to help set the state of the irradiated samples. Controlling the perpendicular and in-plane magnetisation with appropriate fields at first appeared to be a straightforward alignment procedure. Indeed, setting the perpendicularly magnetised into an anti-parallel alignment was easily done. However, gaining control over the magnetisation in the lines proved much more challenging, and occassionally no magnetic contrast was seen from the in-plane lines at all. It is possible that the in-plane magnetisation was very weak and the signal could easily get lost in the noise of the images. It is also possible that the magnetisation was magnetised in plane immediately prior to irradiation in FIB, but after saturating it with a strong out of plane field, it did not relax back in-plane, but either retained some or all of the perpendicular anisotropy. On the occassions that in-plane magnetisation was detected it was a weak signal. All in all it was not found to be possible to reproduce a range of magnetic states for investigation.

From the DPC images that are presented, some conclusions could be drawn. The first grid presented which had been irradiated with 3×10^{13} ions cm^{-2} showed no contrast in the zero tilt image. This suggested that the magnetisation in the lines had either been reduced to zero or had remained perpendicular but with reduced coercivity. The difference signals ruled out the option that the lines were non-magnetic but were consistent with the lines having perpendicular magnetisation. However, this result conflicts with reports in the literature that by a dose of 1×10^{13} ions cm^{-2} perpendicular magnetisation in both Co/Pt and Co/pd samples had been rendered in plane. Therefore, another possibility is that the magnetisation in the line has been rotated away from perpendicular and has reduced moment. This would provide a similar signal profile to that observed for the sample, but again does not account for the lack of contrast in the zero tilt image. However, it is possible that any in-plane magnetisation would be weak and not able to be detected.

The second set of DPC images did show some magnetic contrast in the zero tilt image, and had difference signals that were asymmetric at a sample tilt of $\pm30°$.

This was consistent with there being magnetisation in the line at an angle φ. Another trace was taken from a different region of the grid in order to get a difference signal across two oppositely magnetised squares. There was no clear signal from the line in this measurement, but as the difference signal here was comparable to the size of the signal due to the line it is possible that it was lost in the difference signal from the squares. Much more detailed analysis of the magnetic state would be required here to obtain a specific angle of rotation or reduction in M_s, but this was not possible here due to severe time restraints.

Many more images were recorded in attempts to measure signals across a variety of magnetic states. However, due to the lack of control that was able to be obtained over the in-plane magnetisation, no definitive state with randomly aligned perpendicular and in-plane magnetisation was observed. This is what would have been required in order to do a thorough analysis of the magnetism in the lines subsequent to irradiation.

Bibliography

[1] E. Suharyadi, S. Natsume, T. Kato, S. Tsunashima, and S. Iwata, IEEE Trans. Mag. **41**, 3595 (2005).

[2] R. Hyndman *et al.*, J. Mag. Mag. Mat. **240**, 50 (2002).

[3] R. Hyndman *et al.*, J. Appl. Phys. **90**, 3843 (2001).

[4] T. Devolder, Phys. Rev. B **62**, 5794 (2000).

[5] P. Warin *et al.*, J. Appl. Phys. **90**, 3850 (2001).

[6] C. Chappert *et al.*, Science **280**, 1919 (1998).

[7] E. Suharyadi, T. Kato, S. Tsunashima, and S. Iwata, IEEE Trans. Mag. **42**, 2972 (2006).

Chapter 7

Conclusions & future work

The ability to tailor the magnetic properties of materials on the nanoscale is a critical step forward towards a variety of proposed technologies [1, 2, 3]. In this thesis, modification and patterning of magnetic thin film systems has been demonstrated, quantified and used to create devices that were suitable for the study of magnetic domains and magnetic domain walls. All irradiation was performed using 30kV Ga^+ ions in a focused ion beam system. The physical microstructure and magnetic behaviour were characterised by TEM, both prior to and subsequent to irradiation. As a result of the irradiation, changes in the grain size and magnetic behaviour were observed. At a sufficiently high dose, the thin films were rendered non-ferromagnetic, which meant that magnetically isolated structures could be created in the continuous film. Ion irradiation was then used to modify specific regions of the magnetic structures in an attempt to control the formation of domains and domain walls within them.

7.1 Conclusions

In chapter 3 the magnetic and structural properties of magnetic thin film systems consisting of permalloy and one or more non-magnetic layers, of either Au or Al, were investigated. Structural characterisation by bright field imaging and diffraction showed that the samples were polycrystalline, with a mean grain size of 5nm. Lorentz microscopy was used to characterise the magnetic behaviour of the samples, which were found to have weak anisotropy in spite of having been deposited in the absence of any applied field. The magnetisation reversal of the

samples displayed typical easy and hard axis behaviour and had a coercivity of ∼2 Oe. The samples were irradiated with a range of ion doses from 1×10^{13} to 3×10^{16} ions cm^{-2}, and the resultant changes in both structural and magnetic properties were studied. It was found for all the samples that doses of 3×10^{14} ions cm^{-2} and below had no visible effect on either the structural or magnetic properties. Above this dose, irradiation induced changes began to become apparent. Systems with Al cap layers experienced grain growth, but retained the grain shape, whereas systems with Au cap layers experienced both grain growth and a change in the grain morphology. With increasing dose, a reduction in the mean moment of the samples was observed as a reduction in magnetisation ripple in the dosed regions. At a dose of 3×10^{16} ions cm^{-2} samples which had a 20nm thick layer of permalloy were rendered non-ferromagnetic, whilst those with 10nm of permalloy underwent the same transition at a lower dose of 1×10^{16} ions cm^{-2}. The addition of non-magnetic layer on either side of the 10nm NiFe layer caused this system to be rendered non-magnetic at 3×10^{15} ions cm^{-2}. Importantly, for the doses that were required to render the 10nm NiFe films non-magnetic, milling <4nm had occurred meaning that the magnetic layer had not been compromised. In the following chapters, this knowledge of the effect of dose on the magnetic properties of the thin film systems was used to fabricate and subsequently modify nanoscale magnetic elements.

Magnetic and structural characterisation of a zigzag structure with end shapes designed to favour the formation of an anti-parallel domain state was carried out in chapter 4. The design of the structure takes advantage of the fact that magnetisation in a soft magnetic material, such as permalloy, will tend to align with the edges of a magnetic structure. OOMMF simulations showed that in order for the zigzag structure to support an array of alternately magnetised domains, a line defect or modified region must be included across the structure to break the exchange coupling between adjacent domain regions. In the experiments this was realised by irradiating a single line across the element. The zigzag structures were milled with the 10pA ion beam onto 10nm NiFe / 5nm Al. Initially this defect region was milled, but in subsequent experiments the dose was reduced to investigate the minimum disruption or modification that was required for the anti-parallel state to form. It was found that only the milled structure allowed an array of domains with anti-parallel magnetisation to form. Patterning the defect line with lower doses still had a significant effect on the magnetisation distribution in the sample, but the magnetisation in the domains did not lie completely along the structure the axis of the structure, but at a slight angle. The lowest dose

which had this effect was a dose of 3×10^{15} ions cm^{-2}. The width of the lines was seen to decrease with decreasing dose, and it was also observed that no milling of the sample surface had occurred.

In chapter 5 domain walls in magnetic nanowires fabricated by FIB irradiation were studied. For potential spintronics applications a fundamental understanding of domain wall formation, propagation and pinning is required. Domain wall trap structures were fabricated by ion irradiation and were found to behave in a manner consistant with those made by e-beam lithography. It was found that the vortex domain structure was the preferred wall type for the 300-500nm wide wires fabricated in a system with 10nm NiFe. In place of geometrical notches or protrusions, irradiated lines were introduced along the wire to act as pinning sites. It was found that the ability of the irradiated site to pin a domain wall depended on the dose used to pattern the site and the orientation of the site relative to the length of the wire. For a vertical pinning site to be effective, the irradiated dose had to be 3×10^{15} ions cm^{-2}. However when the angle of the irradiated site was changed to match the orientation the central wall in a vortex domain wall packet, $\sim45^{\circ}$, a pinning site irradiated at 1×10^{15} ions cm^{-2} was successful. It was also noted that the domain wall was much more stable at the angled site and required a larger field to depin it from the site. It was observed that the chirality of domain wall always matched the orientation of the pinning site. A nanowire attached to a large ellipse injection pad was used to investigate this further. This wire geometry allows a vortex domain wall of known chirality to be injected into the wire, and enabled a study of the pinning of domain walls with differently orientated pinning sites. It appears that vortex domain walls which have a symmetry mismatch with the intended pinning site, rotate so that the orientation of the core of the domain wall packet matches the orientation of the pinning site. This could prove to be a novel way to control the chirality of domain walls in nanowires as well as being able to reproducibly pin them at pre-defined locations.

The effects of ion irradiation on Co/Pd multilayers with perpendicular magnetic anisotropy was investigated in chapter 6. The aim was to investigate the variation of induced in-plane magnetisation in a perpendicularly magnetised sample due to irradiation. Simulations were a useful tool in determining the signals expected from a number of known configurations. From these, several key observations were made which helped to interpret the DPC images. However, the information in the DPC images was not as useful as it had been hoped.

7.2 Future work

This section details possible future work that could be carried out to aid the understanding of the irradiation effects on the permalloy systems that have been investigated here. Also discussed are possible developments of the magnetic structures described in chapters 4 & 5, as well as further work to complete the analysis of the perpendicularly magnetised Co/Pd films.

One key outcome from this work is the observation that relatively minor processing and fabrication details can have a profound effect on the magnetic properties of a thin film system and on the response of the system to ion irradiation. It is clear that in future, cross-sections should be made of the samples, followed by high resolution TEM to confirm the thicknesses of the different layers, so that irradiation effects can be qualified accordingly. Further analysis of the irradiated systems by use of magneto-optical Kerr effect microscopy (MOKE) would provide much needed insight into any reduction in magnetic moment or anisotropy that occurred as a result of irradiation. This would provide an alternative and possibly more accurate method for obtaining these values, rather than approximating them from a series of Fresnel images. Additionally, future work in this area could involve chemical or compositional analysis to investigate the actual concentrations of Al and Au that were mixed with the NiFe layer, and be able to determine a threshold value for the concentration of the impurity required to render the NiFe layer non-magnetic.

There are many possible avenues with which to continue the work shown in chapter 4. It was shown that the zigzag structure was able to support an array of domains with alternating magnetisation directions. However, as was seen in the DPC images presented there remained a component of magnetisation along the hard axis of the structure. An amendment to the shape, for example increasing the aspect ratio of the structured ends, may help to align the magnetisation in the structure and cause it to lie parallel to the easy axis in anti-parallel alignment at zero field. It may be worthwhile to pattern these structures on magnetic thin film systems that are known to be much more sensitive to irradiation, for example CoFe or exchange bias systems, so that lower doses could be used to the same effect. These structures are also ideal candidates for making measurements of domain wall magnetoresistance. A particularly interesting possibility would be to use the zigzag structures to measure domain wall magneto-resistive effects. Electrical contacts positioned on the top and bottom domain regions of

the structure would allow a current to be passed perpendicular to the domains and the resistance of different magnetic states to be measured. Currently a TEM rod is being developed which would allow this to be carried out in-situ so that corresponding images of the magnetic state could be recorded.

In chapter 5 the interaction of magnetic domain walls with irradiated pinning sites was investigated and was shown to be a successful way of trapping domain walls at predefined sites. Now that the relationship between the chirality of the domain wall pinned and the orientation of the pinning site has been established, it would be useful to return to the original experiments of chapter 5, involving domain wall trap structures. By doing so, domain walls could be set up in the wire and their structure recorded before they are propagated along the wire to the pinning site. This would allow changes in domain wall structure due to the interaction with the pinning site to be directly observed. Following from this there are many potential experiments that could be carried out, such as varying the orientation of the irradiated lines along the wire to observe how reproducibly the structure of the domain wall can change, or to try and move the domain wall back and forth between two pinning sites.

Finally, in chapter 6 it was not possible to reach a definitive conclusion as to the effects of ion irradiation on perpendicularly magnetised Co/Pd films. Controlling the in-plane and perpendicular magnetisation independently proved to be particularly difficult in these samples, and only a small variety of magnetic configurations were seen. Observations of the magnetic induction in a variety of in-plane and out of plane magnetisation states over a range of dose is required. The signal to noise ratio in the images was poor making accurate measurements of the difference signals impossible. Further refinement of the pattern could be investigated to include larger irradiated regions so that relative signals can be averaged over a larger area. It would also be useful to carry out MOKE measurements on irradiated regions of the sample to determine if there has been a loss of moment. This would eliminate one of the unknowns from the problem and would ease the interpretation of results.

Bibliography

[1] S. S. P. Parkin, Int. J. Mod. Phys. B **01**, 117 (2008).

[2] D. A. Allwood, G. Xiong, and R. P. Cowburn, Appl. Phys. Lett. **89**, 102504 (2006).

[3] R. D. McMichael, J. Eicke, M. J. Donahue, and D. G. Porter, J. Appl. Phys. **87**, 7058 (2000).